Fritz Laboratory Reports   Civil and Environmental Engineering

1976

Stress concentration and fatigue of welded details, Ph.D. dissertation, October 1976

Nicholas Zettlemoyer

STRESS CONCENTRATION AND

FATIGUE OF WELDED DETAILS

by

Nicholas Zettlemoyer

A DISSERTATION

Presented to the Graduate Committee

of Lehigh University

in Candidacy for the Degree of

Doctor of Philosophy

in the

Department of Civil Engineering

Lehigh University

Bethlehem, Pennsylvania

October 1976

CERTIFICATE OF APPROVAL

Approved and recommended for acceptance as a dissertation
in partial fulfillment of the requirements for the degree of
Doctor of Philosophy.

_8-12-76_
(date)

John W. Fisher
Professor in Charge

Accepted: _8-27-76_
(date)

Special Committee directing
the doctoral work of
Mr. Nicholas Zettlemoyer

Professor L. S. Beedle
Chairman

Professor R. Roberts

Professor J. H. Daniels

Professor A. Ostapenko

Professor D. A. VanHorn

ii

iii

The author's wife, Jan, deserves special recognition for a distinct and crucial tenacity of her own during the past four years.

TABLE OF CONTENTS

TABLE OF CONTENTS (Cont.)

LIST OF TABLES

LIST OF FIGURES

x

LIST OF FIGURES (Cont.)

LIST OF FIGURES (Cont.)

xv

ABSTRACT

Accurate prediction of the fatigue life of structural de-
tails primarily depends on knowledge of the range of stress intensity
factor during crack growth. Stress intensity, in turn, depends on
stress distribution, crack shape and length, and crack tip position
in the detail. The main thrust of this dissertation is the determi-
nation of the stress concentration at typical welded detail termina-
tions and the evaluation of how this altered stress distribution
affects stress intensity.

Both fillet- and groove-welded details are studied. The
findings show that stiffeners welded to flanges have a maximum stress
concentration factor between three and four. Cover plates with
transverse end welds have a maximum concentration factor between six
and eight. Gusset plates groove-welded to flange tips and possessing
circular transitions at their ends generally exhibit a maximum concen-
tration factor below three. Lap-welded gussets are similar to cover
plates which have a greater width than the flange. Longitudinal
stiffeners with circular transitions are comparable to groove-welded
gussets with circular transitions. Longitudinal stiffeners and

-1-

groove-welded gussets without circular transitions are roughly analogous to stiffeners with the weld angle depending on taper.

The stress concentration distribution along the prospective crack path is translated into a stress intensity correction factor, depending on crack length, through use of the Green's Function proposed by Albrecht. The resulting correction curve for each geometry is correlated with stress concentration factor decay from either axis end of an elliptical hole in an infinite plate. Formulas for proper ellipse shape and size are subsequently developed which depend upon detail type and specific values of geometric parameters, and permit the prediction of the stress intensity correction for arbitrary geometries.

The interactions of the stress distribution correction factor with the corrections for crack shape and free surfaces are evaluated. New stress intensity expressions are devised which unify the various corrections. These expressions are then used to predict the fatigue lives of experimentally tested details. The life results are typically on the high side of the experimental findings although well below the upper 95 percent confidence limit.

Several by-products of the stress concentration investigation are quite important. Crack coalescence is considered for the first time in the estimation of crack shape during growth. Also, it seems clear that the fatigue limits currently set in AASHTO should be reexamined for several variable geometric parameters.

1. INTRODUCTION

1.1 Problem and Solution Approach

Fatigue failure of steel highway bridges has received much research attention in the past decade for several reasons. First, there has been a steady rise in vehicle frequency over the years and gross weight has also increased, thereby causing the remaining fatigue life of many existing structures to be seriously questioned. Second, welded details have become quite common in bridges and ones with a high accumulation of stress cycles have shown fatigue distress. Welded details are more susceptible to fatigue crack growth than are riveted and bolted ones due to the nature of load transfer in a welded joint and the fact that all welds have inherent, initial discontinuities. Finally, spectacular fracture failures of the Point Pleasant "Silver" Bridge in West Virginia[68] and the King's Bridge in Australia[52] have focused interest on fracture's sister characteristic, namely fatigue performance, as well as fracture itself.

The 1974 Interim AASHTO Bridge Specifications[3] incorporate the findings of two major research programs[19,20]. Through extensive testing, it was found that stress range, S_r, and category of detail are the parameters which are most influential on fatigue life. The allowable stress range values in Table 1.1 (AASHTO Table 1.7.3B[3]) are simply extracted from the Fisher experimental S_r-N curves of Fig. 1.1[21]. These curves represent 95 percent confidence limits (in cycles) for 97.5 percent survival at a given stress range.

Recent years have also seen great strides in the development of techniques to analytically predict fatigue life. It was Paris who, in considering only propagation, recognized that within limits fatigue crack growth per cycle, da/dN, can be empirically related to stress intensity factor, K, from linear fracture mechanics[35], as follows[60]:

$$\frac{da}{dN} = C \ (\Delta K)^n \tag{1-1}$$

where ΔK is the range of stress intensity factor and C and n are based on material properties. By rearranging Eq. 1-1 and integrating between the initial and final crack sizes (a_i and a_f, respectively), the number of cycles, N, can be predicted as:

$$N = \frac{1}{C} \int_{a_i}^{a_f} \frac{1}{(\Delta K)^n} \ da \tag{1-2}$$

If stress range is included in the expression, it takes on the following form:

$$N = \left[\frac{1}{C} \int_{a_i}^{a_f} \frac{1}{(\Delta K/S_r)^n} \ da \right] S_r^{-n} = A S_r^{-n} \tag{1-3}$$

A represents the parameter which Fisher experimentally found changed value for different types of details and therefore resulted in the various category curves (Fig. 1.1)[21]. The slope of these log-log curves, $-n$, is approximately constant at -3.0 for all categories[20,32]. C can be taken as constant for typical bridge steels (A36, A441, A514)[20,32]. Initial crack size, a_i, is known approximately for common welded details[20,32] and a_f, being much larger than a_i, is of little

-4-

consequence. Thus, fatigue life prediction for crack propagation squarely rests on the evaluation of the stress intensity factor range for the detail.

The range of stress intensity factor is often expressed as ΔK for a central through crack in an infinite plate under uniaxial stress, adjusted by numerous (superimposed) correction factors[2,50,62,65].

$$\Delta K = CF * S_r \sqrt{\pi a} = F_s F_w F_e F_g * S_r \sqrt{\pi a} \qquad (1-4)$$

CF is the combined correction factor as a function of crack length-plate width ratio $\frac{a}{w}$, crack shape ratio $\frac{a}{b}$, and geometry. F_s is the correction associated with a free surface at the crack origin (the front free surface), F_w accounts for a free surface at some finite length of crack growth (also called the back surface or finite width correction), and F_e adjusts for shape of crack front (often assumed to be elliptical with major semidiameter b and minor semidiameter a). While in fracture problems stress intensity often includes a plastic zone correction factor, F_p, such is usually disregarded in fatigue analyses since small stress ranges and reversed yielding cause the crack tip plastic zone to be small (Art. 4.4)[66].

F_g is the factor which accounts for either a nonuniform applied stress (such as bending) or a stress concentration effected by the detail geometry. This stress gradient should not be confused with that which occurs at the crack tip, regardless of applied stress field or detail geometry. F_g corrects for a more global condition

than exists at the crack tip. Yet, for stress concentration situations F_g corrects for a more local condition than the nominal stress (strength of materials type) at the detail. Whether the applied stress is nonuniform or a stress concentration exists, S_r represents an arbitrarily selected stress range (usually the nominal maximum value at the detail). Therefore, F_g is inseparably linked to the choice of S_r.

Values of the various correction factors are dependent on the specific overall geometry, crack shape, and distribution of applied stress. Solutions for CF of many idealized problems are available [62,76,81,82]. However, practical bridge details present distinct analytical difficulties – particularly in evaluating F_g. Cracks normally emanate from weld toes[19,20] near which varying degrees of stress concentration exist. For some geometries the crack quickly grows out of this concentration region; for other geometries the effect of concentration is sustained over a broad range of crack sizes. Fillet-welded connections have the added difficulty that they present a theoretically singular stress condition (neglecting yielding) right at the weld toe. Therefore, F_g has been impossible to obtain in a closed-form fashion. Numerical techniques such as the finite element (F.E.) method normally must be employed. In short, existing solutions don't account for the geometric variables or concentration effects encountered in real life details. Yet, F_g is considered of great importance in predicting fatigue failure of bridges[20].

Based on Eq. 1-2 life prediction involves summing the cycle lives for increments of crack growth. F_g as well as other correction factors must be known for each increment. Two approaches are available for determining F_g for varying crack size; both involve finite element analyses. The first, normally termed a compliance analysis, necessitates analyzing the detail for different lengths of embedded crack. The strain energy release rate, G, is found as a function of the slope of the compliance-crack length curve[34]. Irwin showed that there is a direct relationship between G and the stress intensity factor[35,36]. Thus, K can be found and compared, if desired, with some base K for a specimen lacking the influence of a stress gradient (i.e. F_g = 1.0). The ratio of the two stress intensity factors yields F_g for the actual detail under investigation.

Method one can be very expensive in terms of computer usage and can easily require extensive personnel time to revise F.E. mesh data for each crack length of each detail. Method one also presents accuracy difficulties at very small and very large crack depths. Fortunately, a more reasonable alternative exists which requires only one stress analysis for a given detail geometry. Bueckner and Hayes showed that G can be found from the stresses in the crack free body which act on the plane where the crack is to exist[13,31]. Irwin implied the same point when he found G by considering the energy needed to reclose a crack[35]. Based on this concept (often called superposition or difference state) it is possible to describe known stress intensity solutions for stresses or concentrated loads applied directly

to crack surfaces as Green's Functions for loading remote from the crack[62,81,82]. The stress or concentrated load is simply adjusted to suit the stress distribution along that plane with the crack absent. (A concentrated load is represented by stress applied to an incremental area. Through integration, numerical or closed-form, any stress distribution can be represented.) Depending on which Green's Function is used, F_g alone or a combination of correction factors can be evaluated.

The versatility and relative ease of method two are apparent. The only requirement is that the crack path be known. Since actual tests have provided information on crack paths (Art. 3.1)[20,21,22], method two is employed in the dissertation.

1.2 Objectives and Scope

The principal objective of this study is the development of an F_g prediction for welded details common to bridge structures. The objective is reached in four steps. First, two- or three-dimensional stress analyses, using finite elements, are made of details with particular geometries. The stress distribution and maximum stress concentration factor, SCF, along the eventual crack path are determined. Second, these distributions of stress are transformed into distributions of F_g by application of an appropriate Green's Function. Third, the F_g distributions are correlated with stress decay curves for the end of an elliptical hole in an uniaxially stressed, infinite plate. The ellipse size is based on the

correlation. Finally, empirical formulas are developed to predict the proper ellipse size (and therefore F_g) for arbitrary detail geometries.

Three other objectives are part of the investigation; each is affected by the local stress field found for the principal objective. First, correction factors other than F_g are modified for the presence of a nonuniform stress as well as varying crack shape. Next, unified stress intensity expressions are developed for the nonuniform stress fields by the superposition (of stress intensities) procedure[81,82]. Lastly, the new stress intensity relationships are used to predict fatigue lives of several laboratory specimens and one actual bridge structure.

In this dissertation details are placed into two broad categories - fillet-welded and groove-welded. Within the fillet-welded category are cover plates and transverse stiffeners. Both are connected to flanges with fillet welds. The groove-welded category contains gusset plates with circular transitions and groove-welded to flange tips, and longitudinal stiffeners groove- or fillet-welded to a web or flange.

Several important assumptions are made for all details. First, they are considered to be symmetrically positioned about the beam/girder web. Second, the beam/girder is assumed to have a small flange thickness-to-member depth ratio so that little nominal

stress gradient exists through the flange thickness. Thus, uniform stress may be used as input in the analysis without significant error. In actual bridge members the nominal shear stress in the flange is small and is therefore neglected in this study.

An existing finite element computer program, SAP IV[8], is used for the stress analysis. The program is intended for linear elastic systems and does not provide special elements for stress singularity conditions. Nevertheless, sufficient elastic stress accuracy can be attained, even in regions of high stress concentration, through proper selection of mesh size.

1.3 Summary of Previous Work

It has long been recognized that structural details or any sudden changes in geometry produce a stress concentration effect. Strength of materials and elasticity texts abound with solutions (closed-form and otherwise) to plates with holes and notches and other configurations. Peterson summarizes the stress concentration studies of particular importance in machinery design and some structural applications[63]. Many of these solutions resulted from photoelastic investigations.

Certain fillet-welded joints, particularly the lap type, have also undergone photoelastic analysis for stress distribution[14,58,79]. These investigations indicated the influence of joint

geometry on stress concentration for the particular joints involved. However, no unified approach was developed to predict stress concentration in common bridge details. Further, the accuracy of the previous results is somewhat questionable since the photoelasticity technique is difficult to apply to regions of high stress gradient.

Fatigue strength of welded bridge joints became a topic of serious investigation in the latter part of the 1950's. The results of many early experimental studies are summarized in Ref. 25. More recent work expanded the investigations experimentally and, for the first time, employed fracture mechanics to explain fatigue behavior[19,26,29,47]. Yet, reasonable estimates of F_g were not available and crude assumptions for K had to be made. Reliable prediction of fatigue life was not really possible.

Accurate analysis of the influence of stress concentration on stress intensity stems from Bowie's work on cracks emanating from circular holes[11]. Since then good estimates of K have been determied for cracks growing from elliptical holes, rectangular cutouts, and all sorts of notches[54,56,76,81]. With regard to fillet-welded connections, Frank's work on cruciform joints marks an early intensive effort to develop an expression for F_g[22]. A similar study was pursued by Hayes and Maddox shortly thereafter[30]. Unfortunately, the numerical conclusions of these two investigations weren't in agreement. Further, the accuracy of each was questionable at very small crack sizes. Gurney later tried to resolve the differences and did

succeed in producing several helpful graphs involving the geometric variables[27]. However, no general formulas were developed and values at very small crack sizes were left in doubt. Moreover, there was no assurance that graphs or expressions developed by any of the three studies could be applied to other, more complex, fillet-welded bridge details.

The analytical approach used to find F_g in Refs. 22, 27, and 30 was that of a compliance analysis based on finite element discretization of the joint. The Green's Function technique recently became popularized by Kobayashi[42], who successfully estimated Bowie's results, and others[62,82]. Albrecht was apparently the first investigator to have sought F_g for fillet-welded joints using a Green's Function[2]. Yet, this reference only supplies the method of solution, not a range of solutions. Condensed expressions for F_g for bridge details, fillet-or groove-welded, simply don't exist. Heretofore, accurate fatigue life prediction for bridge details, without finite element or other refined stress investigation of each one, has not been possible.

Other correction factors for stress intensity have often relied on known solutions for uniform stress applied to the crack[20,62]. Tada and Irwin have reviewed the variability of the correction values with crack shape and stress distribution[82]. These authors have also suggested development of overall stress intensity factors by adding the K factors associated with the uniform and

variable portions of the stress field. Given this superposition approach, it is possible to make a more realistic appraisal of stress intensity for any detail where the local uncracked stress distribution is known. General correction factor expressions are also possible for each detail type.

Past estimates of fatigue lives of welded details have usually had less than acceptable accuracy - particularly for cover-plated details[20],[27]. Since the range of stress intensity is normally cubed in Eq. 1-2 (i.e. $n = 3$), small errors in correction factors cause large changes in cycle life. Occasionally the errors are self-compensating and the results appear reasonable for certain details, but not for others. The lack of agreement between analytical and observed lives has led some investigators to suggest an initiation phase in the fatigue process[27],[53],[70]. It is therefore important to demonstrate the degree of accuracy attained by using the new correction factor expressions and considering only crack propagation.

2. STRESS CONCENTRATION - SCF

It is well known that stress concentration plays a significant role in distinguishing the details of the various AASHTO fatigue categories[3,20]. Fatigue cracks tend to propagate from geometrical stress raiser regions[20,64,85] as well as locations where initial discontinuities exist. Any condition which raises the stress intensity K, increases the likelihood of crack growth. Since welded detail terminations usually combine high stress with weld discontinuities, cracks should form there first. This prediction has been borne out in actual tests[19,20] and has resulted in detail terminations being classified with greatest severity[3,21].

Correction factor F_g incorporates the influence of stress gradient or stress concentration in the stress intensity expression (Eq. 1-4). F_g is based upon the stress concentration distribution along the path where the crack eventually propagates (Art. 3.2). Therefore, the stress concentration, K_t, at any point in the uncracked section must be determined by some method in order to estimate F_g. The finite element technique is employed in this study. Of special interest is the stress concentration factor, SCF, at the crack origin. Usually SCF represents the maximum value of K_t and F_g (Art. 3.2).

Most texts define stress concentration factor as the actual stress at a point in a given direction divided by the nominal stress

at the same point and in the same direction[63],[64],[71],[85]. In many instances the nominal stress results from taking the total force on the section containing the point and dividing by the section's area. Hence, the nominal stress is that found by strength of materials formulas.

Several modifications of the stress concentration factor definition are warranted for general fatigue studies. First, the critical stress at a point is in a direction perpendicular to the crack path (opening mode-Mode I[62]) and may or may not be in the same direction as the nominal stress (Art. 3.1). The details investigated in this study are attached to a beam/girder flange; nominal stress is taken as parallel to the flange centerline. Second, in the event that the crack path is not perpendicular to the flange, the nominal stress is still assumed to be defined by the cross-sectional flange area and not the actual area along the crack path. This also implies the locations of the two stresses are not necessarily identical since a wandering crack path might lead to a region where the perpendicular cross-section includes the attachment along with the flange. Finally, even in cases where more than one kind of stress is input to the detail (such as a load directly on the attachment), the nominal stress is that which is in the flange, parallel to the length, and caused by forces in the girder alone. These qualifications of the stress concentration simplify the application of Eq. 1-4. Stress range, S_r, is always the nominal value and does not require any abnormal calculations (e.g. Mohr's circle) for its determination.

The nominal stress or stress range is assumed to be uniform across the flange width and through its thickness. This is reasonable for relatively deep members with typical flange widths and no torsion. In order to perform a stress analysis on a given detail the nominal stress must be input at some distance from the detail's extremity. (The strength of materials generalized stress – moment is assumed constant over this length.) It is desirable to go far enough away from the detail to eliminate stress gradient conditions and yet remain as close as possible to restrict the dimension of the finite element stiffness matrix.

The question is, "How far is far enough?" This query is obviously an attempt to quantify Saint-Venant's Principle. Some guidance is provided by Ref. 84 where the problem shown in Fig. 2.1a is considered. With concentrated loading it can be shown that the stress in the plate becomes uniform at a distance, e, equal to about 2w from either end. However, the concentrated load situation is not representative of structural details. One is more interested in the configuration in Fig. 2.1b and the distance from the fixed end beyond which uniform stress exists. A dissertation pilot study of this problem using finite elements has shown that e should be taken as roughly 2.5w.

The assumptions of other investigators provide useful comparison with the above distances. Gurney studied symmetrical cruci-

form joints and used a distance of 2.4w (w represents half of the plate thickness in lieu of width) from the weld toe for uniform stress input[27]. Frank also investigated cruciform joints but chose e to be 6w[22]. Frank's value appears larger than necessary but nevertheless safe.

Structural details present a problem in determining dimension w. By definition Saint-Venant's Principle applies to both linear dimensions of the surface on which the stresses are changed. But in the case of details there is a predominant change in stress pattern along one dimension rather than in both directions at once. Hence, for details fillet-welded to flange surfaces the dimension of interest is the flange thickness while for details groove-welded to flange tips the flange width is important. The actual value of w depends on whether the detail is symmetrical with respect to a plane perpendicular to the direction of interest - the one with the major stress gradient. Fillet-welded details are usually one-sided and can be envisioned as one-half of a symmetrical configuration. Dimension w is then the flange thickness. On the other hand, for two-sided, groove-welded gusset plates attached to flange tips w is equated to one-half of the flange width.

Details which are not symmetrical induce flange bending. Therefore, the bending gradient may extend the region of nonuniform stress beyond 2.4w or 2.5w. However, the cover plate studies of Ref. 59 show this is not a necessary worry. Only four percent error in predicted versus measured stress was found 50 mm from the cover

plate end or 34 mm from the weld toe. Since the flange thickness was 14.5 mm, the value of e was 2.34w.

In general, attachments and the welds connecting them to flanges do not present the uncompromising, fixed end condition shown in Fig. 2.1b. Poisson type movement occurs in the flange at the attachment termination; the amount of such movement depends on the attachment geometry. Dimension e decreases as more movement is permitted or, put differently, the attachment is less noticeable. Stiffeners may have a smaller distance than cover plates. The value of e equal to 2.4w appears reasonable when modeling details, but slightly smaller values may also be acceptable.

One ramification of the e distance evaluation is that it acts as a guide for placing of strain gages for experimental purposes. If the experimenter wants to avoid stress concentration effects near a welded detail, he should place the gage(s) at least 2.4w away from the detail termination.

Finite element stress analyses require assumptions on material properties. In all subsequent work the material is considered to be linear, isotropic, and homogeneous – including even the weld region. Young's modulus, E, is taken as 204,000 MPa. Poisson's ratio, ν, is set at 0.30.

2.1 Fillet-Welded Details

Figure 2.2 describes the type of fillet-welded detail of major interest in this dissertation. Attachments of various types are commonly connected to flanges of beams or girders with transverse fillet welds. The welds themselves are idealized as having a flat upper surface which meets the flange surface at an angle of $\pi/4$. The applied stress is assumed to be in the flange only.

Several references make a distinction between load-carrying and non-load-carrying joints when no longitudinal welds exist[22,27]. The weld in Fig. 2.2 would be classified as non-load-carrying since the plate with the applied stress is continuous through the joint. However, the degree with which a joint is load-carrying must depend on the attachment involved. References 22 and 27 treat cruciform joints where the attachments are all stiffener-like (i.e. short dimension in the direction of applied stress). On the other hand, cover plates, with large dimension in the direction of applied stress, are certainly load-carrying (Art. 2.1.2.2). Thus, classification as load-carrying and non-load carrying is somewhat misleading for the general detail.

Research has shown that the critical location for fatigue crack growth at the detail shown in Fig. 2.2 is the weld toe[20,22,25]. (The weld root may also be a potential crack origin if the joint is load-carrying in the sense of a discontinuous flange or when a

small end weld is used[27].) The idealized sharp geometry change at the weld toe means that elastic stress and stress concentration factor theoretically rise to infinity. This fact can be verified by first assuming there is curvature to the weld surface right at the toe. Peterson has shown that concentration increases more and more rapidly as the radius of curvature decreases[63]. Therefore, the weld toe of the idealized geometry represents a point of singular (elastic) stress conditon.

Chapter 1 noted that SAP IV, the finite element computer program used for the analysis work, is only intended for elastic systems[8]. Hence, points of stress singularity present a special problem in determining the necessary mesh size. With decreasing size the concentration factor at the toe (based on some sort of an extra- polation of adjacent element values) continually rises toward infin- ity. Therefore, comparison of hypothetical stress concentration factors of various researchers is generally impossible due to varying mesh sizes. This is true whether the results stem from a compliance or a Green's Function approach to a stress intensity solution.

Fortunately, when considering fatigue crack propagation one always begins with an initial crack size. Therefore, what happens right at the weld toe is not important. SCF is merely a point to begin the F_g decay curve. The analyst is really only concerned about the accuracy of F_g at and beyond the initial crack length, a_i.

F_g does depend on stress concentration at lengths smaller than the initial crack depth (Art. 3.2), but the K_t decay curve tends to vary less as the mesh size becomes progressively smaller. Such is the case even though SCF (i.e. K_t at the weld toe) rises more rapidly with decreasing size.

Figure 2.3 indicates the schematic trend observed in the K_t curve with changing mesh size. There are two ways to view this plot. First, each individual curve represents an equilibrium condition with balanced areas on either side of 1.0. Second, two curves taken together are in equilibrium with each other; they cross once and again have equal areas on opposite sides. However, the key fact for mesh size discussions is that curve 3 is closer to curve 2 than curve 2 is to curve 1. Furthermore, the position at which the curves merge moves progressively closer to the singular point as the mesh size decreases.

Based on the above observations and to ensure reasonable accuracy in F_g at the initial crack size, the mesh size in the vicinity of the weld toe should not exceed a_i. However, difficulty arises when the results of a study are related to nondimensional geometry. Under those conditions initial crack size is nondimensionalized by flange thickness - the dimension in the direction of crack growth[27]. A larger flange thickness, then, implies a larger initial crack size. Yet, current evidence does not support this

idea[74]; initial crack size does not vary with flange thickness. Hence, a dilemma exists. The mesh size in the actual study may be comparable to initial crack size, but nondimensionalized results mean the mesh size would have to be changed proportionally to reach the same results for a different absolute geometry. If the initial crack size doesn't change too, the principle of relating mesh and initial crack sizes is not observed.

A reasonable compromise on the mesh size problem is to select an actual flange thickness for the study which is near the average of real beams/girders. The mesh size is then related to initial crack size as stated. Results are approximately applicable for somewhat larger and smaller flange thicknesses.

One other point about the idealized joint geometry in Fig. 2.2 concerns weld penetration at the root. Obviously, no penetration is shown although under and over penetration are both clearly possible[14,25]. Frank found that over penetration would have a worsening effect on the stress intensity at a stiffener (non-load-carrying) type of joint[22]. Somewhat conversely, Cherry noted little variance in stiffener weld toe stress concentraton due to penetration provided the stiffeners are not abnormally thick[14]. In any case, the effect for typical weld sizes should not be great. Moreover, since over penetration tends to have the same effect as increasing the weld leg, one might expect the trend to reverse itself for longer attachments like cover plates (Art. 2.1.2.2).

-22-

2.1.1 Transverse Stiffeners Fillet-Welded to Flanges

2.1.1.1 Geometry and Modeling

The discussion on joint terminology (load-carrying versus non-load-carrying) indicated that length of attachment in the direction of applied stress is an important parameter[20]. In fact, current categories in AASHTO are largely based on detail length[3,21]. Transverse stiffeners obviously fall at the short end of the spectrum of length values. The length of the stiffener is actually its thickness, T_s, which typically equates to about one-quarter of the flange thickness, T_f. Since this attachment dimension is quite small it can be treated as though it were zero. (The stiffener height is unimportant in any case.) In this study, the transverse stiffener investigation centers on the effect of back-to-back fillet welds on a flange surface. The only length involved is that of two fillet weld legs, 2Z.

Figure 2.4 shows the detail geometry (one-quarter of it) to be used for the transverse stiffener investigation. The detail is assumed to exist on both sides of the beam/girder web which, therefore, marks a plane of symmetry. Based on the above assumption of zero stiffener thickness, the back surface of the fillet weld also represents a plane of symmetry. The flange width is seen to be over eight times the flange thickness but well within an expected limit on aspect ratio[4]. The distance from the weld toe to the point of uni-

form stress input is over three times the flange thickness and well beyond the requirement of 2.4 stated earlier. Stiffener cope is neglected in the modeling with the assurance that the results without the cope are upper bound. (See later discussion Art. 2.1.1.1 and Arts. 2.1.2.2 and 2.1.3.2.)

The variable under study in Fig. 2.4 is the weld leg, Z. Due to the typical stiffener size and Provision 1.7.2b in the AASHTO Code[4], Z can be expected to range between $0.25T_f$ and $1.00T_f$. Table 2.1 lists the three specific values of Z selected for this study; they are $0.3205T_f$, $0.6410T_f$, and $0.9615T_f$. A stress concentration analysis is required for each value. The actual flange thickness used in the analysis work is 19.812 mm.

Figure 2.4 emphasizes that the stiffener problem is being treated as three-dimensional. The procedure used is the finite element stress concentration analysis diagramed in Fig. 2.5. First, uniform stress is input to a coarse, three-dimensional mesh which makes use of the eight-node brick element of the SAP IV library[8]. Next, a two-dimensional fine mesh analysis of the weld region is made with planar elements and displacement input from the coarse mesh results. Then, a two-dimensional, ultra fine mesh analysis is carried out for the local weld toe area. The elements are again the planar type and displacement input stems from the fine mesh output. Finally, the element stress concentration factors from the ultra fine mesh are extrapolated to give a hypothetical maximum value, SCF, right at the weld toe.

This incremental analysis procedure has two distinct advantages. First, no one finite element problem becomes so large that costs are prohibitive or computer limitations are exceeded. Planar elements are normally cheaper to use than three-dimensional ones so it is important to reduce the problem in dimensions as soon as possible. Two planar meshes are employed at the weld toe region since the combined cost is less than that for one, extensive, very fine mesh. (The synergism effect exhibited by the one, extensive mesh can be attributed to a much large bandwidth and many more blocks of equations to be moved in and out of the computer core.) Second, the fine and ultra fine meshes are usable for problems where the overall geometry varies, but the local weld geometry is constant. In fact, the two finer meshes can be employed even if the coarse mesh is two- rather than three-dimensional.

Figures 2.6 and 2.7 show the coarse mesh used for the transverse stiffener investigation. Figure 2.6 gives the mesh sizes and demonstrates how the different weld leg dimensions are treated. The dashed lines indicate another plane of elements are merely added to accommodate the increasing Z. Other parts of the mesh remain unchanged. Figure 2.7 presents a key sampling of boundary conditions imposed on the coarse mesh. Displacements at and perpendicular to planes of symmetry are invariably prevented. Vertical displacement is prevented where the web meets the flange, and wherever the fillet weld meets the web and stiffener surfaces. Thus, both the stiffener

and the web are considered to inhibit movement of the detail perpendicular to the flange surface.

In order to make the transition between three- and two-dimensional meshes (Fig. 2.5), it is necessary to select a vertical section in Fig. 2.6 for further investigation. Both fine and ultra fine mesh results invariable show that weld toe stress concentration decreases slightly as section moves away from the web. For example, the stress concentration factor extrapolated from the _fine_ mesh results for Z/T_f equal to 0.3205 dropped from 2.726 at the web line to 2.586 one node line away ($0.6410T_f$ in Fig. 2.6). Extrapolated fine mesh results for Z/T_f equal to 0.9615 dropped from 3.515 to 3.464 over the same distance. This trend agrees with that of Albrecht[2] and can be explained on the basis of less bending effect. (Bending due to lack of joint symmetry reduces the stress concentration at the weld toe. However, the amount of bending is small since the stiffener causes little interruption of stress flow in the flange.) Therefore, the vertical plane to be treated two-dimensionally is taken as the one on the web line.

Figures 2.8 and 2.9 address the fine mesh common to both the stiffener and cover plate investigations. The heavy lines in Fig. 2.8 denote the outline of the coarse mesh elements. These borders have been incorporated in the fine mesh. This mesh shows its finest gradation in the region of the weld toe. Figure 2.9

indicates the input to the fine mesh is based on the displacement output of the coarse mesh. (Stress output could have also been used.) Displacements in the direction of applied stress are most important. Therefore, such displacements at new nodes (not part of the coarse mesh) on opposing sides of the fine mesh are found by linear interpolation of displacements at old nodes. (Linear interpolation is reasonable since the displacements involved are close in numerical value.) Displacements perpendicular to the applied stress are less important; thus, only a few vertical values from the coarse mesh output are included. The described set of coarse mesh displacements, when imposed on the original plane of three-dimensional elements, are found to generate essentially the same stresses as found in the actual coarse output. Displacements out-of-plane have little effect on element stresses in the direction of applied stress.

The question naturally arises as to whether the planar elements of the finer meshes should be assumed to have a plane stress or plane strain elasticity matrix. Many researchers have used plane strain elements[2,27]; indeed, Sih has shown that plain strain conditions usually exist when a crack is present[75]. Without the crack the decision on plane stress or strain for the detail as a whole rests primarily on the attachment geometry. However, by first solving the three-dimensional problem, the attachment is properly taken into account. Displacement input to the fine mesh should be reasonably correct regardless of the approximate planar conditions.

Some idea of the difference between plane stress and plane strain can be estimated by rough approximation of the two elasticity matrices[89]. Assuming all strains perpendicular to the direction of applied stress are small and can be neglected, the stress, σ, and strain, ε, in the direction of applied stress are defined as:

Plane Stress:

$$\sigma = \frac{E}{1 - \nu^2} * \varepsilon \qquad\qquad (2\text{-}1a)$$

Plane Strain:

$$\sigma = \frac{E\ (1-\nu)}{(1+\nu)\ (1-2\nu)} * \varepsilon \qquad\qquad (2\text{-}1b)$$

Since only displacements are input to the finer meshes the strains in Eqs. 2-1a and 2-1b can be taken as equal. Assuming Poisson's ratio to be 0.3, the ratio of plane stress to plane strain stress in a given element would be 0.816. Actual comparison runs for cover plate details have yielded a ratio of 0.900 (Art. 2.1.2.2). This ratio only applies to the results of the ultra fine mesh since displacements (which are about equal for the plane stress and strain cases), not stresses, are taken from the fine mesh output. (There is essentially no accumulation of error.) The high ratio means that the decision on plane stress or strain is not overly important.

Nevertheless, a dissertation pilot study was undertaken to reveal which assumption gave closest agreement with the "correct" value.

This "correct" value was found by solving a three-dimensional mesh of fineness equal to the two-dimensional mesh and with all interpolated displacements from the coarse mesh imposed. As might be expected the "correct" value fell between the plane stress and plane strain results (lower and higher, respectively). The "correct" value was closer to the plane stress result than that of the plane strain analysis. Thus, plane stress is assumed for both finer meshes. (Note that the selection of element thickness is unimportant as long as the same assumption is made for all elements of a given mesh.)

Figures 2.10 and 2.11 show the ultra fine mesh and positions of imposed boundary displacement derived from the fine mesh output. Again, displacements at new nodes and in the direction of applied stress are found by linear interpolation. (Here, linear interpolation is reasonable since the nodes with known displacement are numerous and close together.) It is apparent that the smallest mesh dimension - right at the weld toe - is $0.0013T_f$. For an assumed T_f of 19.812 mm the absolute size of mesh is 0.0258 mm. This dimension is near the minimum initial crack (flaw) size for fillet weld toes[20,74,86]. Since the average initial crack size is about 0.075 mm, the flange thickness could increase to 60 mm and still yield reasonable accuracy in F_g during the early stages of crack growth (Art. 2.1).

The fourth and final step of the analysis procedure (Fig. 2.5) is the extrapolation of the stress concentration results of the

ultra fine mesh to give SCF at the weld toe. Several extrapolation
schemes are possible. Gurney has made a _line_ fit of the output of
elements adjacent to the flange surface[27] while Fisher employed a
surface fit for the output of elements in both directions away from
the weld toe[20]. However, in this study extrapolation of values along
the prospective crack path is used. Article 3.1 concludes that the
path can be assumed to run vertical from the weld toe down through
the section. Hence, extrapolation involves averaging the element
output on either side of the assumed path and fitting a polynomial
(4th order) through the points. Due to boundary irregularities the
bottom two points from the ultra fine mesh (Fig. 2.10) are neglected.

2.1.1.2 Results

Figure 2.12 presents a typical example of stress concentra-
tion factor variation along the prospective crack path. Since this
crack path is perpendicular to the direction of applied stress, the
concentration factors are for stresses in the same direction. The
variation curve is plotted with respect to relative distance from the
weld toe.

Figures 2.12 reinforces several points of discussion.
First, the stiffener does indeed cause little disruption of the
stress flow in the flange. Only five percent of the flange thickness
exhibits a sizeable increase in stress for this particular weld geo-
metry. Second, the fine and ultra fine meshes compare in the same
manner as meshes two and three in Fig. 2.3. Finally, equilibrium is

satisfied since the concentration decay curve passes below 1.0. The equilibrium is not necessarily precise since the problem originated as a three-dimensional one and the force per unit width of flange along the weld toe is not exactly constant.

The maximum stress concentration factors, SCF, for the stiffeners are tabulated in Table 2.1 and plotted in Fig. 2.13. Obviously, the trend is increasing SCF at a decreasing rate. This is precisely the same trend predicted by Gurney for non-load-carrying fillet welds at cruciform joints[27]. The variation of SCF does not agree with Ref. 20. Exactly the opposite trend is predicted there.

The conflict with Ref. 20 can be explained on the basis of mesh size. In Ref. 20 the weld leg and mesh around the weld toe were maintained at a constant absolute size while the flange thickness varied. To obtain comparable accuracy at singular details, the mesh size must be in a constant proportion to flange thickness. Hence, the absolute mesh size changes. Due to the constant absolute size maintained in Ref. 20, accuracy increases with flange thickness. Therefore, higher SCF are expected and, indeed, found at larger flange thicknesses, which result in lower values of Z/T_f. This trend is definitely misleading.

The maximum stress concentration factor can be related to the variable Z/T_f by the following least squares curve fit:

$$SCF = 1.621 \log\left(\frac{Z}{T_f}\right) + 3.963 \qquad (2-2)$$

-31-

The standard error of estimate, s, for Eq. 2-2 is negligible at 0.0019.

The thickness (length) of stiffener has been assumed to be zero for the development of Eq. 2-2. The cover plate study described later shows that the increase of SCF with length is most rapid at the smaller length magnitudes (Art. 2.1.2.2). The average for the studied range of weld sizes is a 13 percent increase in SCF for L/T_f varying from 0 to 1. Since the constant of Eq. 2-2 clearly dominates the result for typical weld sizes, one can estimate SCF at finite stiffener thicknesses, T_s, as follows:

$$SCF = 1.621 \, \log\left(\frac{Z}{T_f}\right) + 3.963 \left(1+0.13 \, \frac{T_s}{T_f}\right) \qquad (2-3)$$

Typically SCF from Eq. 2-3 is less than five percent greater than SCF from Eq. 2-2.

One final observation on the stiffener detail reflects the degree of importance associated with the three-dimensional coarse mesh. Z/T_f equal to 0.6410 has also been solved with a two-dimensional plane stress coarse mesh (other meshes remaining the same). SCF turned out to be 3.998 rather than 3.651. (Note that use of plane strain rather than plane stress in the coarse mesh would have led to an SCF below 3.998 unless the finer meshes also used plane strain elements.) This is understandable since the two-dimensional coarse mesh had the same boundary conditions as along the web (Fig. 2.7). Thus, no bending effects, due to lack of joint symmetry, were introduced.

(Bending is also absent in cruciform joints.) Since bending tends to reduce stress concentration at the weld toe, the two-dimensional coarse mesh provides an upper bound for real stiffener details. The difference with actual values is on the order of ten percent. The closeness of the values leads to the conclusion that stiffener results can be reasonably compared with those of non-load-carrying cruciform joints[22,27,30]. Also, use of a two-dimensional coarse mesh to represent stiffener details is acceptable[2].

2.1.2 Cover Plates With Transverse End Welds

2.1.2.1 Geometry and Modeling

Figure 2.14 shows one-quarter of the detail geometry to be used for the cover plate investigation. Similar to the stiffener case, the web and midlength of cover plate mark planes of symmetry. The flange width is also the same as that used for the stiffener investigation. The cover plate is assumed to be smaller in width, W_{cp}, than the flange. Hence, the fillet always has one leg on the flange surface and the other on the side of the cover plate. The length of cover plate is set at over $2.5W_{cp}$ (Art. 2.1.2.2).

Two variables are under study. The first is the weld leg, Z, which assumes the same specific values used for the stiffener detail. The second variable is the cover plate thickness, T_{cp}. Provision 1.7.67 in the AASHTO Code limits T_{cp} to a maximum of $2T_f$[4].

Therefore, three values of T_{cp} are selected to cover the permissible range; they are $0.6410T_f$, $1.4360T_f$, and $2.000T_f$. The corresponding values of Z and T_{cp} for a particular case are listed in Table 2.1. In all, five different cases are investigated. The actual flange thickness used is again 19.812 mm.

The same stepped analysis procedure is used for the cover plate details as was used for the stiffener details (Fig. 2.5). In fact, the very same fine and ultra fine meshes are employed (Figs. 2.8 and 2.10, respectively). Only the coarse mesh needs to change and the one devised is shown in Fig. 2.15. Like the stiffener detail the cover plate is initially treated three-dimensionally. The elements are all the solid, eight-node brick type of the SAP IV library[8].

Special explanation of Fig. 2.15 is required regarding the treatment of the weld. Unlike the stiffener coarse mesh (Fig. 2.6) the total length of the detail is always constant. When the weld leg size is changed extra elements are merely added (dashed lines). Among other things this addition pushes the weld toe closer to the point of uniform stress input. However, at the maximum size the toe is still about $2.9T_f$ from the stress input end. This dimension is well beyond the $2.4T_f$ or $2.5T_f$ required.

The cover plate thickness is always as great as the weld leg size. Based on the T_{cp} selected, at least two layers of elements

are always necessary. As the weld leg is increased the number of layers in the cover plate is increased. The maximum number of layers (4) occurs for the one case at a weld leg size of $0.9615T_f$. Changing the number of element layers in the cover plate is assumed to have a negligible effect on stress concentration conditions at the weld toe.

A change in weld leg size also affects the flange discretization along the longitudinal side of the cover plate. For the smallest weld leg the line between the two dashed lines is the boundary between element rows. However, for the next larger value of Z, The solid line position is replaced by the inner (closest to the web) dashed line. The largest Z requires the addition of a second dashed line nearer the flange tip. These modifications to the flange discretization are of little concern when comparisons between results are made. By Saint-Venant's Principle, modifications well removed from the section of interest should have no affect on the behavior there. While the variation of stress concentration along the transverse weld toe of a cover plate is greater than for a stiffener, the maximum still exists over the web (Art. 2.1.2.2).

One last remark regarding the discretization concerns the weld elements at the corner of the cover plate. Figure 2.16 shows a schematic isometric of the "corner weld" as discretized for the smallest weld leg. Notice that angles of $\pi/4$ are maintained on the exposed sides which are coplanar with the transverse and longitu-

dinal fillet welds. This shape is, of course, a rough assumption, but it is not too important when a transverse end weld exists. (As stated above, the section of interest is well removed from the corner position.) Only six nodes are given in the isometric, implying that two nodes act in a dual capacity to reach the eight total.

Figure 2.17 presents an isometric of the boundary conditions associated with the coarse mesh (Fig. 2.15). Like the stiffener coarse mesh boundary conditions (Fig. 2.7), displacements perpendicular to planes of symmetry are invariably prevented. However, two differences between Figs. 2.7 and 2.17 occur in the case of vertical displacements. First, a difference is observed along the web line where, due to a change in the actual relative positions of the attachment and web, vertical displacement in Figs. 2.17 is prevented along the bottom nodes of the flange as shown. This change in position was found to have little effect on the final results although it is more realistic. Second, no vertical displacement is prevented on the other plane of symmetry since the cover plate and flange undergo considerable bending and displacement perpendicular to the flange surface due to lack of joint symmetry perpendicular to the flange plane. Such movement is not inhibited except along the web line.

2.1.2.2 Results

The selection of length for the cover plate geometries (Fig. 2.14) is worthy of amplified discussion. Actual cover plates obviously represent the upper bound of attachment length mentioned in Art. 2.1.1.1. Research has shown that stress concentration and, consequently, detail severity increase with attachment length in the direction of applied stress[20]. Fortunately, additional length increments are expected to have a diminishing effect until a stress concentration plateau is finally reached[20]. Thus, it is not necessary to investigate a detail with extremely long attachment length in order to properly represent a cover plate. The question is, "How long is long enough?"

The results of a pilot study on attachment length are given in Fig. 2.18. Here, the variation of maximum stress concentration factor, SCF' (as extrapolated from output of the fine mesh - not ultra fine mesh), is plotted against nondimensionalized cover plate length, L/W_{cp}. The trends shown are expected to be representative of both fine mesh and ultra fine mesh extrapolations; only the actual magnitudes of concentration change, not the relative magnitudes.

The starting point of each curve in Fig. 2.18 is the zero length attachment where only the end fillet welds are present. This position is comparable to the assumed stiffener condition although the boundary conditions of Fig. 2.17 are not exactly the same as in

Fig. 2.7. The curves rise at a decreasing rate until a plateau is reached in the neighborhood of L = 2.5W_{cp}. Any length above this value can be expected to give an adequate representation of a real life cover plate. Fig. 2.14 shows a slightly longer length was, in fact, used in the model.

The plateau concept is related (although not exactly) to a minimum length for full effectiveness of the cover plate or conformance to the theory of flexure. It has been shown that such conformance is reached at a distance of about 2W_{cp} when a transverse weld exists[59]. (Provision 1.7.67 of the AASHTO Code suggests a terminal distance of 1.5W_{cp} for designing the weld beyond the cover plate's theoretical end[4].) The minimum total length of cover plate required to obtain full effectiveness at midlength is 4W_{cp}. Since this length is much greater than 2.5W_{cp}, it can be deduced that end weld reaches full capacity well before the cover plate is fully effective. The longitudinal fillet welds transfer the extra force needed for conformance.

The stiffener discussion asserted that the section with highest stress concentration is over the web (Art. 2.1.1.1). Figure 2.19 demonstrates that this conclusion also holds for cover plates. Using the extrapolated fine mesh results, the variation of SCF' along the transverse weld toe is plotted. As the attachment length increases the change in stress concentration from point to point is more distinct. Bending increases with length, thereby causing cover

plates to have a more pronounced variation than stiffeners, regardless of differences in assumed boundary conditions. In all cases where the attachment position does not exceed the flange tip, the maximum concentration is at the web line.

While the web line has the highest stress concentration, fatigue crack growth can easily occur at other weld toe positions. Growth depends on the range of stress intensity (Chap. 1) which is affected by crack size as well as stress range and the various correction factors. Initial discontinuities are not necessarily largest over the web. Hence, cracks tend to grow along the entire weld toes of both stiffeners and cover plates. The web line is here selected since it represents the worst concentration condition and is therefore conservative in that respect.

The assumed crack path is taken to be identical to that for stiffeners (Arts. 2.1.1.1 and 3.1). Therefore, stress concentration for local stress in the direction of applied stress is of interest. Figure 2.20 presents such stress concentration factor contours for a sample cover-plate detail. (The actual geometric parameters are unimportant.) High stress concentration is quite localized although redistribution from the uniform state occurs over a broad range in either direction from the weld toe.

Figure 2.21 gives a particular stress concentration factor decay curve along the assumed crack path. By comparing Fig. 2.21 with

Fig. 2.12 it is apparent that the cover plate detail causes much more disruption of the stress flow in the flange. About 15 percent of the flange thickness exhibits sizable increase in stress compared with 5 percent for stiffeners. (Different geometrical values would make these percentages vary somewhat.) This difference is primarily due to the fact that significant force is developed in cover plates and a relatively large change occurs in the position of the overall force centroid of the detail section. Considerable local, longitudinal bending stems from the centroid shift; bending increases with distance from the web.

Table 2.1 records the SCF values for each combination of geometrical parameters studied. These results are plotted in Figs. 2.13 and 2.22. Figure 2.13 shows the SCF trend is downward at a decreasing rate as Z increases. Conversely, Fig. 2.22 indicates SCF increases at a decreasing rate of T_{cp} increases. (This second trend is opposite that evident in fillet-welded lap joints where the "flange" is not continuous through the joint[25]. SCF increases in such joints as "T_{cp}" decreases.) A least squares curve fit of the values leads to the following equation:

$$SCF = -3.539 \log\left(\frac{Z}{T_f}\right) + 1.981 \log\left(\frac{T_{cp}}{T_f}\right) + 5.798 \qquad (2\text{-}4)$$

The standard error of estimate, s, for Eq. 2-4 is 0.0922. While this error is much greater than that for stiffeners, it is still not significant. The increase in error is explainable on the basis of two

rather than one independent variables. Due to the value of the co-
efficients, weld leg, Z, is more important in determining SCF than
thickness, T_{cp}.

Several aspects of Fig. 2.13 deserve further comment. The
trend in SCF with respect to Z is seen to be opposite for stiffeners
and cover plates. Interestingly, Gurney's curve for load-carrying
fillet welds[27] is of the same shape as the curves for cover plates.
Apparently, a transition from non-load-carrying to load-carrying
occurs as the length of the attachment increases. This finding is
supported by Fig. 2.18 where the curves with different weld leg sizes
are seen to cross over each other at a length of about $0.8W_{cp}$. An
attachment with length $0.8W_{cp}$ could be expected to result in a hori-
zontal line in Fig. 2.13, the value of SCF depending on cover plate
thickness.

Figure 2.13 also acts as a guide to the effects of varying
weld penetration. Since SCF increases with Z in stiffeners, one
would expect SCF to increase with over penetration. Frank, indeed,
found such a trend for non-load-carrying joints[22]. Frank[22] and
Gurney[27] both note an opposite trend for load-carrying joints.
Again, Fig. 2.13 is helpful since SCF decreases with increasing Z
in cover plates. Moreover, it is apparent that the effect of pene-
tration depends upon the nominal weld leg size. For small values of
Z the increment in SCF with an increment in Z is more significant,

whether the joint is load-carrying or non-load-carrying. Frank[22] and Gurney's[27] studies are compatible with this observation.

The stiffener study mentioned the difference between a two- and three-dimensional approach at the coarse mesh level (Art. 2.1.1.2). The conclusion was that the two-dimensional coarse mesh always leads to an upper bound on SCF. Unfortunately, the same statement can not be made for cover plates. The case of Z/T_f equal to 0.6410 and T_{cp} equal to 0.6410 was solved with a two-dimensional, plane stress (constant element thickness), coarse mesh (longitudinal fillets neglected and other meshes remaining the same). The resulting SCF was 5.991 versus 6.040 when the three-dimensional analysis was used at step one (Table 2.1). If the planar elements of the cover plate had been assigned lesser thickness than the flange elements to account for the difference in cover plates and flange widths, SCF would have been less than 5.991.

The reversed relationship with the two-dimensional result can be attributed to the joint being load-carrying rather than non-load-carrying. Figures 2.23 and 2.24 help to explain this point. A specific detail geometry was selected (Z/T_f = 0.6410, T_{cp}/T_f = 0.6410) for investigation. Figure 2.23 shows a plan view of points near the cover plate termination where stress output from the coarse mesh analysis has been used. The results at these points were used to plot the stress concentration factor distribution across the

flange and cover plate. In general the average concentration factor (with respect to the input stress) through the flange or cover plate thickness is recorded. However, since the SAP IV solid elements yield stress results on the element surfaces as well as at the centroid, the distribution of the flange top surface concentration factor is recorded for line 1 too. Distribution of the cover plate top surface concentration is noted for lines 2 and 3.

Figure 2.24 plots the various stress concentration factor distributions at the three sections. Line 1 is represented by a curve for concentration through the flange thickness as well as a curve for the flange surface. Lines 2 and 3 are represented by the curves for average concentration through the flange and cover-plate thicknesses, and the curve for the cover plate surface. The curve of particular interest is 2CP which, by recording average stress, gives an indication of force transferred through the transverse end weld. Obviously, the force (per unit width) is significantly greater at the web centerline, which agrees with Albrecht's finding[2]. This distributional aspect of load transfer is not taken into account by a two-dimensional, coarse mesh model. Note also that 3CP, when compared to 2CP, shows the initial contribution of load transfer through the longitudinal fillet weld. The cover plate edge has been brought up to the same concentration as the centerline position. One could predict that sections further removed from the cover plate end, but before the point of flexural conformance, would demonstrate higher concentration at the cover plate edge than at the web line.

The flange surface results (curve 1F*) are misleading since line 1 does not accurately represent the weld toe. Fine mesh analyses have consistently demonstrated that the concentration at the web centerline is greater than concentration elsewhere along the weld toe (Fig. 2.19). Curve 2CP* tends to support this contention by giving some indication of the amount of bending in the cover plate. Since the entire curve is in the negative zone, longitudinal bending is significant across the entire cover plate width. (The boundary conditions in Fig. 2.17 only restrict local bending of the flange along the web.) The negative aspect infers the bending of the flange at the weld toe (except over the web) would reduce stress even though there is a singularity condition. (Stress rises to infinity more slowly.) Apparently, considerable changes in stress distribution occur within a very small distance from the weld toe.

Local flange bending occurs, although in different magnitudes, whether the detail is a stiffener or a cover plate. This causes the web centerline position of the weld to be most critical and the two-dimensional coarse mesh model yields an adequate upper bound SCF. However, given the load-carrying requirement the web is still the worst position, but the two-dimensional model doesn't necessarily lead to an upper bound SCF. Hence, analysis of fillet-welded, load-carrying joints should generally commence on a three-dimensional basis. The closeness of the two results for the case studied is by chance; the separation could be far more pronounced in other geometries.

One other fruitful comparison stems from Fig. 2.24. Ozell and Conyers investigated transfer of stress into cover plates by experiment[59] and the findings had influence on Provision 1.7.67 of the current AASHTO Code[4]. Based on strain gage readings, Ozell and Conyers plotted strain distribution across the cover plate at various sections. The curves appear much like 3CP*. The curves would have appeared quite different if the gage lines had been closer to the cover plate end (curve 2CP*). Curves such as 3CP* don't necessarily reflect the average stress distribution through the cover plate thickness. (Compare curve 3CP* with 3CP.) Local bending makes surface stress results near the cover plate end rather misleading. However, the Ozell and Conyers conclusions with regard to conformance length are not in question.

The main cover plate investigation has held the cover plate and flange widths constant (Fig. 2.14) and was only concerned with variable weld leg size and cover plate thickness. However, a pilot study on the effects of cover plate and flange widths was also conducted. The associated auxiliary detail geometries are given in Table 2.2 along with resulting SCF. The coarse mesh for each geometry is similar in element size although of different extent than Fig. 2.15. No changes have occurred in coarse mesh boundary conditions or either of the finer meshes. In all cases SCF has been evaluated at the web line.

The first case in Table 2.2 has the reference geometrical parameters from the main investigation (Fig. 2.14 and Table 2.1) connected with lines. The effect of a shorter cover plate length is also noted; this trend coincides with that in Fig. 2.18. The second case doubles both plate widths without changing any other parameters. Therefore, the length-to-width ratios of the cover plate have been cut in half. While such a reduction should lead to smaller SCF, the reduction is more than negated by additional force transfer distribution to the web line (Fig. 2.24). Apparently, higher flange and cover plate aspect ratios lead to higher SCF. Note also that the ratio of plane stress to plane strain results for the one set of parameters is 0.900.

The third case in Table 2.2 addresses a small cover plate-to-flange width ratio. The results are below Case 2 even though the cover plate length-to-width ratios are considerably larger. It seems that SCF decreases as the cover plate-to-flange width ratio decreases. However, comparison with Case 1 results proves even more enlightening. If the slight difference in SCF's is mostly attributed to the slight differences in L/W_{cp}, an interesting picture emerges. The effect of a rise in the flange aspect ratio is almost exactly balanced by the effect of a decline in the ratio of the two widths. Multiplication of the two parameters together suggests that the governing variable is the ratio of cover plate width to flange thickness (W_{cp}/T_f). Case 2 indicates that SCF increases as W_{cp}/T_f increases.

-46-

Finally, the fourth and last case in Table 2.2 deals with a cover plate which is wider than the flange. In light of the comments for Case 3, one might expect results identical to those of Case 2. However, a cover plate wider than the flange introduces two new aspects to the problem. First, the longitudinal fillet weld is no longer adjacent to the cover plate edge. Rather, the weld runs along the flange tip. This positioning tends to reduce flange bending induced by lack of symmetry. Secondly, the force transfer distribution in the transverse end weld is no longer as concentrated at the web line. In fact, for an even wider cover plate a higher SCF would occur at the flange tip (Art. 2.1.3.2). (SCF at the flange tip is not greater than at the web line for the specific geometry studied although the values are close.) Therefore, SCF at the web line drops when W_{cp}/W_f exceeds 1.00 (Art. 2.1.3.2).

The results for the auxiliary geometries are reasonably close to each other and to the findings of the basic geometries. From a practical point-of-view the flange and cover plate widths are much less important than weld size and the flange and cover plate thicknesses. Equation 2-4 is a good approximation for all width conditions.

The results of the single cover plate investigation should be approximately applicable to multiple cover plate situations. It is assumed the various cover plate terminations are stepped back far enough from each other that each lower cover plate has sufficient

-47-

conformance distance from its termination before the next cover plate begins. Under these conditions the sum of lower cover plate and the original flange thicknesses can be treated as equivalent T_f at any detail. T_{cp} is the thickness of the secondary plate.

While the stress concentration results are reasonably applied to multiple cover-plate details, fatigue crack growth will be somewhat different. After growing through one lower cover plate a crack would tend to be arrested except at weld points. Assumption of continuous material through the new T_f would yield a lower bound on fatigue life.

2.1.3 Related Cases

Pilot studies have been conducted on two other details which are related to the cover plate detail of Art. 2.1.2. One of the related cases is the cover plate without the transverse end weld. The other case is the lap-welded gusset plate. These results should give some idea of the details' comparative fatigue performance and provide a foundation for future research.

2.1.3.1 Cover Plates Without Transverse End Welds

One of the geometries of Table 2.1 ($Z/T_f = 0.6410$, $T_{cp}/T_f = 1.4360$) was used to investigate stress concentration when the transverse end weld is absent. AASHTO prohibits elimination of the weld when W_{cp}/W_f is greater than 1.0 since fatigue tests of this detail

-48-

yielded less fatigue strength. Therefore, the overall geometry and coarse mesh of Figs. 2.14 and 2.15 are well suited for the study. Only the weld from the web centerline to the cover-plate corner needs to be discarded. However, the corner weld or weld termination in Fig. 2.16 is maintained.

The section of interest for fine mesh analysis is coincident with the outside edge of the cover plate. The specific point where stress concentration is evaluated is the key node in Fig. 2.16 where the above section meets the transverse weld toe. The investigation has only been carried to the fine mesh level although these stress concentration factors have been extrapolated - just as for the data points on Fig. 2.18. The resulting SCF' at the weld toe are plotted in Fig. 2.25.

Figure 2.25 suggests that the plateau of stress concentration is not reached as rapidly if the cover plate is without a transverse end weld. Whereas the plateau for the "with" case is at about L/W_{cp} = 2.5, the plateau for the "without" case is nearer L/W_{cp} = 3.5. The general trend of these numbers is in agreement with the investigation on development length by Ozell and Conyers[59]. They found conformance is reached at a distance of about $3W_{cp}$ from the cover-plate end when the end weld is absent. In order to reach conformance at midlength the cover plate must have a total length of at least $6W_{cp}$.

The relative magnitudes of SCF' for the two curves shown in Fig. 2.25 is misleading. One problem is that the emphasis of the "without" case rests on the shape of the corner weld (Fig. 2.16). Such a smooth and steep profile is rarely found at real longitudinal fillet terminations - particularly with the end weld absent[19]. A smaller angle to the flange surface would lead to a smaller stress concentration factor[22,27].

A second problem with the "without" results centers on the planar, fine mesh analysis. Plane stress elements of uniform thickness were used as in the other cover plate studies. However, this assumption is certainly erroneous since the flange is very much wider than the weld. Perhaps plane strain for the flange and plane stress for the weld would have been better choices. Alternatively, using plane stress elements throughout, but with different thicknesses for flange and weld elements, would provide a more accurate measure of relative stiffness. This second possibility has been explored for a particular cover plate length and the results are plotted in Fig. 2.26.

Figure 2.26 shows SCF' declines sharply as the assumed ratio of thicknesses (or stiffnesses) is reduced. (The curve does not extrapolate to SCF' = 1.0 at a thickness ratio of zero since the coarse mesh analysis already introduced a gradient into the flange.) For a thickness ratio below 3/4, SCF' for the "without" case falls below that for the "with" case. Hence, even though the shape of the

"without" curve in Fig. 2.25 is probably correct, its vertical position may not deviate as much from the "with" curve as implied. The plotted position is an upper bound. The true position is probably lower due to weld shape and/or relative stiffness between weld and flange.

A final problem of the without end weld case centers on the crack path. A typical example of crack path at a corner weld is given in Fig. 2.27[19]. Note that due to a common cold lap condition the crack first follows the flange surface in a "sheared off" manner. Eventually, the crack turns downward at a significant angle and finally becomes perpendicular to the applied stress. SCF' at the weld toe, then, is not an accurate measure of the severity of the detail. It appears desirable to investigate stress concentration at the end of the cold lap. Based on the initial stress distribution the stress concentration under the weld is less than at the weld toe. However, the redistribution of stresses when the crack surpasses the cold lap is important and should be considered in the analysis.

Article 4.5 contains additional comments on cover plates without transverse end welds and their comparison with cover plates which are end-welded. In general, the two details have been found to have comparable fatigue lives[19]. If anything, the "without" case is slightly _less_ severe.

2.1.3.2 Lap-Welded Gusset Plates

Figure 2.28 presents the detail geometry used for the lap-welded gusset plate investigation. The geometry is similar to that used for one of the cover plates (Fig. 2.14) with a few notable exceptions. The gusset plate does not reach the web centerline; rather, it is set off some distance to permit welding all around. Since symmetrical gussets are assumed, only one-quarter of the detail is studied. The variables involved are the gusset plate width $(W_{gp1} = 3.85T_f$, $W_{gp2} = 9.62T_f)$ and length.

The coarse mesh discretization employed is very close to that shown in Fig. 2.15. Of course, the mesh for the gusset plate is shifted several rows beyond the flange tip. For W_{gp2} additional rows are added. But the size of mesh – particularly in the transverse end weld – is directly comparable. Fine and ultra fine meshes (Figs. 2.8 and 2.10) are totally unchanged.

Two points along the transverse weld toe are of interest. One (denoted "inner edge") is where the line of the inner edge of the gusset plate meets the transverse weld toe. The second point (denoted "flange tip") is at the intersection of the transverse weld toe and the flange tip. The objective is to determine how SCF varies at these two points with changes in gusset plate width and length.

Figure 2.29 indicates the SCF variation with the gusset plate length-to-flange thickness ratio. It is observed that after

a certain length the flange tip position becomes more critical for both gusset plate widths. The curve representing the inner edges moves vertically as this position changes relative to the web line. (Discussion of Case 4 of the auxiliary cover plate geometries – Table 2.2 – stated the web is always worse than the flange tip for those particular geometrical parameters.) Note the wider gusset plate does not have quite as high a plateau at the inner edge position as the smaller width plate. However, at the flange tip the wider plate curve diverges significantly from the smaller width curve as length increases. The longer length gives the stress flow a chance to make use of the wider plate.

Article 2.1.2 linked conformance length and length for the SCF plateau to width of cover plate. A comparable parameter for symmetrical, lap-welded gussets is the effective width, W*, from outer plate edge on one side to outer plate edge on the other side (i.e. twice the distance from web line to outer gusset plate edge). Effective width permits comparison of gusset plates of different width as well as plates with different proximity of their inner edges to the web line. The variation of SCF with the length-to-effective width ratio of the gusset plates is plotted in Fig. 2.30. While the inner edge of the wider plate appears to reach its plateau more quickly than the inner edge of the smaller width plate, the situation at the flange tip is distinctly reversed. Clearly, the second gusset plate must be much longer than the first plate in order to reach the SCF plateau.

The lap-welded gusset plate investigation indicates that the flange tip position can easily be more critical for crack growth than the inner edge location. Both length and width are important in determining the SCF value and critical position. Experimental evidence is supportive of this conclusion[20].

2.2 Groove-Welded Details

References 3 and 21 point out that the groove-welded details of greatest concern (worst category) are those where the weld is parallel to the direction of applied stress. The weld in this case is normally intended to connect some sort of attachment whose greatest dimension is along the weld. The length is typically sufficient to cause the detail's end rating to fall into Category E[3]. Therefore, the details subsequently investigated are chosen for their potential severity and greater concern to bridge designers.

2.2.1 Gusset Plates Groove-Welded to Flange Tips

One class of details which is particularly common in bridge structures is the groove-welded gusset plate. Such plates are often welded to flange tips or webs and may or may not possess a smooth circular transition at the ends. The transition can reduce the severity of the detail although clearly the radius involved is crucial.

The intent here is to study stress concentration near the ends of gusset plates which are groove-welded to flange tips and exhibit a circular transition at each end. The geometry of the entire plate, including the radius, is varied in order to yield the stress concentration trend. The results are compared, where possible, with those recorded by Peterson for stepped, flat tension bars with shoulder fillets[63]. (The Peterson results stem from photoelastic studies by others.) However, the Peterson findings are expanded to parametric values common in gusset plates. Such expansion includes gusset plate-to-flange thickness ratios less than 1.0. Also, a few pilot cases are analyzed to sense the effect of secondary stress directly input from bracing members to the gusset plates.

The fact that a transition radius (magnitude other than zero) is assumed greatly simplifies the finite element investigation. A radius means singularity doesn't exist and, as a result, very fine mesh sizes are unnecessary. However, as the radius decreases SCF can be expected to rise and the emphasis on mesh size is correspondingly increased. In other words, a coarse mesh alone may be adequate for some geometries but not for others. Unlike the fillet-welded details, results from different mesh sizes are obviously comparable provided each mesh is at least fine enough to capture the maximum concentration.

Several assumptions are made concerning the weld. Full penetration is the only case considered; the weld depth is taken as

constant and equal to the gusset plate thickness. The termination
of the weld at the circular transition point of tangency is assumed to
be ground smooth to maintain the intended contour. The weld thick-
ness in the plane of the flange and gusset is unimportant.

2.2.1.1 Geometry and Modeling

The general detail geometry for the gusset plate investi-
gation is shown in Fig. 2.31. Symmetrical gussets are assumed for
two reasons. First, inner bridge girders often have cross bracing
attached at opposite flange tips at a given position along the gird-
er length. Second, symmetrical gussets prevent cross bending of
the flange. Gurney notes such bending leads to lower values of
SCF[25]. Therefore, the symmetrical gusset plate assumption leads to
an upper bound stress concentration and a lower bound fatigue life.

A few dimensional aspects of Fig. 2.31 need amplifica-
tion. The distance from uniform stress input to the point of transi-
tion tangency is slightly greater than $2.4w$ (w equals $W_f/2$ in this
case - Fig. 2.1) as recommended in earlier discussion. The gusset
plate width, W_{gp}, is measured from the flange tip outward, thereby
including any groove weld thickness. Finally, the length of gusset
is measured from the point of transition tangency, not the outer cor-
ner of the gusset plate as used in Peterson[63].

The above decision on length measurement is advisable on
several counts. First, it is consistent with general fatigue cate-

gorization on the basis of attachment length[3,20]. Hence, results can even be compared with those of tapered attachments such as longitudinal stiffeners (Art. 2.2.2). Second, transition radius, R, can be greater than W_{gp}, making a quarter-circular transition impossible. Figure 2.32 demonstrates that under this condition the total length of attachment, L, can not be simply equated to the outer edge length, L', plus two transition radii. Thus, a stress concentration factor based on L' would not follow the same trend as SCF based on L once R exceeds W_{gp}. In fact, changes in SCF for Fig. 2.32 should be due to only changes in R since the other parameters (excluding L') have not changed. Therefore, the length is consistently measured from the point of tangency without regard to the outer gusset plate edge length.

Four variables were studied. They are the transition radius, R, the attachment length, L, the gusset plate width, W_{gp}, and the gusset plate thickness, T_{gp}. AASHTO places few limitations on these parameters so a rather broad range investigation is required. Table 2.3 lists the parametric combinations actually studied. Each of the gusset plate variables is nondimensionalized by either the flange width or flange thickness. The actual flange width used is typically 305 mm. Since all problems are treated as two-dimensional, only the relative plate thicknesses are important. Thus, eccentricity of the gusset plate's centroidal plane at midthickness relative to the flange centroidal plane is neglected.

The stress concentration analysis procedure for gusset plates follows Fig. 2.33. This flow diagram is obviously more simplified than the one for stiffeners and cover plates (Fig. 2.5). The procedure begins with uniform stress input to a two dimensional coarse mesh which uses plane stress elements from SAP IV[8]. (All out-of-plane effects are neglected.) For gussets with large transition radii ($R/W_f \geq 0.5$), the element with the maximum stress concentration factor is located and that value represents SCF. For gussets with small transition radii ($R/W_f < 0.5$), it is necessary to go to a fine mesh (plane stress elements) which makes use of nodal displacements from the coarse mesh. Since R is not zero, SCF is simply the maximum centroidal concentration factor found in any of the fine elements. No extrapolation is required.

A sample coarse mesh is given in Fig. 2.34. The boundary conditions prevent nodal displacments at and perpendicular to lines of symmetry (Fig. 2.31). In general, the flange discretization is unaffected by the various parametric changes (Table 2.3). In fact, the discretization of the gusset plate is also basically constant except the extent varies with the parametric values. Other discretization can be developed by sketching the perimeter of the other gusset plates on Fig. 2.34 and observing the mesh pattern with the boundaries. Should extension of the width be required, the element sizes are identical to those in the current outer row. In the transition zone the mesh for a small radius is found by simply extending

the given mesh lines. The rule of thumb for the triangular elements is to always extend the lines perpendicular to the flange edge straight to the circular border. The lines parallel to the flange edge are normally stopped one mesh line before the circular border and a skewed connection is made with a point on the border.

The coarse mesh does contain some error due to the inaccurate representation of the circular transition with straight lines (chords) between nodes. The nodes themselves have been positioned directly on the curve. One way to measure the geometrical error is by the largest deviation of any chord from the curve, as a percent of the radius[7]. Figure 2.34 shows this error can be estimated from the chord length and the curve radius. The maximum chord length can vary significantly from radius to radius since the larger radii reach the larger mesh sizes. However, the largest error has been found for the smallest radius and amounts to under five percent. In the crucial tangency region the error is always less than one percent. Such error in geometry is considered to have a negligible effect on results — particularly since the element's centroidal stress is used for SCF without extrapolation. Theoretically, singular stress conditions do exist at the skewed intersections of chords, but the angle difference between chords is always very slight and the intersections themselves receive no special finite element treatment.

The region of interest for highest stress concentration is in the vicinity of the point of transition tangency (Fig. 2.31).

Many references suggest that the maximum concentration occurs precisely at the point of tangency[55,63,71,85]. However, the findings of this study indicate the worst condition is slightly away from this point. The basis of the results in the cited references is photoelastic studies. Although photoelasticity can't really be termed precise, the deviation of the point of maximum concentration from the point of transition tangency was thought to be caused by the chord approximation of the smooth curve.

In order to examine this premise, the results from two different coarse mesh discretizations were compared. One mesh size was equal to that in Fig. 2.34 while the other was twice as large in the region of interest. The resulting position of SCF from the point of tangency was found to increase with the radius and the distance was roughly R/5 for both discretizations. (This approximation seems to be reasonable no matter what the gusset plate length, width, or thickness.) Therefore, it does not appear that the chord approximation was the cause. In any case, the value of SCF is typically less than two percent greater than the stress concentration at the point of tangency.

One conclusion of Art. 3.1 is that the crack path can be assumed perpendicular to the flange tip or the direction of stress input. Hence, SCF represents stress in the direction of applied stress but not generally right at the point of tangency.

Nevertheless, the nominal stress used to evaluate SCF is that which is input (i.e. that across the flange width prior to the transition).

Figures 2.36 and 2.37 present a typical fine mesh discretization and imposed boundary displacements derived by linear interpolation from the output of the coarse mesh (Fig. 2.34). The mesh size is typical of fine discretization for other radii. Since the maximum stress concentration is normally away from the point of tangency, the fine mesh usually doesn't straddle that location. However, the cases of $R \leq 0.1W_f$ are exceptions to this rule since SCF is close to the tangency point.

2.2.1.2 Results

Figure 2.38 presents stress concentration factor contours for one of the gusset plate details. It is useful to compare this figure with the sample cover plate detail (Fig. 2.20). Basically, the two figures are quite similar. The only major difference is the sharp rise in concentration near the singular point in Fig. 2.20. If the fillet weld toes of stiffeners and cover plates were somewhat rounded by grinding or other means, the contours for a given R/W_f (gusset plate) would be almost identical to those for the same $R/2T_f$ (stiffener or cover plate). Small differences would still exist, however, due to the other geometrical parameters.

The stress concentration factor decay for the mesh geometry shown in Figs. 2.34 and 2.36 is plotted in Fig. 2.39. (Division of distance by W_f is approximate since the element with SCF is a small distance from the flange tip. The error in total width to the centroid of the element is less than one percent.) This curve exhibits the same pattern established by the stiffeners and cover plates (Figs. 2.12 qnd 2.21, respectively). Since SCF is lower, the rate of decay is more gradual. The stress concentration factor reaches 1.0 at a distance of about 0.14 W_f. W_f is comparable to $2T_f$ since symmetrical gusset plates were used. Thus, K_t equal to 1.0 is reached at a comparable distance of about 0.28T_f. For the cover plate detail plotted in Fig. 2.21, K_t equal to 1.0 is reached at 0.23T_f while the stiffener shown in Fig. 2.12 crosses this level at 0.10T_f. The actual distances vary with geometry although the general trend exhibited here is typical.

The SCF value resulting from each combination of geometrical parameters is given in Table 2.3. The trend of each of the parameters is more clearly visible in Figs. 2.40 through 2.43. Basically, SCF increases with increasing length, width, and thickness of gusset plate. As expected, SCF increases with decreasing transition radius.

Also plotted in Figs. 2.40 through 2.42 are curves derived by interpolation of Peterson's findings[63]. (No data are available in Peterson or elsewhere for varying thickness ratios - Fig. 2.43.)

-62-

In all cases the results of this study have the same trend as those recorded by Peterson, but exceed them somewhat. The increase is generally on the order of 10 percent.

A least squares curve fit of the values summarized in Table 2.3 yield the following SCF equation:

$$SCF = 1.115 \log\left(\frac{R}{W_f}\right) + 0.537 \log\left(\frac{L}{W_f}\right) +$$
$$0.138 \log\left(\frac{W_{gp}}{W_f}\right) + 0.285\left(\frac{T_{gp}}{T_f}\right) + 0.680 \qquad (2-5)$$

The standard error of estimate, s, for Eq. 2-5 is 0.1322. This error is somewhat larger than that for cover plates due to the two additional variables involved. However, the error is still quite small.

The form of Eq. 2-5 permits a comparative rating of the importance of different variables. The coefficients indicate that radius, R, is more critical than length, L, which is more critical than the width, W_{gp}. The thickness ratio does not appear in the equation in logarithmic form so an exact comparison with other variables is not possible. However, the indication is that thickness has importance comparable to the length.

The singular case of R = 0 is of special interest. While not a part of the basic gusset plate investigation, a pilot study was conducted for the sets of parameters listed in Table 2.4. The coarse mesh used in the investigation had a gradation identical to

the previous gusset plates (Fig. 2.34). However, the fine mesh was altered to that shown in Fig. 2.44. The kind of displacement input to this mesh was comparable to that of the other gusset plates (Fig. 2.37). SCF was found by extrapolating the element stress concentration factors to the gusset plate end.

Table 2.4 indicates the trends in SCF with regard to the length, width, and thickness variables are unchanged by the singular condition. But the SCF magnitudes are all exceptionally high and, therefore, of particular concern. Note that the element size near the point of interest is only $0.0008W_f$. Since W_f is comparable to $2T_f$ from the stiffener and cover plate investigations, the size can be considered equivalent to $0.0016T_f$ in those studies. The finest mesh size used at the weld toe of stiffeners and cover plates was $0.0013T_f$. Hence, the fillet-welded details had a slightly finer discretization adjacent to the singular point than the above gusset plates, but the resulting SCF for gusset plates are much larger for most geometries (compare Tables 2.1 and 2.4).

The main instigator of the comparatively high SCF in the singular gussets is the angle between the plate end and the flange tip. Gurney[27], Frank[22], and others have indicated SCF increases significantly with the weld toe angle of both load-carrying and non-load-carrying joints. In fact, the SCF-weld angle relationship is approximately linear[27]. Therefore, in changing from a weld angle (in the fillet-welded details) of $\pi/4$ to $\pi/2$, SCF would be expected to double.

A useful exercise is to "equate" parameters of the gus-set plate detail to those of the stiffener. (The stiffener is used rather than the cover plate since the gusset plate is connected all along its length.) The analogy, then, is that the gusset plate length, L, equates to twice the weld leg size, Z, and flange width, W_f, equates to twice the flange thickness, T_f. The thickness ratio in the gusset detail is assumed to be 1.00 since the symmetrical stiffeners span the flange width. Also, the elements of the finer meshes (Figs. 2.8 and 2.10) were assumed to have uniform thicknesses. The only variable remaining is the gusset plate width. It should be as large as possible since the fillet weld's vertical leg increases with an increase in the horizontal leg and/or an increase in the weld toe angle.

Given the preceding "equalities", Eq. 2-2 (multiplied by 2) is used to predict SCF for several of the geometries in Table 2.4. The results are given in Table 2.5. It can be seen that in spite of the slight difference in mesh size, Eq. 2-2 gives a very good pre-diction of SCF when the gusset plate length is small. However, the predictions are on the low side for lengths greater than the flange width. Of course, Eq. 2-2 isn't really intended for weld legs much greater than the flange thickness.

The comparison in Table 2.5 confirms the reason for the high stress concentrations for singular gusset plates. But from a

practical point-of-view fabricated gusset plate connections don't usually have the abrupt right angle idealized for the singular condition. Weld runout is typically observed, thereby reducing the angle at the singular point. Experimental results acquired to date show the singular, groove-welded gusset plates of common length are comparable to cover plates[20]. Nevertheless, it seems clear that gusset plates should possess a transition if at all possible. Even a small radius formed by grinding the groove weld termination can, theoretically, substantially reduce fatigue susceptibility.

To this point the only force input to the gusset plate detail has been located in the flange (Fig. 2.31). Naturally, force may also be imposed on an actual joint by the bracing member(s) connected to the gusset. The question arises as to whether these secondary forces have a significant effect on the stress concentration as given by Eq. 2-5.

A pilot study into geometry and secondary force effects was conducted by making use of the two loading schemes in Fig. 2.45. It has been assumed that the force input to the gusset plate is maintained at a constant proportion of the force input to the flange. Two different distributions of force are employed. One distribution (termed Distribution 1) is in the form of uniform stress along the outer edge of the gusset. The magnitude of this stress depends on gusset length and thickness. The second force distribution (termed

-66-

Distribution 2) is in the form of two concentrated forces (simulating bolts) at the midlength of the gusset. The force is taken to be equally divided between the two positions. (The forces are divided by two again due to symmetry about the midlength.)

The secondary force effect is measured at the previous point of maximum concentration for each geometry. The concentration factor, as before, relates local stress in the direction of flange stress to nominal stress input to the flange. For the given force ratio of 1/12, the point of maximum concentration thus defined is actually unchanged for the range of geometries studied. However, stress concentration factors for other directions of local stress at other locations increase. These concentration factors are usually much smaller than the one evaluated here. One exception is the singular juncture (in section) of the gusset plate and flange tip when the thickness ratio is less than 1.0. Study of the singular location requires a three-dimensional coarse since the stress gradient of concern is through gusset plate thickness. Such a study is beyond the scope of this dissertation although SCF estimates could be made from one of the fillet weld equations (Eq. 2-2 or 2-4).

The percentage change in concentration factor for selected geometries is given in Fig. 2.46. It can be seen that the percentage only becomes significant when both the transition radius and the length are small. This trend with regard to length is opposite to the trend in the basic SCF (Fig. 1.41). Although the percentage

becomes large at small L, the percentage is applied to a relatively small SCF. In terms of absolute change in SCF, the curve would not be as steep over the range of length plotted.

Gusset plate thickness and the manner of secondary loading are not particularly important variables. However, even though the percentages for the two thicknesses are about equal at small length, the percentage for the higher thickness is more meaningful since it is applied to a higher base SCF. (Recall that the uniform stress input varies with plate thickness.) As expected, the two secondary load distributions are equivalent when the length is small. At large lengths a separation occurs since the uniform stress continues to influence the concentration in a positive manner while the concentrated loads yield a Poisson effect (negative for secondary tension). For large transition radii, all effects are of the Poisson type.

The general conclusion with regard to secondary effects is that they can be ignored unless the gusset transition radius and length are both small. A rule of thumb suggests that secondary effects are negligible unless R is less than $0.1W_f$ and L is less than $1.0W_f$. These two values are specifically related to the assumed force ratio. For a lesser ratio the limits could be even smaller.

One other possible point of concern for the gusset plates is the change from local stress (concentration) in the direction of applied flange stress to local principal stress (concentration).

As mentioned earlier, stress perpendicular to the crack is the only stress of importance. It is of interest to examine the stress concentration assuming the crack follows the minimum principal stress trajectory (Art. 3.1). Figure 2.47 indicates the change in base SCF (Eq. 2-5) required to reach the principal stress concentration factor. Figure 2.47 includes curves for the cases of no secondary force and the secondary forces as defined in Fig. 2.47. Therefore, the curves for Distribution 1 and 2 can be viewed as the curve for no secondary force with an additional modification for secondary loading. Again, all principal concentration factors are at the previous points of maximum concentration.

Principal stress only becomes critical when the radius is small (say less than $1.0W_f$). A check of changes for $R = 0.5W_f$ has shown values always less than 2.0 percent.

2.2.2 Longitudinal Stiffeners

The gusset plate findings can provide insight to the stress concentration at other details. For example, consider the case of longitudinal stiffeners. These attachments are connected to plate girder webs or box girder flanges and webs with either fillet or groove welds. The region of greatest interest for fatigue susceptibility is the attachment's termination. The stiffener may or may not be tapered at its end and the weld termination may or may not be ground into a smooth transition.

Consider the tapered longitudinal stiffener with smooth transition in Fig. 2.48. For this study it is assumed that the stiffener is attached to a flange and that the stress concentration analysis can be viewed as two-dimensional. (Strictly speaking there is minor three-dimensional action - particularly if fillet welds are used and full penetration doesn't exist.) The objective is to analyze this detail and see how the results compare with the gusset plate findings.

For such a large, nondimensional radius the finite element mesh is not crucial. However, mesh sizes comparable to those in Fig. 2.34 are used. The only variance beyond the change in the gusset dimensions is that flange thickness in Fig. 2.47 is assumed to represent half of the flange width in Fig. 2.34.

Boundary conditions for the stiffener problem deserve special attention. Displacements at and perpendicular to the line of symmetry (at midlength)are prevented. However, consideration must also be given to displacement perpendicular to the flange. Such displacement must be prevented for at least one node to insure stability. Other nodes can be left free to move. Limited vertical movement must occur in flanges at stiffeners, cover plates, and other nonsymmetrical details.

An upper bound value of SCF can be determined by assuming bending or vertical movement of the flange is prevented. Trials on

the detail in Fig. 2.48 without restraint led to negative SCF. Thus, restriction of vertical displacement at all nodes along the flange bottom provides the other extreme. Note that this assumption is comparable to assuming the detail is symmetrical about the flange bottom. Hence, the longitudinal stiffener detail becomes comparable to a gusset plate detail provided there is a circular transition.

The last modeling problem is what to assume for planar conditions – plane stress or plane strain. The stiffener should logically use plane stress elements with the proper stiffener thickness. The flange elements might be taken as plane strain or plane stress with large thickness. The flange is typically stiffer than the stiffener and relative stiffness affects SCF (Art. 2.1.3.1). Assumption of plane stress conditions permits direct comparison with the gusset plate results (Eq. 2-5). Further, assumption of thickness equal to that of the stiffener leads to an upper bound solution.

The longitudinal stiffener problem was solved with two different assumptions for the planar elements in the flange. First, assuming plain strain conditions in the flange and a stiffener thickness of 6.35 mm, the resulting SCF is 1.05. Second, assuming plain stress for the flange and thickness equal to the stiffener, the SCF is 1.20. The prediction by Eq. 2-5 for equal thicknesses and W_f (in Eq. 2-5) equated to $2T_f$ (in Fig. 2.48) is 1.62.

The over estimate of Eq. 2-5 is partially attributable to the fact that very long lengths or wide gussets were not included in the supporting data. Peterson's graphs[63] place the expected value for equal thicknesses at about 1.28. Since the gusset results from the finite element investigation exceed the Peterson values by 10 percent, one would expect an SCF near 1.20. In any case, it appears the taper has a favorable influence on stress concentration. Equation 2.5 and Peterson's graphs for non-tapered specimens lead to upper bound solutions. Also, the plane stress approach to the problem is more severe than plane strain.

For stiffeners without a circular transition the taper is more important. The intersection of the taper and the flange surfaces is a singular point in any event. But since the hypothetical SCF is proportional to the angle (Art. 2.2.1.2), the taper becomes a crucial factor. The upper bound stress concentration factor for singular, longitudinal stiffeners can be estimated in a manner similar to singular gusset plates (Art. 2.2.1.2) with an appropriate reduction for relative stiffness. The number by which Eq. 2-2 is multiplied depends on the ratio of the taper angle to $\pi/4$.

3. STRESS GRADIENT CORRECTION FACTOR - F_g

3.1 Crack Path

Chapter 1 noted that the Green's Function approach to a stress intensity solution requires that the crack path be known. (Actually, the crack path must also be known for the compliance technique.) Stress perpendicular to the crack plane is evaluated and used to predict F_g at any crack length. Thus, F_g relates only to the crack opening mode of displacement (Mode I)[62]. Shearing stresses in the plane of the crack (if present) resulting in Mode II and Mode III displacements are neglected.

In considering potential crack paths it is helpful to recall crack patterns in concrete beams[18]. There, cracks form perpendicular to the tensile (principal) stress trajectories. In other words, the crack paths tend to follow the compressive (principal) stress trajectories. More generally, a crack originates first at the location of maximum tensile stress and propagates along the minimum (algebraic) principal stress trajectory through that origin.

Figures 3.1 and 3.2 present maximum (algebraic) principal stress concentration factor contours for sample cover plate and gusset plate details. (The specific geometries used in these figures are unimportant.) Such contours do not represent stress trajectories (or isostatics)[64] although they do provide insight on how the principal

stress is changing in the vicinity of maximum concentration. Also, it is interesting to compare these contours with those representing local stress in the direction of applied stress (Figs. 2.20 and 2.38). The comparison shows the contours for a specific detail have the same general shape, but for principal stress they are further apart.

By using the finite element output it is possible to define stress trajectories. The minimum principal stress trajectory which passes through the point of maximum stress concentration of each detail has been superimposed on the principal concentration factor contours in Figs. 3.1 and 3.2. (Since the contours are not the same as trajectories, mutual orthogonality with the minimum principal stress trajectory is purely coincidental.) It can be seen that the trajectory for the gusset plate meets the free surface at a right angle in the same fashion as an equipotential line in a fluid flow net. However, due to the abrupt change in geometry at a fillet weld toe, the trajectory splits the total angle (as required for symmetry) between the intersecting surfaces. Given a weld angle of $\pi/4$, the trajectory initially has an angle of $\pi/8$ to the vertical direction. The trajectory for each detail turns perpendicular to the applied stress direction with increasing distance from the maximum concentration point.

The minimum principal stress trajectories represent probable crack paths in cases where propagation is of the unstable, catastrophic variety. In fatigue crack propagation, the stress field has time to redistribute itself with each increment of crack growth.

Thus, the minimum principal stress trajectory based on the initial

stress field gives a distorted view of actual crack path. Frank

noted from actual measurements that the crack angle to the vertical

averaged about $\pi/14$ in cruciform joints[22]. He took this angle to be

constant. On the other hand, Albrecht notes that for stiffeners and

cover plates the deviation from a vertical plane is barely noticeable

and can be neglected[2]. This conclusion seems to be supported by the

visual evidence in Refs. 19 and 20. Indeed, most investigators dis-

regard any angle in crack growth and base stress intensity estimates

on stresses perpendicular to the vertical plane[27,45,50].

The minimum principal stress trajectory and a crack line

constantly perpendicular to the applied stress represent the physical

limits of the path. However, the position of the minimum principal

stress trajectory may be altered slightly from that shown in Figs.

3.1 and 3.2 if the weld angle or transition varies from the idealized

geometry. In any case, the distance over which deviation from a

straight perpendicular path occurs is likely to be small compared to

other geometrical parameters. Further, the difference in perpendicu-

lar stress for the actual and perpendicular path at any given dis-

tance is not great.

Based on the preceding arguments the assumed crack path is

the straight line through the point of maximum concentration and per-

pendicular to the direction of applied stress. Hence, local stress

in the direction of applied stress (Figs. 2.20 and 2.38) is of

interest and shear stress is disregarded. (There would be no shear stress, of course, if the minimum principal stress trajectory were assumed as the crack path.)

3.2 Green's Function

The relationship between stress intensity and stresses on the prospective crack plane with the crack absent is clarified by Fig. 3.3[45]. The stress intensity for Case 3 is desired. In order to evaluate it, two other load cases are considered and superposition results in the actual load case. Thus, the crack plane tractions in Cases 1 and 2 are equal and opposite. Furthermore, the magnitude and distribution of the tractions in Case 1 are such that the crack is completely closed, as though it weren't even there. Thus, the magnitude and distribution of the crack plane tractions are equal to those of the stress distribution on that plane with the crack absent. Given such traction only Case 2 has an associated stress intensity which, according to linear fracture mechanics principles[81], must equate to the stress intensity for Case 3.

The distribution of tractions in Case 2 (Fig. 3.3) is usually irregular for real structural details and appropriate stress intensity solutions rarely appear in the various handbooks[76,81]. However, a solution can be developed by taking the solution for concentrated splitting forces on the crack, converting the force (per unit thickness) into stress over an incremental distance, and

integrating over the crack length. Thus, any solution for splitting forces can be termed a Green's Function. (In mathematics a Green's Function is one which satisfies the given boundary conditions and represents the inverse of a differential operator[88]. The solution of a nonhomogeneous differential equation is found by multiplying its right-hand side by the proper Green's Function and integrating between limits. Therefore, in fracture mechanics a Green's Function is the stress intensity solution for splitting forces of unit magnitude.)

Albrecht chose to work with the Green's Function related to the crack loading in Fig. 3.4[2]. A through crack is assumed to be located in an infinite plate of unit thickness and subjected to symmetrical pairs of splitting forces. The stress intensity for the configuration in Fig. 3.4 is[2,81]:

$$K = \frac{2P}{\sqrt{\pi a}} \left[\frac{a}{\sqrt{a^2 - \ell^2}} \right] \qquad (3\text{-}1)$$

where $\dfrac{2}{\sqrt{\pi a}} \left[\dfrac{a}{\sqrt{a^2 - \ell^2}} \right]$ = Green's Function

While many crack configurations with splitting forces are possible, this particular one is favored because it isolates the influence of gradient (i.e. F_g) from the other stress intensity correction factors. Free surface and crack shape effects can be imposed separately (Eq. 1-4). Thus, Fig. 3.4 purposely doesn't resemble the geometry at a fillet weld toe or groove weld termination.

Force P in Eq. 3-1 can be broken down into stress over an incremental length.

$$P = \sigma_\ell * d\ell \tag{3-2}$$

The stress intensity for stress along the entire crack length can then be written as follows:

$$K = \sqrt{\pi a} * \frac{2}{\pi} \int_0^a \frac{\sigma_\ell d\ell}{\sqrt{a^2 - \ell^2}} \tag{3-3}$$

If the nominal stress, σ, at the section (or the one input into the finite element mesh - Chap. 2) is now introduced into the formula, the stress intensity becomes:

$$K = \sigma\sqrt{\pi a} * \frac{2}{\pi} \int_0^a \frac{\sigma_\ell}{\sigma\sqrt{a^2 - \ell^2}} * d\ell \tag{3-4}$$

The stress ratio under the integral sign represents the stress concentration factor, K_t. Since $\sigma\sqrt{\pi a}$ is the stress intensity for a through crack under uniform stress, the remainder of the equation equals F_g.

$$F_{ga} = \frac{2}{\pi} \int_0^a \frac{K_{t\ell}}{\sqrt{a^2 - \ell^2}} * d\ell \tag{3-5}$$

where F_{ga} = stress gradient correction as a function of crack size

F_g is seen to be nondimensional and directly related to the stress concentration decay. Therefore, F_g is also related to the selection of nominal stress (Chap. 1). Due to the general nature of Eq. 3-5, K_t could represent an input of stress gradient, as in bending, or residual stress just as easily as a detail stress concentration. In fact, K_t could include all gradients at once.

-78-

Several trial cases of stress distribution lend credibility to Eq. 3-5. If K_t is unity for all ℓ, then Eq. 3-5 is integrated to the form:

$$F_{ga} = \frac{2}{\pi} \left[\sin^{-1} \left(\frac{\ell}{a} \right) \right]_0^a = 1 \text{ for any a} \tag{3-6}$$

If K_t has the gradient form $\left(1 - \frac{\ell}{a} \right)$ (making σ the maximum stress at a = 0), Eq. 3-5 gives the following result:

$$F_{ga} = \frac{2}{\pi} \left[\frac{\pi}{2} - 1 \right] = 1 - \frac{2}{\pi} \text{ for any a} \tag{3-7}$$

Both of the preceding answers agree with published results[76,81,82], although the stress distributions involved are obviously special cases.

A more general solution to Eq. 3-5 is found by assuming K_t can be equated to the maximum concentration factor, SCF, multiplied by a decay polynomial[20,22].

$$\frac{K_{t\ell}}{SCF} = 1 + A\ell + B\ell^2 + C\ell^3 + D\ell^4 \tag{3-8}$$

where   A, B, C, D = decay constants (dimensional forms)

Substituting Eq. 3-8 into Eq. 3-5 yields:

$$\frac{F_{ga}}{SCF} = 1 + \frac{2A}{\pi}a + \frac{B}{2}a^2 + \frac{4C}{3\pi}a^3 + \frac{3D}{8}a^4 \tag{3-9}$$

Equation 3-9 can be applied to polynomials of lesser order by merely equating the appropriate decay constants to zero.

It is possible that certain instances require two polynomials linked end-to-end (at $\ell=L$) in order to accurately describe the stress concentration factor decay.

$$\frac{K_{t\ell 1}}{SCF} = 1 + A_1\ell + B_1\ell^2 + C_1\ell^3 + D_1\ell^4 \qquad \ell \leq L \qquad\qquad (3\text{-}10a)$$

$$\frac{K_{t\ell 2}}{SCF} = E + A_2\ell + B_2\ell^2 + C_2\ell^3 + D_2\ell^4 \qquad \ell \geq L \qquad\qquad (3\text{-}10b)$$

where $\qquad E = 1 + \left(A_1 - A_2\right)L + \left(B_1 - B_2\right)L^2 + \left(C_1 - C_2\right)L^3 + \left(D_1 - D_2\right)L^4$

Assuming $a > L$, the integral of Eq. 3-5 must be broken into two parts.

$$F_{ga} = \frac{2}{\pi}\left[\int_0^L \frac{K_{t\ell 1}}{\sqrt{a^2-\ell^2}} * d\ell + \int_L^a \frac{K_{t\ell 2}}{\sqrt{a^2-\ell^2}} * d\ell\right] \qquad\qquad (3\text{-}11)$$

Substituting Eqs. 3-10 into Eq. 3-11 gives:

$$\frac{F_{ga}}{SCF} = E + \frac{2(1-E)}{\pi}\sin^{-1}\left(\frac{L}{a}\right) + \frac{2A_1}{\pi}a + \frac{2\left(A_2-A_1\right)}{\pi}\sqrt{a^2-L^2} + \frac{B_2}{2}a^2 +$$

$$\frac{\left(B_2-B_1\right)}{\pi}L\sqrt{a^2-L^2} + \frac{\left(B_1-B_2\right)}{\pi}a^2\sin^{-1}\left(\frac{L}{a}\right) + \frac{4C_1a^3}{3\pi} +$$

$$\frac{2\left(C_2-C_1\right)}{3\pi}\sqrt{a^2-L^2}\left(L^2+2a^2\right) + \frac{3D_2}{8}a^4 + \qquad\qquad (3\text{-}12)$$

$$\frac{3\left(D_1-D_2\right)}{4\pi}a^4\sin^{-1}\left(\frac{L}{a}\right) + \frac{\left(D_2-D_1\right)}{2\pi}\left[L^3+\frac{3a^2L}{2}\right]\sqrt{a^2-L^2}$$

For the case of $a \leq L$ the equation for F_g reduces to Eq. 3-9 with the constants represented by the first set.

K_t depends on position, ℓ, while F_g depends on crack length, a. When using polynomials the connection between the two decays is provided by the polynomial constants. As an example of the comparison of the two curves, suppose that in Eqs. 3-8 and 3-9 constants A and B are -.13 and +.006, respectively, while C and D are both zero. Assuming a and ℓ are in millimeters, the plots of F_g and K_t are given in Fig. 3.5. It is noted that both decays begin at the same level (F_g and K_t both equal SCF) and initially diverge. The stress concentration factor at the crack tip ($\ell = a$) is always less than the stress gradient correction for that crack length provided stress concentration is decaying rather than rising. (Note that the constants selected for the example cause K_t to rise when ℓ is greater than about 11 mm. K_t actually crosses over F_g when $\ell = a = 15.75$ mm.) If the stress concentration factor decay reaches a lower plateau and levels off, the F_g curve converges asymptotically to the same plateau. Hence, for crack lengths well into the plateau region the difference between F_g for a given crack length and K_t at the crack tip can be neglected. (A case in point is Bowie's solution for a double crack emanating from a circular hole in an infinite plate under uniaxial stress[2,11,42]. Both K_t and F_g decay to 1.0 when the distance from the hole and crack size become large compared to the hole radius.)

Based on the forgoing concepts of $F_g - K_t$ relationships and knowledge of stress concentration decay at typical structural details (Figs. 2.12, 2.21, and 2.39), Fig. 3.6 shows the predicted trend of the stress gradient correction for real details. K_t itself drops sharply to a sort of plateau below 1.0, as required for equilibrium. Meanwhile, F_g also decays but not as rapidly as K_t. Eventually F_g becomes less than 1.0 and slowly converges to K_t. The separation of the two curves at any point obviously depends on detail geometry except at the origin where the curves always converge.

The polynomial approach to an F_g solution has several inherent disadvantages. First, the decay constants must be established and, no doubt, they will vary with the detail geometry. Second, due to the shape of the K_t curve, at least two polynomials (perhaps both fourth order - eight independent constants must be defined) would be required to accurately describe the decay over the entire range of length. Of course, other forms of the K_t equation are possible besides a polynomial. However, the closed form integration in Eq. 3-5 is then usually impossible.

It is not really necessary to establish an equation for the stress concentration factor decay. Equation 3-5 can be solved numerically as suggested by Albrecht[2].

$$F_{ga} = \frac{2}{\pi} \sum_{j=1}^{m} K_{tj} \left[\sin^{-1}\left(\frac{\ell_{j+1}}{a}\right) - \sin^{-1}\left(\frac{\ell_j}{a}\right) \right] \qquad (3-13)$$

where K_{tj} = stress concentration factor in element j of the

                    finite element analysis or the average between two

                    adjacent elements, both of equal distance along

                    the decay line

$$\left.\begin{array}{c} \ell_j \\ \ell_{j+1} \end{array}\right\} = \left\{\begin{array}{l} \text{distance from crack origin to the near and far} \\ \text{sides of finite element j} \end{array}\right.$$

      m   = number of elements to crack length a

Equation 3-13 actually represents a mixed numerical/closed form solution since within a given element the concentration is assumed constant and integration of the remainder of Eq. 3-5 is carried out over the element length. This approach is considered superior to the purely numerical representation, given as follows:

$$F_{ga} = \frac{2}{\pi} \sum_{j=1}^{m} \frac{K_{tj}}{\sqrt{a^2 - \ell_j^2}} * \Delta\ell_j \qquad (3\text{-}14)$$

3.3   Geometry Influences

Equation 3-13 has been employed to find the F_g decay curves for each set of geometrical parameters in Chapter 1. The trend of the results is clarified by Figs. 3.7 and 3.8.

Generally speaking, it is apparent that the detail geometry can have a significant influence on F_g[27]. The more geometrical

parameters involved, the wider the possible range of F_g curves.

Even details with equivalent SCF and lengths over which decay occurs

can have quite different values of F_g at a common point. Likewise,

details with similar F_g/SCF curves usually have dissimilar F_g curves

due to varied SCF. However, it is possible that different combina-

tions of geometrical parameters have equal SCF values and F_g decay

curves.

Figure 3.7 presents standardized F_g decay curves (F_g/SCF)

for sample stiffener and cover plate details. Several conclusions

can be drawn by comparing the geometrical parameters. For stiffeners

the curve is lower when the weld leg-flange thickness ratio (Z/T_f) is

higher. This is reasonable since SCF for stiffeners rises with in-

creasing Z/T_f (Fig. 2.13). The trend also agrees with Gurney's find-

ings for cruciform joints[27]. In the case of cover plate details

the curve is lower when Z/T_f is lower. This too is plausible because,

contrary to stiffeners, SCF decreases with increasing Z/T_f (Fig. 2.13).

The F_g/SCF curve is also lower for higher cover plate-flange

thickness ratios (T_{cp}/T_f) due to increasing SCF (Fig. 2.22).

Standardized F_g curves for sample gusset plate configura-

tions are given in Fig. 3.8. The curves are only plotted to half

flange width; thereafter they would actually begin rising again due

to the two-sided gusset plates assumed in the finite element analyses.

(This particular aspect is neglected later in the dissertation since

little fatigue life remains when half the flange is cracked.) The curves show the same basic relationship exemplified by the stiffener/ cover plate curves. When the combination of geometric parameters is such that SCF rises, the standardized F_g curve tends to drop. However, the sharpness of the decay cannot be attributed purely to SCF. Note that the curve with the second highest SCF actually decays more slowly than two geometries with lower SCF.

It is apparent that SCF plays an important role in F_g curves whether or not they are standardized. The schematic comparison of nonstandardized F_g curves in Fig. 3.9 helps put the findings of Fig. 3.7 and 3.8 into perspective. Higher SCF usually means that F_g is larger at small crack sizes but smaller at large crack sizes. (Recall that the stress concentration factor decay curve, from which F_g is derived, must provide for equilibrium. Higher on one end means lower somewhere else.) Thus, actual F_g curves for two different geometries cross each other in a manner similar to the stress concentration factor decay curves of the fine and ultra fine finite element meshes (Figs. 2.3 and 2.12).

3.4   Ellipse Correlations

Ultimately, the fatigue analyst needs a way of predicting the entire F_g decay curve without going through a time- and money-consuming finite element study. Some sort of equations are necessary which reflect the entire influence of geometry (not just SCF -

Art. 3.3). One possibility is the development of expressions for each decay coefficient in the polynomial equations (Eqs. 3-8 and 3-9). However, four or more such expressions would be required depending on the number of terms and number of different polynomials linked together. Obviously, polynomials are not particularly well suited to representation of stress decay at singular details or any situation where the concentration rises sharply over a small range but is relatively flat elsewhere.

The characteristics of the F_g decay curve (and K_t curve too) at structural details are actually quite similar to features of stress concentration factor decay (based on gross section stress) from the end of an elliptical hole in an infinite, unaxially stressed plate[9,55]. Each curve begins at a maximum concentration factor, SCF, and decays to a value near 1.0. (The asymptote for F_g at details is close to 1.0 - Fig. 3.6. The asymptote for stress concentration factor decay from an arbitrarily shaped hole in an infinite plate is exactly 1.) Therefore, it would seem advantageous to correlate a hypothetical elliptical hole to actual F_g decay curves (Art. 3.3) such that any curve could be estimated from knowledge of the appropriate hole shape and size.

The proper hole shape is based upon the maximum stress concentration factor at the detail (Chap. 2). Figure 3.10 shows that the maximum stress concentration factor at an elliptical hole, including the special case of a circular hole, is a function of the ratio of

the semidiameters, h/g. Hence, knowledge of the SCF (Chap. 2) sets

the shape of the ellipse. Since SCF can vary from 1.0 to over 6.0,

it is necessary to consider stress concentration at both the minor

and major axis ends of the ellipse. The circular hole provides the

link between the two axis possibilities.

Knowledge of the correct ellipse shape does not by itself

establish the required decay correlation. Figure 3.11 demonstrates

that two steps are necessary since ellipses with equivalent shapes

(h/g) can have very different decay curves. Stress concentration at

any point x (or y if decay is in the direction of the minor axis) is

a function of both h/g and x/g (or y/h). As the absolute size of the

ellipse increases, the K_t decay over absolute distance becomes more

gradual (Fig. 3.11b). Therefore, once the ellipse shape is set so as

to give the necessary SCF, either the major or minor semidiameter

must be established to set the ellipse size and associated decay

curve. This second step is also necessary if the hole is circular.

3.4.1 Stress Concentration Decay from Circular
and Elliptical Holes

The stress concentration decay from a circular hole is

readily available in the literature[71]. If the hole radius is denoted

by g and the distance from the hole center by x, the concentration

factor for $x \geq g$ is as follows:

$$K_t = 1 + \frac{1}{2}\left(\frac{g}{x}\right)^2 + \frac{3}{2}\left(\frac{g}{x}\right)^4 \qquad (3\text{-}15)$$

An equation for stress concentration decay from either axis end of an elliptical hole is not often cited in elasticity texts since the expressions are relatively complicated and normally involve elliptical coordinates[1,43,84]. Elliptical coordinates imply an orthogonal system of confocal ellipses, u, and hyperbolas, v, through which the position of any point in a plane can be established (in the same manner as a square grid with values of x and y establish a position in rectangular coordinates). However, due to the fact that decay occurs along the major or minor axis of the ellipses where v is constant at 1 or 0, respectively, it is only necessary to consider the value of u in establishing a position. Figure 3.12 shows the system of confocal ellipses which is of interest.

There are several ways of expressing the equation of an ellipse. One useful form contains a mixture of rectangular and elliptical coordinate parameters.

$$\frac{x^2}{f^2 u^2} + \frac{y^2}{f^2\left(u^2-1\right)} = 1 \qquad (3\text{-}16)$$

where   f = focal distance

u = elliptical coordinate $1 < u < \infty$

An alternative set of elliptical coordinates, η and ζ, are related to the initial set, u and v, as follows:

$$u = \cosh(\eta) \qquad\qquad (3\text{-}17a)$$

$$v = \cos(\zeta) \qquad\qquad (3\text{-}17b)$$

Substituting Eq. 3-17a into Eq. 3-16 and using a hyperbolic function identity gives another important form of the ellipse equation:

$$\frac{x^2}{f^2\cosh^2(\eta)} + \frac{y^2}{f^2\sinh^2(\eta)} = 1 \qquad\qquad (3\text{-}18)$$

Equation 3-18 can be used to establish the relationship between rectangular and elliptical coordinates when the point in question is on the major or minor (x or y) axis

Major Axis: $\qquad \cosh(\eta) = \dfrac{x}{f} \qquad\qquad (3\text{-}19a)$

Minor Axis: $\qquad \sinh(\eta) = \dfrac{y}{f} \qquad\qquad (3\text{-}19b)$

For the specific case of the elliptical hole with semidiameters g and h, let $\eta = \gamma$ and Eqs. 3-19 become:

Major Axis: $\qquad \cosh(\gamma) = \dfrac{g}{f} \qquad\qquad (3\text{-}20a)$

Minor Axis: $\qquad \sinh(\gamma) = \dfrac{h}{f} \qquad\qquad (3\text{-}20b)$

Both sets of equations (3-19 and 3-20) involve the focal distance, f, which is constant for confocal ellipses by definition. Thus, f can be established from the elliptical hole semidiameters[72].

$$f = \sqrt{g^2 - h^2} \qquad\qquad (3\text{-}21)$$

Substituting Eq. 3-21 into Eqs. 3-20 gives the following expression:

$$\gamma = \cosh^{-1}\left[\frac{1}{1-\left(\frac{h}{g}\right)^2}\right]^{1/2} = \sinh^{-1}\left[\frac{1}{\left(\frac{g}{h}\right)^2-1}\right]^{1/2} \tag{3-22}$$

As stated previosuly, the ellipse shape (h/g or g/h) is established by the maximum stress concentration factor, SCF (Fig. 3.10). Therefore, γ can be found for cases of SCF less than 3.0 (minor axis decay) as well as SCF greater than 3.0 (major axis decay). At precisely 3.0 (a circle) a singularity develops. Hence, it is expedient, particularly when using the computer, to make use of Eq. 3-15 for the singular case.

Equation 3-21 can also be substituted directly into Eqs. 3-19. However, with γ known it's simpler to define f in terms of Eq. 3-20a or 3-20b and use this form in Eqs. 3-19.

Major Axis: $\cosh(\eta) = \frac{x}{g}\cosh(\gamma) = \frac{x}{h}\sinh(\gamma)$ (3-23a)

Minor Axis: $\sinh(\eta) = \frac{y}{g}\cosh(\gamma) = \frac{y}{h}\sinh(\gamma)$ (3-23b)

In these forms it is apparent η depends on the ratio of the x or y coordinate to semidiameter g or h as well as γ, which depends on the ratio of semidiameters. Assuming the stress concentration factor decay depends only on γ and η, the functional relationship of Fig. 3.11 is verified. Moreover, it is seen that if the exact size of the ellipse is known through the stress concentration factor (Chap. 2) and correlation equations (Art. 3.4.2), K_t can be found for any assumed point x or y.

References 55 and 9 lead to solutions for K_t in terms of γ and η. First, for uniaxial tension in the minor axis direction and decay in the major axis direction, two equivalent forms of the K_t equation are presented.

Ref. 55:

$$K_{t\eta} = 1 + \frac{1}{2} \frac{\cosh(\gamma)}{\sinh^2(\eta)} \left[e^{\gamma}\left(e^{2\gamma}-3\right)\left(1+\frac{1}{2}\coth(\eta)\right)e^{-2\eta} + \cosh(\gamma)\coth(\eta)\right]$$

(3-24)

Ref. 9:

$$K_{t\eta} = \left[\frac{1}{8}\left\{1 - 2e^{2\gamma} + e^{4\gamma}\right\}\left\{3 - 4e^{-2\eta} + e^{-4\eta}\right\} - \frac{1}{8}e^{4(\gamma-\eta)} + \right.$$

(3-25)

$$\left. \sinh(2\eta)\left\{\cosh(2\eta) + \frac{1}{2}\cosh(2\gamma) - \frac{3}{2}\right\}\right] \Big/ \left(\cosh(2\eta)-1\right)^2$$

Second, for uniaxial tension in the major axis direction and decay in the minor axis direction, only one K_t equation is derived.

Ref. 9:

$$K_t = \left[\frac{1}{8}\left\{1 + 2e^{2\gamma} + e^{4\gamma}\right\}\left\{3 + 4e^{-2\eta} + e^{-4\eta}\right\} + \right.$$

(3-26)

$$\left. \sinh(2\eta)\left\{\cosh(2\eta) + \frac{1}{2}\cosh(2\gamma) + \frac{3}{2}\right\}\right] \Big/ \left(\cosh(2\eta)+1\right)^2$$

While Eqs. 3-24, 3-25, and 3-26 are somewhat tedious to solve by hand, they present no difficulty whatever for the computer.

3.4.2 Correlation Equations

Now that equations have been developed to evaluate stress concentration factor decay from either axis end of an elliptical hole, the idea is to formulate equations for optimum ellipse size. The basis assumed for this optimization is equal cycle life for a certain amount of crack growth, depending on the type of detail. In other words, the life using the Green's Function F_g curve (Art. 3.3) is compared with life predicted using the stress concentration factor decay from an elliptic hole in place of F_g. The size of the hole is adjusted using a bisection approach until the lives are equal (maximum relative error - 0.05 percent).

Life predictions require knowledge of ΔK (Eq. 1-3) which, in turn, requires values for other correction factors as well as F_g (Eq. 1-4 and Chap. 4). ΔK also requires an input of stress range, S_r. However, the extensive correlation study for all details in Chapter 2 has shown that the form of the other correction factors has negligible effect on the correlation results. Furthermore, the choice of S_r makes no difference since it is constant and does not need to be included in the integration process (Eq. 1-3).

It is necessary to consider the dimensionless geometrical parameters incorporated in the SCF equations (Chap. 2) when formulating the correlation (optimization) equations. Such equations are not developed in terms of SCF since SCF alone does not dictate the shape of the decay curve, even when it is presented in terms of

nondimensional distance. (Note that certain details in Figs. 3.7 and 3.8 with nearly equal SCF have dissimilar decay curves.) Fortunately, the ellipse stress concentration decay concept is versatile and the ellipse size can be made to suit all circumstances.

One additional geometrical parameter which enters into the correlation process is initial crack size, a_i. The optimized stress concentration factor decay curve for the elliptical hole does not necessarily coincide with the actual F_g curve at every position. It's just that their effect on a certain amount of crack growth is made equal. Therefore, the optimum curve shifts position somewhat as a_i varies.

3.4.2.1 Stiffeners and Cover Plates Attached to Flanges with Transverse Fillet Welds

Generally, SCF for stiffener and cover-plated details exceeds 3.0 (Fig. 2.13). Thus, stress concentration factor decay is taken from the major axis end of the elliptical hole (Eq. 3-24 or 3-25). While the decay can be evaluated in terms of x/g or x/h (Eq. 3-23a), x/g is preferred since x equates to g plus crack length a.

For both stiffeners and cover plates the ellipse correlation is made for growth through the flange thickness. Figure 3.13 compares a typical F_g approximation curve (from the ellipse) with the actual F_g curve (from the Green's Function - Art. 3.2) and the original stress concentration factor decay at the detail. It is apparent that the approximate F_g curve is in close agreement with the actual F_g curve and

both are above the K_t curve from the finite element analysis. Commonly, the two F_g lines cross each other twice.

It has already been mentioned that initial crack size has a bearing on the correlation results. Figure 3.14 indicates the kind of variance in optimum ellipse size, g_{opt}, which is typical of all details. The trend is somewhat parabolic. This shape is understandable since for very small initial cracks the two F_g curves cross over one another at two points (Fig. 3.13). Naturally, the lower limit of g_{opt} is zero and occurs when the initial crack size is so large (in the vicinity of $a_i/T_f = 0.4$) that correlation is no longer possible. However, at this and larger crack lengths F_g can be assumed to be 1.0 without significant error.

The optimum ellipse sizes found by correlation study of the geometries in Chapter 2 can be related to the geometrical parameters involved by least squares curve fits. The resulting relationships for stiffeners and cover plates are as follows:

Stiffeners:

$$\frac{g_{opt}}{T_f} = -0.002755 + 0.1103 \left(\frac{Z}{T_f} \right) - 0.02580 \left(\frac{Z}{T_f} \right)^2 +$$

$$0.6305 \left(\frac{a_i}{T_f} \right) - 7.165 \left(\frac{a_i}{T_f} \right)^2 \tag{3-27}$$

<u>Cover Plates</u>:

$$\frac{g_{opt}}{T_f} = 0.2679 + 0.07530 \left(\frac{Z}{T_f}\right) - 0.08013 \left(\frac{Z}{T_f}\right)^2 + \tag{3-28}$$

$$0.2002 \log \left(\frac{T_{cp}}{T_f}\right) + 1.391 \left(\frac{a_i}{T_f}\right) - 11.74 \left(\frac{a_i}{T_f}\right)^2$$

The standard errors of estimate for the stiffener and cover plate equations are 0.0041 and 0.0055, respectively.

One remote possibility for stiffeners is that SCF will drop below 3.0. Then, the approximation of F_g should no longer be taken from stress concentration factor decay from the major axis end of an elliptical hole. The question arises as to what to do about Eq. 3-27. An approximate procedure is simply to replace g_{opt} by h_{opt} and employ Eq. 3-26 rather than Eq. 3-24 or 3-25. Elliptical coordinate η would be established by Eq. 3-23b where y is h plus the crack length, a.

The optimum ellipse size equations can be used to predict F_g for values of geometrical parameters not specifically studied in Chapter 2. Knowledge of SCF (Chap. 2) sets the ellipse shape (Fig. 3.10) and elliptic parameter γ (Eq. 3-22). A given crack length, optimum ellipse size, and γ yield elliptic coordinate η (Eq. 3-23a). Both η and γ fix the value of K_t (Eq. 3-24 or 3-25) which has been correlated to F_g. Thus, F_g at the given crack length is approximated.

A useful comparison of F_g curves for a cruciform joint is presented in Fig. 3.15. (For the ellipse correlation the joint is

treated as a stiffener with B equal to twice T_f.) Gurney's decay stems from a finite element compliance analysis[27] and is seen to be generally higher than the correlated ellipse decay. The Hayes and Maddox curve[30] is in good agreement with the ellipse approximation. While the Hayes and Maddox F_g also resulted from a finite element compliance analysis, it involved loading the crack surface directly with the crack free stresses[31] in the same manner as the Green's Function concept (Art. 3.2). Also, Hayes and Maddox had only a one-sided crack which caused plate bending of increasing magnitude with increasing crack length.

One reason for the lack of agreement with Gurney's results is the difference in mesh size. While Gurney does not present his mesh in real units (everything is relative to B), it is probable that the size was considerably larger than that in Chapter 2. From a comparison of results of fine and ultra fine meshes it is known that SCF rises as mesh size decreases. However, the stress concentration factor decays less sharply for the fine mesh leading to higher values of F_g at the larger crack lengths.

Another source of discrepancy between the Gurney and ellipse correlation curves is Gurney's calculation of F_g from the compliance results. Chapter 1 noted that a compliance analysis leads to stress intensity, K. In order to find F_g, assumptions must be made for the other correction factors. Gurney simply assumed K for a double edge cracked plate under uniform tension is representative of K for the

actual joint divided by F_g. (Gurney does admit, however, that the assumption is weak at large crack sizes since, for symmetry, four cracks are implied by the finite element modeling - Fig. 3.15.) Chapter 4 shows that the front free surface correction, F_s, rises when there is a stress concentration at the crack origin. Therefore, Gurney's curve appears to include some amplification for F_s as well as F_g.

3.4.2.2 Gusset Plates Groove-Welded to Flange Tips

Since SCF for gusset plates with circular transitions rarely exceeds 3.0, stress concentration factor decay is taken from the minor axis end of the elliptical hole (Eq. 3-26). The decay is evaluated in terms of y/h rather than y/g (Eq. 3-23b) because coordinate y is equal to h plus the crack length, a.

Ellipse correlation is made for crack growth across half of the flange width to the web line. F_g begins to rise shortly after that point since K_t rises for a two-sided detail. Using the correlated ellipse decay beyond the web is then actually erroneous. However, so little life remains that the error is unimportant. The ellipse correlation curve is also too high if the detail is only one-sided although it leads to a conservative cycle life estimate (Chap. 2).

Correlation studies of the gusset plate geometries in Chapter 2 produce optimum ellipse sizes, h_{opt}. As in the cases of the stiffeners and cover plates, the ellipse size can be related to the

various geometrical parameters and initial crack size by a least squares curve fit. The resulting equation is as follows:

Gusset Plates:

$$\frac{h_{opt}}{W_f} = -0.01620 - 0.1105 \left(\frac{R}{W_f}\right) + 0.03307 \left(\frac{R}{W_f}\right)^2 + 0.02821 \left(\frac{L}{W_f}\right) -$$

$$0.002436 \left(\frac{L}{W_f}\right)^2 - 0.008776 \left(\frac{W_{gp}}{W_f}\right) + 0.004437 \left(\frac{W_{gp}}{W_f}\right)^2 +$$

$$0.08587 \left(\frac{T_{gp}}{T_f}\right) - 0.03291 \left(\frac{T_{gp}}{T_f}\right)^2 + 1.673 \left(\frac{a_i}{W_f}\right) - 43.49 \left(\frac{a_i}{W_f}\right)^2$$

$$(3-29)$$

The standard error of estimate for Eq. 3-29 is 0.0107. This is about double those values for Eqs. 3-27 and 3-28 due primarily to the greater number of variables involved.

Equation 3-29 is intended for flange thicknesses less than or equal to 25 millimeters. Flange thickness has a special effect due to its relationship to crack shape (Art. 4.5). Figure 3.16 emphasizes that the crack shape regions delineating the trend in shape with crack growth depend on flange thickness as well as initial crack size. Therefore, flange thickness affects the number and phases of crack shapes which are exhibited. For thicknesses up to 25 mm h_{opt} is unaffected by crack shape considerations.

Flange thicknesses greater than 25 mm require a modification

to Eq. 3-29. The amplification factor by which Eq. 3-29 should be

multiplied is as follows:

$25 \text{ mm} \leq T_f \leq 50 \text{ mm}$:

$$1.0 + \frac{U}{34.54 \log \left(\frac{L}{W_f}\right)} \qquad (3\text{-}30)$$

where $\quad U = \frac{T_f}{25} - 1.0$

$T_f > 50 \text{ mm}$:

$$1.0 + \frac{1}{34.54 \log \left(\frac{L}{W_f}\right)} \qquad (3\text{-}31)$$

Typically, this factor results in a change of less than 15 percent.

The procedure for predicting F_g for arbitrary gusset plate

geometries is similar to that outlined for stiffeners and cover

plates. SCF can be found from Eq. 2-5 and used to fix the ellipse

shape (Fig. 3.10) and parameter γ (Eq. 3-22). Elliptical coordinate η is

evaluated (Eq. 3-23b) using γ, ellipse size h (Eq. 3-29, amplified if

required), and an assumed crack length. Substitution of η and γ into

Eq. 3-26 gives the stress concentration factor at the assumed crack length. This stress concentration factor corresponds to F_g.

In the unlikely event that SCF exceeds 3.0, h_{opt} in Eq. 3-29 can be treated as g_{opt}. Then, Eq. 3-23a should be employed to find η and substituted into one of the equations for stress concentration factor decay from the major axis end (Eq. 3-24 or 3-25). The resulting value of K_t is taken as F_g.

4. OTHER CORRECTION FACTORS

The compliance approach to evaluating stress intensity (Chap. 1) has the distinct advantage that the combination of correction factors, CF, is that which is output. An individual correction factor can be evaluated from this combination by making assumptions for the remaining individual factors. But since it is the total correction at any crack length which is important in fatigue life prediction, accuracy of the assumptions is not overly important unless several of the individual corrections are to be reused in an unrelated problem. Such reuse is encouraged because fatigue life investigators rarely have the time and funds to run a complete compliance analysis on each new detail configuration.

Albrecht's method of evaluating F_g isolates this correction factor from all others by solving a problem different from the one at hand. Thus, it is necessary to make decisions on the other correction factors before fatigue life can be estimated. However, it is important to recognize that these other corrections are affected by the nonuniform stress distribution[81]. Likewise, all corrections are affected by crack shape[62] even though one correction, F_e, is specifically intended for this purpose. Therefore, any assumptions on correction factors must consider the influence of stress distribution and crack shape.

Some hesitation exists in using solutions for correction factors – particularly F_s – which are related to idealized plate geometries. Geometries at real bridge details are often irregular; perhaps the form of each correction from an idealized geometry is not precise. Nevertheless, the state-of-the-art in stress intensity evaluation is such that most actual details have not been solved. Approximate solutions from idealized cases are inevitable. Moreover, the cumulative validity of these approximations can be judged on the basis of correlations between estimated and actual fatigue lives (Chap. 6).

4.1 Crack Shape Correction – F_e

Based on the work of Green and Sneddon[23] the effect of crack shape on stress intensity is dependent upon the complete elliptic integral of the second kind.

$$E(k) = \int_0^{\pi/2} \left[1 - k^2 \sin^2 \beta\right]^{1/2} d\beta \qquad (4-1)$$

where $\quad k = 1 - \left(\dfrac{a}{b}\right)^2$

$\qquad a$ = minor axis semidiameter

$\qquad b$ = major axis semidiameter

For any given position along the crack front, described by angle ϕ to the major axis, F_e is given by the equation[38]:

$$F_e = \frac{1}{E(k)} \left[1 - k^2\cos^2\phi \right]^{1/4} \qquad (4-2)$$

Generally, interest is directed to the minor axis end of the ellipse where $\phi = \pi/2$. For this particular position:

$$F_e = \frac{1}{E(k)} \qquad (4-3)$$

The limits of F_e are readily determined by inspection of the ratio a/b. When the two semidiameters are equal the ratio a/b is 1.0. Thus, k is zero. F_e by either Eq. 4-2 or 4-3 is therefore $2/\pi$. However, when b is much larger than a as in a through crack configuration, the ratio approaches zero and k goes to 1.0. $E(k)$ also approaches 1.0 and F_e by Eq. 4-2 reduces to

$$F_e = [\sin\phi]^{1/2} \qquad (4-4)$$

For $\phi = \pi/2$, F_e obviously is 1.0. Thus, for $\phi = \pi/2$, F_e varies between 1.0 and $2/\pi$ as the ratio a/b varies between zero and 1.0. At ϕ equal to zero, F_e varies between zero and $2/\pi$ as the ratio a/b varies between zero and 1.0.

F_e is seen to be maximized at the minor axis end of the ellipse, thereby maximizing stress intensity (neglecting the variation of other correction factors). Thus, surface cracks tend to grow more rapidly at their minor axis ends - approaching semicircular conditions. Minor axis length, a, then corresponds to the critical crack length parameter, a. Unless otherwise indicated it is assumed

that the stress intensity at the minor axis end of the crack front ($\phi = \pi/2$) is desired and Eq. 4-3 is used to evaluate the crack shape correction factor.

4.2 Front Free Surface Correction - F_s

Whether or not a free surface correction is necessary (is other than 1.0) depends upon the boundary condition at the crack origin. In an early study on stress intensity Irwin considered Westergaard's periodic array of through cracks across an infinite plate[35,62,87]. The through crack permits no Poisson type displacement along lines perpendicular to the cracks and cutting them in half. Thus, no free surface correction was required.

For edge cracks F_s is generally necessary since stress, not displacement, is zero on the free boundary. Attachments like stiffeners, cover plates, and gussets, as well as webs do provide some restrction to displacement at weld toes or terminations. The magnitude of such restriction is not known to any specific degree although it is estimated to be quite modest. At least it is often on only one side of the crack. Thus, in this dissertation Poisson type displacement restriction by attachments is disregarded completely and F_s is related to simple edge crack specimens.

The approach with this correction factor is to determine the values for the extreme conditions of through (a/b = 0) and circular

(a/b = 1) crack fronts. The circular fronts are further divided into half-circles and quarter-circles since stiffeners and cover plates have half-elliptical surface cracks while groove-welded gusset plates tend to have quarter-elliptical surface cracks (i.e. The crack originates from the corner of a flange cross-section rather than along the side – Art. 4.5).

4.2.1 Through Crack

Tada and Irwin have tabulated the variability of F_s with the distribution of stress applied to the crack[81,82]. Figure 4.1a shows this variability for the types of stress distributions common to bridge details. If the stress is uniform over the crack length, F_s is 1.122. If the stress varies linearly to zero at the crack tip, F_s is 1.210. And if a concentrated load exists at the crack origin, F_s is 1.300. Hence, if the stress distribution decreases from the crack origin more rapidly than the linear condition, F_s must have a value between 1.210 and 1.300.

4.2.2 Half-Circular Crack

Reference 82 also directs attention to the half-circular crack (Fig. 4.1b). For a uniform stress over the entire crack plan area, F_s is 1.025. For a stress which varies linearly to zero at the crack tip, F_s is 1.085. The solution for a line load over length 2b at the crack origin is not known. F_s for this condition is estimated

at 1.145 which incorporates twice the increment increase as is present in changing from a uniform to a linear stress pattern.

4.2.3 Quarter-Circular Crack

Less is known about free surface correction for quarter-circular cracks than for the previous crack geometries. The stress intensity is desired at one of the free surfaces ($\phi = \pi/2$ in Ref. 82), and existing solutions are not accurate there. F_s must actually account for both free surfaces as well as stress distribution. Based on extrapolation of solutions for positions other than the free surfaces, F_s is estimated to be 1.380 for uniform stress (see also Ref. 17) and 1.067 for linearly varying stress. {Note that 1.380 is not merely the square of F_s for the half-circular or through crack case. Tada and Irwin also state it is not the product of F_s ($\phi = 0$) and F_s ($\phi = \pi/2$) for the half circle.} As with the half-circular crack a solution is unknown for a line load over length b at the crack origin. Thus, the limiting F_s is estimated at 0.754. The manner of deriving this estimation is identical to that in the half-circle.

Comparison of the quarter-circular case with the half-circular and through crack cases provides one interesting conclusion. For through and half-circular cracks F_s increases as more stress is concentrated at the crack origin. However, F_s declines sharply for quarter-circular cracks as concentration increases. Apparently the

free surface directly adjacent to the crack tip tends to relieve more and more of the stress condition as the applied loading becomes more remote. Plane stress exists at the crack tip rather than plane strain.

4.3 Back Free Surface Correction - F_w

The solutions for F_s consider infinite half or infinite quarter spaces. When the space is not infinite, thought must be given to the back surface correction, F_w. Once again the form of the correction depends on stress distribution and crack shape. However, F_w also is quite sensitive to whether or not the section is permitted to bend as crack growth occurs. The bending tendency is natural for any strip in which crack growth is not symmetrical with respect to the strip centerline.

The literature often cites two forms of F_w (almost interchangeably) for the symmetrical crack cases presented in Fig. 4.2[62,76,81,82]. These two expressions are also applicable to nonsymmetrical crack configurations where bending is prevented by imposed boundary conditions. Thus, the strips in Fig. 4.3 are comparable to those in Fig. 4.2. In real structural details the roller supports might be provided by a web and/or stiffener.

Bending amplifies the back surface correction - particularly at high values of a/w where more bending occurs. If the rollers on either strip of Fig. 4.3 are removed, the back surface correction takes on the following form[15,17]:

$$F_w = Q* \left(\frac{2}{\pi \alpha} \tan \left(\frac{\pi \alpha}{2} \right) \right)^{1/2} \qquad (4-5)$$

where
$$Q = \frac{0.752 \_ 2.02\alpha + 0.37 \left(1 - \sin \left(\frac{\pi \alpha}{2} \right) \right)^3}{1.122 \cos \left(\frac{\pi \alpha}{2} \right)}$$

$$\alpha = \frac{a}{w}$$

The coefficient by which the tangent correction is modified, Q, is plotted in Fig. 4.4. While it is true that the change only becomes very large at high α values, actual life predictions have shown the bending coefficient to have significant influence on the results - particularly when stress range is small and early fracture unlikely (Chap. 6). Since stress intensity range is raised to the third power in order to predict life, even small changes in correction factors are important.

Tada and Irwin mention that it is possible to have an in-between situation where local bending of the strip at the crack is possible but remote bending is restrained[82]. In Fig. 4.3 this constitutes removing those rollers near the crack position. For such a condition a reasonable expression for the back surface correction is:

$$F_w = \frac{1.122 - 0.561\alpha + 0.085\alpha^2 + 0.180\alpha^3}{1.122 \sqrt{1 - \alpha}} \qquad (4-6)$$

Equation 4-6 can be divided by the normal tangent correction to determine the amount of amplification. This amplification coefficient is also plotted in Fig. 4.4.

It is readily apparent that little difference exists between Eq. 4-6 and the tangent correction. Removing only the local rollers in Fig. 4.3 has no effect on F_w. However, when such restraint is removed from the crack origin, F_s changes from 1.0 to 1.122. Stress rather than displacement becomes zero locally.

The choice between bending and no bending depends on the structural detail as well as how the crack is growing. For both cover plates and stiffeners fillet-welded to flanges, cracks originate at weld toes and grow through the flange thickness. (Flange thickness is then equated with strip width, w, in Figs. 4.2 and 4.3 and Eq. 4-5.) Yet, the two details are believed to be different as far as bending is concerned.

The stiffener and web combine to restrict flange bending, which is caused by the presence of cracks across the entire flange width. However, cover plates are much more flexible than stiffeners (depending primarily on thickness) and longitudinal flange bending due to cracks is really only prevented along the web line. Therefore, stiffener details are assumed to have bending prevented while cover plates are taken to have unrestricted bending. The fact that longitudinal bending is prevented directly over the web in both cases is not a dominant factor since cracks originate at many sites across the flange width (Art. 4.5).

It is possible to have small plate attachments fillet-welded in an upright position across a flange. Series AQB in

Ref. 20, for example, is representative of this sort of detail.
Stress concentration is again related to the weld-flange thickness
ratio, and even though the attachments are not connected to the web,
little local flange bending is induced or permitted. Therefore,
while not precisely the same as a stiffener, fatigue performance
shoule be, and indeed was similar.

Gusset plate details have been found to exhibit considerable
flange bending during crack growth[12]. Such is true even if plates of
identical geometry are symmetrically positioned on opposite flange
tips. Some crack growth may occur at both details, but soon one side
dominates and bending causes the crack at the other side to close.
For practical purposes such details are comparable to cover plates as
far as back surface corrections are concerned. Strip width, w, should
be taken as the full flange width, not simply half of it. (Half
flange width would be used if a symmetrical double edge crack truly
exists, but then there would be no bending.)

Figure 4.5 presents the back surface corrections for through
cracks with and without bending. Without bending the familiar secant
correction is used for a uniform stress while the secant is amplified
as stress concentration occurs at the crack origin. This amplifica-
tion has maximum value 1.297 $\sqrt{\pi/2}$ for a concentrated load at the crack
origin and $\alpha = 1.0$. Both no bending solutions stem from a finite width
plate with a central through crack[81]. The linearly varying stress
case is assumed to be the average of the two extremes. A sharper

stress decline has a correction somewhere between the concentrated load and the linearly varying stress values.

The back surface corrections associated with bending show significant amplification of the secant correction. Figure 4.4 plots the uniform stress correction divided by the tangent correction. Since the tangent and secant corrections are similar, the plot gives a good indication of the uniform stress amplification as defined here. (e.g. At $\alpha = 0.9$ the uniform stress amplification is 12.29 while the concentrated load amplification if 29.78.) These back surfaces solutions are directly linked to front surface corrections since bending demands lack of symmetry. The combined correction factors for through cracks found in Refs. 81 and 82 were divided by the associated front surface corrections (Fig. 4.1) to isolate the back surface correction factors.

To this point all discussion of back free surface correction factors has centered on the through crack configuration (a/b = 0). Maddox[51] recently condensed the work of numerous researchers[24,41,77,83] and estimated how F_w varies for crack shape ratios and α values between zero and 1.0. Uniform stress and unrestricted bending were assumed. His results essentially agree with Fig. 4.5b when a/b equals zero, but vary nonlinearly to almost 1.0 for any α value when a/b equals 1.0. In other words, F_w might well be disregarded for the half-circular crack. The net ligament on either side of the crack inhibits bending and even restricts the crack from "seeing" the upcoming free surface.

The curves Maddox produced are approximations since few data points exist for crack shape ratios between zero and 1.0. Nevertheless, it is reasonable to assign F_w a value of 1.0 for any α if the crack shape is half-circular, regardless of the bending and stress distribution considerations[15,73].

4.4 Plastic Zone Correction - F_p

Earlier studies have indicated that the plastic zone correction, F_p, is normally small for fatigue problems and can be disregarded (Chap. 1). While a detailed investigation of this premise is not intended, a brief outline of the basis of the decision is warranted. Interest is particularly centered on how the other correction factors affect the magnitude of F_p.

Stress intensity factors stem from the elastic stress distribution near a crack tip. The stress ahead of the crack tip and normal to the crack plane has the following form.

$$\sigma = \frac{K}{\sqrt{2\pi r}} \tag{4-7}$$

where   r = distance from crack tip

Obviously, σ increases as r decreases and eventually reaches the yield stress σ_y. The distance, r_y, to where the yield condition ends is

$$r_y = \frac{1}{\Omega} \left(\frac{K}{\sigma_y}\right)^2 \tag{4-8}$$

where σ_y = yield stress of material from standard tensile test

-112-

Factor omega (Ω) is used in lieu of 2π in Eq. 4-8 since the yield stress of the material, σ_y, as defined by a standard uniaxial tensile test, is elevated when plastic flow is restricted. This restriction is provided by the elastic regions away from the crack tip. The amount of restriction and the effect on yield depends on whether a two- or three-dimensional stress state is created. Thus, the Ω associated with plane stress differs from that required for plane strain conditions.

Some redistribution of elastic stress must occur to accommodate the yield zone. This redistribution can be viewed as a simple increase in effective crack length[5]. Irwin estimated the additional length to equal r_y[36]. The effective stress intensity, K_{eff}, is then:

$$K_{eff} = CF'*\sigma\sqrt{\pi(a+r_y)} \tag{4-9}$$

where $$CF' = CF'\left(\frac{a+r_y}{w}, \frac{a+r_y}{b}, \text{geometry}\right)$$

$$= F_s'F_w'F_e'F_g'$$

Since r_y depends on K (i.e. K_{eff}) which, in turn, depends on r_y, an iteration process between Eqs. 4-8 and 4-9 is required for a stress intensity solution. However, the additional accuracy garnered may not be worth the iteration effort. One intermediate suggestion is to use material toughness, K_c, if available, in place of K in Eq. 4-8[12]. This would maximize the zone size and, as far as Eq. 4-9 is concerned, have maximum effect at small crack sizes.

Another possibility in lieu of iteration is to leave the correction factors in Eq. 4-9 unmodified for zone size and only modify the crack length under the radical. This approach is essentially the same one taken by Irwin when he employed only two correction factors, F_s and F_e, and considered them both constants[37]. The effective stress intensity equation is then:

$$K_{eff} = F_s F_e * \sigma \sqrt{\pi(a+r_y)} \tag{4-10}$$

Using K_{eff} in Eq. 4-8, substituting Eq. 4-8 into Eq. 4-9, and rearranging gives:

$$K_{eff} = \frac{F_s * \sigma \sqrt{\pi a}}{\left[\dfrac{1}{F_e^2} - \dfrac{F_s^2 \pi \sigma^2}{\Omega \sigma_y^2} \right]} \tag{4-11}$$

Irwin used Φ in lieu of $\frac{1}{F_e}$, $4\sqrt{2}\pi$ in place of Ω and let F_s^2 equal 1.2. Thus, Eq. 4-11 appeared as follows[38]:

$$K_{eff} = \frac{1.1 \, \sigma \sqrt{\pi a}}{\left[\Phi^2 - 0.212 \dfrac{\sigma^2}{\sigma_y^2} \right]^{\frac{1}{2}}} = 1.10 \, \sigma \sqrt{\frac{\pi a}{Q}} \tag{4-12}$$

It is apparent that crack tip plasticity was treated as a modification of the crack shape correction, F_e. The ratio a/Q was termed the normalized crack depth. Curves of Q versus crack shape ratio, a/b, have been developed for various ratios of applied stress to yield stress[65].

-114-

Equation 4-11 can also be expressed as:

$$K_{eff} = F_p F_s F_e * \sigma \sqrt{\pi a}$$ (4-13)

where $\quad F_p = \dfrac{1}{\left[1 - \dfrac{\pi}{\Omega} \left(\dfrac{F_e F_s \sigma}{\sigma_y}\right)^2\right]^{\frac{1}{2}}}$

In considering the general case of all correction factors, the Irwin method leads to the following formula for effective stress intensity.

$$K_{eff} = CF_p * \sigma \sqrt{\pi a}$$ (4-14)

where $\quad CF_p = F_p * CF$

$$F_p = \dfrac{1}{\left[1 - \dfrac{\pi}{\Omega} \left(\dfrac{CF * \sigma}{\sigma_y}\right)^2\right]^{\frac{1}{2}}}$$

There is another possibility for solving Eq. 4-9 without iteration. That is to include r_y in the correction factors, but use unmodified K instead of K_{eff} in Eq. 4-8. K_{eff} would only be used in Eq. 4-8 when modifying crack length, a, under the radical. The resulting equation, similar to Eq. 4-14, would be:

$$K_{eff} = CF_p'' * \alpha \sqrt{\pi a} \qquad\qquad (4\text{-}15)$$

where

$$CF_p'' = F_p * CF''$$

$$F_p = \frac{1}{\left[1 - \frac{\pi}{\Omega}\left(\frac{CF''\sigma}{\sigma_y}\right)^2\right]^{\frac{1}{2}}}$$

$$CF'' = CF''\left(\frac{a+r_y'}{w}, \frac{a+r_y'}{b}, \text{geometry}\right)$$

$$r_y' = \frac{\pi a}{\Omega}\left(\frac{CF*\sigma}{\sigma_y}\right)^2$$

Whether K_c, Eq. 4-14, Eq. 4-15, or the original iterative technique is favored depends on the problem and accuracy needs. In light of uncertainities in other correction factors for real structural details, iteration is generally not warranted. Equation 4-15, being somewhat more accurate than Eq. 4-14, is favored in fracture problems where the applied stress, σ, and plastic zone are often large. The format of Eq. 4-14 (with correction factors unmodified for effective crack length) seems sufficient for most fatigue problems. However, two further modifications to the equation are required.

Paris noted that it is necessary to replace stress, σ, with stress range, S_r, and the yield stress, σ_y, with $2\sigma_y$ when a fatigue problem is encountered[61]. The latter adjustment is required since for alternating plasticity the elastic stress must reach twice the static

yield stress. Therefore, the size of successive yield zones in fatigue is one-quarter that found in fracture problems. The resulting expression for effective stress intensity is:

$$K_{eff} = CF_{pf} * S_r \sqrt{\pi a} \qquad (4\text{-}16)$$

where $CF_{pf} = F_{pf} * CF$

$$F_{pf} = \cfrac{1}{\left[1 - \cfrac{\pi}{4\Omega}\left(\cfrac{CF * S_r}{\sigma_y}\right)^2\right]^{\frac{1}{2}}}$$

The factor Ω has been investigated by Irwin[37,39], Liu[46], Schijve[69], and Rice[66,67]. Due to the influence of the crack itself, plane strain conditions are predominant at the tip, even with very thin plates[75]. Maddox records that Rice's latest solution for plane strain ($\Omega = 2.82\ \pi$) is probably the most accurate solution available for that category[48]. Making the substitution for Ω results in the following plastic zone correction for fatigue.

$$F_{pf} = \cfrac{1}{\left[1 - \left(\cfrac{CF * S_r}{3.36\sigma_y}\right)^2\right]^{\frac{1}{2}}} \qquad (4\text{-}17)$$

It is obvious that the plastic zone correction increases with the other correction factors. F_p also increases with stress range but decreases with the yield stress of the material. If F_p had

significant importance in fatigue, Eq. 4-17 leads to the conclusion that the log-log S_r-N curves of Ref. 21 would not be straight lines, and the various category curves would not necessarily be parallel to each other. However, experimental data on structural members of all common yield strengths is the basis of the essentially parallel S_r lines and Code provisions in the first place[3,19,20]. Yield strength in the range normally encountered (210-760 MPa) was found to be statistically unimportant[19].

Since the combined correction factor, CF, varies with crack growth, F_p is largest where CF is largest. Regardless of the form of the individual corrections, the maximum CF occurs at either the crack origin or at the back free surface. Little fatigue life is associated with relatively large crack sizes. Thus, it hardly matters whether or not F_p is included for the back surface. (In some cases the ratio $(CF*S_r)/(3.36 \sigma_y)$ exceeds 1.0 at the back surface, thereby making Eq. 4-17 useless. Of course, gross plasticity also makes linear fracture mechanics useless. Fortunately, the life increment at back surfaces is very small.) The origin may prove of greater importance if F_g is high (cover plates), stress range is high, and yield stress is low. In fact, the theoretically singular stress condition associated with an idealized weld toe would itself cause stress redistribution without the presence of a crack. However, the extremely rapid decay of the stress concentration effect means the plastic zone correction is important over a very small distance of

crack growth. The larger the initial crack size, the less important

F_p becomes.

A fatigue life estimate using Eq. 4-17 was compared with one made without a plastic zone correction (Art. 6.2). The results differed by only a minor amount. Therefore, neglect of F_p is considered to be normally justified.

4.5 Crack Shape Variations During Growth

Of the various decisions affecting correction factors none is so important as the crack shape during growth. Gurney has found that the importance increases (has more effect on life) as the stress concentration or detail severity increases (Art. 6.2)[27]. All four of the individual corrections comprising the parameter CF are affected by the crack shape ratio, a/b. The fact that investigators designate the shape as an ellipse (with limits of circular and through cracks) is itself a significant approximation. Experimenters have recognized that many if not most cracks are actually irregular in shape[65,80].

Crack shape ratio, a/b, is not solely dependent on the crack length-to-plate width ratio, a/w, although the relative positions of all free surfaces have an effect. Plates of different width (or thickness if the crack is growing in that direction) can have different overall correction factors, CF, at the same relative position of crack growth, a/w. Stress intensity at a common relative

position of two geometries varies due to crack shape as well as the fact that crack length, a, appears in dimensional form under the radical. Therefore, fatigue performance of proportional geometries can be quite different. Since existing Code guidelines are based upon flange thicknesses in the range of 10 to 13 mm[3,19,20], caution is warranted when these regulations are applied to larger thicknesses. Large thickness can also cause layering[80] and changes in residual stress patterns, thereby affecting crack shape variation equations.

In order to establish a crack shape equation it is necessary to rely on actual physical measurements of crack size during growth. Unfortunately, these measurements can only be performed accurately by breaking apart structural details at different stages of crack growth. The situation is made much worse by the realization that growth characteristics are not the same for all details. The complexity and economics involved make it easy to understand why only a limited amount of data is available on crack shape variation during growth[12,20,51]. Data are particularly sparse at very small crack sizes.

4.5.1 Crack Shape Variation Characteristics

Figures 4.6, 4.7, 4.8, 4.9, 4.11, and 4.12 identify several of the different types of crack shape variation which can be expected at welded details. (The reference for each picture indicates the

experimental program within which the picture was taken. The reference does not mean the picture can actually be found in the final report.) The simplest sort of growth is one which is essentially constant in a penny-shape configuration. Such is shown in Fig. 4.6 for a web-to-flange fillet. (Other examples of penny-shape growth at welded details are shown in Ref. 32 as well as Ref. 19.) Theoretically, the stress intensity along the crack front varies due to free surface effects, thereby intimating equilibrium in a slightly non-circular shape[78]. However, the real crack front shows the penny-shape to be a good assumption, regardless of the irregularity of the initial flaw. Apparently the regular correction factors tend to be self compensating and/or the elastic regions in the web and flange tips make the crack sense it's in an infinite solid[32].

Figure 4.7 shows the growth of a crack from the termination of a longitudinal cover plate weld. (The cover plate has no transverse end weld.) Any weld with short dimension perpendicular to the applied stress direction shows similar characteristics. The crack orginates in the flange as a shallow surface flaw and grows through the flange as a semiellipse. For very thick flanges the shape would approach semicircular, but perhaps not attain it precisely (as explained above), before penetrating the back flange surface and becoming a through crack. About 90 percent of fatigue life of an attachment fillet-welded longitudinally to a flange is consumed while a semiellipse[19].

Figure 4.8 shows that fatigue cracks originate at weld terminations for stiffeners welded only to webs. It is possible that cracks will originate at several sites along the weld toe. However, the tensile stress range gradient in the web places greatest emphasis on the termination region. Therefore, the fatigue surface is dominated by a single elliptical crack in much the same manner as Fig. 4.7. Growth through the web is not as serious as through the flange; only 80 percent of the fatigue life is thereby consumed[20]. A total life prediction has to include subsequent growth as a two-ended through crack in the web. Growth as a three-ended through crack, after the flange has been fully penetrated, is of little importance, just as for the cover-plated details.

When a transverse fillet weld is placed on a flange for either stiffener or cover plate details (even cover plates wider than the flange), Fig. 4.9 shows that multiple fatigue cracks usually occur. (This assumes essentially nominal uniform tension in the flange. If a significant stress gradient exists due to warping, as in curved girders, a single crack may be predominant as in Fig. 4.8.) The cracks begin at individual sites along the weld toe and eventually coalesce. The number of sites and thus the rapidity of coalescence depends on the straightness of the weld toe and the uniformity of weld profile[57]. The more irregular the weld along its length, the more separated the initial cracks and the later the coalescence. (Reference 57 shows the same trend for toe cracks at transverse butt welds.) Machine welds are more uniform and straighter than hand welds

although almost all transverse welds of this kind are made by hand. The sooner coalescence commences, the more fatigue crack growth is enhanced due to increased F_s.

Crack coalescence is expected to occur several times during the growth process. Since initial cracks are neither equally spaced nor of equal size, coalescence continues during much of the time the crack is semielliptical. Thus, the trend of a given crack toward semicircular shape is constantly interrupted by unification with another crack. The crack shape ratio of this combined crack is usually small – closer to a through (edge) crack than a semicircle. Schematically, the crack shape variation is represented by Fig. 4.10.

When the combined crack finally reaches the back surface 96 percent of the fatigue life is gone[20]. It is easy to understand this precentage because, unlike the single crack of Fig. 4.7, most of the flange width has already been consumed. This point also helps explain why cover plates (of smaller width than the flange) with only longitudinal welds tend to have slightly longer lives than similar details with transverse end welds[4]. The life comparison is also explained on the basis that the smaller crack shape ratios associated with coalescence increase CF and therefore ΔK.

Fatigue crack growth at groove-welded gusset plates is more complex than many of the foregoing situations. Cracks originate near the gusset plates' circular transitions where they meet the flange

tips[12]. Regardless of the gusset plate-flange thickness ratio, the initial crack tends to be quarter-elliptical. Figure 4.11 shows that the crack shape is transformed from quarter-elliptical to quarter-circular (provided the flange is thick enough - Fig. 3.16) and finally to an edge crack. Vertification of this growth pattern is provided by Ref. 33. The predominant crack growth is across the flange width rather than through the thickness as in previous details.

Crack growth at groove-welded gusset plate details sheds light on the behavior expected from cover plates wider than the flange. Such attachments have longitudinal welds which connect the cover plate to the flange tip. If a transverse end weld also exists, cracks would grow in the manner of Fig. 4.9 (i.e. little different than cover plates of smaller widths than the flange). However with only longitudinal flange tip welds, cracks would likely begin as quarter-ellipses and, depending on flange thickness, soon become edge cracks growing across the flange width. The front free surface correction factors are generally higher for quarter-ellipses and edge cracks than for semiellipses. Thus, shorter life would be predicted without the transverse end weld. Reference 19 experimentally determined that such is indeed the case.

Lap-welded gusset plates provide an even more complicated crack growth pattern than the groove-welded variety. Figure 4.12 shows that cracks originate along the transverse fillet weld toe.

The early growth is semielliptical and coalescence may or may not be a factor, depending on the weld length. The crack length is that dimension measured in the thickness direction.

Since the cracks often originate near the flange tip, the end of the crack soon penetrates the flange tip and growth continues quarter-elliptically. However, unlike the groove-welded detail the minor axis of the ellipse is in the thickness rather than width direction. Thus, the predominant growth continues through the thickness. It is possible that the crack shape will become quarter-circular if the flange is thick enough and if little coalescence occurs. In any case, the crack eventually reaches the back surface of the flange and becomes an edge crack growing across the width. The life remaining varies with the flange aspect ratio and the length of lap weld.

4.5.2 Crack Shape Variation Equations

4.5.2.1 Stiffeners and Cover Plates Attached to Flanges with Transverse Fillet Welds

Reference 20 provides numerous measurements on the size of cracks growing from stiffener fillet weld toes. The curve fitting equation derived to relate b to a (both in mm) is given as follows:

$$b = 1.296 \, a^{0.946} \qquad (4\text{-}17)$$

It is apparent that the shape ratio gets closer to 1.0 as growth occurs and theoretically reaches half-circular when the crack size is 121 mm.

Unfortunately, it is not at all clear that Eq. 4-17 accurately represents any one of the types of shape variation discussed in Art. 4.5.1. The data are comprised of measurements at stiffeners welded to the web and flange as shown in Fig. 4.8 and 4.9. While multiple crack sizes (after some degree of coalescence) appear in the reference, they were not used in deriving the equation. However, data used in developing Eq. 4-17 did include measurements taken at compression as well as tension flanges. These two positions could be expected to have similar shape variation characteristics while the crack remains in the residual tensile zone. After leaving the zone the shape ratio for compression flange cracks would probably decline faster with coalescence than the ratio for tension flange cracks.

The smallest crack depth found in Ref. 20 is 0.2286 mm, but very few measurements are less than 0.635 mm. Crack coalescence for stiffeners welded to flanges is recorded as beginning when the depth reached the 1.27 mm mark.

If only the data associated with stiffeners welded to flanges are used in equation development, quite a different picture emerges. Single cracks in the compression or tension flange yield the least squares equation:

$$b = 1.300 \, a^{1.090} \tag{4-18}$$

Now the shape becomes more elliptical with crack growth and is only half-circular when the depth is 0.054 mm. This apparent elliptical

tendency by single cracks is considered the outfall of few data points (9) rather than actual behavior. Also, measurement techniques are more strained at small (single) crack depths.

The shape trend of Eq. 4-18 is amplified by considering both single and multiple cracks for stiffeners welded to flanges. Using both compression and tension flange data:

$$b = 1.506 \ a^{1.241} \tag{4-19}$$

Using only tension flange data:

$$b = 1.431 \ a^{1.212} \tag{4-20}$$

In both instances the crack shape is half-circular when the depth is about 0.183 mm.

The shallow ellipse shape trend represented by either Eq. 4-19 or 4-20 is explainable on the basis of crack coalescence. The difference between the two equations reflects the influence of the compression flange crack data. But since these data are comprised of large crack depths compared to the tension flange, it is not certain whether the residual stress zone limit or additional crack coalescence is responsible. Nevertheless, the equations are close to each other. Eq. 4-19 is favored due to the extra data points included.

The only other extensive investigation in the literature on crack shape variation from welds is due to Maddox[51]. He investigated a gusset plate which was fillet-welded on its side (not lap-

welded) to the face of a plate as shown in Fig. 4.13. Single cracks grew from the toe of the short transverse fillet at either end of the gusset. Based on many data points Maddox developed the following equation.

$$b = 3.355 + 1.29 \, a \qquad (4-21)$$

Interestingly, the equation is a straight line where a half-circular shape is approached but never reached. The upper bound crack shape ratio is 0.775. This value is at the high end of what might be considered the equilibrium position when the free surface correction factor and its variation along the crack front are considered [78]. (Ref. 78 is not precise since stress gradient and back surface corrections haven't been considered. However, it is probably close.)

Equation 4-21 characterizes single surface crack growth in a flange when only a short transverse weld length exists. Equation 4-17 is intended for single crack growth when a relatively long transverse weld length is present. One would expect that the longer transverse weld length would produce shallower cracks since the stress concentration along the weld toe hastens growth in that direction. Yet, such a shape trend is not evidenced by the two equations. Starting at initial crack sizes, Eq. 4-17 yields shapes which are almost semicircular while Eq. 4-21 predicts shapes which are much more elliptical.

Support of Maddox's crack shape equation is provided by Ref. 70. A longitudinal fillet weld with short transverse dimension

was found to produce a shape (a/b) which was roughly constant at 0.50 up to relatively large crack depths (at least 9.5 mm). At a depth of 9.5 mm Eq. 4-21 predicts a ratio of 0.61 while Eq. 4-17 yields 0.87. The support data for Ref. 70 were not extensive although the results obviously favor the shallower shape.

None of the mentioned studies provides extensive data at very small crack sizes. Yet, this is the range in which single rather than multiple cracks exist. Regardless of the length of transverse weld the various equations should merge into one common shape prediction at the smaller crack sizes. Since Eq. 4-17 and 4-21 are so much at odds with each other, it is necessary to select the one which seems to most accurately describe the early shapes. Maddox's equation is chosen because the data are numerous and relatively far ranging, making the trend more accurately extrapolated to small crack levels. Also, all data represent growth in a flange-like plate as opposed to the mixture of flange and web for Eq. 4-17.

Two equations have been defined to describe crack shape variation from transverse weld toes. When cracks are very small they are individual ones (single) and are represented by Eq. 4-21. After some crack growth coalescence begins the continued shape variation is represented by Eq. 4-19. Even though the data stem from different tests, it is proposed to combine the equations in describing crack shape while growing through the flange. Figure 4.14 plots

both curves and shows the intersection to be at a crack depth of roughly 4 mm. This dimension is more than three times greater than that recorded in Ref. 20 as the earliest commencement of coalescence observed. Yet, the statistical trend is probably closer to the higher figure; lack of data makes a conclusive decision impossible.

The two equations will be applied to cracks at transverse fillet welds regardless of whether they connect stiffeners or cover plates to the flange. Some error may exist in this generalization due to higher stress gradients at the weld toes of cover plates. The variation of the free surface correction factor along the crack front is dependent on the stress gradient. The higher the gradient the greater the tendency to remain a shallow semiellipse, resisting growth toward a semicircle[82]. Such a point is beyond the scope of the dissertation, but deserves later investigation. Little quantitative data on crack shape variation at the transverse weld toes of cover plates are known to exist in the literature although the qualitative findings at large crack sizes in Refs. 19 and 20 indicate shallower cracks than at stiffeners.

4.5.2.2 Gusset Plates Groove-Welded to Flange Tips

Very little data on shape variation at gusset plate connections are available. However, one recent experimental program included groove-welded gusset plates with circular transitions and several rough crack shape measurements on the fatigue surface were made[12].

The resulting equation for quarter-elliptical crack growth is as follows:

$$b = 10.36 \ a^{0.202} \qquad (4\text{-}22)$$

Equation 4-22 is used in this study to describe the crack shape relationship for groove-welded gussets. The equation shows the crack grows toward a quarter-circular shape and actually reaches it provided the flange thickness is at least 41 mm. For crack depths greater than 41 mm the crack is assumed to grow as a quarter-circle until b is equivalent to the flange thickness. At this point edge crack conditions are immediately used without special consideration of the insignificant transition period. If the flange thickness is less than 41 mm edge crack conditions are again immediately used when b equals T_f.

5. UNIFIED STRESS INTENSITY EXPRESSIONS

Chapter 4 summarizes the limits on stress intensity correction factors. Given this information it is possible to develop unified stress intensity factors which account for the real stress distribution and crack shape. The approach used is to first develop stress intensity expressions for the crack shape limits (0 and 1) and then combine them (by interpolation of individual correction factors) to provide for intermediate crack shapes.

The initial step involves finding the stress intensity for a nonuniform stress distribution. Figure 5.1 shows the type of local stress gradient which is common to stress concentration regions (maximum concentration at the crack origin). This distribution may be separated into uniform and variable constituents. Since stress intensity is linear in σ, superposition applies provided the crack displacement mode is unchanged[81,82]. Hence, the actual stress intensity can be found by adding the stress intensities, K_u and K_v, for two "sub" stress distributions which sum to the actual stress distribution. The stress intensity correction factors for the uniform subdistribution are already known (Figs. 4.1 and 4.5); correction factors for the variable subdistribution can be estimated.

-132-

5.1 Stiffeners Fillet-Welded to Flanges

5.1.1 Through Crack (a/b = 0)

Using the correction factors of Figs. 4.1 and 4.5 (no bending) the stress intensity for uniform stress can be written as:

$$K_u = 1.122 * K_{t\alpha} * \sigma \sqrt{\pi a} * \left[\sec \left(\frac{\pi \alpha}{2} \right) \right]^{1/2} \tag{5-1}$$

Since this is a through crack, F_e is 1.0. Note that for uniform stress the only stress gradient correction is that which relates actual stress at the crack tip to nominal stress. Obviously, it has constant value $K_{t\alpha}$.

Development of the stress intensity for varying stress is more complex. Figure 4.1 shows that F_s is somewhere between 1.300 and 1.210. The correct intermediate value depends on the shape of the actual stress concentration factor decay curve (K_t) relative to a linear decay line. Figure 5.2a demonstrates that the proximity to a linear condition varies with α. As α increases F_s increases from 1.210 to a value near 1.300.

If TERM1 represents the desired value of F_s, then:

$$TERM1 = 1.300 - FACTOR(1.300-1.210) = 1.30 - 0.09 * FACTOR \tag{5-2}$$

where   FACTOR = measure of proximity to linearity; has value 1.0 if actually linear

FACTOR may be evaluated on the basis of Fig. 5.2b. ξ represents that value of λ at which the slope of the stress concentration decay curve equals the slope of a hypothetical straight decay line from SCF to α. The lower limit of ξ is zero while the upper limit is $\alpha/2$. Thus, FACTOR is taken as:

$$FACTOR = \frac{\xi}{\alpha/2} = \frac{2\xi}{\alpha} \tag{5-3}$$

Proper resolution of Eq. 5-3 depends on knowledge of the concentration factor decay curve which varies for each detail geometry. However, since the change in TERM1 is small over the full spectrum of FACTOR values, reasonable accuracy is attained by using an equation of the following form for all cases:

$$\frac{K_{t\lambda}}{SCF} = \frac{1}{1 + \frac{1}{c}\lambda^p} \tag{5-4}$$

where $\lambda = \ell/w$

ℓ = position in the crack growth direction

If the stress gradient results for an average stiffener geometry from Chapter 2 are used, values of c and p are evaluated as 0.3546 and 0.1543, respectively. These results are summarized in Table 5.1.

Equation 5-4 (in its present and differentiated forms) can be used to evaluate the slopes at $\lambda = \alpha$ and $\lambda = \xi$. A nonlinear "characteristic" equation results (Eq. 5-5) which must be solved for ξ.

$$\frac{1}{c^2} \xi^{2p} + \frac{2}{c} \xi^p - \frac{p}{D} \xi^{p-1} + 1 = 0 \qquad (5-5)$$

where
$$D = \frac{\alpha^{p-1}}{1 + \frac{1}{c} \alpha^p}$$

The solution of Eq. 5-5 is readily obtained for any given α by the bisection method. Thus, FACTOR can be calculated and TERM1 defined.

FACTOR is also employed in calculating the appropriate back free surface correction, F_w, for the variable stress subdistribution. Figure 4.5a indicates that F_w is:

$$F_w = COEF1 * \left[sec \left(\frac{\pi \alpha}{2} \right) \right]^{1/2} \qquad (5-6)$$

where
$$COEF1 = \left(1 - \frac{1}{2} FACTOR \right) \left[1.297 - 0.297 cos \left(\frac{\pi \alpha}{2} \right) \right] * \left[\frac{\pi \alpha}{2} cosec \left(\frac{\pi \alpha}{2} \right) \right]^{\frac{1}{2}} + \frac{1}{2} FACTOR$$

The stress gradient correction factor for the subdistribution, $\bar{F}_{g\alpha}$, is related to $F_{g\alpha}$ calculated for the whole distribution (Chap. 3). Albrecht's Green's Function in nondimensional form yields:

$$K = \sqrt{\pi a} * \frac{2}{\pi} \int_0^\alpha \frac{\sigma_\lambda}{\sqrt{\alpha^2 - \lambda^2}} d\lambda \qquad (5-7)$$

where $\sigma_\lambda = \sigma (K_{t\lambda} - K_{t\alpha})$ for the subdistribution

Thus,

$$\bar{F}_{g\alpha} = \frac{2}{\pi} \int_0^\alpha \frac{\left(K_{t\lambda} - K_{t\alpha}\right)}{\sqrt{\alpha^2 - \lambda^2}} \cdot d\lambda \qquad (5\text{-}8)$$

Equation 5-8 produces the following relationship:

$$\bar{F}_{g\alpha} = F_{g\alpha} - K_{t\alpha} \qquad (5\text{-}9)$$

The stress intensity expression for the variable stress sub-distribution can now be estimated using Eqs. 5-2, 5-6, and 5-9.

$$K_v = \text{TERM1} * (F_{g\alpha} - K_{t\alpha}) * \sigma\sqrt{\pi a} * \text{COEF1} \left[\sec\left(\frac{\pi\alpha}{2}\right) \right]^{1/2} \qquad (5\text{-}10)$$

Combining Eqs. 5-1 and 5-10 yields the stress intensity expression, K_{total}, for stiffeners with through cracks.

$$K_{total} = \left\{ 1.122 * K_{t\alpha} * \left[\sec\left(\frac{\pi\alpha}{2}\right)\right]^{\frac{1}{2}} + \text{TERM1} * (F_{g\alpha} - K_{t\alpha}) * \text{COEF1} \left[\sec\left(\frac{\pi\alpha}{2}\right)\right]^{\frac{1}{2}} \right\} * \sigma\sqrt{\pi a} \qquad (5\text{-}11)$$

It is helpful to rearrange Eq. 5-11 in the following form:

$$K_{total} = [\text{TERM1} * \text{COEF1} + (1.122 - \text{TERM1} * \text{COEF1}) * X] * F_{g\alpha} * \sigma\sqrt{\pi a} * \left[\sec\left(\frac{\pi\alpha}{2}\right)\right]^{\frac{1}{2}} \qquad (5\text{-}12)$$

where $\quad X = \dfrac{K_{t\alpha}}{F_{g\alpha}}$

The leading expression in brackets is assumed to be the combined front free surface correction and the unmodified secant radical is assumed to be the combined back free surface correction.

-136-

Evaluation of X in Eq. 5-12 can be performed with the stress gradient correction provided by the artificial ellipse correlation given in Art. 3.4. However, it is also possible to define an approximate equation for F_g, similar to Eq. 5-4, which sacrifices little accuracy in the bracketed expression. This equation is given as:

$$\frac{F_{g\alpha}}{SCF} = \frac{1}{1 + \frac{1}{d}\alpha^q} \qquad (5\text{-}13)$$

For an average stiffener geometry, d and q were evaluated to be 0.3602 and 0.2487, respectively (Table 5.1). Therefore, combining Eqs. 5-4 and 5-13, X is given as follows:

$$X = \frac{1 + \frac{1}{d}\alpha^q}{1 + \frac{1}{c}\alpha^p} \qquad (5\text{-}14)$$

Equation 5-13 provides a reasonable means to determine X since the entire bracketed term of Eq. 5-12 varies little over a wide range of c, d, p, and q values. However, Eq. 5-13 is not applicable to the stress gradient correction outside the brackets. There the artificial ellipse correlation should be employed.

5.1.2 Half-Circular Crack (a/b = 1)

The stress intensity for the uniform stress subdistribution of a half-circular crack can be defined as (Fig. 4.1):

$$K_u = 1.025 * K_{t\alpha} * \frac{2}{\pi} * \sigma\sqrt{\pi a} \qquad (5\text{-}15)$$

-137-

Crack shape correction, F_e, is represented by $2/\pi$ and F_w is assumed to be 1.0 (Art. 4.3).

For the varying stress condition F_s is represented by TERM2 as follows:

$$TERM2 = 1.145 - 0.06*FACTOR \qquad (5\text{-}16)$$

FACTOR is the same term calculated for the through crack case.

The stress gradient correction associated with the circular crack front, $\overline{F}'_{ga}$, is defined as:

$$\overline{F}'_{g\alpha} = F'_{g\alpha} - K_{t\alpha} \qquad (5\text{-}17)$$

It is important to recognize that $F'_{g\alpha}$ is not of the identical numerical value as $F_{g\alpha}$ calculated for the through crack Green's Function. Using a circular crack (infinite solid) Green's Function[82], Table 5.2 shows that $F'_{g\alpha}$ and $F_{g\alpha}$ diverge as the stress becomes less and less uniform. The limiting ratio of $F'_{g\alpha}/F_{g\alpha}$ for a line load at the crack origin is estimated to be 0.548, which deviates from 1.000 by twice the change recorded between the uniform and linear stress cases. The ratio of circular to through crack stress gradient correction factors is summarized in Fig. 5.3.

Equations 5-16 and 5-17 can be used to develop the stress intensity factor for the variable stress subdistribution. This yields:

$$K_v = TERM2 * (F'_{g\alpha} - K_{t\alpha}) * \frac{2}{\pi} * \sigma\sqrt{\pi a} \qquad (5\text{-}18)$$

-138-

Adding K_v to K_u (Eq. 5-15) gives K_{total} for the half-circular crack shape.

$$K_{total} = \left[1.025 * K_{t\alpha} * \frac{2}{\pi} + TERM2 * (F'_{g\alpha} - K_{t\alpha}) * \frac{2}{\pi}\right] * \sigma\sqrt{\pi a} \qquad (5\text{-}19)$$

Rearranging Eq. 5-19 gives:

$$K_{total} = [TERM2 * Y + (1.025 - TERM2) * X] * F_{g\alpha} * \frac{2}{\pi} * \sigma\sqrt{\pi a} \qquad (5\text{-}20)$$

where

$$Y = \frac{F'_{g\alpha}}{F_{g\alpha}}$$

Evaluation of ratio Y is assisted by Fig. 5.3. However, it must be borne in mind that F_g and F'_g are evaluated for the <u>total</u> stress distribution, not just the variable subdistribution. The Y ratio for the total distribution is dependent on the relative influe-ence of the variable stress subdistribution as compared with the uni-form stress subdistribution. Thus, Y is taken as the sum of two parts.

$$Y = W * Y' + (1-W) * Y'' \qquad (5\text{-}21)$$

where $Y' = 0.548 + 0.226 * FACTOR$

$Y'' = 1.000$

W = weighting factor of variable stress subdistribution relative to the uniform stress subdistribution

Factor W may be based upon the relative areas of stress subdistribution up to crack length α. This amounts to determining the ratio of the two shaded areas under the concentration decay curve in Fig. 5.4.

$$W = \frac{A_v}{A_u} = \frac{\int_0^\alpha \left(K_{t\lambda} - K_{t\alpha}\right) d\lambda}{K_{t\alpha} * \alpha} = \frac{\int_0^\alpha K_{t\lambda} \, d\lambda}{K_{t\alpha} * \alpha} - 1 \tag{5-22}$$

Substituting Eq. 5-4 into 5-22 gives

$$W = \frac{\int_0^\alpha \dfrac{1}{1 + \dfrac{1}{c} \lambda^P} \, d\lambda}{\dfrac{\alpha}{1 + \dfrac{1}{c} \alpha^P}} - 1 \tag{5-23}$$

The integral in the numerator can be evaluated numerically; therefore, factor W is easily obtained. However, note that W decreases with increasing relative crack length, α, and must be reevaluated for each crack position. Also, W is affected by decay constants c and p.

For the benefit of later calculations it is worthwhile making one adjustment to Eq. 5-20. Multiplying and dividing by the secant radical gives the following form:

$$K_{total} = \left[\frac{\text{TERM2}*Y + (1.025 - \text{TERM2})*X}{\left[\sec\left(\frac{\pi\alpha}{2}\right)\right]^{1/2}}\right] * F_{g\alpha} * \frac{2}{\pi} * \sigma\sqrt{\pi a} * \left[\sec\left(\frac{\pi\alpha}{2}\right)\right]^{1/2} \tag{5-24}$$

5.1.3 Interpolation for Half-Elliptical Cracks $\left(0 \le \dfrac{a}{b} \le 1\right)$

An intermediate (unified) position between Eqs. 5-12 and 5-24 is necessary for half-elliptical crack shapes. Comparison of the two equations reveals that each contains the $F_{g\alpha}$ factor and the secant radical. In unified terminology these will henceforth be known as the

-140-

stress gradient and back free surface correction factors, respectively. It is also apparent that each equation contains the appropriate, isolated, crack shape correction factor, F_e. ($F_e = 1.0$ is implied in Eq. 5-12.) Therefore, use of the normal elliptical integral (Art. 4.1, Eq. 4-3) for the unified crack shape correction is warranted. This integral automatically provides a nonlinear interpolation.

Only the leading bracketed expressions in each equation differ and require adjustment. The simplest approach is a straight linear interpolation based on the crack shape ratio, a/b. The interpolated value represents the unified front free surface correction, F_s. The resulting F_s is:

$$F_s = \left(1 - \frac{a}{b}\right) * \left\{ TERM1 * COEF1 + (1.122 - TERM1 * COEF1) * X \right\} + $$
$$\frac{a}{b} * \left\{ \frac{TERM2 * Y + (1.025 - TERM2) * X}{\left[\sec\left(\frac{\pi\alpha}{2}\right)\right]^{1/2}} \right\} \qquad (5-25)$$

The unified stress intensity correction factors for stiffeners are summarized in Table 5.3.

5.2 Cover Plates with Transverse End Welds

5.2.1 Through Crack ($a/b = 0$)

The major difference between the stiffeners and cover plates occurs in the back surface correction, F_w, for the individual subdistributions. The stress intensity for uniform stress subdistribution

(Eq. 5-1) has to be modified by COEF2 (Fig. 4.5) which accounts for bending.

$$K_u = 1.122 * K_{t\alpha} * \sigma\sqrt{\pi a} * COEF2 \left[\sec\left(\frac{\pi\alpha}{2}\right)\right]^{1/2} \tag{5-26}$$

where

$$COEF2 = \left\{\frac{0.752 + 2.02\alpha + 0.37\left[1-\sin\left(\frac{\pi\alpha}{2}\right)\right]^3}{1.122\ \cos\left(\frac{\pi\alpha}{2}\right)}\right\} * \left[\frac{2}{\pi\alpha}\ \sin\left(\frac{\pi\alpha}{2}\right)\right]^{\frac{1}{2}}$$

Likewise, the stress intensity for the variable stress subdistribution (Eq. 5-10) is modified by coefficient COEF3 replacing COEF1 (Fig. 4.5).

$$K_v = TERM1 * \left(F_{g\alpha}-K_{t\alpha}\right) * \sigma\sqrt{\pi a} * COEF3 \left[\sec\left(\frac{\pi\alpha}{2}\right)\right]^{1/2} \tag{5-27}$$

where

$$COEF3 = \left[1 - \frac{1}{2}\ FACTOR\right] \left[\frac{3.52}{(1-\alpha)^{3/2}} - \frac{4.35}{(1-\alpha)^{1/2}} + \right.$$

$$\left. 2.13\ (1-\alpha)\right] * \frac{\left[\cos\left(\frac{\pi\alpha}{2}\right)\right]^{1/2}}{1.30} + COEF2 * \frac{1}{2}\ FACTOR$$

The decay constants in Eqs. 5-4 and 5-13 also change. The constants are summarized in Table 5.1 for an average cover plate geometry.

Combining Eqs. 5-26 and 5-27 yields the total stress intensity for a through crack.

$$K_{total} = [TERM1 * COEF3 + (1.122\ COEF2 - TERM1 * COEF3) * X]$$

$$F_{g\alpha} * \sigma\sqrt{\pi a} * \left[\sec\left(\frac{\pi\alpha}{2}\right)\right]^{1/2} \tag{5-28}$$

-142-

Equation 5-28 is seen to be quite similar to Eq. 5-12.

5.2.2 Half-Circular Crack ($a/b = 1$)

Equation 5-24 applies directly to the half-circular crack since the back surface correction as well as other corrections are unchanged from the stiffener case. However, the decay constants in Table 5.1 must be taken from the cover plate column.

5.2.3 Interpolation for Half-Elliptical Cracks $\left(0 \leq \dfrac{a}{b} \leq 1\right)$

The unified crack shape, back free surface, and stress gradient correction factors are seen to be unchanged from the stiffener case. Only the front free surface correction needs modification.

$$F_s = \left(1 - \frac{a}{b}\right) * \left\{ \text{TERM1} * \text{COEF3} + (1.122\ \text{COEF2} - \text{TERM1} * \text{COEF3}) * X \right\} +$$
$$\frac{a}{b} * \left\{ \frac{\text{TERM2} * Y + (1.025 - \text{TERM2}) * X}{\left[\sec\left(\frac{\pi\alpha}{2}\right) \right]^{1/2}} \right\} \tag{5-27}$$

The unified correction factors for cover plates are summarized in Table 5.4.

5.3 Gusset Plates Groove-Welded to Flange Tips

5.3.1 Through Crack ($a/b = 0$)

No changes occur from the cover plate case except for the stress concentration factor and gradient correction decay constants

(Table 5.1). Also, relative crack length, α, is crack length divided by flange width rather than flange thickness.

5.3.2 Quarter-Circular Crack (a/b = 1)

Change from the cover plate and stiffener cases occurs due to differences in the front free surface correction, F_s (Fig. 4.1). In Eq. 5-24 the number 1.025 must be replaced by 1.380 and TERM3 is substituted for TERM2.

$$TERM3 = 0.754 + 0.313 * FACTOR \qquad (5\text{-}29)$$

The total stress intensity can be written as follows:

$$K_{total} = \left\{ \frac{TERM3 * Y + (1.380 - TERM3) * X}{\left[\sec\left(\frac{\pi\alpha}{2}\right) \right]^{1/2}} \right\} * F_{g\alpha} * \frac{2}{\pi} * \sigma\sqrt{\pi a} * \left(\sec\left(\frac{\pi\alpha}{2}\right) \right)^{1/2}$$

$$(5\text{-}30)$$

5.3.3 Interpolation for Quarter Elliptical $\left(0 \leq \frac{a}{b} \leq 1 \right)$

F_e, F_w, and F_g are still unchanged from the other two details. F_s now has the following expression:

$$F_s = \left(1 - \frac{a}{b}\right) * \left\{ TERM1 * COEF3 + (1.122\ COEF2 - TERM1 * COEF3) * X \right\} +$$

$$\frac{a}{b} * \left\{ \frac{TERM3 * Y + (1.380 - TERM3) * X}{\left[\sec\left(\frac{\pi\alpha}{2}\right) \right]^{1/2}} \right\} \qquad (5\text{-}31)$$

The unified correction factors for gusset plates are summarized in Table 5.5.

5.4 Comparisons of Unified Correction Factors

Figure 5.5 summarizes the comparative magnitudes of unified front free surface corrections in Tables 5.3, 5.4, and 5.5. Sample detail geometries were arbitrarily selected and the resulting values of F_s plotted. Crack shape variation was defined by Eqs. 4-21 and 4-19 for the stiffener and cover plate while Eq. 4-22 was used for the gusset plate up to the point when edge crack conditions existed. Figure 5.5 demonstrates the pronounced effect of bending. The difference between the gusset plate and cover plate primarily reflects the influence of quarter-elliptical and through (edge) crack shape versus half-elliptical crack shape. The choice of shape variation equation (Art. 4.5.2) also plays a role in F_s values.

Gurney and Maddox have noted that the collective crack shape, front free surface, and back free surface correction can be taken as 1.0 for semielliptical cracks at cruciform joints[27,28,51]. The collective correction for each detail shown in Fig. 5.5 is plotted in Fig. 5.6. The Gurney-Maddox assumption of 1.0 appears reasonable only for the stiffener case. (Most fatigue life is consumed at $\alpha < 0.5$; hence, errors in correction factors for $\alpha > 0.5$ has little consequence on fatigue behavior.) While the non-load-carrying cruciform joint is indeed similar to a stiffener detail, it is interesting to recall that F_w proposed by Maddox includes bending (Art. 4.3).[51] As in the case of symmetrical gusset plates, bending would depend on whether or not symmetrical cracks existed. If bending were

incorporated in the unified stiffener stress intensity expression (Table 5.3), the resulting curve in Fig. 5.6 would be close to the cover plate. The Gurney-Maddox assumption does not consider crack coalescence. Elimination of coalescence (Eq. 4-19) from the crack shape relationship would lower the curve at higher α values. Thus, the modifications tend to compensate.

6. FATIGUE LIFE CORRELATIONS

The unified correction factors developed in Chapter 5 (Tables 5.3, 5.4, and 5.5) can be used in fatigue life predictions. After replacing stress, σ, with stress range, S_r, in the stress intensity expressions, the resulting range of stress intensity is inserted in Eq. 1-2. It is rare that this equation can be solved closed-form - particularly when the combined correction factor, CF, is a complex function of crack length, a. Therefore, the cycle life is commonly estimated on the basis of the following numerical integration:

$$N = \frac{1}{C} \sum_{j=1}^{m} \frac{1}{\left(\Delta K_j\right)^n} \Delta a_j \qquad (6-1)$$

where $C = 1.21*10^{-13} \dfrac{mm^{11/2}}{N^3 \text{ cycles}}$ (Refs. 20,32)

$n = 3.0$

ΔK = range of stress intensity, $\dfrac{N}{mm^{3/2}}$

Δa = crack length increment, mm

The fact that both C and n change value at high growth rates (when the crack growth mode changes from plane strain to plane stress[50]) is of little consequence since most life is consumed at growth rates below $25*10^{-6}$ mm/cycle[20,32].

The manner of evaluation of ΔK_j in Eq. 6-1 is of some interest. Since ΔK changes over the interval, a crude assumption would be to use some intermediate crack length in calculating an average ΔK. Given this procedure the investigator would be obliged to use very small growth increments in order to assure reasonable accuracy.

An alternate proposal is to treat the combined terms behind the summation sign as an integral of itself. One is looking for the area under the curve representing $1/(\Delta K)^n$ between the two crack limits of the interval. Evaluation can be effected by several approaches − among them the 32-point Gauss quadrature formula[44]. The accuracy of this approach permits use of larger crack increments in the summation process. Thus, the Gauss quadrature formula is applied in all subsequent life estimates.

A sense of the relative importance of stress range and initial and final crack sizes in life estimates may be developed by again considering Eq. 1-2. If the combined correction factor is assumed (for this exercise) to be constant, the cycle life is predictable in closed-form fashion.

$$N = \frac{2}{C*CF^3*S_r^3*\pi^{3/2}} \left[a_i^{-1/2} - a_f^{-1/2} \right] \qquad (6\text{-}2)$$

where a_i = initial crack size

         a_f = final crack size

Since stress range is cubed and both crack lengths have a square root sign attached, error in the nominal stress range is more important than errors in the initial and final crack sizes. Likewise, error in the correction factor, CF, is more important than crack size. Even though CF in reality depends on crack size, added importance is obviously attached to establishment of the correct form of each individual correction factor.

The negative radical associated with each crack length typically places the weighted importance on initial crack size. Experimental work outlined in Refs. 19 and 20 used an excessive deflection (net section yielding) criterion for fatigue failure and the establishment of a_f. A more recent study terminated fatigue life with fracture, although this life was close to that found using a generalized yielding condition[12]. Both definitions of failure generally cause a_f to be much larger than a_i. The greater the difference between a_i and a_f, the greater the importance of a_i.

There is a link between the relative importance of crack size and the various correction factors. Inclusion of F_g in the stress intensity expression increases the percentage of fatigue life at the larger crack sizes. Yet, incorporation of bending (as for cover plates) in the unified F_s acts to reduce the importance of the larger cracks. In general, the correction factors tend to enforce or diminish the significance of a_i relative to a_f, depending on the

detail involved and the various expressions for correction factors.

(The crack shape variation equation obviously plays a role here too.)

However, regardless of these secondary relationships the initial crack

size dominates the fatigue life of practical bridge details.

In light of the relative importance of a_i, it is indeed

unfortunate that a_i is much more difficult to estimate than a_f. Such

is even true for a test specimen where the crack surface is exposed

after failure (a_f is usually clearly evident). Nevertheless, several

investigations have established lower and upper limits of initial

crack size for weld toes of a stiffener and cruciform joint at about

0.025 mm and 0.50 mm, respectively[20,74,86]. The average a_i is be-

tween .076 mm and .10 mm.

Initial crack size studies to date have been primarily

directed at the size of nonmetallic inclusions and defects at weld-

base metal interfaces[74,86]. No particular concern has been expressed

at possible changes in initial size with the type of detail, weld

size, weld electrode and process, or even different steel strengths.

While fatigue evidence doesn't clearly suggest a variation in initial

crack size, it is difficult to be sure without further research at

the microscopic level.

Initial crack size for groove-welded gusset plates has not

yet been discussed in the literature. Cracks normally originate at

the weld termination which could exhibit initial flaw sizes similar
to the fillet weld toe. The crack shape, being quarter-elliptical
rather than quarter-circular, may have a deviating effect. In any
case, it is unlikely the initial size would be of the magnitude
(1.0 mm) found at an average internal gas pore (Fig. 4.6)[32]. There-
fore, the initial crack size limits of 0.025 mm and 0.50 mm will be
used for the gusset plate life estimates.

Given the expression for stress intensity, the life integra-
tion technique, and information on initial crack sizes, the analyst
is in a position to make fatigue life (cycle) estimates. Several
sample details are subsequently investigated and their lives are com-
pared with those found under actual fatigue test conditions.

6.1 Stiffeners Fillet-Welded to Flanges

Reference 20 provides a broad experimental base for fatigue
failure at stiffeners. Stiffeners fillet-welded to flanges are
therein designated Type 3. One particular series (in this case the
SGB-SBB combined series) is selected for investigation and values of
the crucial geometric variables are tabulated in Table 6.1.
(Appendix E of Ref. 20 notes that the actual weld size was closer to
6.35 mm rather than the 4.76 dimension specified.) The objective is
to assess how accurately the results of various estimate approaches,
N_{est}, predict the actual cycle life, N_{act}. All lives are also
recorded in Table 6.1.

The actual cycle life in Table 6.1 relates to the logarithmic average of data points for the given series and stress range (Table E-3 of Ref. 20). Logarithmic average means that variable N is assumed log-normally distributed (base 10) and the mean is approximated by the average logarithm of the data points. For this particular series and stress range, eight data points are available. On average, failure occurred after the crack had fully penetrated the flange and was growing in a through crack configuration. Since the unified life estimates are based on cycle life for growth through the flange, 96 percent (Art. 4.5.1) of the actual life found by the logarithmic average is recorded.

Three estimated lives were derived from the unified stress intensity relationships (Chap. 5). The first two represent approximate average and maximum initial crack sizes and both are plotted in Fig. 6.1. The third unified estimate uses the average initial crack size and arbitrarily increases the overall correction factor, CF, at all crack lengths by five percent. (This five percent can be considered a calibration correction not accounted for elsewhere.)

In comparison with N_{act}, it is recognized that the unified expression gives a high (unconservative) estimate at the average initial crack size but a low (conservative) estimate at the upper bound of initial crack size. However, both estimates are reasonably close for a fatigue analysis. A combined error tolerance of five

percent on CF is seen to provide excellent agreement with N_{act} at the average initial crack size.

It is worthwhile considering the implications of two other unified estimates which are not given in Table 6.1. First, if bending had been included in the stiffener stress intensity, the estimate at the average initial crack size would have been 1.216 million cycles. Second, if the initial crack shape variation equation had been taken as Eq. 4-17 rather than Eq. 4-21, the estimate at the average initial crack size would have been 2.388 million cycles. Obviously, bending and crack shape assumptions have a pronounced effect on life estimates.

Reference 20 provides two regression equations which can be used to estimate life. The mean equation for all stiffeners (not just those connected to the flange) is as follows:

$$\log N = 12.6821 - 3.097 \log S_r \qquad (6\text{-}3)$$

where S_r = stress range, MPa

Since 96 percent of N is to be used for comparison purposes, Eq. 6-3 can be modified accordingly.

$$\log (.96N) = 12.6644 - 3.097 \log S_r \qquad (6\text{-}4)$$

The mean equation for Type 3 stiffeners only (all series) is:

$$\log N = 13.5342 - 3.505 \log S_r \qquad (6\text{-}5)$$

For 96 percent of N the regression equation appears as follows:

$$\log (.96N) = 13.5165 - 3.505 \log S_r \qquad (6-6)$$

It is noted that neither regression equation has a slope of exactly -3.0. However, the discrepancy is minor. In fact, the estimates by Eq. 6-3 and 6-5 or 6-4 and 6-6 are normally quite close due to the adjustment provided by the equation constants (Fig. 6.1). A common slope of -3.0 guided the AASHTO Specifications[3,21] although round off of stress range values left the slope slightly off of the mark. Regardless, equating n to 3.0 is reasonable in life integral procedure (Eq. 6-1).

Since both of the above regression equations are based upon the specific series under study here, close agreement between predicted and actual cycle life is expected and, indeed, found (Table 6.1 and Fig. 6.1). However, it is also fruitful to compare the value at the (approximate) upper 95 confidence limit. Again assuming log-normal distribution and incorporating the standard deviation (s = 0.1024) from the Type 3 regression analysis, Eq. 6-6 is adjusted to the upper 95 percent confidence limit.

$$\log (.96N) = 13.5165 - 3.505 \log S_r + 2s$$
$$= 13.7213 - 3.505 \log S_r \qquad (6-7)$$

The large separation between the upper confidence limit and the mean value emphasizes the wide variability of results (Table 6.1 and Fig. 6.1). This separation thereby gives a measure of accuracy of the unified estimate at the average initial crack size.

Chapters 4 and 5 noted that the fatigue performance of cruciform (non-load-carrying) joints should be reasonably comparable to stiffeners welded to flanges. A recent study on cruciform joints by Gurney offers an opportunity to evaluate this premise[27]. The stress range, geometry, and various life estimates are recorded in Table 6.1. (Flange thickness must be taken as one-half of the full plate thickness since the joint is symmetrical with respect to the plate's centroidal plane and symmetrical cracks – no bending – are assumed.)

Gurney provided an actual cycle life which is assumed to be that corresponding to growth of symmetrical cracks to middepth of the plate. Thus, his figure can be related directly to the unified life estimates without need for the 96 percent correction. The initial crack sizes were taken to be those Gurney assumed which, like those of the stiffeners, were based upon the work of Signes[74]. In the manner of the stiffener unified life estimates, the one corresponding to the smaller initial crack size was slightly higher than the actual value. However, a larger initial crack size or a five percent tolerance on the overall correction at all crack sizes leads to excellent

agreement between predicted and actual cycle life.

The estimates resulting from Eqs. 6-4 and 6-6 are not nearly as good as the unified estimate (Table 6.1). Equation 6-6 now yields a value larger than Eq. 6-4; they have reversed their relative positions exhibited for the stiffener, due to the differing slopes. Yet, the estimates are still close to each other while jointly further removed (significantly unconservative) from the real value. The probable reason for this trend is the abnormally high weld leg-flange thickness ratio $Z/T_f{}^4$. The lack of agreement between Refs. 20 and 27 is further justification for future study on the effect of geometry on fatigue performance. In the unified approach the F_e and F_s factors are automatically adjusted for varying geometry; thus, reasonable agreement is found for both the stiffener and cruciform joint cases.

Gurney produced an estimate of life which is also given in Table 6.1. He made the assumption that the collective crack shape, front free surface, and back free surface can be taken as 1.0, which is reasonable for cruciform joints (Art. 5.4). But his stress gradient correction was greater than that evaluated in Chapter 3. Thus, the life predicted was quite conservative and led to the thought that a period of crack initiation should be added to the propagation life.

The concept of crack initiation has been supported by other recent work[53, 70]. However, the fact that all unified estimates (see also Arts. 6.2, 6.3, and 6.4) turned out greater than actual cycle lives leads one to conclude that initiation is relatively non-existent and can be disregarded. Obviously, the burden of the decision partly rests on the expressions for the various correction factors, the crack shape variation equations, and the various material constants assumed for crack growth (Eq. 6-1). In any case, there is reluctance to increase analysis difficulties by including some initiation calculation requirements before many aspects of crack propagation at real structural details are resolved (Art. 6.5). Also, initiation estimates tend to be highly empirical and arbitrary since it is difficult to prove what happens at microscopic defects and inclusions.

6.2 Cover Plates With Transverse End Welds

Reference 19 is a source of considerable data on cover plates. Combined series CWB-CWC was selected for investigation and the important geometrical parameters are summarized in Table 6.1. (Series CWA had a slightly different flange thickness, Table D-2 of Ref. 19, and was therefore omitted from the combination.) The stress range assumed is 110 MPa. Thus, using the logarithmic average of the 12 available data points (Tables F-2 and F-3 of Ref. 19), the 96 percent life is set at 0.356 million cycles.

The unified life estimates for the average and maximum initial crack sizes are given in Table 6.1 and Fig. 6.2. Unlike the stiffener the estimate at the expected maximum initial crack size slightly surpasses the actual life. Nevertheless, the deviation between the estimated and actual life at the average initial crack size is about equal to that found for the stiffener. If the overall correction factor is increased by 15 percent (as a calibration) at all crack sizes, the unified estimate at the average initial crack size is nearly equal to the average life.

Several other unified estimates provide informative comparison with Table 6.1. If bending were not included, the estimate at the average initial crack size would be 0.976 million cycles. If the initial crack shape variation equation were taken as Eq. 4-17 as opposed to Eq. 4-21, the estimate at the average initial crack size would be 1.036 million cycles. Finally, if a plastic zone correction were included (Art. 4.4) and the yield stress were successively assumed to be 385 MPa and 760 MPa[19], the corresponding estimates at the average initial crack size would be 0.509 million and 0.529 million cycles, respectively. Here again the importance of bending and crack shape variation is emphasized while the plastic zone correction at the given stress range is seen to have a minor effect.

Reference 19 gives the following regression equation for all cover plates with transverse end welds:

$$\log N = 11.8873 - 3.095 \log S_r \qquad\qquad (6\text{-}8)$$

Incorporation of the 96 percent life for crack growth through the flange modifies Eq. 6-8 as follows:

$$\log (.96N) = 11.8695 - 3.095 \log S_r \qquad\qquad (6\text{-}9)$$

For the specific stress range in Table 6.1, it can be seen that the estimated life from Eq. 6-9 (by chance) precisely equals the actual life for the particular series being studied. By making use of the standard error for Eq. 6-8 (s = 0.101), it is again possible to define the equation for the upper 95 percent confidence limit.

$$\log (.96N) = 11.8695 - 3.095 \log S_r + 2s$$

$$\qquad\qquad = 12.0715 - 3.095 \log S_r \qquad\qquad (6\text{-}10)$$

The result of Eq. 6-10 is also given in Table 6.1 and Eqs. 6-9 and 6-10 are both plotted in Fig. 6.2. As with stiffeners the value corresponding to the upper 95 percent confidence limit surpasses all of the unified estimates. Thus, even the unified estimate at the average initial crack size is not considered too far removed from the actual life.

Gurney makes the observation that the smaller the SCF the greater is the reduction in life as a result of an increase in initial crack size[27]. He derives this conclusion from studies on different joints with identical changes in the ratio of initial crack

size, a_i, to plate thickness, T_f (b in Ref. 27). The ratio of life at the larger value of a_i/T_f to life and the smaller a_i/T_f was found to increase asymptotically toward 1.0 as SCF increased. (Nominal stress range has no effect on the life ratio.) Hence, the smallest life ratio or biggest effect of initial crack size occurred at the smaller SCF.

The flange thicknesses of the stiffener and cover plate examples (Table 6.1) are not precisely equal. Thus, even though the initial crack sizes are equal an exact comparison is not possible. However, unified estimates can be made at equal a_i/T_f ratios for both details and typical results are recorded in Table 6.2. It is seen that initial crack size does indeed have more importance in the case of the stiffener detail, where SCF is much smaller, than for a cover plate.

Gurney notes that the above revelation with regard to initial crack size places emphasis on reducing initial size at those details with less severe stress concentration[27]. Yet, this suggestion has somewhat false economy since the details with highest stress concentration (Category E – cover plates, etc.) usually control the design of a typical bridge structure. (The stress ranges at higher category details are often below the fatigue limits.) Worry about less severe details such as stiffeners (Category C) may divert attention away from the weakest links in the fatigue design.

Article 4.5 mentions that the choice of crack shape varia-

tion equation has more effect on life for details with higher stress

concentration[27]. This point is supported by the results of changing

from Eq. 4-21 to Eq. 4-17 for early crack growth at both the stiffener

and cover plate. Even though the a_i/T_f ratio is not exactly constant,

the life ratio for the stiffener was 1.484 while the ratio for the

cover plate was 1.933. Realizing the questionable nature of the

crack shape variation equations, it is easy to understand the larger

relative error for cover plates at the average initial crack size.

6.3 Gusset Plates Groove-Welded to Flange Tips

Several test results exist for groove-welded gusset plates

with circular transitions[12, 16, 33]. All of the data points are for

small radii. Hence, life comparisons for a full spectrum of geome-

tries is not yet possible; generalized regression equations haven't

been derived. Still, it is interesting to see how unified life

estimates (Chap. 5) fare for those particular geometries which have

already undergone testing.

The specific sample details selected for analysis are re-

corded in Table 6.3. The actual lives and associated unified esti-

mates are presented in Table 6.4. One contrasting aspect of this

table versus Table 6.1 is the addition of final crack sizes. These

lengths don't necessarily relate to failure in the sense discussed

for stiffeners and cover plates. However, if the actual life is known at a specific crack size, a life estimate can be made to that point. (As noted earlier the final crack size is not too important when it is large – but some a_f in Table 6.4 are not excessive. Thus, the final crack size is considered of interest.)

Looking first at the Ref. 12 details, it is seen that the unified estimates at the average initial crack size are roughly twice the actual lives. For both detail types the initial crack size would have to be much larger in order to yield the actual life prediction. However, the required initial crack size is dependent upon the final crack size. This dependency can be seen in Fig. 6.3. Using other final crack sizes from Ref. 12, the necessary initial crack sizes for a life of two million cycles were calculated. Obviously, the data cover a broad spectrum of crack sizes and the estimating process for new details is subsequently rather tenuous.

The fatigue life estimate for Ref. 33 is comparable to those for Ref. 12. Again, the initial crack size would have had to be quite large (at the maximum expected initial size) in order for the estimate and actual lives to be equal. Only one other data point is given by Ref. 33. It would suggest an initial crack size of about the same magnitude (0.5 mm) for equality of actual and estimated lives.

The analytical results for the Ref. 16 details reflect a marked contrast with the estimating success for the previous references. The actual lives experienced are comparable to the average initial crack size or smaller. While regression equations and associated confidence limits are not available, the estimates at the given initial crack sizes can be approximately used in their stead[20]. Thus, Figs. 6.4 and 6.5 show the regression lines for various initial crack sizes. Imposed on the graphs are all data points (actual lives) in Ref. 16 (not just the ones in Table 6.4) and category limits from Refs. 3 and 21. (The category lines do not have precise slope -3.0 - Art. 6.1).

Comparison of Fig. 6.4 and 6.5 reveals that Category D (as it now exists) might be adequate for geometry A, but Category E is surely necessary for geometry B. This differentiation is interesting since both geometries have the same transition radius. Reference 21 places both geometries in Category E based on radius alone. However, it is apparent that length of detail also plays a role in detail severity. The length for geometry B is twice that of A, making B more severe. In general, all variables described in Art. 2.2 affect the fatigue performance. Thus, future research effort could well be directed at sorting out the category limits for various combinations of the geometrical (dimensionless) variables.

Figure 6.6 makes a comparison between all results in the three cited references and the category limits. For purposes of this plot the last recorded number of cycles was used for cycle life even though the definitions of failure vary. (For Ref. 12, N at the point of fracture was used rather than the two million cycles on which the analytical comparison in Table 6.4 was based.) Regardless, Ref. 12 gusset plates appear most fatigue prone, followed by Ref. 16 and Ref. 33 details, in that order. In light of the comparative values of geometric variables, this relative positioning of the details appears justified.

The lack of success in reasonably predicting the fatigue lives of certain of the gusset plate details is explainable. The range of stress intensity predicted at the smaller crack sizes was quite low for details in Refs. 12 and 33, leading to very large life estimates. In fact, early ΔK values were below what might be considered a threshold value for fatigue crack growth ($\Delta K_{th} \approx 104$ MPa $\sqrt{mm}^{28}$). However, the rapidity of fatigue failure can be attributed to local irregularities in geometry which amplified ΔK. Reference 12 shows a picture of a circular transition which can hardly be termed smooth. Reference 33 diagrams a transition which is <u>purposely not tangent</u> to the flange tip. While the intent of such a design is not understood (perhaps easier fabrication), it is clear Ref. 33 details began with a stress singularity condition at the weld terminations.

The difficulty in fatigue life prediction for certain gusset plates underscores the importance of careful detail preparation. For circular transitions where weld terminations have been gound smooth and (for large radii) where the plate has been cautiously cut out, prediction of fatigue life based on average initial crack size is possible. Unfortunately, such careful preparation can't be expected in real life bridge fabrication - particularly where the radius is small and formed by grinding.

The difference between actual and idealized geometries can be taken into account in the cycle life prediction process. While it is possible to introduce a local (additional) gradient effect into ΔK, the simplest approach is probably just an increase in the initial crack size. In fact, inspection of several specimens from Ref. 12 showed a starter notch where grinding occurred. Based on Table 6.4, an average initial crack size of 0.5 mm is recommended for cases where strict controls are not imposed on detail fabrication. The choice of initial crack size is particularly important for setting the above proposed category limits for variations in the geometric variables. Two sets of recommendations appear warranted.

6.4 Yellow Mill Pond Bridge

In the early 1970's fatigue cracking was detected in the steel (simple span) beams of the Yellow Mill Pond Bridge servicing Interstate Route 95 near Bridgeport, Connecticut. Subsequent stress

history studies[10, 40] led to the conclusion that fatigue crack growth should not have occurred since measured stress ranges were well below the fatigue limits developed from small scale beams[19, 20]. Hence, the Yellow Mill Pond Bridge has been a constant question mark; it has demonstrated worrisome contradiction with basic experimental findings[3, 19]. It is therefore appropriate to determine if the analytical approach of this dissertation sheds new light on the failure – particularly the fatigue limit positioning.

The most serious crack occurred at the end of a cover plate detail in one of the eastbound spans. Between the bridge erection in 1958 and 1970 the crack completely penetrated one beam flange and even propagated 400 mm up the web. The detail dimensions of interest are given in Fig. 6.7.

The variance in the stress range fatigue limit, $\bar{S}_r$, is plotted in Fig. 6.8 using a threshold ΔK of 104 MPa $\sqrt{mm}$. The fatigue limit is seen to have a general downward trend with increasing crack size. However, due to the sharp drop in F_g a short plateau occurs around the 20 MPa level, temporarily interrupting the decline of $\bar{S}_r$. While this particular fatigue limit curve was developed with the additional 15 percent correction factor (Art. 6.2), with or without the 15 percent the entire curve falls well below the (lower confidence) fatigue limit observed on smaller scale beams[19, 20].

Figure 6.8 also positions two stress range levels of interest. First, the maximum stress from the stress history study is indicated. Second, the upper bound stress range for almost all recorded stress ranges is given. The fatigue limit curve is seen to fall between the two levels. It is noteworthy that these levels aren't associated with stress ranges recorded at the specific detail investigated here since it had already failed. The stress history data was collected at a similar detail on a different span. Thus, some vertical shift in the lines for the actual detail in question could be expected.

The crack length in Fig. 6.8 can be viewed as either initial size or size at some point during crack propagation. Using the maximum stress range and assuming the initial crack size to be 0.076 mm (average expected), the life estimate for growth to 0.5 mm is nearly one million cycles. Life for growth from 0.076 mm through the flange is estimated at 19 million cycles. Both of these figures are in marked contrast to the 20 thousand cycles estimated for stress ranges above 20 MPa[10]. (Traffic surveys accompanied the stress history studies.)

In light of the preceding findings the analysis of the Yellow Mill Pond Bridge failure can be considered a partial success. On the positive side it is clear that the fatigue limits for certain geometries might be well below the existing AASHTO regulations[3]. This

does not necessarily mean new detail categories are required; perhaps only a choice of runout levels (as for Category C) is sufficient. Future research appears warranted in order to accommodate the full spectrum of detail geometries in AASHTO. Also, while resetting the fatigue limits on a geometrical basis, consideration should be given to the drop in the limits as cracks propagate, thereby making more of the stress range histogram (and associated cycles) effective in causing growth[28].

The negative side of the Yellow Mill Pond analysis picture is obviously the discrepancy in life cycle estimates. Even allowing for a very large initial crack size and/or occasional overloads, the estimated and actual cycles are far out of line. Errors are, of course, possible in the development of the stress intensity expressions (in addition to the 15 percent) and material constants (Art. 6.5). However, it appears the greatest discrepancy is associated with the stress history study. Certainly there would have to be a great number of cycles near the 20 MPa level which could be considered the root-mean-square or Miner stress range required for sustained crack growth[70]. In this case the two stress range limits in Fig. 6.8 would be substantially higher.

6.5 Sources of Error

Given the preceding results of various fatigue life correlations it is worthwhile collectively highlighting the potential

sources of discrepancy between estimated and actual lives. These sources or "pitfalls" in the analytical procedure may be grouped under the headings of stress gradient correction, other correction factors, and life integration. Knowledge of weak assumptions can and hopefully will lead to research which will strengthen the fatigue analysis capability of all investigators. However, it should be understood that variability in the actual lives makes precise estimating in all instances a virtual impossibility.

. . . 6.5.1 Stress Gradient Correction

Chapters 2 and 3 were devoted exclusively to coming to grips with F_g. Yet, from the start important assumptions were made. First, the geometry of the detail was idealized. Fillet weld angles were taken as $\pi/4$ radians although the angle at the toe often exceeds this value – particularly for handmade welds. Gurney has shown that stress concentration increases with weld angle and F_g at small crack sizes is significantly affected[27]. The geometry also has great importance for groove-welded gusset plates where the transition radius results from grinding the weld termination. Lack of careful transition fabrication can seriously increase the rapidity of early crack growth[12].

Important decisions for the stiffeners and cover plates were the section used for two-dimensional analysis and subsequent SCF and F_g calculations, the distance from the weld toe for input of uniform

stress, the length of cover plate beyond which conditions at the weld toe do not change, and the plane stress versus plane strain controversy when switching from the three-dimensional to the two-dimensional analysis. But perhaps the key decision for any geometry with a singular (eleastic) stress distribution is the mesh size. The contention in this dissertation is that the size near the singular point must be smaller than the expected initial crack size. Variation in mesh size makes comparison of results of different investigators of singular geometries very difficult at small crack sizes.

If the geometry were truly singular it would imply localized yielding. The associated redistribution of stress would raise the stress concentration and F_g correction at crack-lengths just beyond the plastic zone. (Within the zone K_t and F_g would, of course, be constant.) The size of the zone depends on stress or stress range in a manner similar to that presented for crack tip plastic zone correction, F_p. However, like F_p a modification for geometric singularity yielding was assumed to be small and thus neglected. If yielding had been included the estimated life would have been closer to the actual life.

The gusset plate geometries only underwent two-dimensional analysis. Since the middepth of the plate is not normally coincident with the middepth of the adjacent flange, some out-of-plane bending will occur. This bending is neglected by the two-dimensional approach

-170-

although the bending is probably responsible for early growth as a corner crack.

The gusset plates presented difficulty in developing SCF and ellipse decay correlation equations. The equations do not demonstrate the same goodness of fit that was exhibited for cover plates and stiffeners. Obviously, the number of variables was partially responsible for this condition. Application of the correlation is also questioned for crack growth beyond the web line. F_g would actually begin rising rather than continuing the decay. Regardless, the generally low F_g for gusset plates reduces the concern about equation inaccuracies. Cycle life for growth beyond the web is so small a percentage of total life that error in correction factors can be considered to have neglibible importance.

Application of Albrecht's Green's Function requires that the crack path be known in advance. It was assumed that the path extended from the weld toe in the direction of the flange thickness (stiffeners and cover plates) or from the circular transition point of tangency in the direction of the flange width (gusset plates). Actual tests have shown slight deviation from these directions in the very early stages of crack growth (Art. 3.1)[12,22]. Use of the proper direction does raise F_g somewhat.

The ellipse decay correlation equations for stiffeners, cover plates, and gusset pates are most valid when the dimensionless

geometrical parameters are within the limits used in the equations'
development. Use of the equations for excessive parametric values
should be done with caution even though the trend indicated by the
equations is correct.

6.5.2 Other Correction Factors

Evaluation of the limits of the F_s and F_w correction fac-
tors (Chapter 4) involved some judgment. This is particularly true
in the case of the quarter-circular crack for which existing solu-
tions are rather tenuous. Application of these factors, which stem
from simple plate specimens, to details where changes in cross-
section occur is questionable. Unknown is how the detail affects
Poisson displacement parallel to the crack at its origin. If such
displacement is restricted to a significant degree, F_s must be
reduced. F_s also is less if growth along the minimum stress tra-
jectory is considered rather than perpendicular to the applied stress
(Fig. 3.1)[82]. The gap between estimated and actual life would then
widen. However, stress perpendicular to the crack is higher when
growth is along the trajectory and the rise in F_g would tend to
balance the drop in F_s.

Yielding due to the crack tip was discussed and incorporated
in the plastic zone correction, F_p (Art. 4.4). This factor is small
for reversed yielding conditions, as in fatigue, where the alternating
plastic zone is one quarter that of a noncyclic stress. F_p is also

low due to low stress ranges in real bridges and a modern tendency toward steels with increased yield strength. However, F_p is affected by detail type and increases for those attachments (Category E) which result in a high overall correction factor, CF. While F_p is generally neglected in the dissertation, it brings actual and estimated lives closer together (Art. 6.2).

A very important decision for every detail is whether or not bending occurs as a crack grows (Art. 4.3). Cover and gusset plates are considered to exhibit bending while stiffeners do not. Obviously, though, geometry can affect the degree with which either limit is attained. Bending can easily reduce the estimated life by several hundred thousand cycles (Arts. 6.1 and 6.2).

Even if the form of all the correction factors is properly ascertained, the crack shape variation during growth must be known for an accurate life estimate (Art. 4.5). The stiffener detail has been studied for crack shape variation although results by different investigators are in considerable disagreement. There are the further complications of crack coalescence and, for thick flanges, an eventual dominance by corner cracks (rather than semielliptical ones) growing in the thickness direction (comparable to Fig. 4.12). Shape variation equations are unknown for cover plates although the shape ratio, a/b, may remain small due to a higher stress gradient. In any case the stiffener equations were used for cover plates in the present study.

The equation used for gusset plates was based on crude, limited data in Ref. 12 and, quite likely, will undergo modification in the future. Depending on the magnitude of stress concentration, the shape variation decision can affect the life estimate by as much as 100 percent (Art. 6.2) or possibly more[27].

6.5.3 Life Integration

In the numerical integration process several decisions must be made. Naturally, the method of integration and the crack increments have some small influence on the results. However, much more important is the initial crack size. Tables 6.1 and 6.4 show a marked difference in results when the initial size is permitted to vary within expected limits[20,74]. The limits themselves are in question for different types of details, different weld leg sizes, and even different strength steels.

C and n in Eqs. 1-1 and 6-1 are primarily material constants, but they are also affected by environment, frequency, and temperature (air and room temperature assumed here). Barsom has set an upper bound on the crack growth rate for ferrite-pearlite steels (e.g. A36 and A441) as follows[6]:

$$\frac{da}{dN} = 2.18 * 10^{-13} (\Delta K)^{3.0} \qquad (6-11)$$

where $\frac{da}{dN}$ = mm/cycle

$\Delta K = MPa \sqrt{mm}$

The upper bound was intended to limit the growth rate in weld metal
and the heat affected zone (HAZ) as well as the parent plate. With
the same inclusive approach Maddox has set upper and lower limits of
C at $3.0*10^{-13}$ and $0.9*10^{-13}$, respectively[49,50]. Exponent n was very
close to 3.0 and was taken as such. Meanwhile, Hirt and Fisher found
C to be $1.21*10^{-13}$ and n again 3.0[32]. It is safe to conclude that the
findings of all of these investigators show good agreement and the C
value by Hirt and Fisher is a reasonable intermediate assumption.
Exponent n is taken as 3.0 although certain regression equations like
the Type 3 stiffener one (Art. 6.1) show some deviation from this
value.

Controversy arises, however, when assuming growth rate
constants for martensitic steels (e.g. A514). Barsom's upper bound
for these steels is

$$\frac{da}{dN} = 0.40*10^{-11} \ (\Delta K)^{2.25} \qquad (6-12)$$

Naturally, an assumption of equal initial crack sizes and range of
stress intensity expressions would cause the life estimates from
Eqs. 6-11 and 6-12 to differ considerably[45]. Yet, test results from
actual structural details have shown the regression curves of A36 and
A514 specimens fall almost on top of each other[6,19,20].

The paradox is not resolved by consideration of a crack
initiation phase. Barsom notes that the observed difference in

fatigue life of steels having different tensile strengths decreases as stress concentration increases[6]. Stress concentration negates differences associated with crack initiation in various steels, thereby relegating the total useful fatigue life to fatigue crack propagation behavior. Thus, crack initiation is disregarded on two counts. First, life estimates are generally higher than actual fatigue lives and presumption of an initiation phase would only widen the gap. Second, high stress concentration at details makes an initiation phase nonexistent for all common bridge steels.

The disagreement between Eqs. 6-11 and 6-12 can not be fully explained at this time. However, based on the testing experience on real structural details, Eq. 6-11 suggests the performance trend expected for all steels. The Hirt and Fisher value of C is taken as the statistical mode.

7. SUMMARY, CONCLUSIONS, AND RECOMMENDED RESEARCH

The intent of this study has been to improve the accuracy associated with fatigue life estimates for typical structural, welded details. A large measure of the improvement stems from determination of the stress gradient correction factor, F_g, which modifies the stress intensity at any given crack length. Also, development of stress intensity expressions which properly consider differences in crack shape as well as the influence of the variable stress field has aided the fatigue estimate correlations. The more important steps and findings of the dissertation and recommendations for further work may be itemized as follows:

(1) Stress concentration factors have been established for fillet weld toes of transverse stiffeners and cover plates with end welds by use of the finite element technique. For each idealized geometry a singular elastic stress condition exists at the weld toe. Thus, local stress concentration continues to rise as the mesh size is reduced. Reasonable accuracy of the stress gradient correction at small crack lengths requires that the mesh size adjacent to the weld toe be less than the expected initial crack size.

(2) Stress concentration at weld toes increases at a decreasing rate as attachment length increases. Concentration for the limits of length represented by stiffeners and cover plates

is primarily related to weld leg size, flange thickness, and attachment thickness. (Attachment thickness for stiffeners is represented by the stiffener height and, for such large magnitudes, the stress concentration has attained constant value for the variable involved.) Typical stiffeners were found to have concentration factors between three and four while cover plates with end welds have concentration factors between six and eight.

(3) Stress concentration for groove-welded gusset plates with circular transitions is not affected by a singular geometry but the mesh size required does decrease for smaller transition radii. Gusset plates with circular transitions normally have concentration factors between one and three depending on gusset plate and flange dimensions. However, as the radius decreases below $0.1W_f$, the theoretical SCF rises rapidly and can reach values well above those of cover plates. Use of gusset plates without circular transitions is therefore discouraged. In general, the concentration factors show reasonable agreement with Peterson values[63] although additional information is here provided on variable thickness ratios and the effect of imposed secondary stress.

(4) The results for cover plates with transverse end welds represent an upper bound for cover plates without transverse end welds and some lap-welded gusset plates, depending on

width. Fillet- or groove-welded longitudinal stiffeners with slight circular transitions at the ends (by weld termination grinding) can be conservatively treated as groove-welded gusset plates. Such solutions also reasonably apply to longitudinal stiffeners with circular transitions when the stiffener end is tapered.

(5) Given the stress concentration factor distribution along the prospective crack path (prior to insertion of the crack), the stress gradient correction factor, F_g, is evaluated using the Green's Function proposed by Albrecht[2]. The stress gradient correction curve (with maximum value SCF) is always above the stress concentration factor decay curve for structural details. However, at large distances from the point of maximum concentration the two curves converge.

(6) The stress gradient correction factor curves derived from Albrecht's Green's Function are correlated with expressions for stress concentration factor decay from an elliptical hole in a plate. The relative size of the ellipse and appropriate axis are established by the stress concentration factor for the detail. The absolute size of the ellipse is determined by geometry with particular emphasis on the dimension over which decay occurs. The correlated ellipse is used to predict the F_g correction at any crack size for fatigue life estimate purposes.

(7) All correction factors stem from stress intensity solutions for simple plate specimens[76,81,82]. Use of these solutions for structural details where rapid changes in cross-sectional geometry occur is questionable. Future study should be directed at determining the error involved in assuming the simple plate correction factors are applicable. Particular attention should be given to F_s.

(8) Front free surface correction factors are established for through, half-circular, and quarter-circular crack shapes with variable stress distributions. However, additional theoretical work should be directed at the quarter-circular cracks since values at the crack tip for the various stress distributions are only approximate.

(9) A major decision affecting the back free surface correction factor for each detail is whether or not cross section bending occurs with increasing crack length. Cover plates exhibit considerable bending due to longitudinal flexibility. Gusset plate details also exhibit bending (in plane) even if identical details are symmetrically positioned with respect to the web. Usually different crack lengths at the two transitions negate symmetry. Contrary to cover and gusset plates, stiffeners are assumed to lack bending since those joints are comparably stiff.

(10) Regardless of the bending situation, little is known about F_w for crack shapes between zero and 1.0. Linear interpolation is used in this dissertation although Maddox predicts a nonlinear relationship between F_w and crack shape[51]. More analytical effort should be directed at F_w for variable crack shape and variable proximity to the back free surface.

(11) Crack growth generally originates at several locations along transverse weld toes. Hence, for stiffener and cover plates with transverse welds, crack coalescence occurs and is considered in the decision on crack shape. At early stages of growth the shape variation equation reflects a tendency to a circular shape. A second equation for later growth incorporates coalescence and a trend toward a flat, through shape.

(12) Crack shape has a pronounced influence on cycle life predictions. Whether or not coalescence is considered, all crack shape equations are questionable. Extensive research is required to determine the crack shape variation at different details and how shape relates to correction factors F_g, F_s, and F_w. Stiffeners fillet-welded to flanges exhibit more circular cracks than cover plates with transverse end welds. For both details the shape also appears related to flange thickness although the data base is sparse. The data base is even more sparse for groove-welded gusset plates.

(13) Expressions for stress intensity due to an arbitrary stress field are developed by dividing the stress distribution for a given crack length into uniform and variable (decreasing to zero at the crack tip) subdistributions. The stress intensities for the subdistributions are superimposed (added together) to give the unified stress intensity factor. Crack shape is taken into account by developing unified F_s expressions for both extremes of crack shape and linearly interpolating between them for the specific shape predicted by the crack shape variation equation.

(14) Initial crack (discontinuity) size is quite important to the cycle life prediction. Yet, the extent of study on discontinuities at weld toes is rather limited. Current estimates put the average size between 0.075 and 0.10 mm[20,74,86]. Future study should resolve if and how the discontinuity size varies for different types of details, different weld sizes, different weld electrodes and processes, and even different steel strengths.

(15) Correlations between estimated and actual fatigue lives for stiffeners and cover plates show the estimated values to be on the high (unconservative) side. The estimated lives are within the upper 95 percent confidence limits. Estimates for stiffeners with an average initial crack size can be brought into more accurate agreement with the mean regression

line by increasing the overall stress intensity correction factor by five percent. Cover plates require a 15 percent correction.

(16) Fatigue life correlations for groove-welded gusset plates are quite sensitive to the tolerance permitted in fabrication of the circular transitions. Careful fabrication results in good agreement between actual life and life estimated from the average initial crack size. Crude fabrication reduces the actual fatigue life considerably and an adjustment must be made in the estimating procedure. While the stress intensity expressions could be appropriately modified to reflect geometric irregularities, a simpler approach is to increase the initial crack size from the average value to the upper limit expected.

(17) AASHTO fatigue categories for groove-welded gusset plates with circular transitions are now based on dimensional radius alone[4,21]. New provisions currently being considered are as follows:

	Category
$R \leq 51$ mm	E
$51 < R < 152$ mm	D
$152 \leq R < 610$ mm	C
$610 \leq R$	B

These provisions appear conservative for practical detail geometries, even in light of potential fabrication problems. However, the correct AASHTO category should depend on nondimensionalized radius as well as other nondimensionalized, geometric variables. New investigative effort should be directed at bounding the category "kernels" for all possible variations in detail geometry. Consideration must also be given to differences caused by the fabrication tolerance required.

(18) Detail geometry affects the stress concentration and stress gradient correction factors and ultimately influences fatigue limits. Details with high F_g at the initial crack size can have fatigue limits well below those published in the AASHTO Specifications[3]. New research should be directed at repositioning the fatigue limits to more properly reflect the extremes of detail geometries. This research should also consider the variability of the fatigue limits with crack growth and the eventual effectiveness of lower values in the typical bridge detail, stress range spectrum.

(19) Crack initiation appears to play a negligible role in the fatigue life of a bridge detail. Since life estimates based on propagation alone are greater than actual lives, crack initiation estimates would only increase the magnitude of disagreement. Also, high stress concentration at fillet-welded details seriously curtails any possible initiation activity.

a	crack size; minor semidiameter of elliptical crack
a_i	initial crack size
a_f	final crack size
A	number of cycles when stress range equals 1.0; stress concentration factor decay polynomial coefficient
A_u	area of uniform stress subdistribution
A_v	area of variable stress subdistribution
b	major semidiameter of elliptical crack
B	stress concentration factor decay polynomial coefficient; plate thickness in cruciform joint
c	stress concentration factor decay coefficient
C	crack growth coefficient; stress concentration factor decay polynomial coefficient
CF	combined total correction factor for stress intensity
CF_p	total correction factor including factor including plastic zone
CF_{pf}	total correction factor for fatigue including plastic zone
d	stress gradient correction factor decay coefficient
D	stress concentration factor decay polynomial coefficient; constant in characteristic equation for ξ; chord length on gusset plate circular transition
e	distance from detail at which stress concentration is negligible
E	Young's modulus; stress concentration factor decay polynomial constant
E(k)	complete elliptic integral of the second kind

f	focal distance of ellipse
F_e	crack shape correction factor
F_g	stress gradient correction factor
$\bar{F}_g$	stress gradient correction factor for variable stress subdistribution
F_p	plastic zone correction factor
F_{pf}	plastic zone correction factor for fatigue
F_s	front free surface correction factor
F_w	back free surface correction factor
g	major semidiameter of elliptic hole in an infinite plate
g_{opt}	optimum major semidiameter of elliptic hole for representing the stress gradient correction factor decay
G	strain energy release rate
h	minor semidiameter of elliptic hole in an infinite plate
h_{opt}	optimum minor semidiameter of elliptic hole for representing the stress gradient correction factor decay
K	stress intensity factor
K_c	material toughness
K_{eff}	effective stress intensity factor after stress redistribution due to crack tip plasticity
K_t	stress concentration factor
K_u	stress intensity factor for uniform stress subdistribution
K_v	stress intensity factor for variable stress subdistribution
ΔK	range of stress intensity factor
ΔK_{th}	stress intensity range at crack growth threshold
ℓ	distance along crack path from origin

log	logarithm to base 10
L	attachment length; length to division of two stress concentration factor decay polynomials
L'	outer edge length of groove-welded gusset plate
m	number of finite elements to crack length a; maximum distance between gusset plate circular transition and chord approximation
n	crack growth exponent; negative slope of log-log S_r-N curve
N	fatigue life
p	stress concentration factor decay exponent
P_f	total force directly input to flange
P_{gp}	total force directly input to gusset plate
q	stress gradient correction factor decay exponent
Q	coefficient for back surface tangent correction to account for bending; crack shape correction modified for crack tip plasticity
r	distance from crack tip
r_y	distance from crack tip to where yield condition ends
R	radius of circular transition at end of groove-welded gusset plate
s	standard error of estimate
S_r	nominal stress range
$\overline{S}_r$	nominal stress range representing fatigue limit
SCF	maximum stress concentration factor; stress concentration factor for the crack origin
t_f	thickness of planar finite elements representing flange
t_w	thickness of planar finite elements representing weld

T_{cp}	cover plate thickness
T_f	flange thickness
T_{gp}	gusset plate thickness
T_s	stiffener thickness
u	elliptical coordinate representing confocal ellipses
U	flange thickness in inches minus 1.0
v	elliptic coordinate representing confocal hyperbolas
w	crack length at which rate of growth becomes infinite
W	ratio of area of variable stress subdistribution to area of uniform stress subdistribution, A_v/A_u
W_{cp}	cover plate width
W_f	flange width
W_{gp}	gusset plate width
W^*	effective width of symmetrical lap-welded gussets, measured from outer edge to outer edge
x	distance from ellipse center in major axis direction
X	ratio of stress concentration factor at α to stress gradient correction factor for α
y	distance from ellipse center in minor axis direction
Y	ratio of F'_g for circular crack to F_g for through crack
Z	weld leg size

α	nondimensionalized crack length, a/w
β	dummy angle variable for integration purposes
γ	value of elliptic coordinate η representing elliptic hole perimeter

ε	strain
ζ	alternative elliptic coordinate related to v
η	alternative elliptic coordinate related to u
θ	half of angle delineating chord length of gusset plate circular transition
λ	nondimensionalized distance, ℓ/w
ν	Poisson's ratio
ξ	value of λ at which slope of decay curve equals slope of straight line from SCF to K_t at α
σ	stress
σ_y	yield stress
ϕ	angle from major axis of elliptic crack
Φ	inverse of F_e
Ω	crack yield zone size factor depending on planar conditions

TABLES

Table 1.1 AASHTO Allowable Range of Stress for Fatigue[3]

Detail Category	Cycles			
	100,000	500,000	2,000,000	over 2,000,000
A	413.7 MPa (60 ksi)	248.2 (36)	165.5 (24)	165.5 (24)
B	310.3 (45)	189.6 (27.5)	124.1 (18)	110.3 (16)
C	220.6 (32)	131.0 (19)	89.6 (13)	69.0, 82.7* (10, 12*)
D	186.2 (27)	110.3 (16)	69.0 (10)	48.3 (7)
E	144.8 (21)	86.2 (12.5)	55.2 (8)	34.5 (5)
F	103.4 (15)	82.7 (12)	62.1 (9)	55.2 (8)

* For transverse stiffener welds on webs or flanges

Table 2.1 Summary of Maximum Stress Concentration Factors
for Stiffener and Cover Plate Geometries

Detail	$\dfrac{Z}{T_f}$	$\dfrac{T_{cp}}{T_f}$	SCF
Stiffener	0.3205		3.161
↓	0.6410		3.651
▽	0.9615		3.934
Cover Plate	0.3205	0.6410	7.198
↓	0.6410	0.6410	6.040
	↓	1.4360	6.762
	▽	2.0000	7.014
▽	0.9615	2.0000	6.542

Table 2.2 Auxiliary Geometries for Cover Plate
and Flange Width Effects

CASE	$\dfrac{W_f}{T_f}$	$\dfrac{W_{cp}}{W_f}$	$\dfrac{W_{cp}}{T_f}$	$\dfrac{L}{W_{cp}}$	SCF
1	8.64 —— 0.667 ——	0.667 —— 5.76	5.76	1.778	6.557
				2.667 ——	6.762
2	17.28	0.667	11.52	0.889	6.921
				1.333	7.418
					(8.242)*
3	17.28	0.296	5.11	2.000	6.690
				3.000	6.818
4	8.64	1.333	11.52	0.889	6.480
				1.333	6.945

For all geometries in this table:

$$\frac{Z}{T_f} = 0.6410 \qquad \frac{T_{cp}}{T_f} = 1.4360$$

* Plane strain conditions assumed for finer meshes

Table 2.3 Summary of Maximum Stress Concentration
Factors for Gusset Plate Geometries

$\dfrac{R}{W_f}$	$\dfrac{L}{W_f}$	$\dfrac{W_{gp}}{W_f}$	$\dfrac{T_{gp}}{T_f}$	SCF
0.056	0.44	0.67	1.00	1.987
			0.50	1.496
	0.67		1.00	2.114
			0.50	1.803
	1.11		1.00	2.457
			0.50	2.245
	2.89		1.00	3.216
			0.50	2.787
0.083	0.67	1.00	1.00	2.022
			0.75	1.924
			0.50	1.770
			0.25	1.642
	1.00		1.00	2.277
			0.75	2.137
			0.50	1.922
			0.25	1.852
	1.67		1.00	2.554
			0.75	2.371
			0.50	2.163
			0.25	2.110
	4.33		1.00	2.737
			0.75	2.570
			0.50	2.519
			0.25	2.431

Table 2.3   Summary of Maximum Stress Concentration
(Cont.)   Factors for Gusset Plate Geometries

$\dfrac{R}{W_f}$	$\dfrac{L}{W_f}$	$\dfrac{W_{gp}}{W_f}$	$\dfrac{T_{gp}}{T_f}$	SCF
0.167 ↓	1.33 2.00 3.33 8.67 ↓	2.00 ↓	1.00 ↓	1.967 2.101 2.189 2.229
0.250 ↓	1.00 ↓ 1.67 ↓ 4.33 ↓	1.00 ↓	1.00 0.50 1.00 0.50 1.00 0.50	1.658 1.492 1.790 1.638 1.870 1.789
0.417 ↓	1.67 ↓ 4.33 ↓	1.00 ↓ 1.50 0.50	1.00 0.50 1.00 0.50 1.00 ↓	1.536 1.392 1.580 1.425 1.579 1.562
0.500 ↓	1.67 ↓ 2.33 4.33 ↓	1.00 ↓	1.00 0.50 1.00 ↓ 0.50	1.440 1.305 1.461 1.465 1.386
1.000 ↓	4.33 ↓	1.00 ↓	1.00 0.50	1.254 1.189
1.500 ↓	4.33 ↓	1.00 ↓	1.00 0.50	1.179 1.117
2.000 ↓	4.33 ↓	1.00 ↓	1.00 0.50	1.132 1.097

Table 2.4 Summary of Maximum Stress Concentration
Factors for Singular Gusset Plate Geometries

$\dfrac{R}{W_f}$	$\dfrac{L}{W_f}$	$\dfrac{W_{gp}}{W_f}$	$\dfrac{T_{gp}}{T_f}$	SCF
0.0	0.33	1.00	1.00	6.311
	0.67		↓	8.469
	↓		0.50	5.515
	1.00		1.00	10.058
	1.67		↓	12.226
	↓		0.50	7.530
	2.33		1.00	13.658
	4.33		↓	14.786
	↓	↓	0.50	9.032
	0.67	0.50	1.00	8.466
	1.67			12.019
↓	4.33	↓	↓	13.325

Table 2.5 Prediction of Maximum Stress Concentration
            Factors for Singular Gusset Plate Geometries

$\dfrac{L}{W_f}$ or $\dfrac{Z}{T_f}$	SCF Table 2.4	SCF Eq. 2.2
0.33	6.311	6.365
0.67	8.469	7.362
1.00	10.058	7.926
1.67	12.226	8.648
2.33	13.658	9.119
4.33	14.786	11.719

For all geometries in this table:

$$\frac{R}{W_f} = 0.0 \qquad \frac{W_{gp}}{W_f} = 1.00 \qquad \frac{T_{gp}}{T_f} = 1.00$$

Table 5.1   Decay Constants of Approximate Stress
Concentration and Stress Gradient
Correction Factor Curve Formulas

$$\frac{K_{t\lambda}}{SCF} \simeq \frac{1}{1 + \frac{1}{c}\lambda^p} \qquad\qquad \frac{F_{g\alpha}}{SCF} \simeq \frac{1}{1 + \frac{1}{d}\alpha^q}$$

Constant	Stiffener	Cover Plate	Gusset Plate
c	0.3546	0.1159	0.9623
p	0.1543	0.3838	0.5077
d	0.3602	0.1473	1.1579
q	0.2487	0.4348	0.6051

Table 5.2 Comparison of Stress Gradient Corrections for Through and Circular Crack Shapes

$$\text{Assume} \quad \frac{K_{t\ell}}{SCF} = 1 - A\left(\frac{\ell}{a}\right) + B\left(\frac{\ell}{a}\right)^2$$

Stress Distribution		F_{ga}/SCF		Ratio, Y
		Through	Circular	
Uniform	$A=B=0$ sym. a	1.000	1.000	1.000
Linear	$A=1 \quad B=0$	0.363	0.281	0.774
Parabolic	$A=\frac{5}{4} \quad B=\frac{1}{4}$	0.329	0.251	0.763
Parabolic	$A=2 \quad B=1$ ℓ	0.227	0.162	0.714

Table 5.3 Summary of Correction Factors for
Unified Stress Intensity Expressions
for Stiffeners

Correction Factor	Expression
Front Free Surface, F_s	$$\left(1-\frac{a}{b}\right)\left\{TERM1*COEF1+(1.122-TERM1*COEF1)*X\right\}+\frac{a}{b}*\left\{\frac{TERM2*Y+(1.025-TERM2)*X}{\left[\sec\left(\frac{\pi\alpha}{2}\right)\right]^{1/2}}\right\}$$
Crack Shape, F_e	$$\frac{1}{E(k)}$$
Back Free Surface, F_w	$$\left[\sec\left(\frac{\pi\alpha}{2}\right)\right]^{1/2}$$
Stress Gradient, F_g	as evaluated by the correlated stress decay from an elliptical hole in an infinite plate

Table 5.4 Summary of Correction Factors for
Unified Stress Intensity Expressions
for Cover Plates

Correction Factor	Expression
Front Free Surface, F_s	$\left(1 - \dfrac{a}{b}\right) \left\{ \text{TERM1*COEF3} + (1.122\text{COEF2} - \text{TERM1*COEF3})*X \right\} + \dfrac{a}{b} * \left\{ \dfrac{\text{TERM2*Y} + (1.025 - \text{TERM2})*X}{\left[\sec\left(\dfrac{\pi\alpha}{2}\right) \right]^{1/2}} \right\}$
Crack Shape, F_e	$\dfrac{1}{E(k)}$
Back Free Surface, F_w	$\left[\sec\left(\dfrac{\pi\alpha}{2}\right) \right]^{1/2}$
Stress Gradient, F_g	as evaluated by the correlated stress decay from an elliptical hole in an infinite plate

TABLE 5.5 Summary of Correction Factors for
Unified Stress Intensity Expressions
for Gusset Plates

Correction Factor	Expression
Front Free Surface, F_s	$\left(1-\dfrac{a}{b}\right)\left\{\text{TERM1*COEF3}+(1.122\text{COEF2}-\text{TERM1*COEF3})*X\right\} + \dfrac{a}{b} * \left\{\dfrac{\text{TERM3*Y}+(1.380-\text{TERM3})*X}{\left[\sec\left(\frac{\pi\alpha}{2}\right)\right]^{1/2}}\right\}$
Crack Shape, F_e	$\dfrac{1}{E(k)}$
Back Free Surface, F_w	$\left[\sec\left(\dfrac{\pi\alpha}{2}\right)\right]^{1/2}$
Stress Gradient, F_g	as evaluated by the correlated stress decay from an elliptical hole in an infinite plate

Table 6.1 Cycle Life Comparisons for Sample Stiffener and Cover Plate Details

Detail	S_r-MPa	T_f-mm	Z-mm	T_{cp}-mm	N_{act}*	Unified N_{est}	Other N_{est}
Stiffener Fillet-Welded to Flange (Ref. 20, Series SGB-SBB)	127.	12.3	6.35	--	1.346	1.609 (a_i = .076mm) 1.195 (a_i = .508mm) 1.390 $\left(\begin{array}{c} a_i = .076mm \\ 1.05*CF \end{array}\right)$	1.409 (Eq. 6-4) 1.389 (Eq. 6-6) 2.226 (Eq. 6-7)
Cruciform Fillet-Welded Joint (Ref. 27, Non-load-carrying fillet weld)	100.	12.5	20.0	--	1.842	2.158 (a_i = .125mm) 1.871 (a_i = .500mm) 1.865 $\left(\begin{array}{c} a_i = .125mm \\ 1.05*CF \end{array}\right)$	2.954 (Eq. 6-4) 3.210 (Eq. 6-6) 0.979 $\left(\begin{array}{c} a_i = .125mm \\ Gurney\ mean \end{array}\right)$

* All cycle lives in millions

Table 6.1 Cycle Life Comparisons for Sample Stiffener and Cover Plate Details (Cont.)

Detail	S_r-MPa	T_f-mm	Z-mm	T_{cp}-mm	N_{act}*	Unified N_{est}	Other N_{est}
Cover Plate With Transverse End Weld	110.	9.98	6.35	14.0	0.356	0.536 (a_i = .076mm)	0.356 (Eq. 6-9)
						0.444 (a_i = .508mm)	0.567 (Eq. 6-10)
(Ref. 19, Series CWB-CWC)						0.353 $\left(\begin{array}{c}a_i = .076\text{mm} \\ 1.15*CF\end{array}\right)$	

* All cycle lives in millions

Table 6.2 Effect of Initial Crack Size on
Cycle Life for Different Details

Detail	a_i/T_f		Life Ratio
	0.0076	0.0509	
Stiffener Fillet-Welded to Flange (Ref. 20, Series SGB-SBB)	1.574*	1.106	0.703
Cover Plate With Transverse End Weld (Ref. 19, Series CWB-CWC)	0.536	0.444	0.828

* All cycle lives in millions

Table 6.3 Sample Groove-Welded Gusset Plate Geometries

Detail		W_f-mm	T_f-mm	R-mm	L-mm	W_{gp}-mm	T_{gp}-mm
Ref.	Desig.						
12	A	156.	39.6	19.1	343.	305.	25.4
	B	178.	51.2	19.1	343.	305.	25.4
33	-	170.	12.0	70.0	200.	50.	8.0
16	A	200.	20.0	20.0	240.	100.	20.0
	B	200.	20.0	20.0	440.	125.	20.0

Table 6.4 Cycle Life Comparisons for Sample Gusset Plate Details

Detail		S_r-MPa	a_f-mm	N_{act}*	Unified N_{est}
Ref.	Desig.				
12	A	60.	22.2	1.983	4.623 (a_i = .076mm) 1.983 (a_i = .800mm)
	B	62.	9.5	2.015	3.655 (a_i = .076mm) 2.015 (a_i = .269mm)
33	—	120.	67.0	0.798	2.126 (a_i = .076mm) 0.798 (a_i = .503mm)
16	A	153.	95.0	0.407	0.466 (a_i = .025mm) 0.293 (a_i = .076mm) 0.146 (a_i = .508mm)
	B	253.	130.0	0.054	0.084 (a_i = .025mm) 0.053 (a_i = .076mm) 0.027 (a_i = .508mm)

* All cycle lives in millions

FIGURES
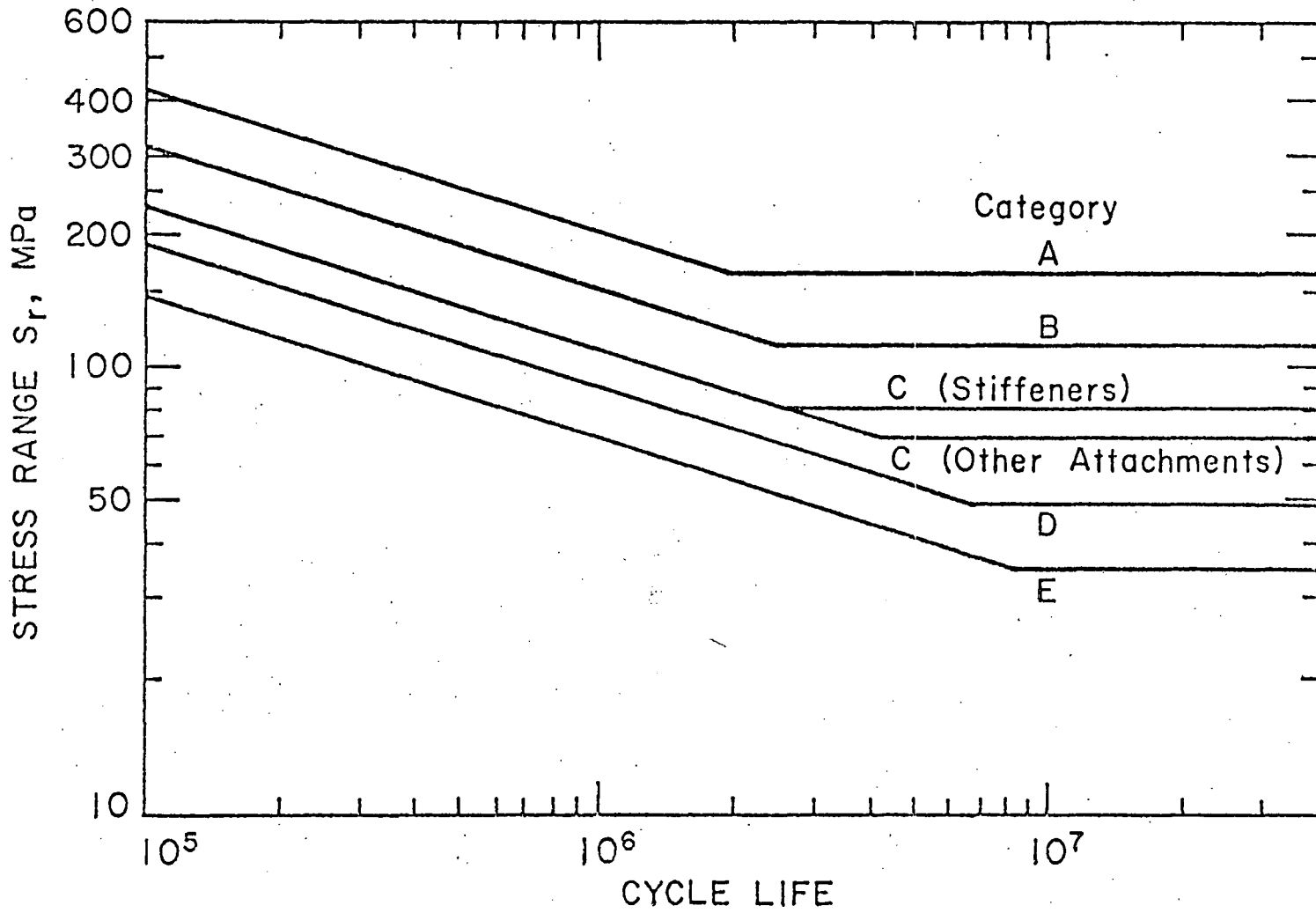
Fig. 1.1 Design Stress Range Curves for Detail Categories A to E[21]
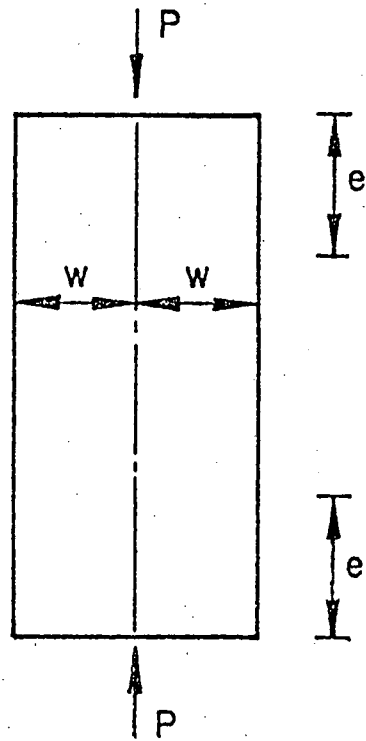
a. Plate Under Concentrated
Loads (84)
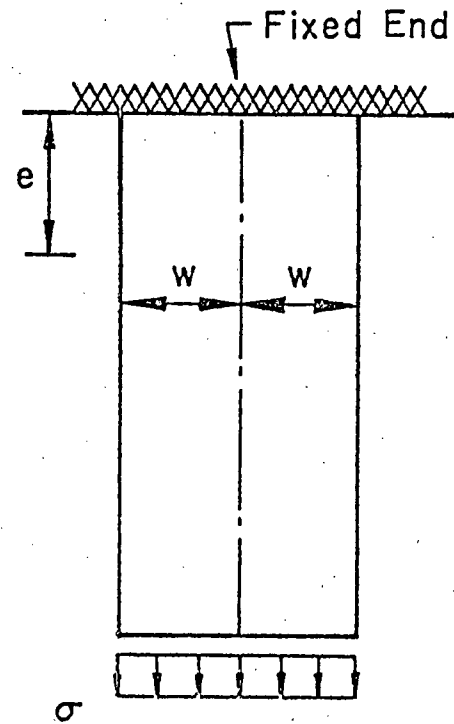
b. Fixed-Ended Plate Under
Uniform Stress

Fig. 2.1 Configureations for Quantifying Saint-Venant's Principle
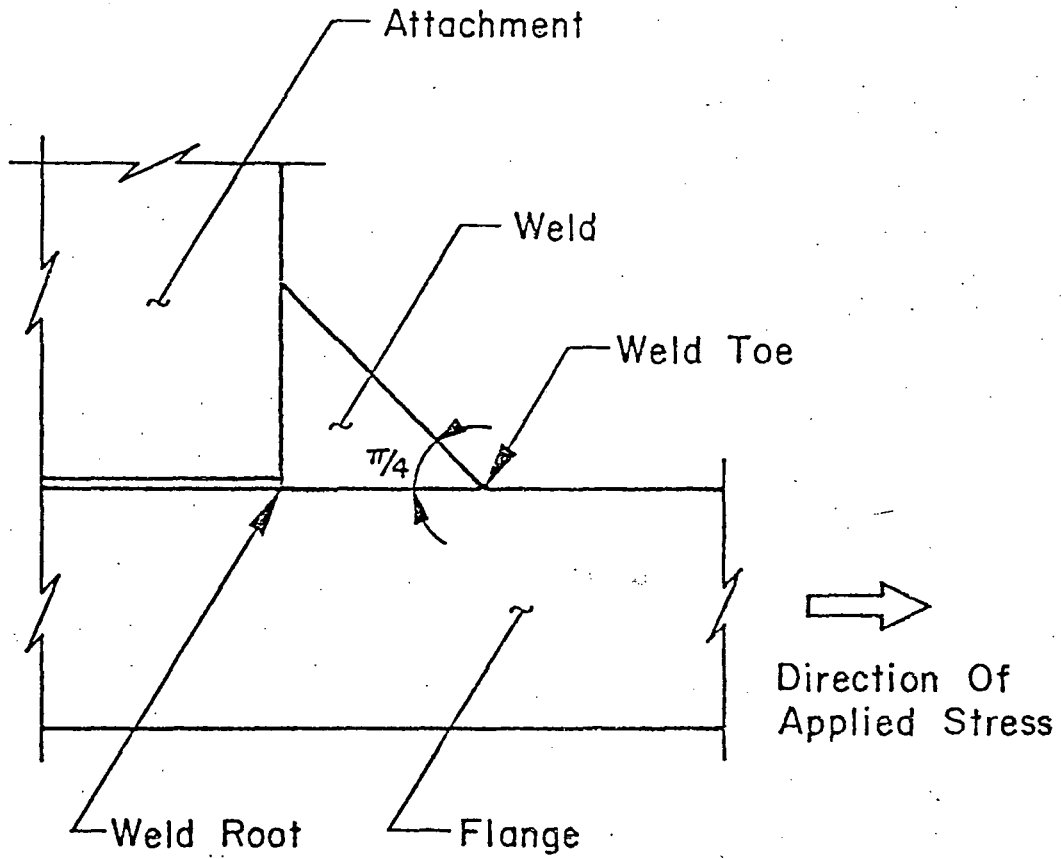
Fig. 2.2   Flange Attachment with Transverse Fillet Weld
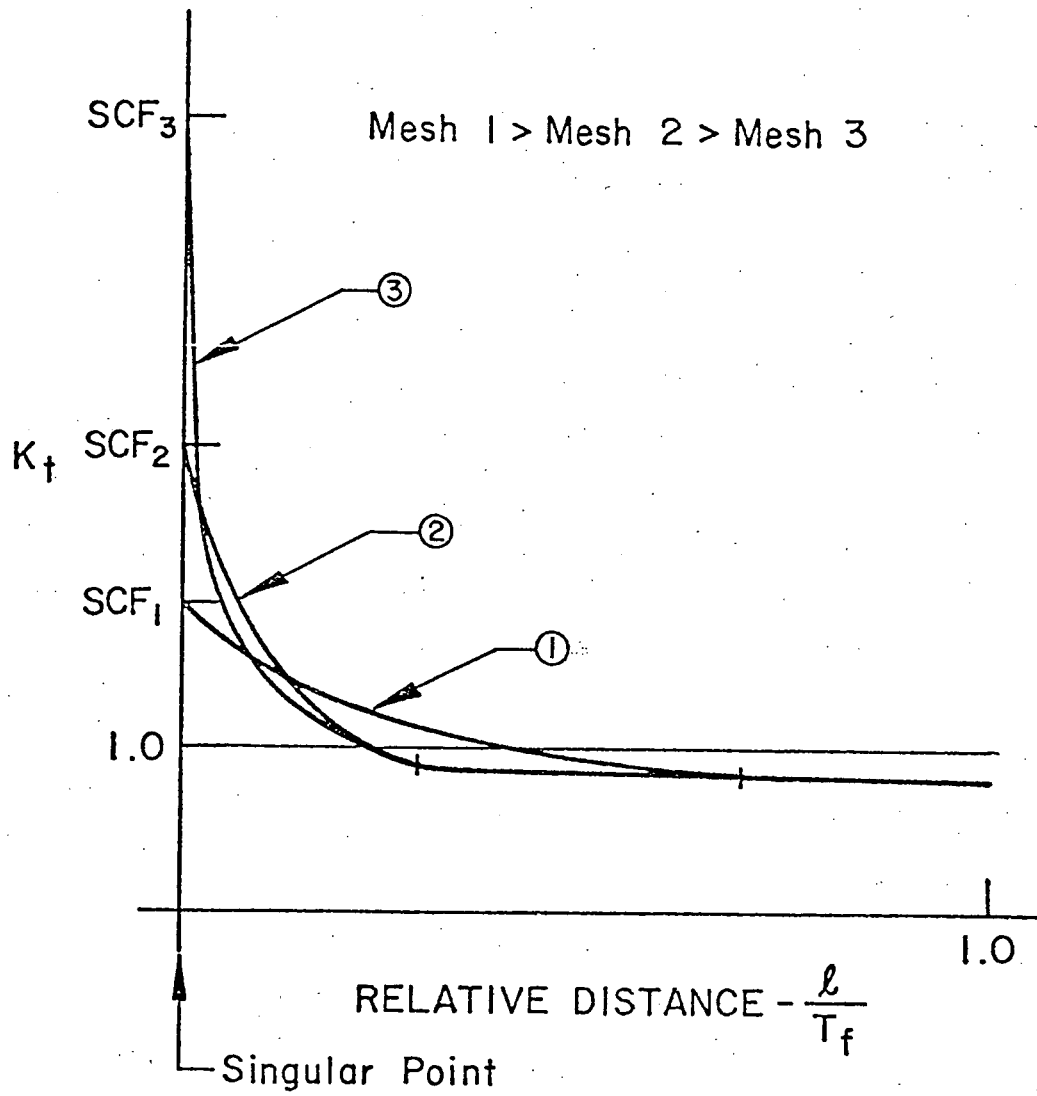
Fig. 2.3 Schematic Variation of Stress Concentration Factor
with Distance through Flange Thickness
for Different Mesh Sizes
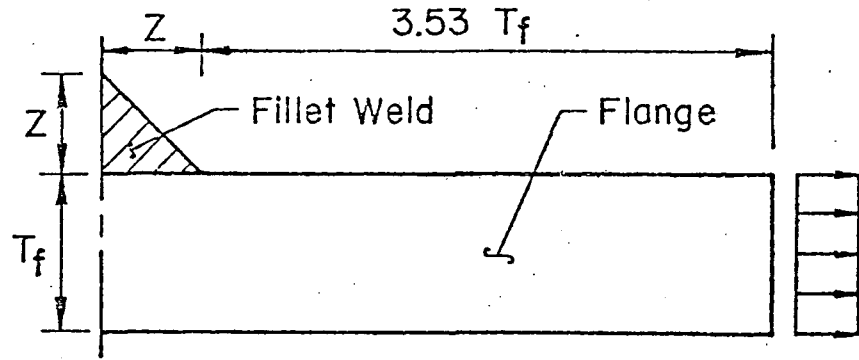
a. Section
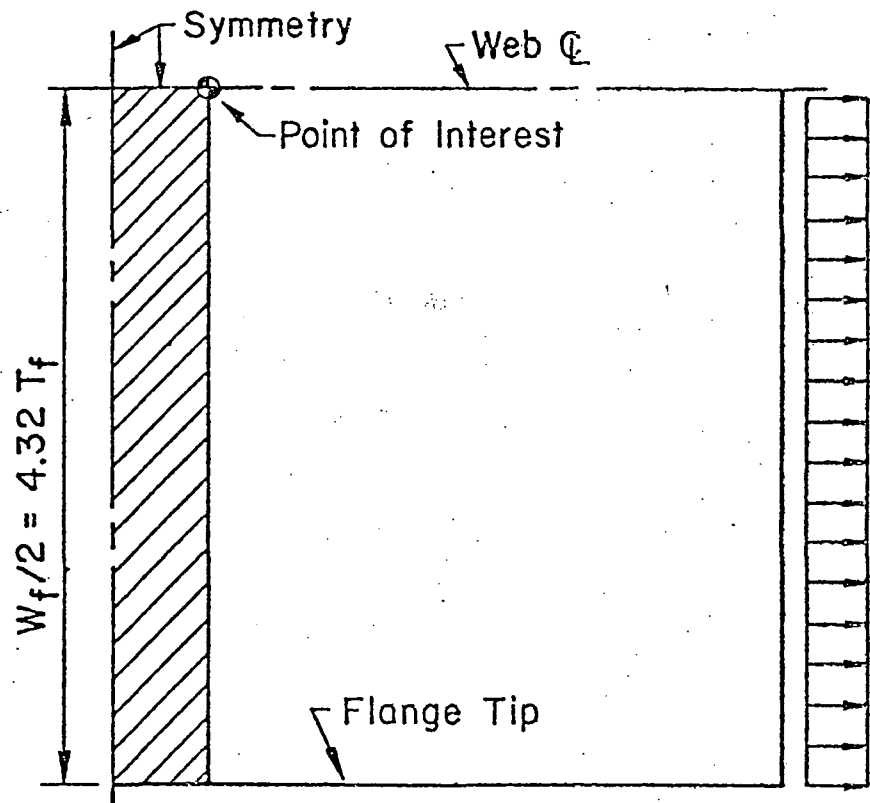
b. Plan View

Fig. 2.4   Detail Geometry for Transverse
Stiffener Investigation

-213-

```
          ※
          │
          │  Uniform
          │  Stress
          ▼
┌───────────────────────┐
│    3D Coarse Mesh      │
└───────────────────────┘
          │
          │  Node
          │  Displacements
          ▼
┌───────────────────────┐
│     2D Fine Mesh       │
└───────────────────────┘
          │
          │  Node
          │  Displacements
          ▼
┌───────────────────────┐
│   2D Ultra Fine Mesh   │
└───────────────────────┘
          │
          │  Element
          │  Stress
          ▼  Concentrations
┌───────────────────────┐
│     Extrapolation      │
└───────────────────────┘
          │
          │
          ▼
        ╭─────╮
        │ SCF │
        ╰─────╯
```
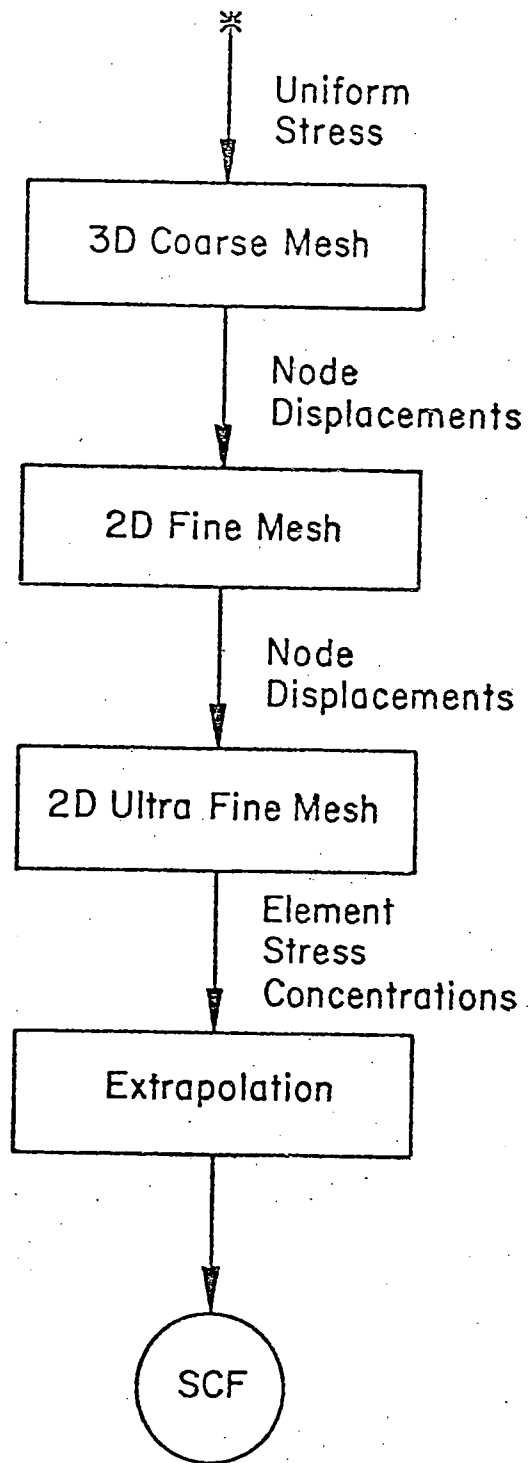
Fig. 2.5 Stress Concentration Analysis Procedure
for Stiffeners and Cover Plates

6 @ 0.3205 T_f 4 @ 0.6410 T_f

3 @ 0.3205 T_f

0.1795 T_f

0.8205 T_f

a. Section

Point Of Interest

6 @ 0.6410 T_f

0.4744 T_f
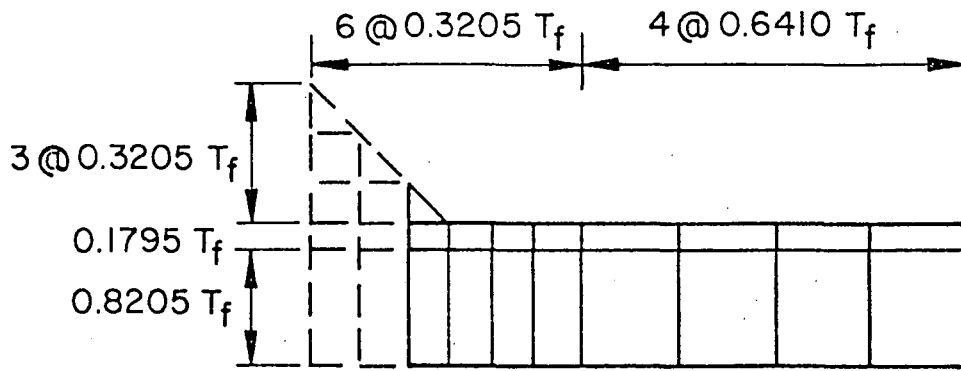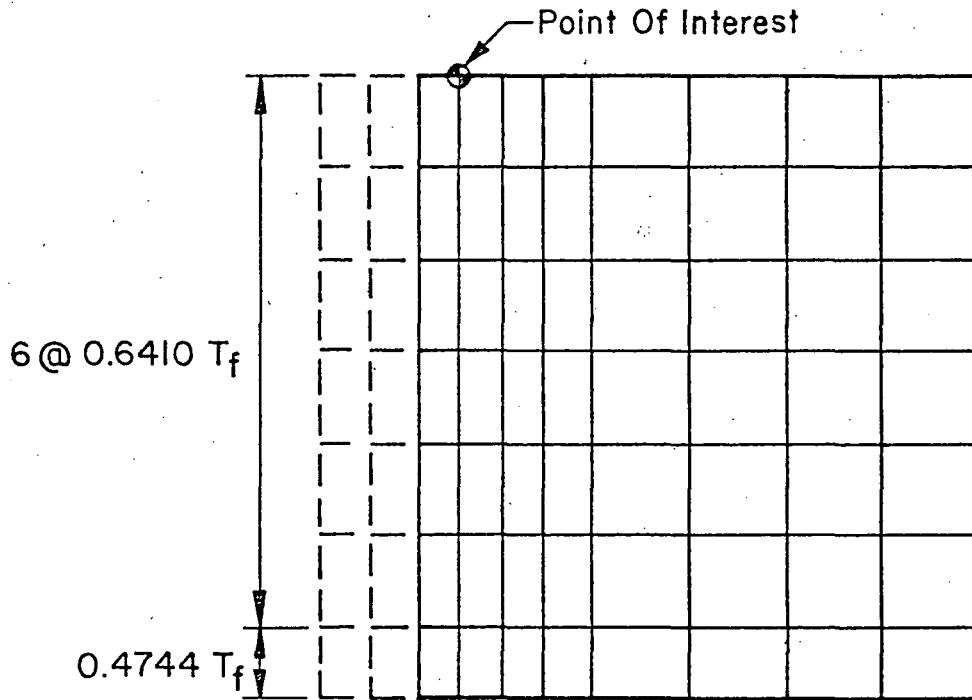
b. Plan View

Fig. 2.6 Coarse Mesh for Transverse Stiffener Investigation
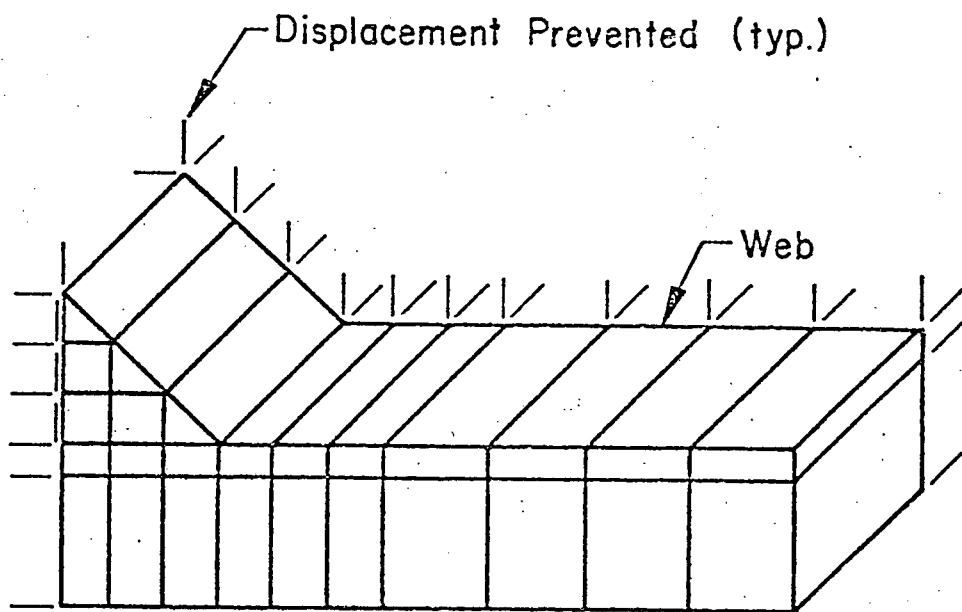
Fig. 2.7 Schematic Isometric of Coarse Mesh Boundary
Conditions for Elements Adjacent to
Web at Transverse Stiffener Detail

0.3205 T_f 0.3205 T_f

4 @ 0.0513 T_f

0.3205 T_f

3 @ 0.0256 T_f

7 @ 0.0128 T_f

5 @ 0.0256 T_f

0.1795 T_f

6 @ 0.0513 T_f

0.8205 T_f

5 @ 0.1026 T_f

6 @ 0.0128 T_f

4 @ 0.0513 T_f 3 @ 0.0513 T_f

3 @ 0.0256 T_f 5 @ 0.0256 T_f
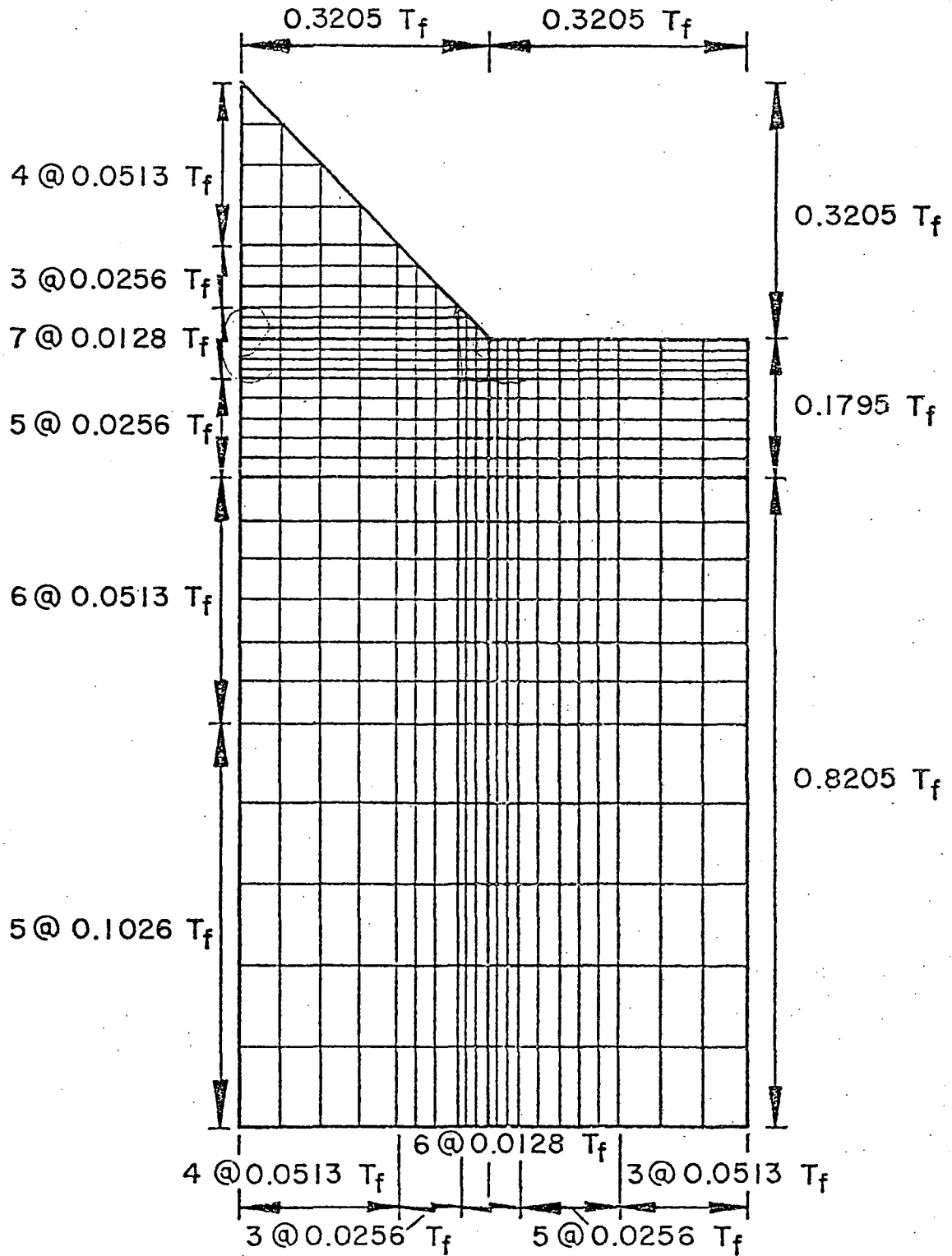
Fig. 2.8 Fine Mesh for Stiffener and Cover Plate Investigations

-217-
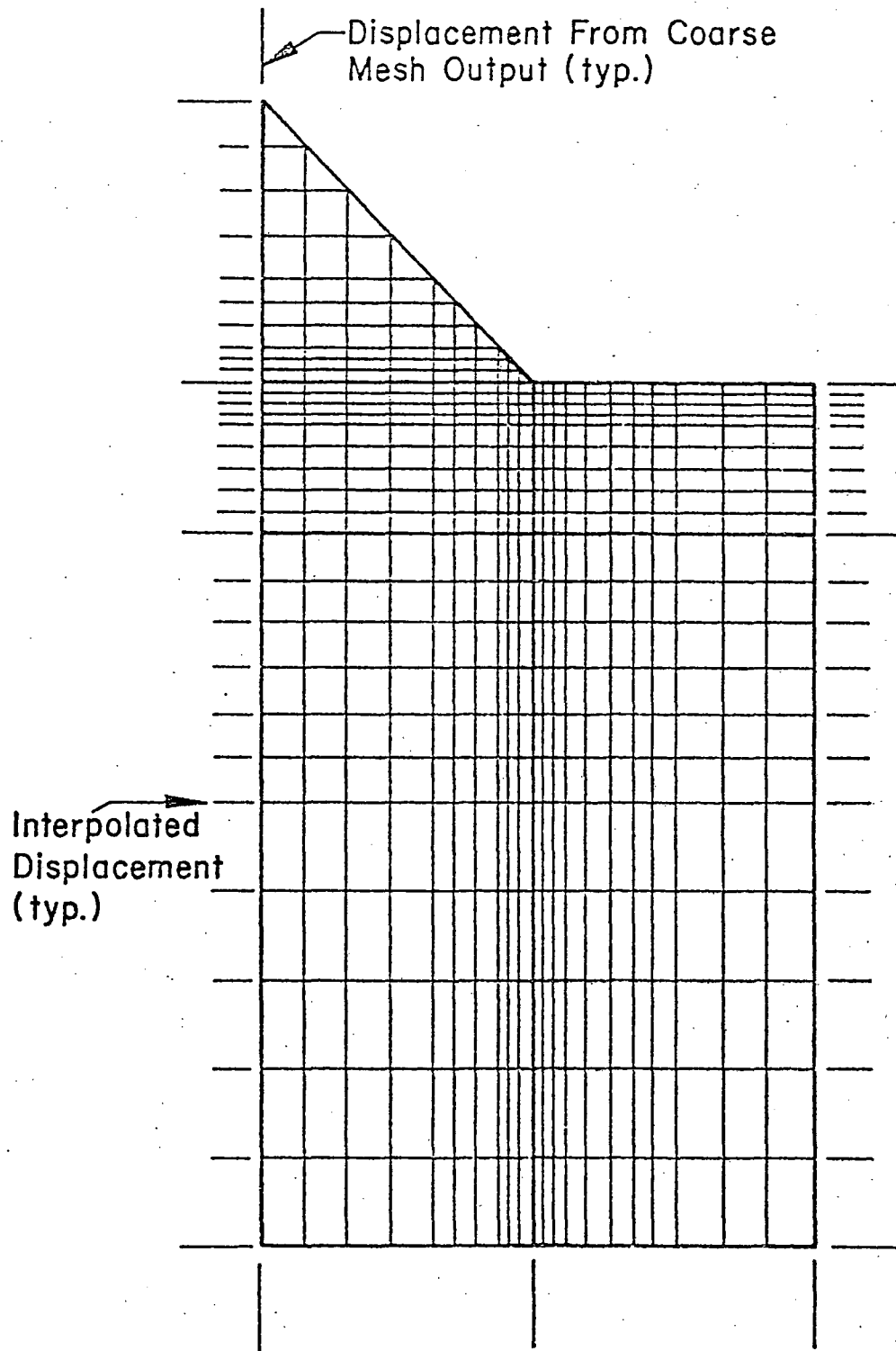
Fig. 2.9 Displacement Input to Fine Mesh from Coarse Mesh Output
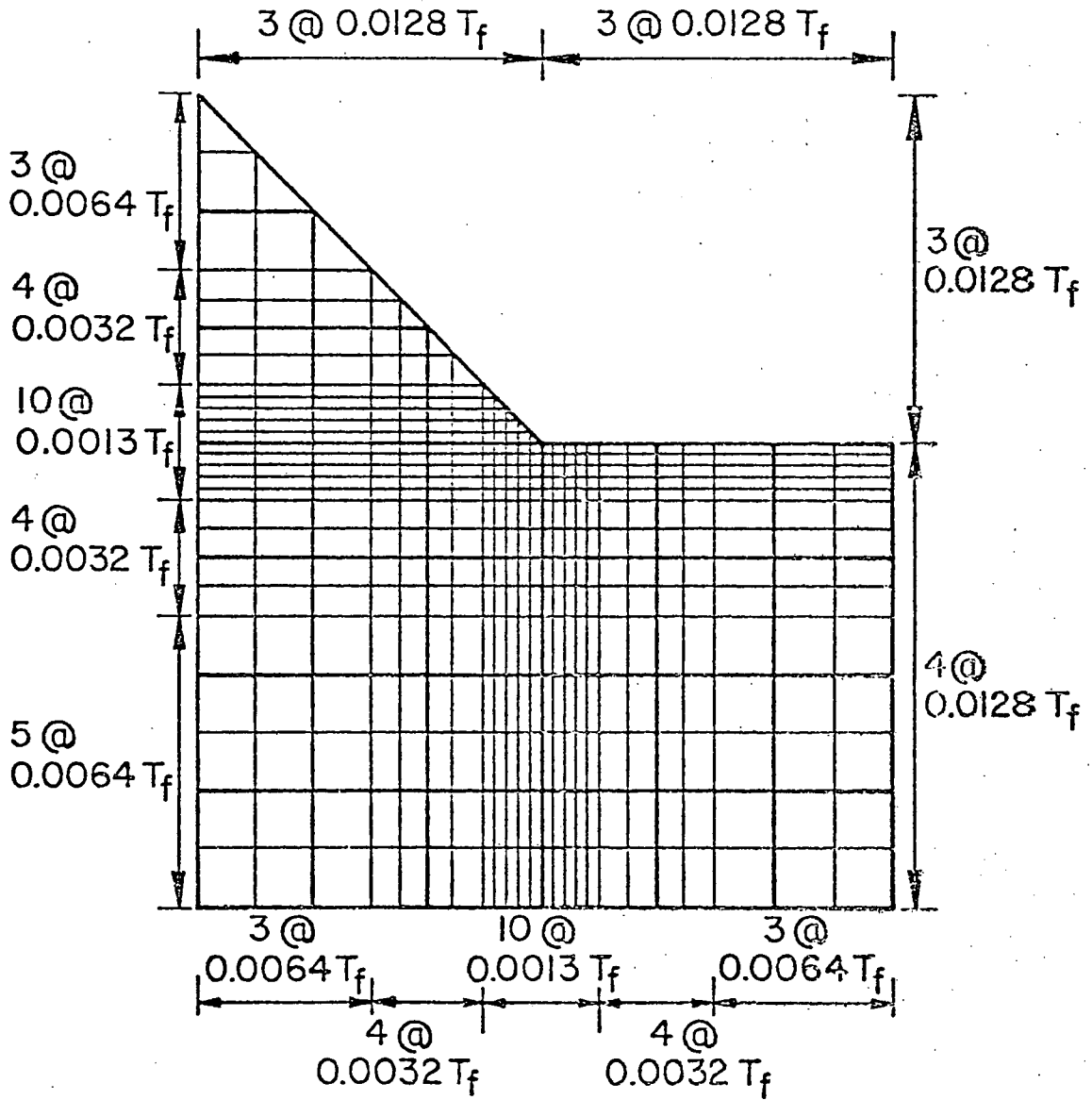
Fig. 2.10 Ultra Fine Mesh for Stiffener
and Cover Plate Investigations
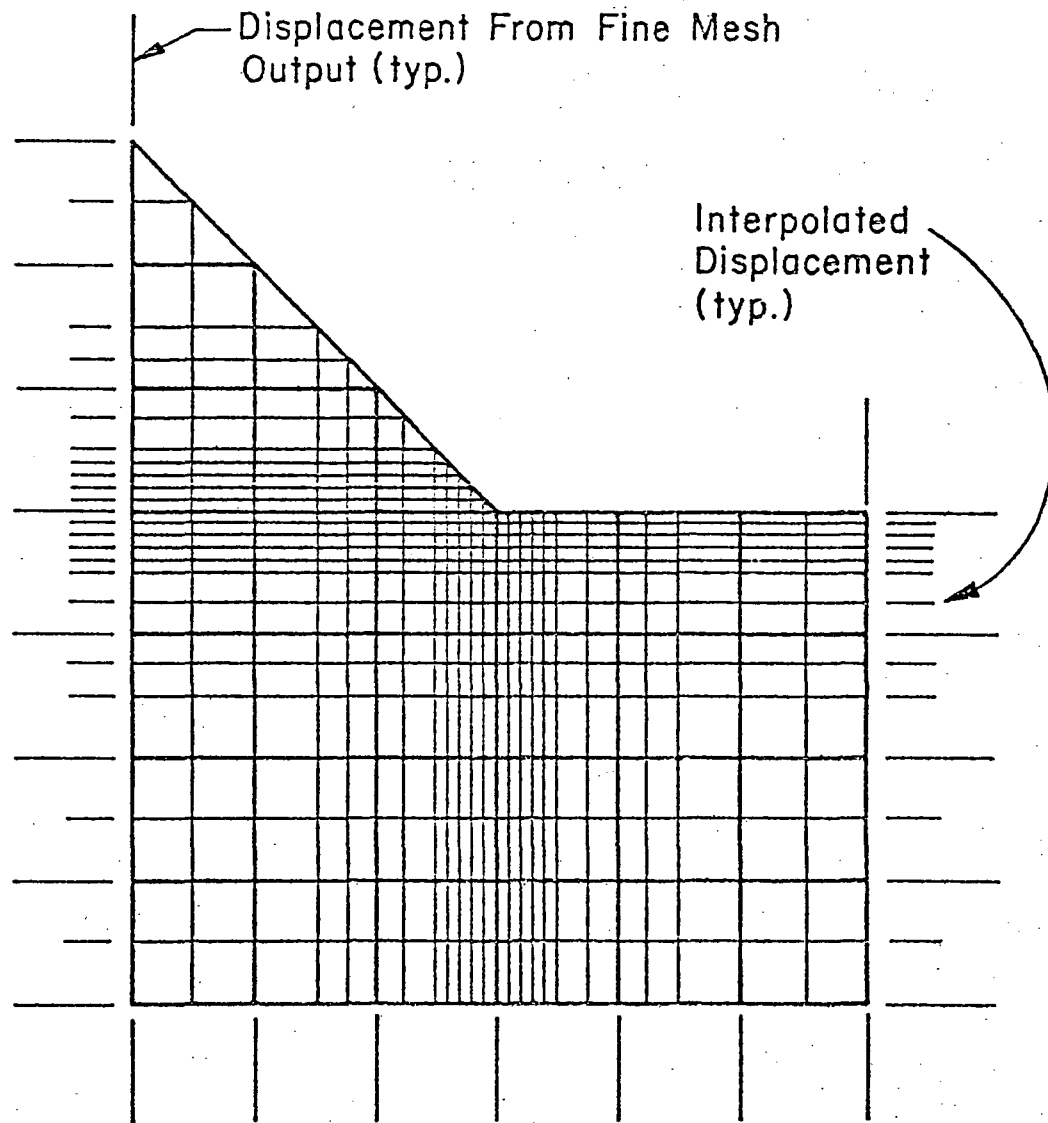
Fig. 2.11   Displacement Input to Ultra Fine Mesh
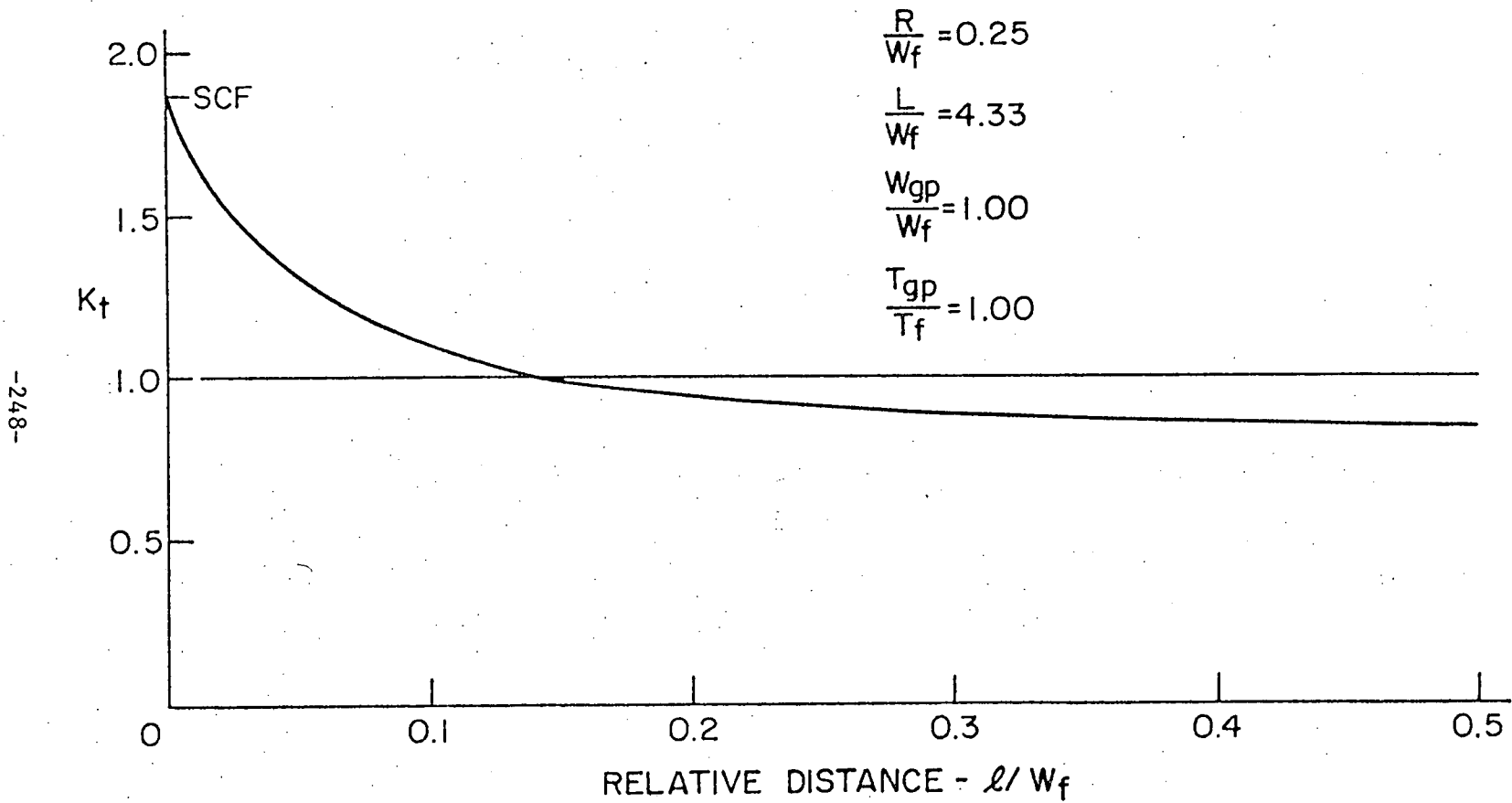from Fine Mesh Output
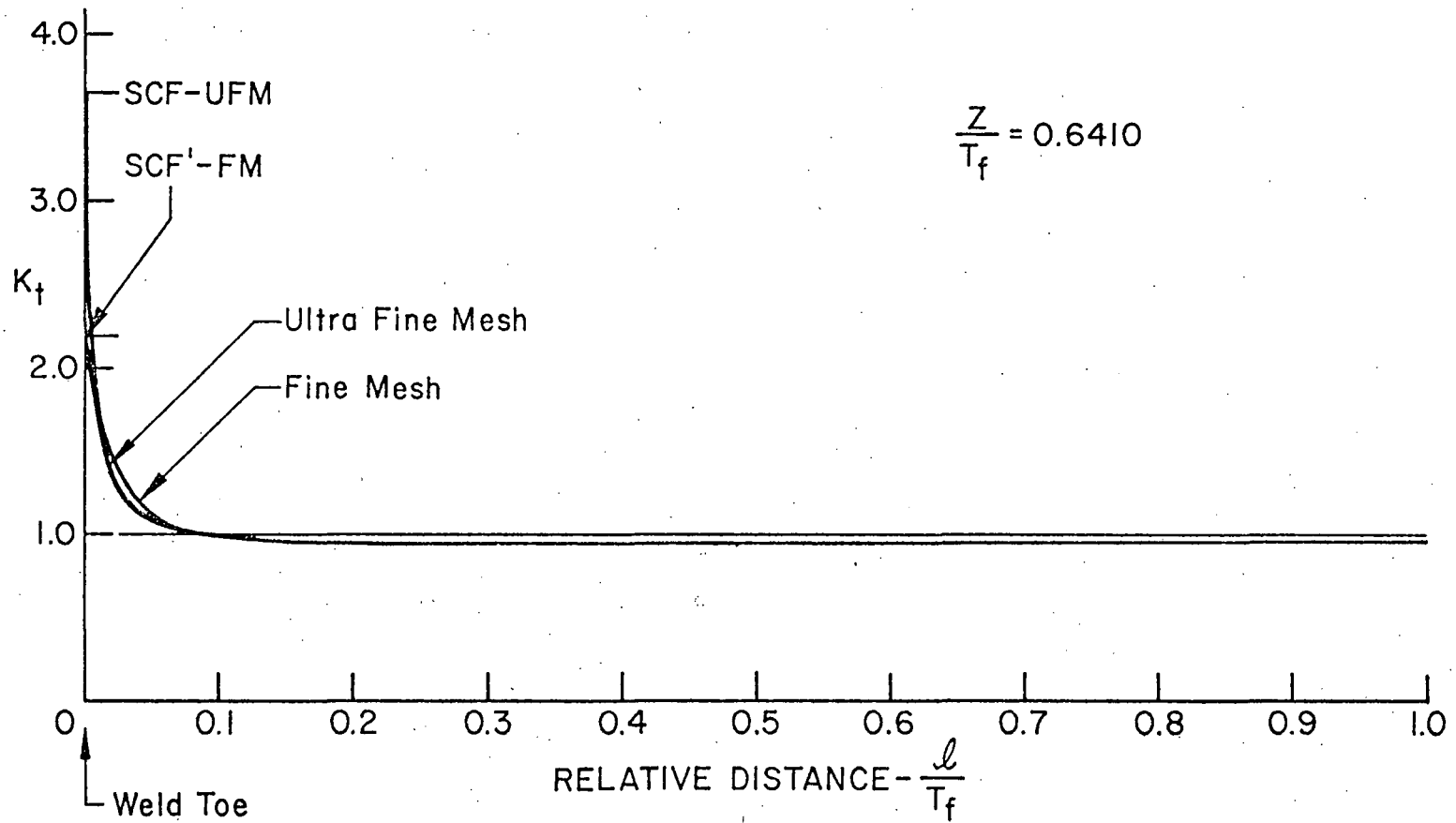
Fig. 2.12   Stress Concentration Factor Variation along Prospective Crack Path
through Flange Thickness at Sample Stiffener Detail
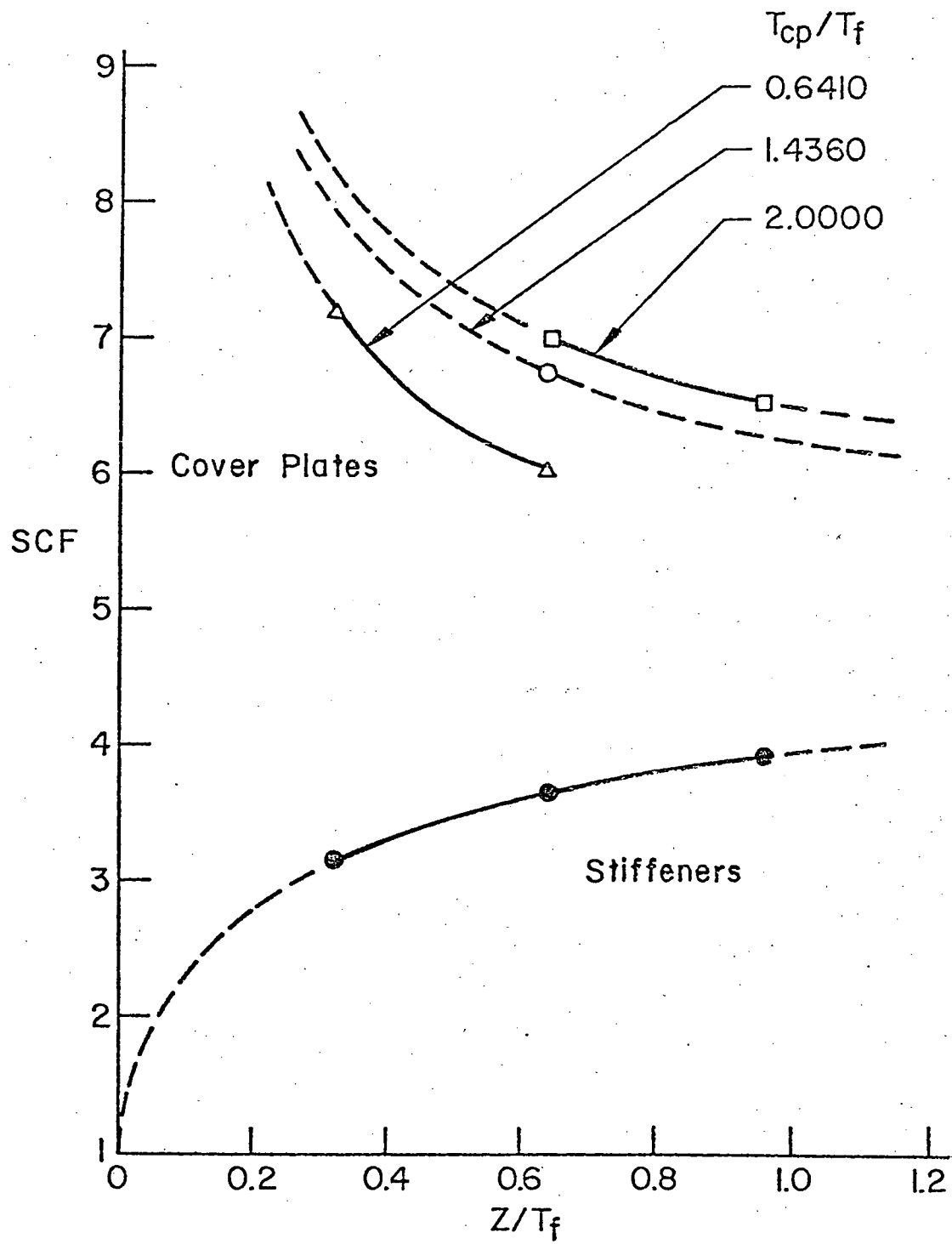
Fig. 2.13 Variation of Maximum Stress Concentration Factor
with Weld Size at Stiffener and Cover Plate Details

-222-
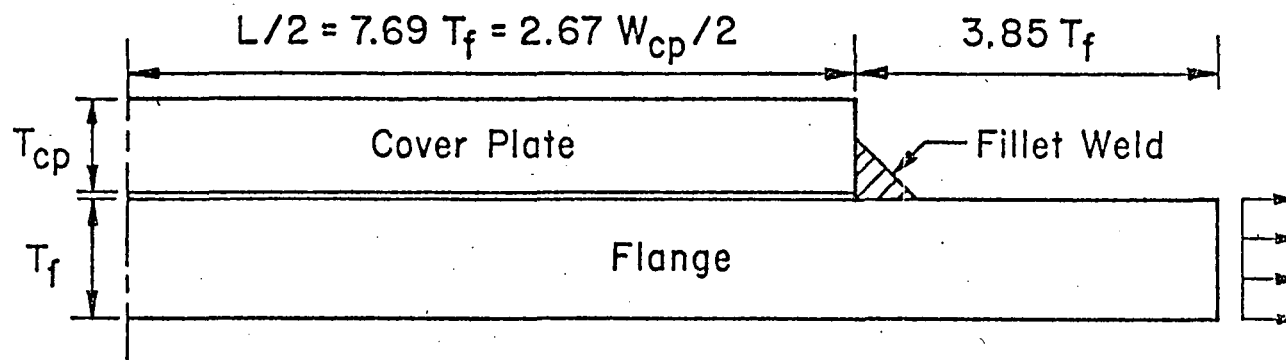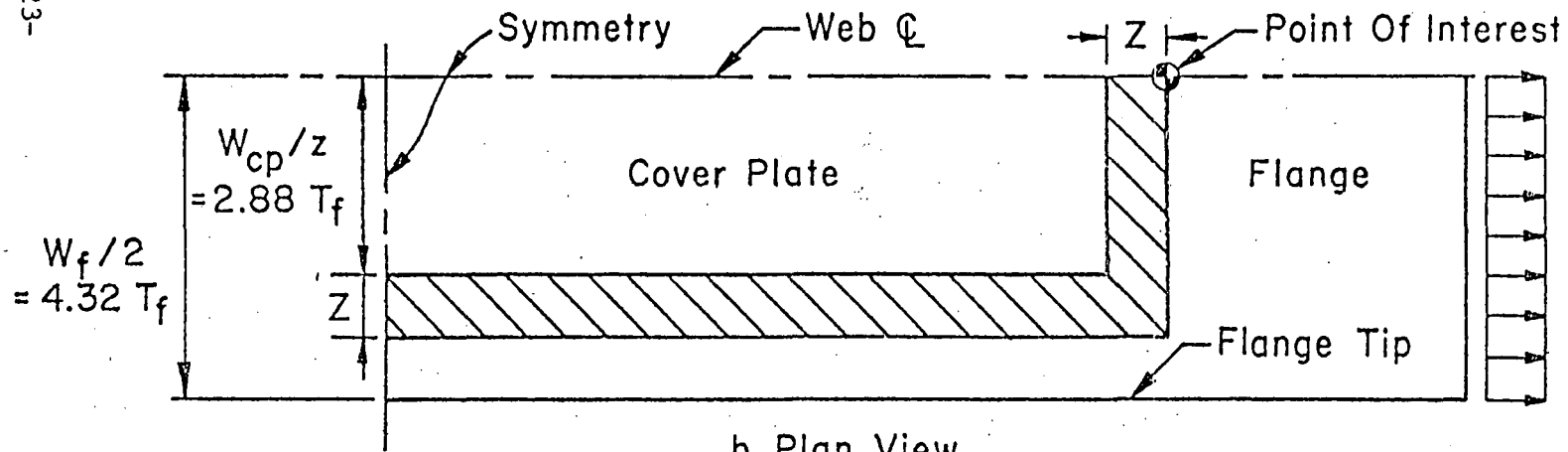
a. Section

b. Plan View

Fig. 2.14 Detail Geometry for Cover Plate Investigation
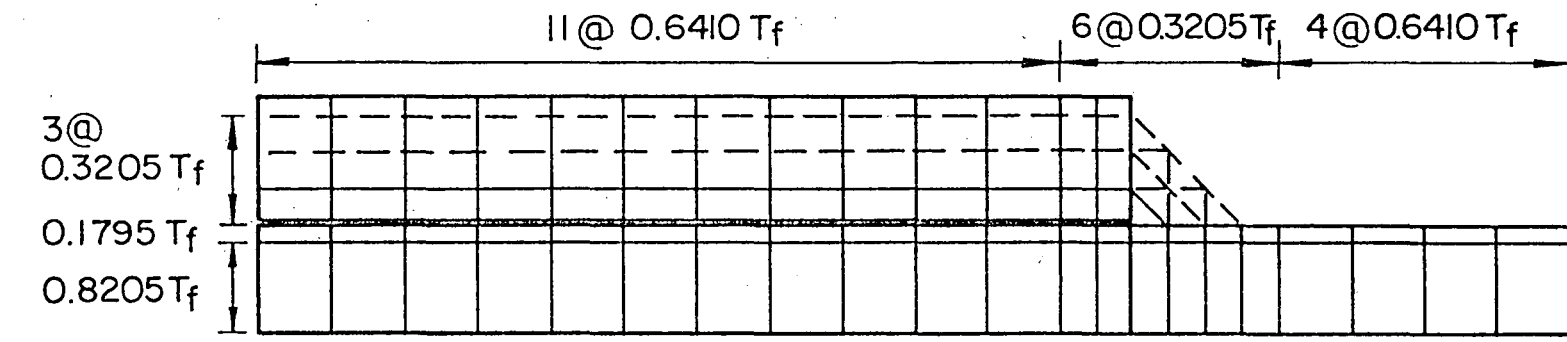
a. Section
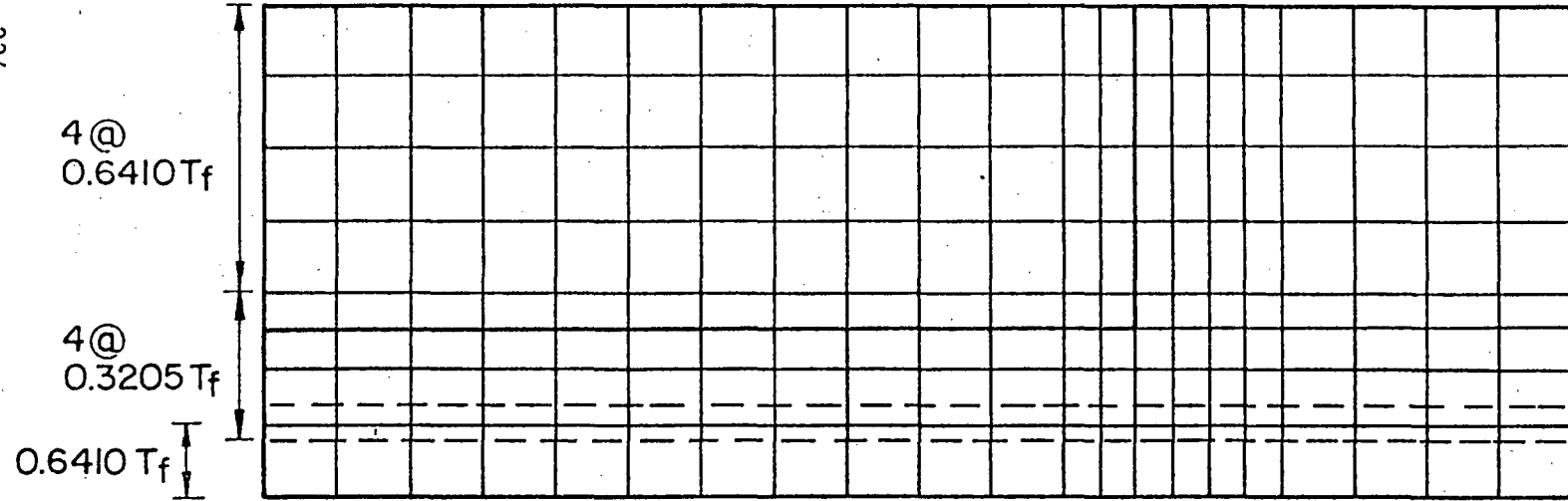
b. Plan View

Fig. 2.15   Coarse Mesh for Cover Plate Investigation
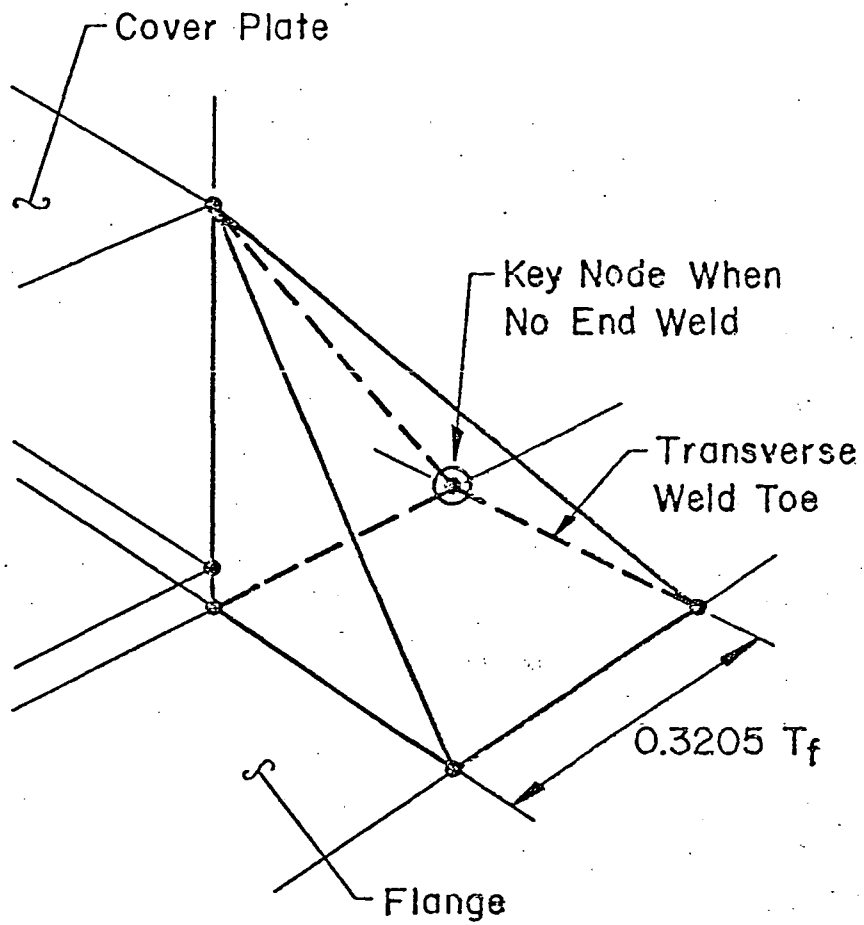
Fig. 2.16 Schematic Isometric of Corner Weld Discretization
for Cover Plate Detail
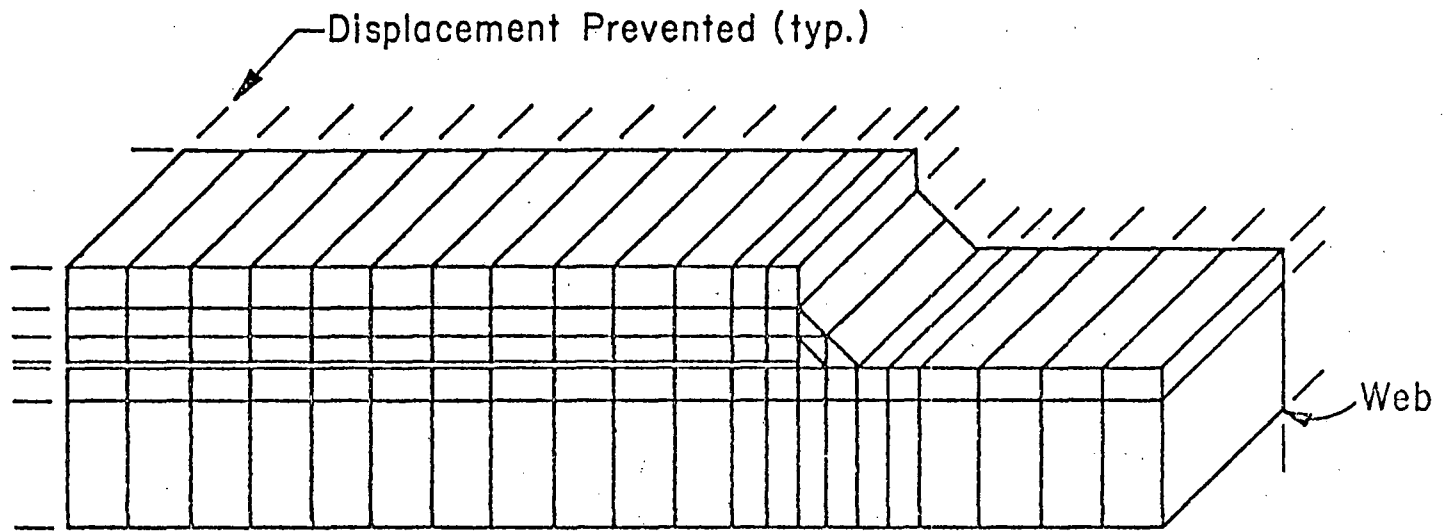
Fig. 2.17   Schematic Isometric of Coarse Mesh Boundary Conditions
for Elements Adjacent to Web of Cover Plate Detail
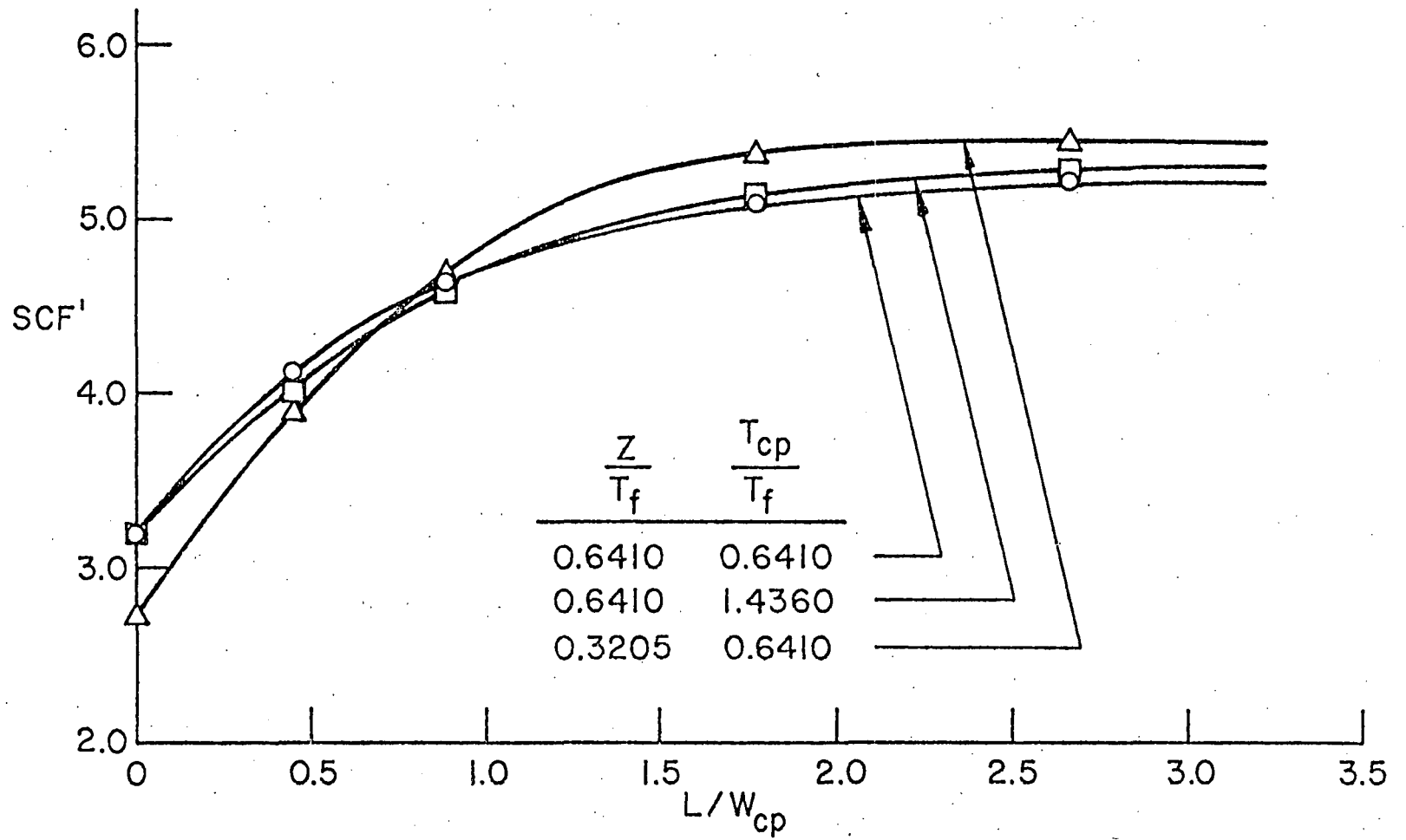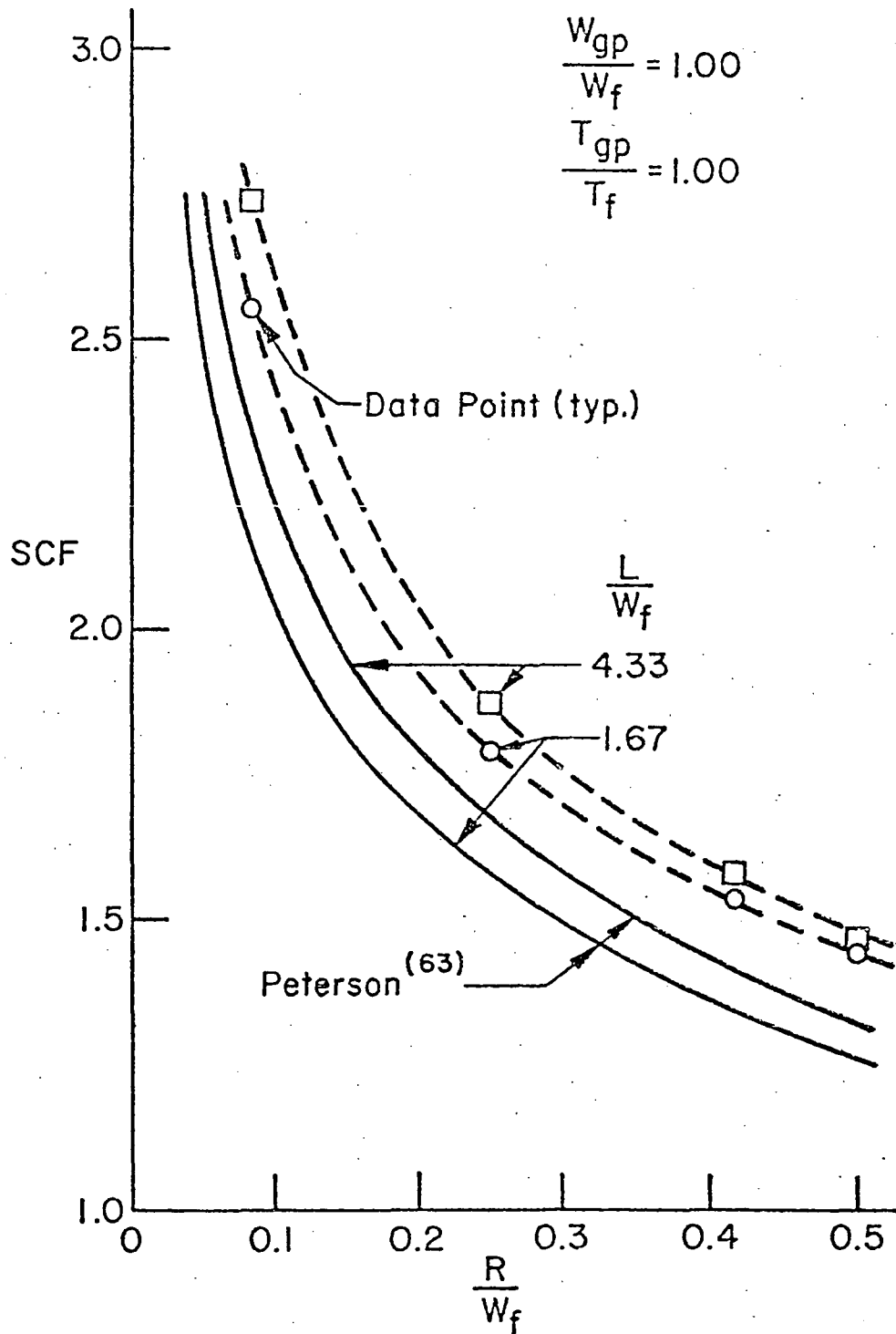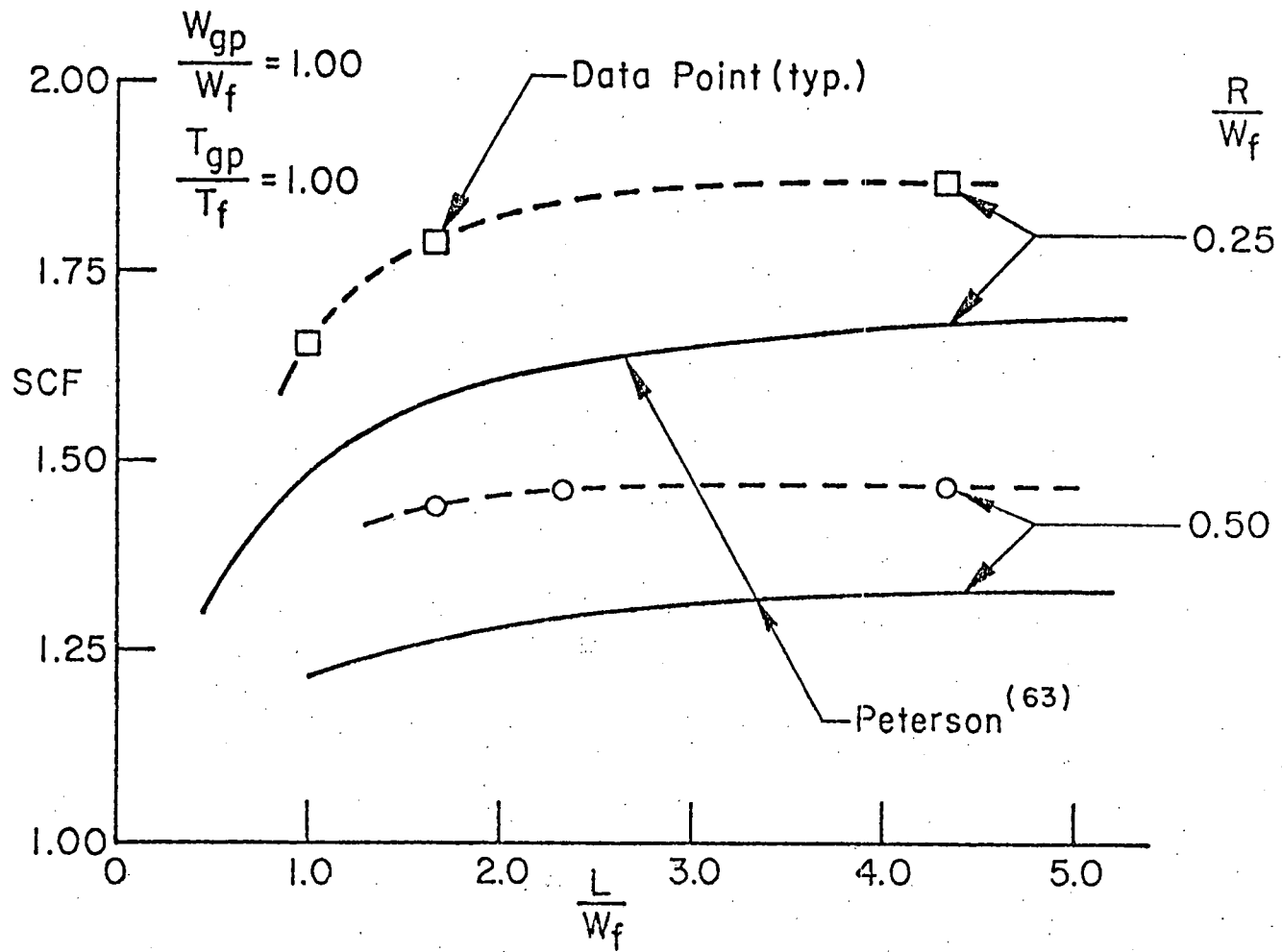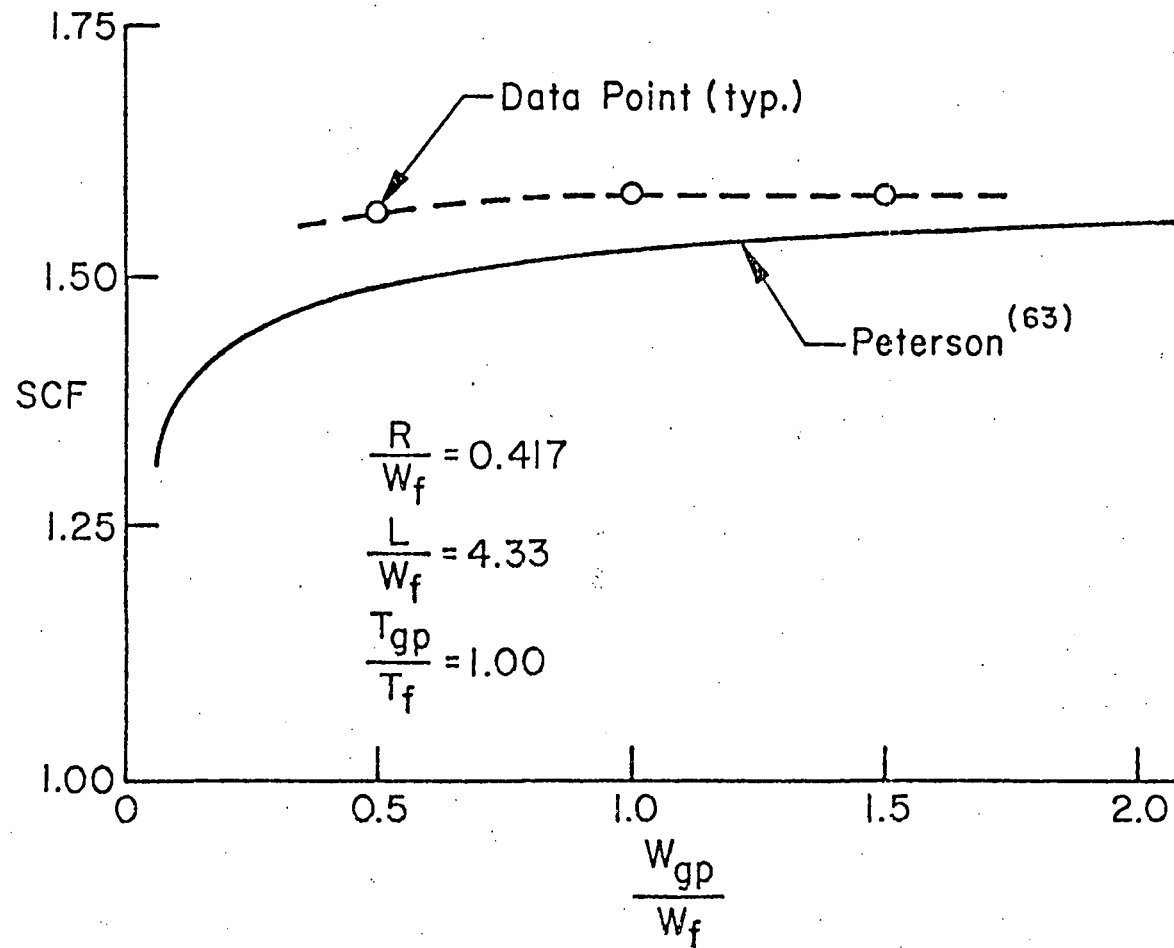
Fig. 2.18 Variation of Maximum Stress Concentration Factor with Cover Plate Length
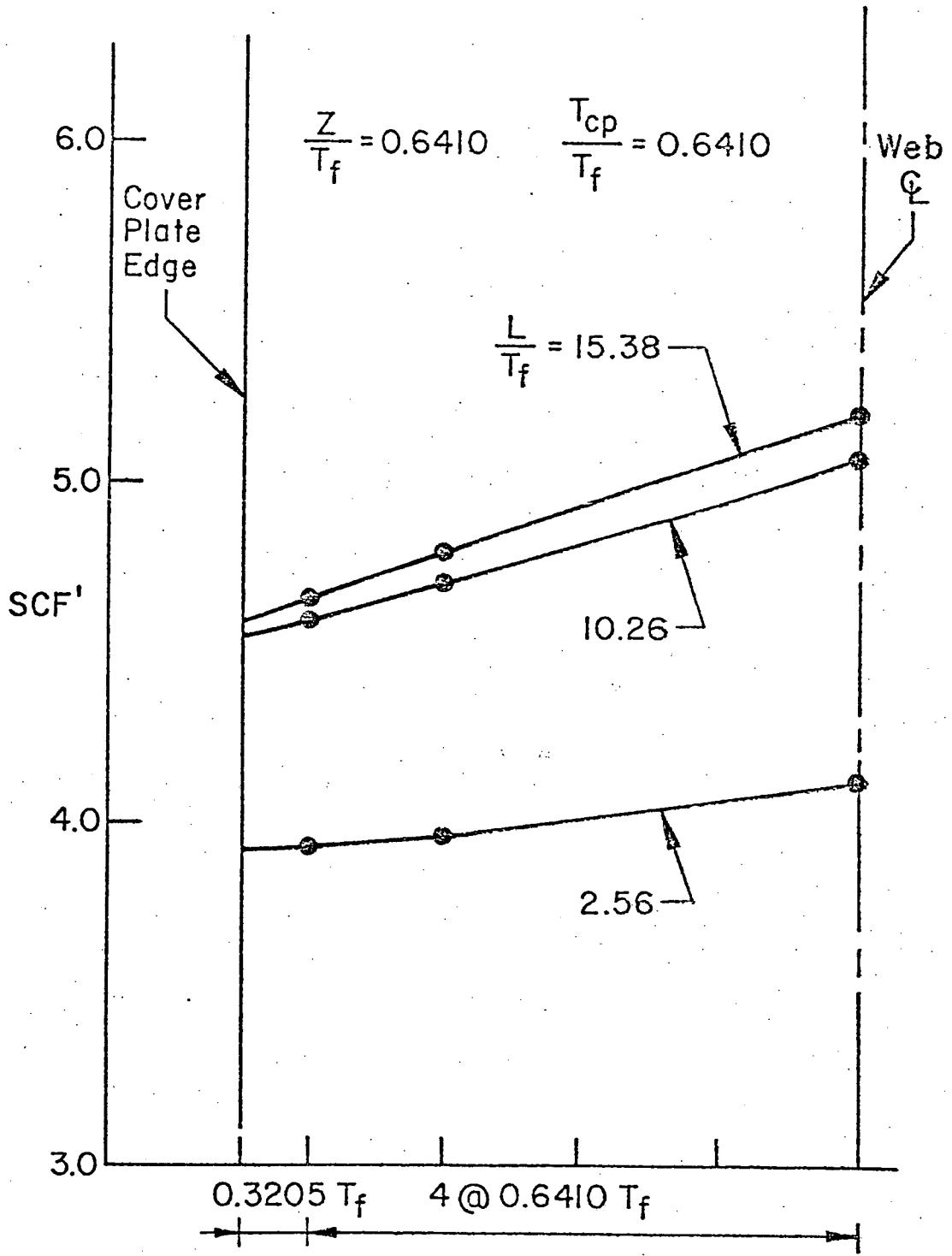
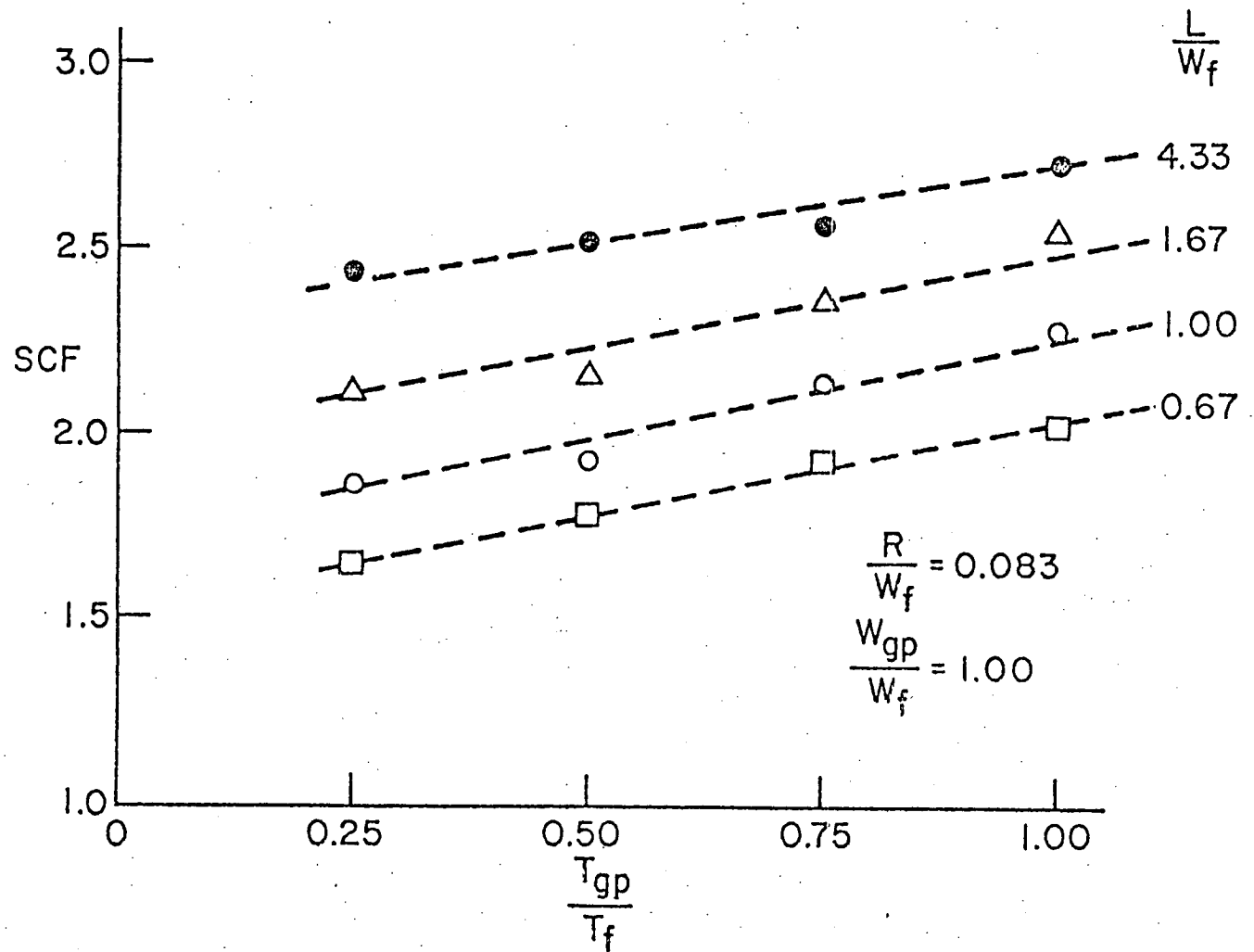Fig. 2.19   Variation of Maximum Stress Concentration Factor along
Transverse Weld Toe of Sample Cover Plate Detail

-228-
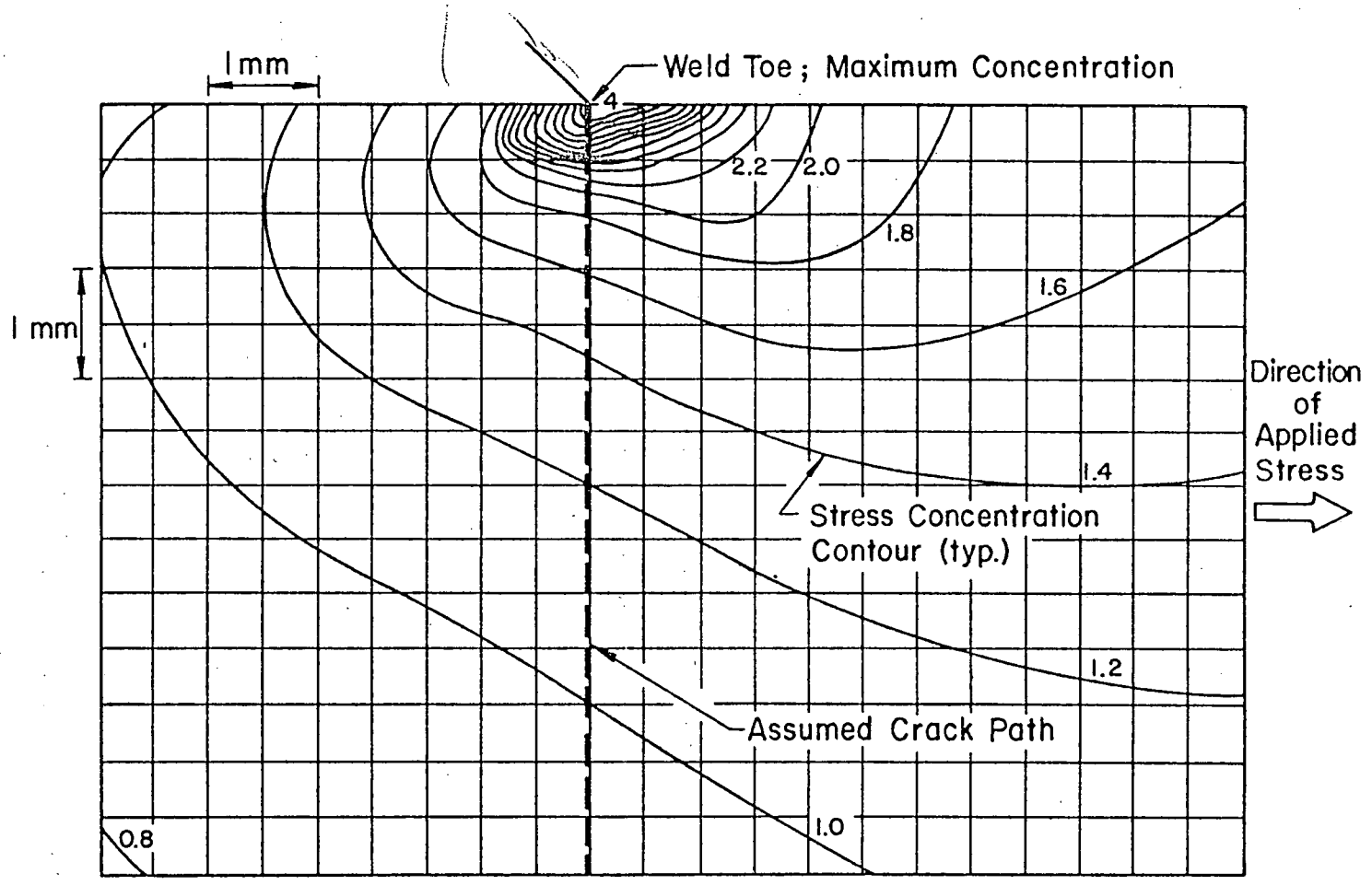
Fig. 2.20   Sample Cover Plate Detail Stress Concentration Factor Contours
for Local Stress in Direction of Applied Stress
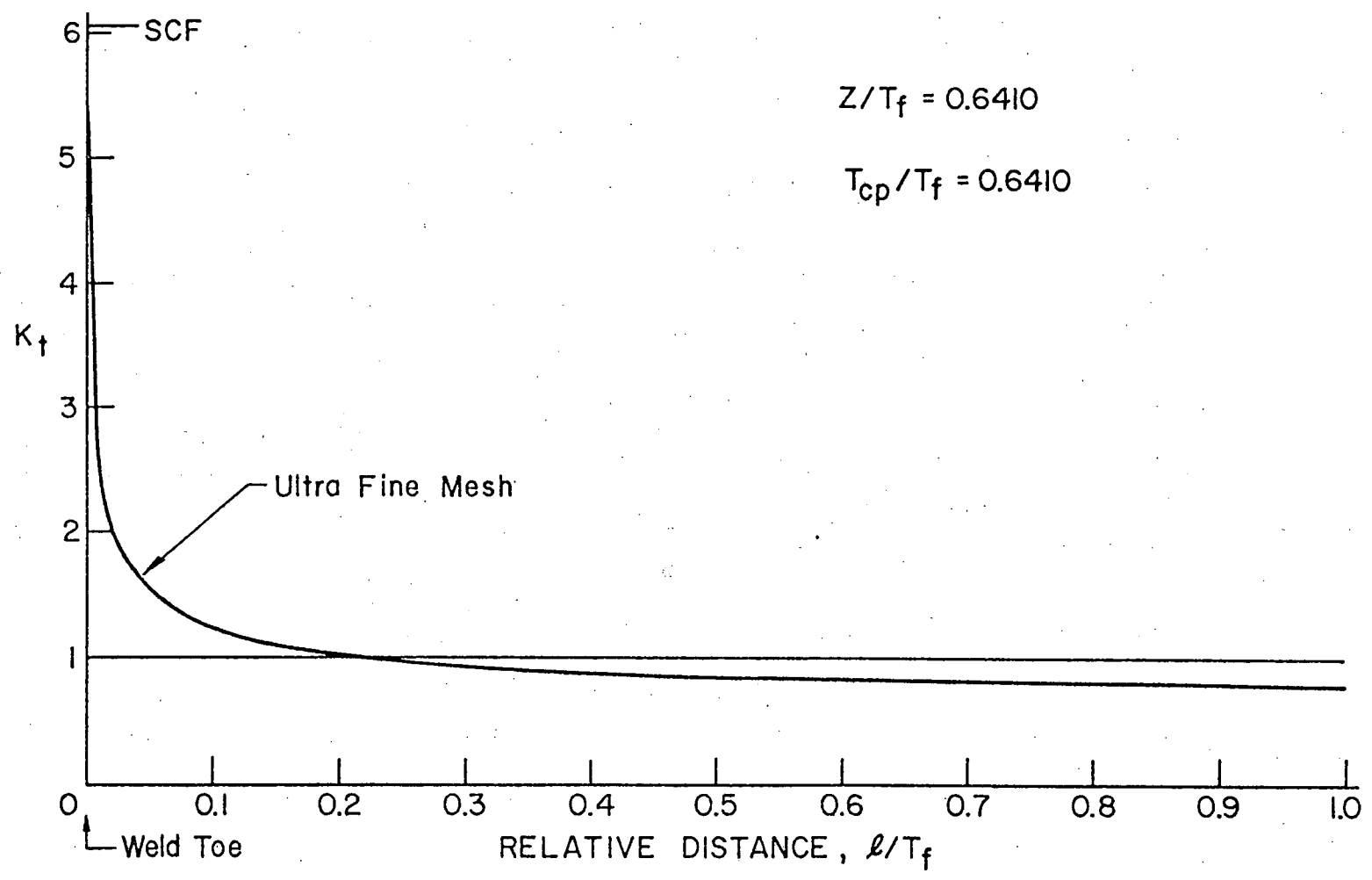
Fig. 2.21   Stress Concentration Factor Variation along Prospective Crack Path
through Flange Thickness at Sample Cover Plate Detail
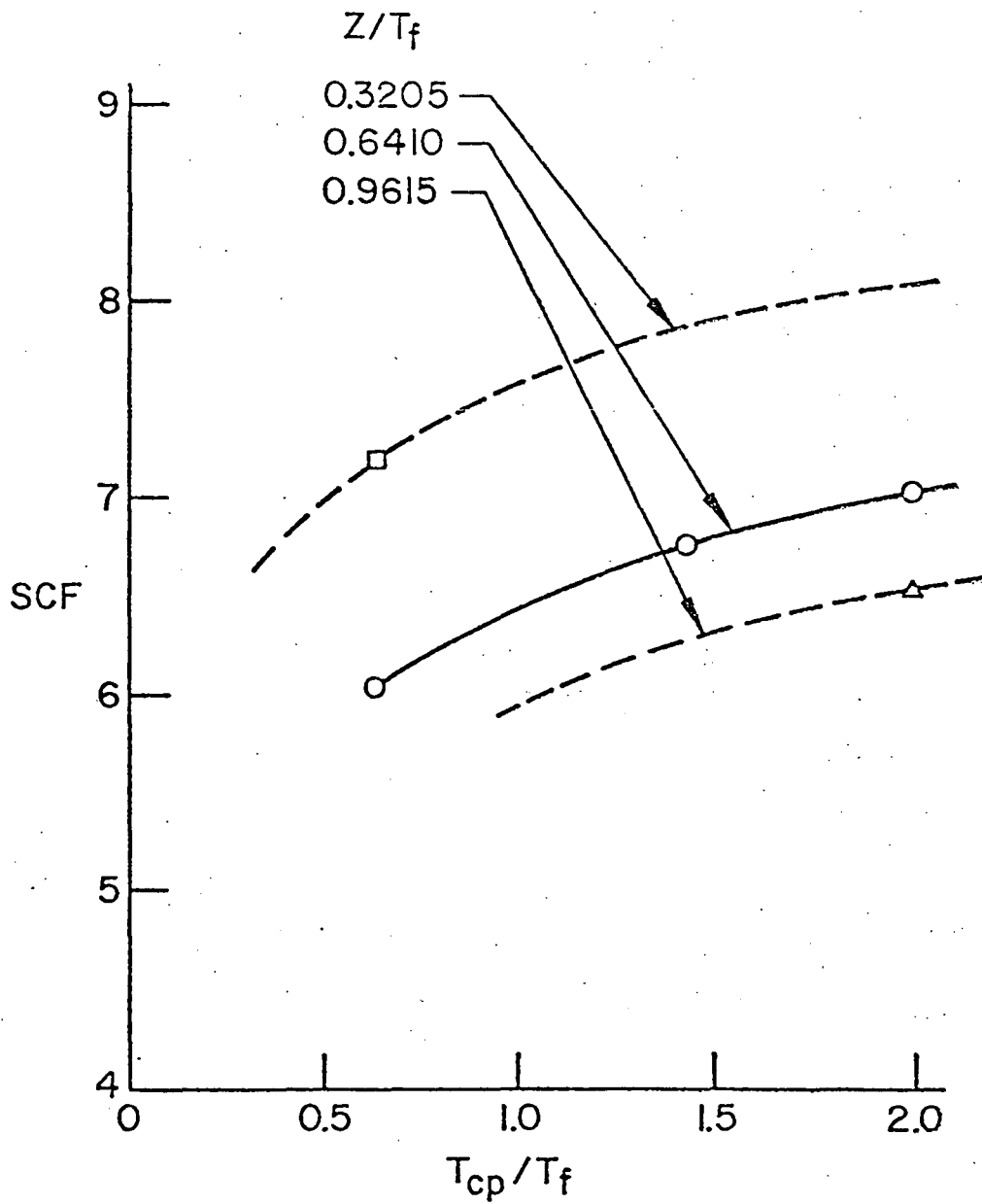
Fig. 2.22   Variation of Maximum Stress Concentration Factor
with Cover Plate Thickness
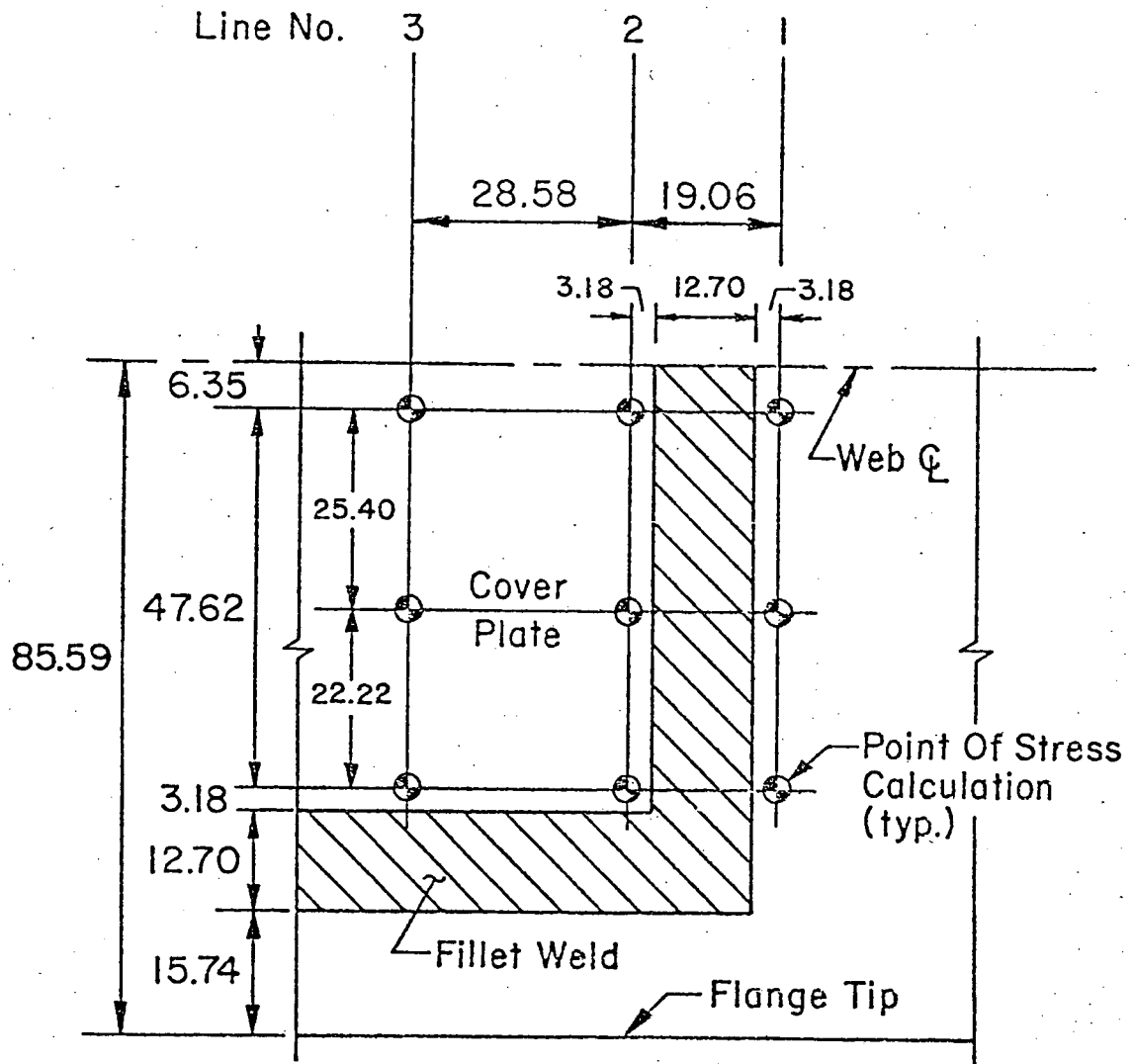
Fig. 2.23   Plan View of Stress Calculation Points
for Sample Cover Plate Detail
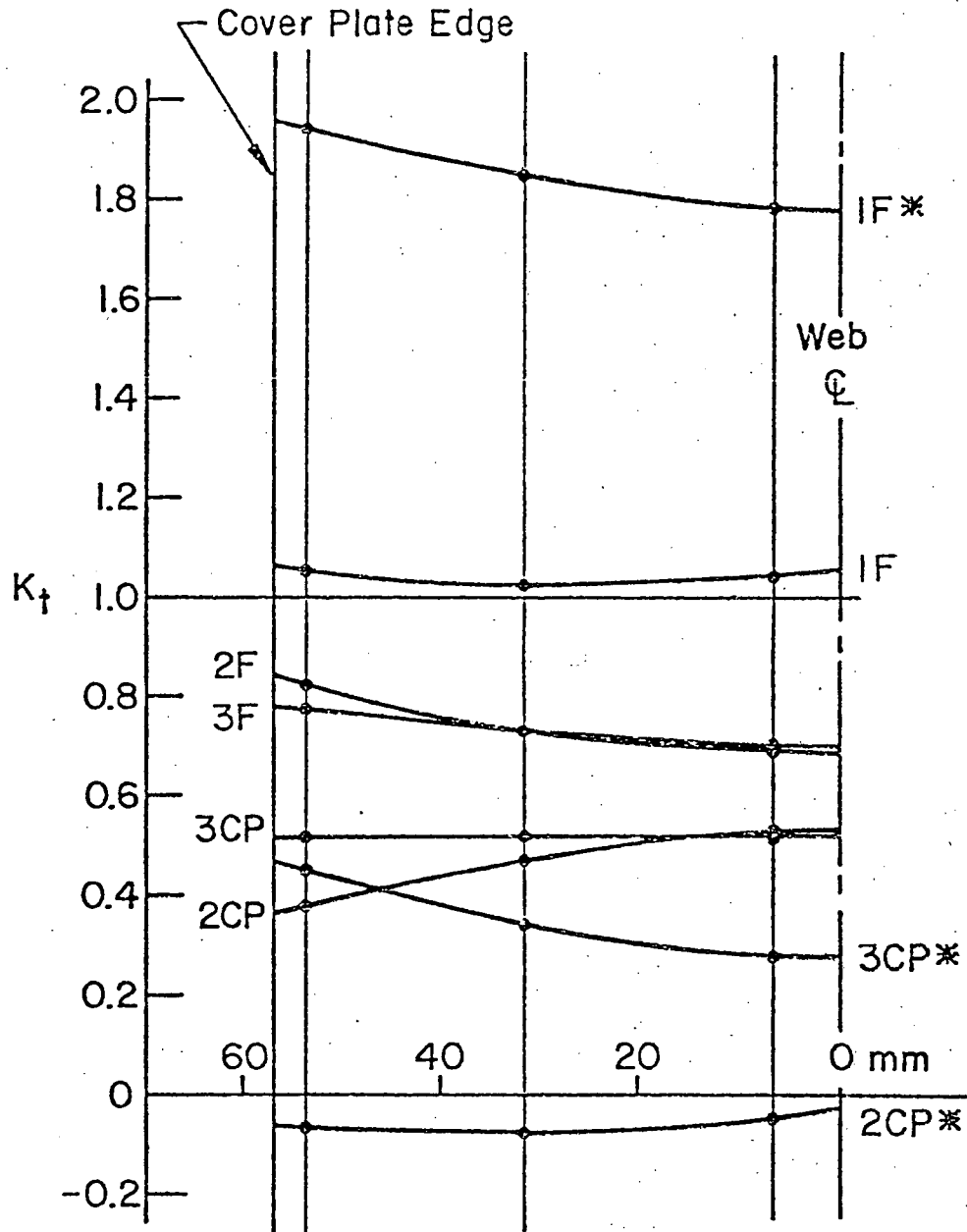
Fig. 2.24   Stress Concentration Factor Distribution
for Various Sections Perpendicular
to Web and near Cover Plate Termination

$$\frac{Z}{T_f} = 0.6410$$

$$\frac{T_{cp}}{T_f} = 1.4360$$

Without End Weld (upper bound)
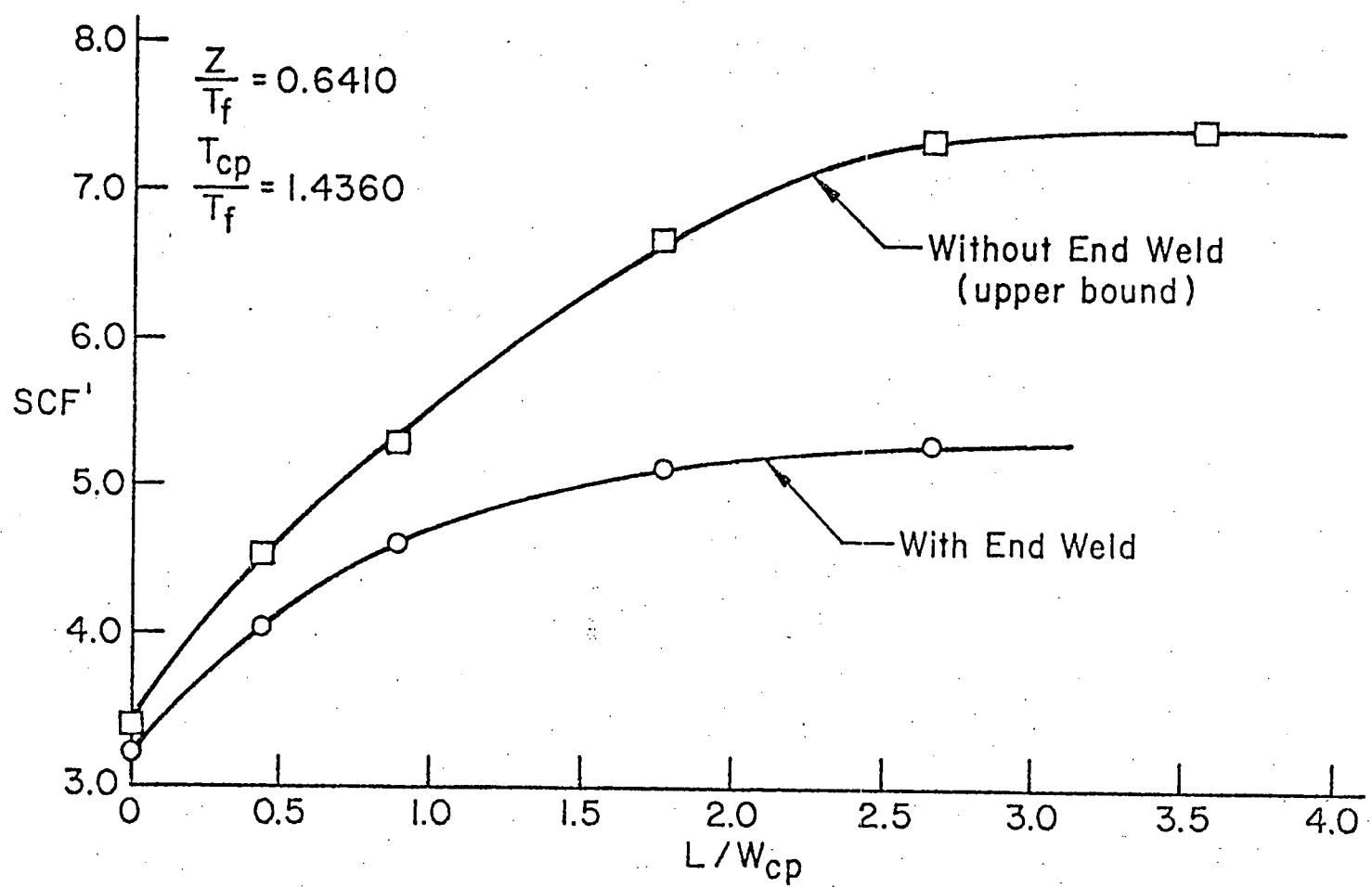
With End Weld

Fig. 2.25 Comparison of Maximum Stress Concentration Factors for Sample Cover Plate Detail With and Without Transverse End Weld
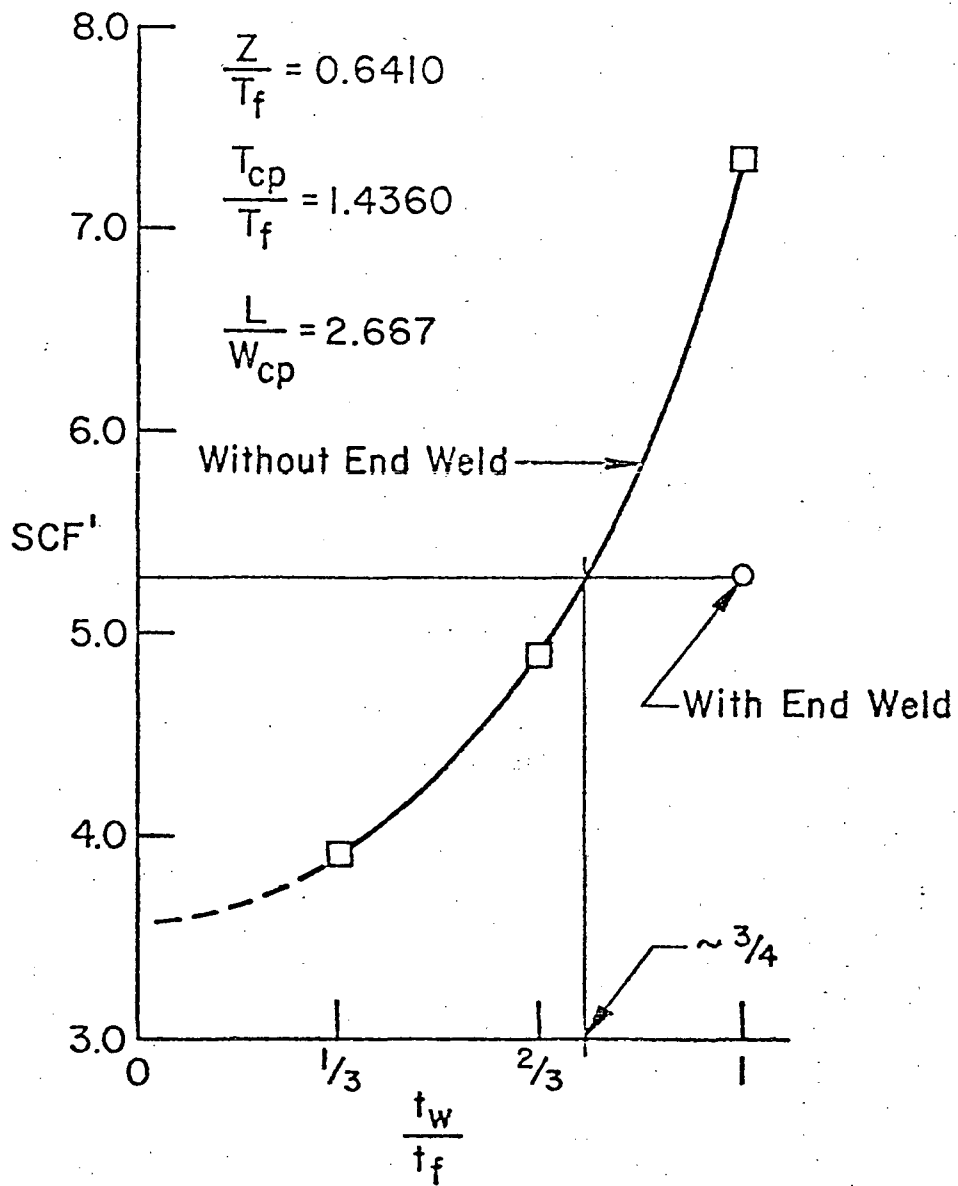
Fig. 2.26 Variation of Maximum Stress Concentration Factor
with Assumed Thickness Ratio of Planar Elements
in Weld to Planar Elements in Flange
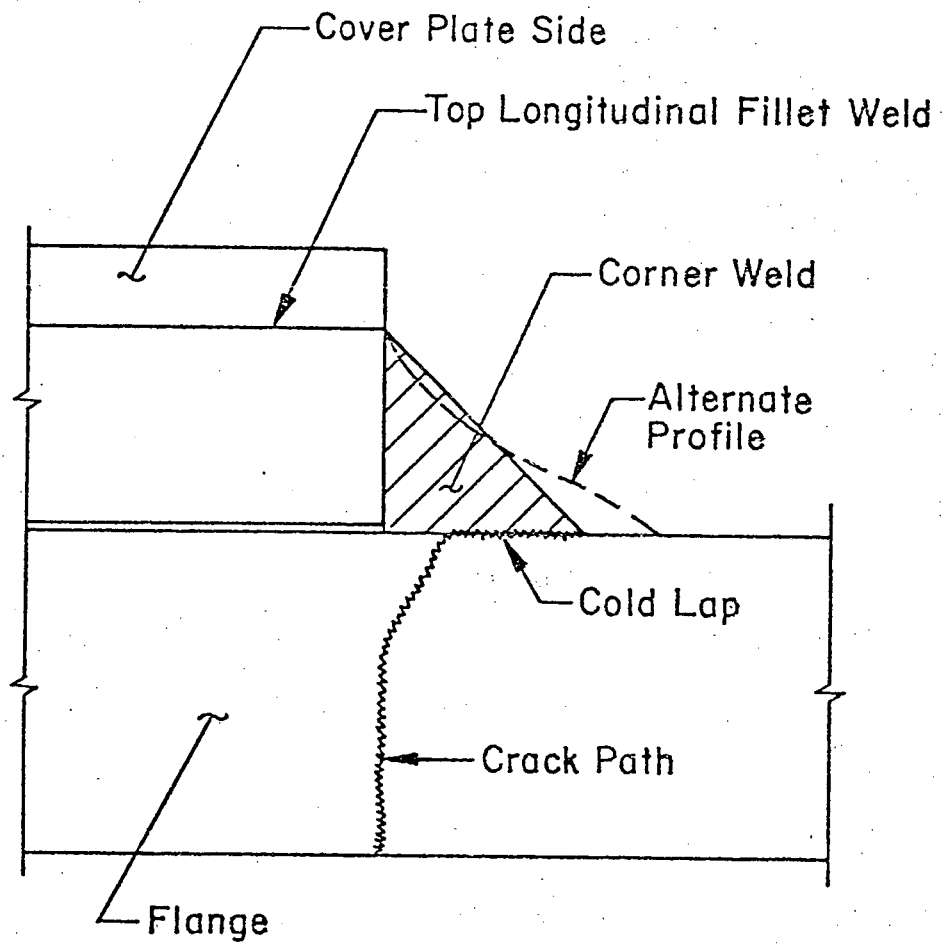
Fig. 2.27   Schematic Section of Cover Plate Detail
Without Transverse End Weld Showing Crack Path
from Longitudinal Fillet Weld Termination
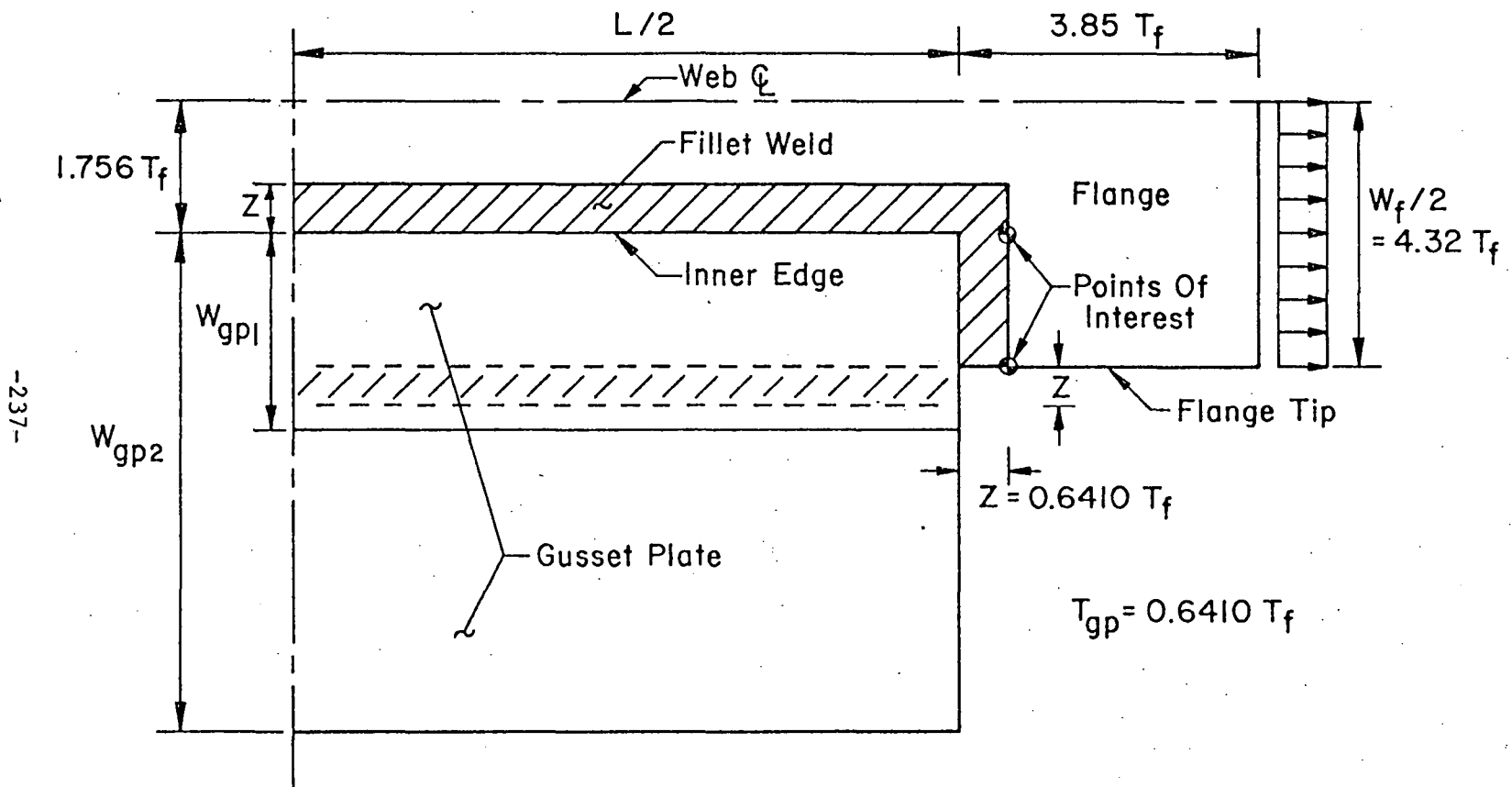
Fig. 2.28   Detail Geometries for Lap-Welded Gusset Plate Investigation
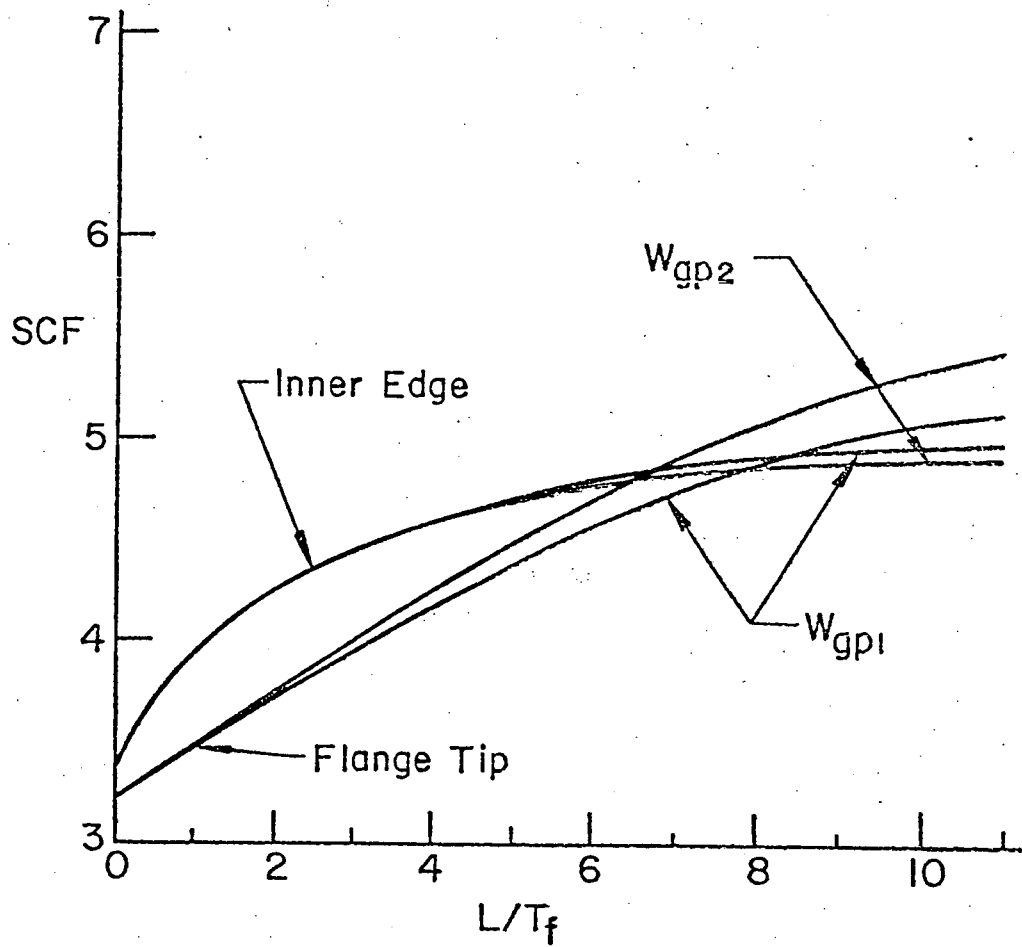
Fig. 2.29   Variation of Maximum Stress Concentration Factor with
Lap Gusset Plate Length-to-Flange Thickness Ratio
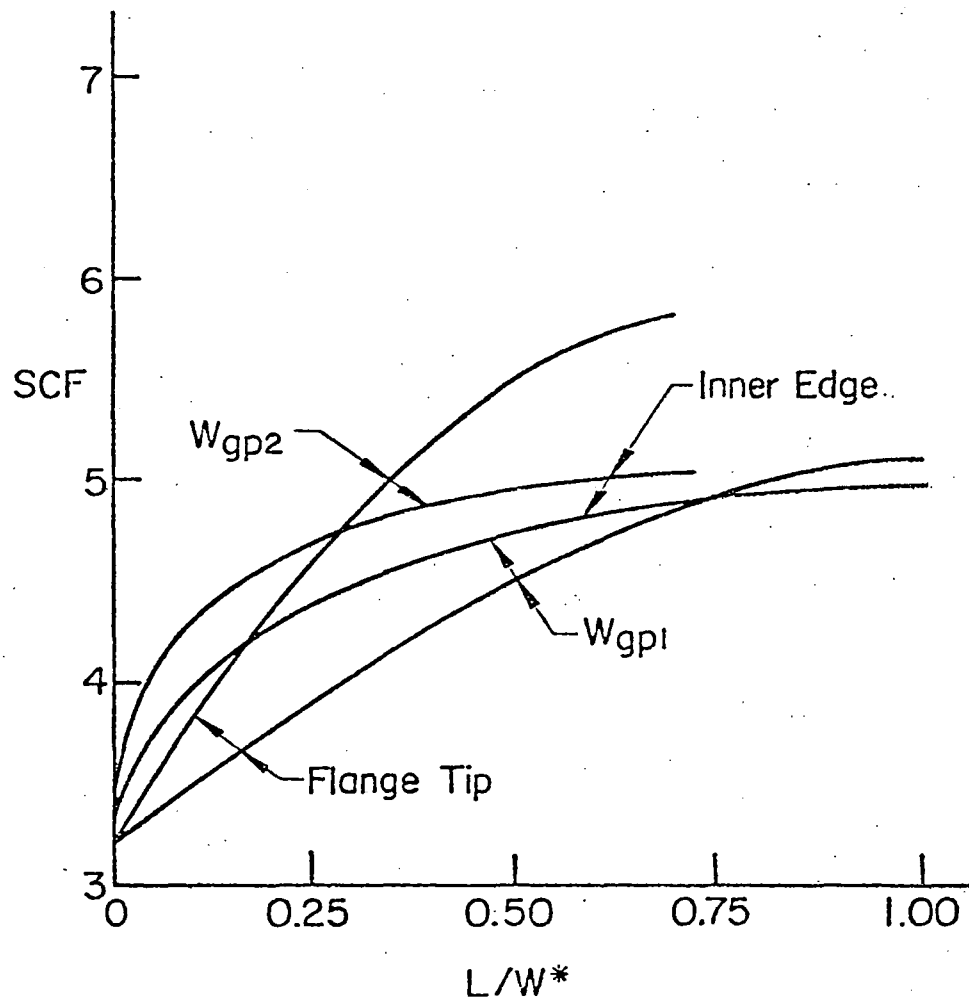
Fig. 2.30 Variation of Maximum Stress Concentration Factor with
Lap Gusset Plate Length-to-Effective Width Ratio
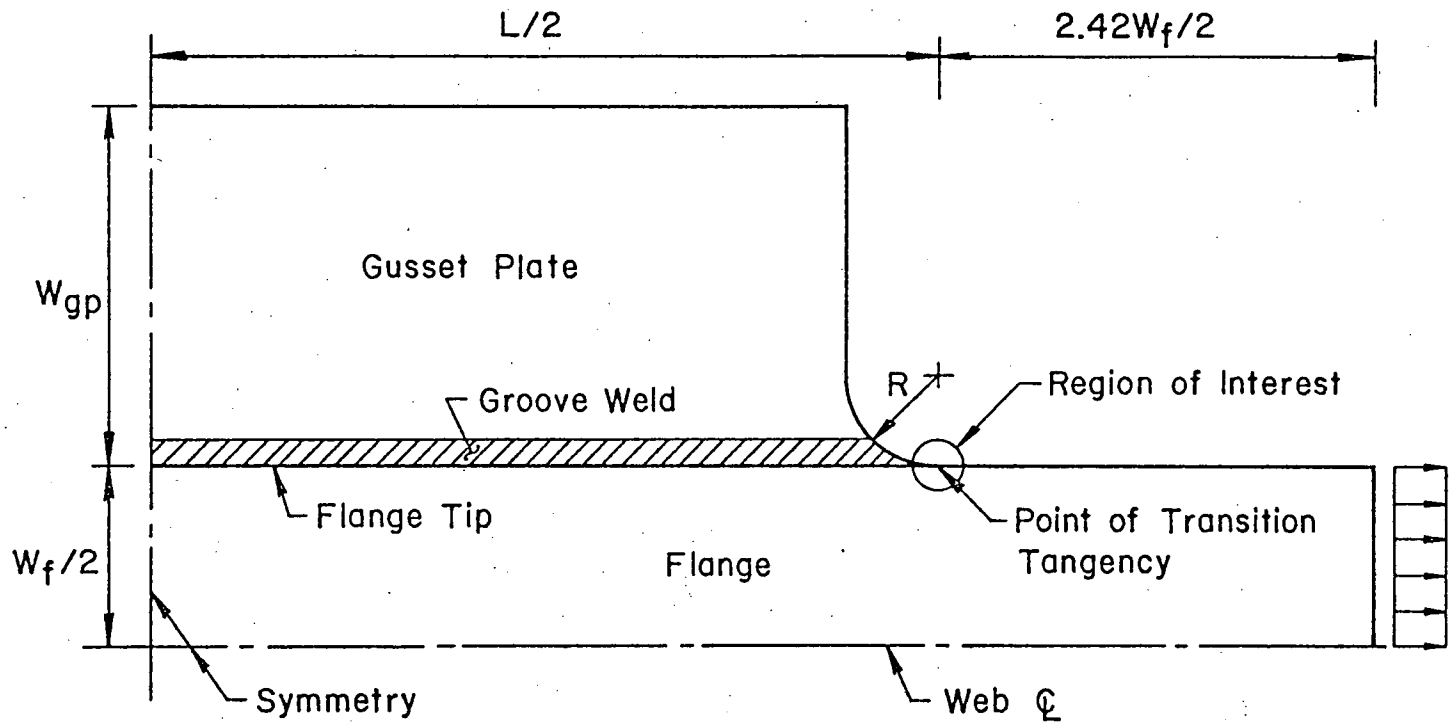
Fig. 2.31 Plan View of Detail Geometry for Gusset Plate Investigation
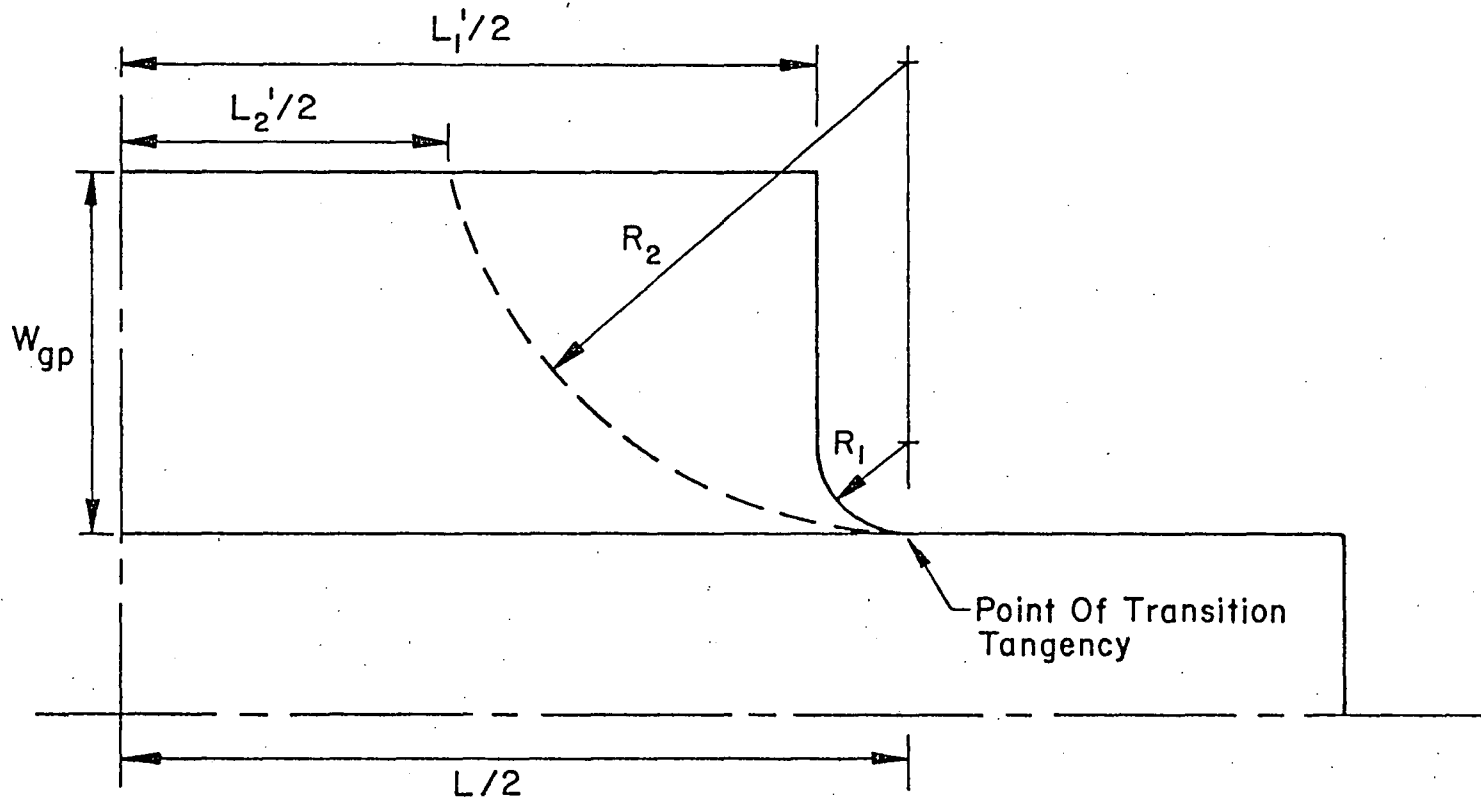
Fig. 2.32   Selection of Gusset Plate Length Parameter
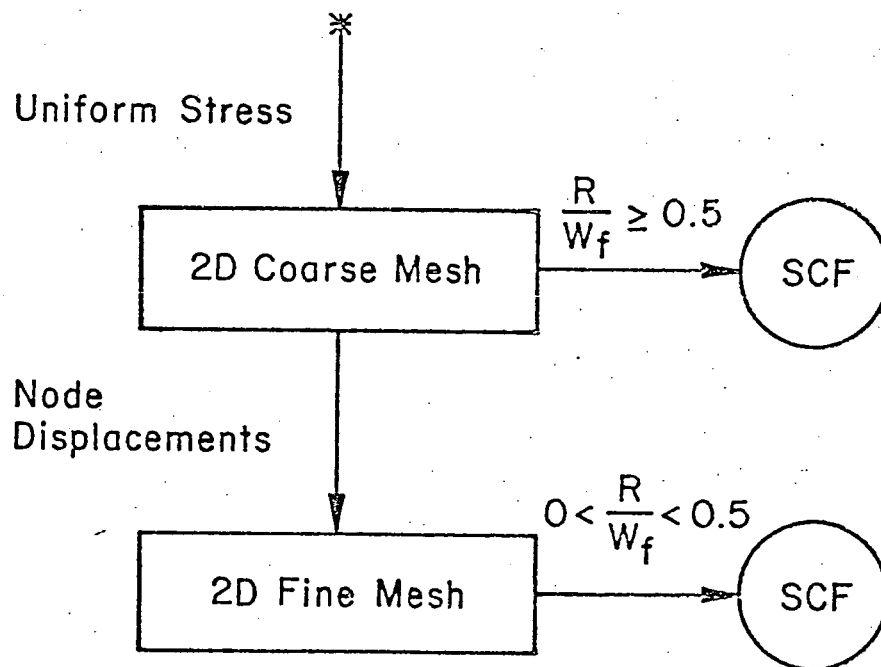
Fig. 2.33 Stress Concentration Analysis Procedure
for Gusset Plates
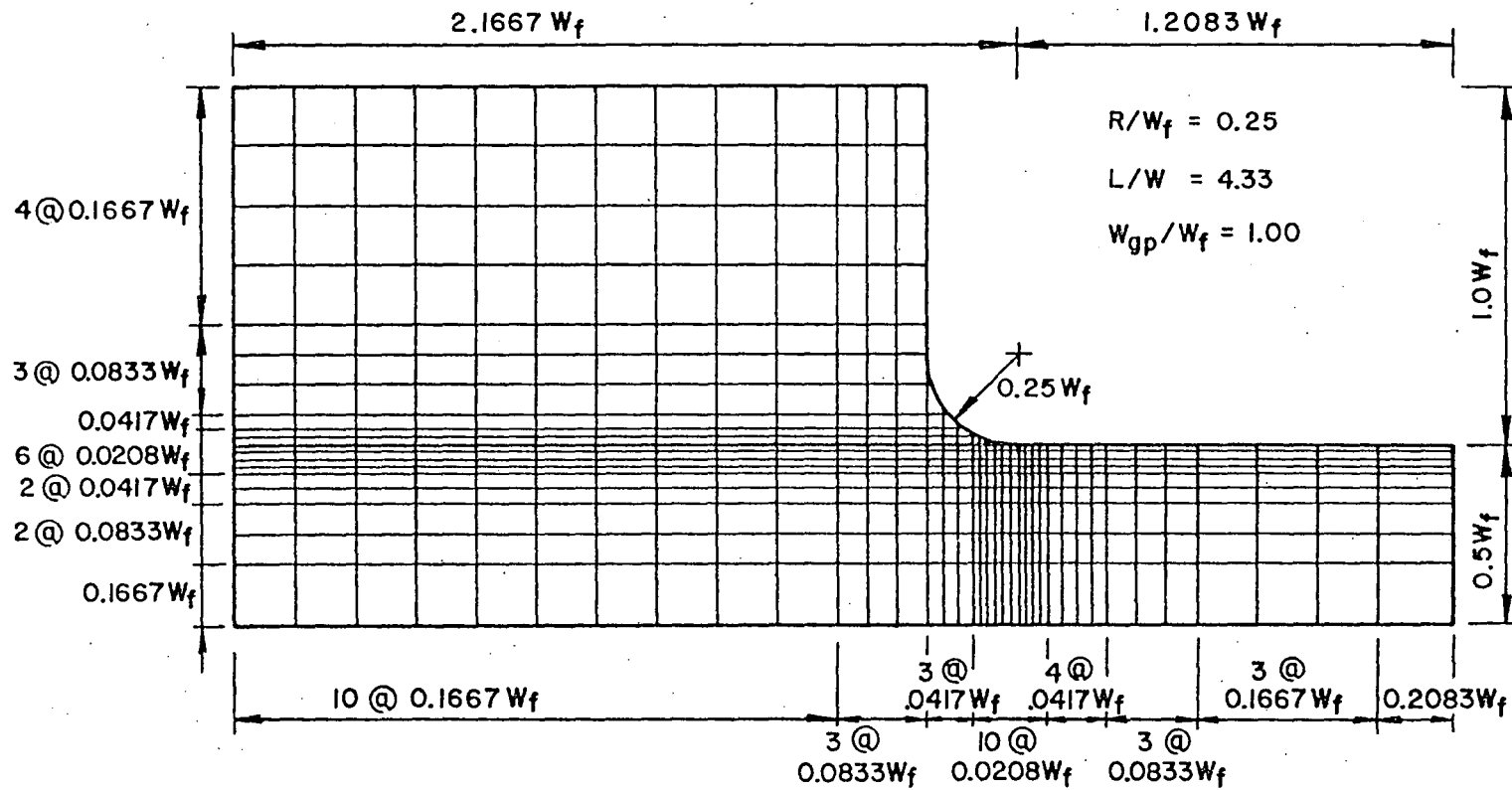
Fig. 2.34 Sample Coarse Mesh for Gusset Plate Investigation

$$\% \text{ Error} = 100\left[\frac{m}{R}\right] = 100\left[1 - \cos(\theta)\right] = 100\left[1 - \sqrt{1 - \left(\frac{D}{2R}\right)^2}\right]$$
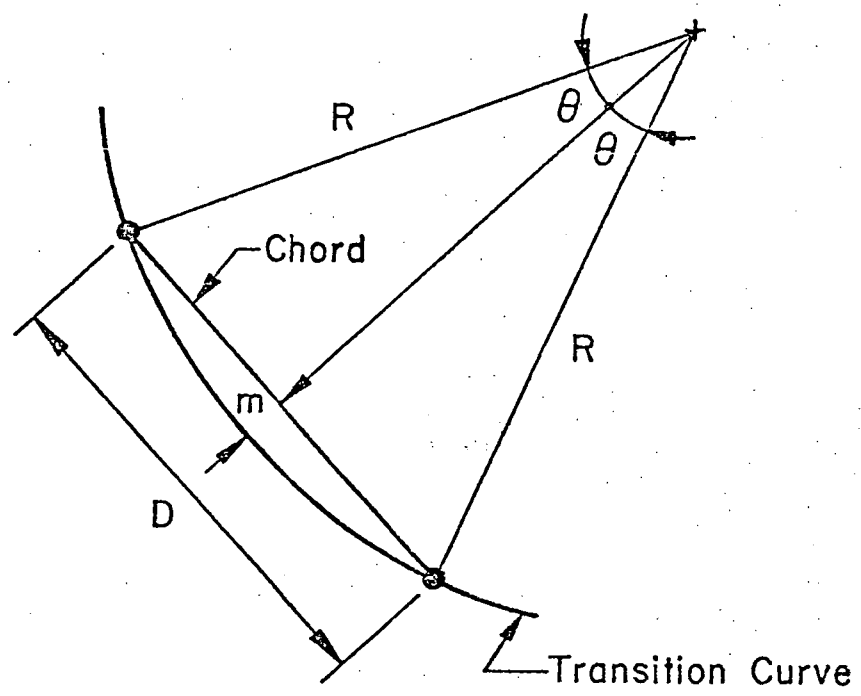
Fig. 2.35   Geometric Error due to Approximation
of Transition Curve by Chords
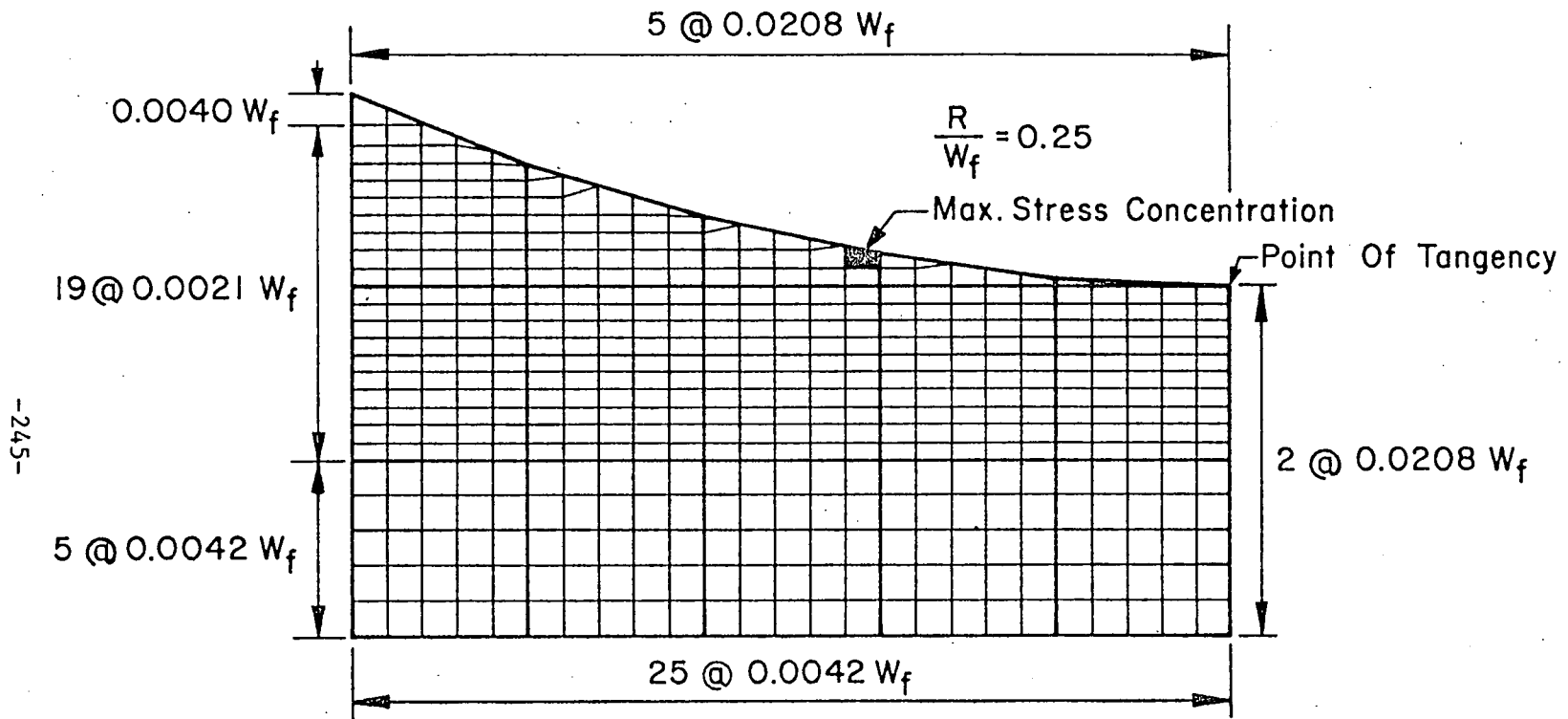
Fig. 2.36   Sample Fine Mesh for Gusset Plate Investigation

-246-

$\frac{R}{W_f} = 0.25$

Displacement From Coarse Mesh Output (typ.)

Displacement Input Both Directions (typ.)

Interpolated Displacement (typ.)
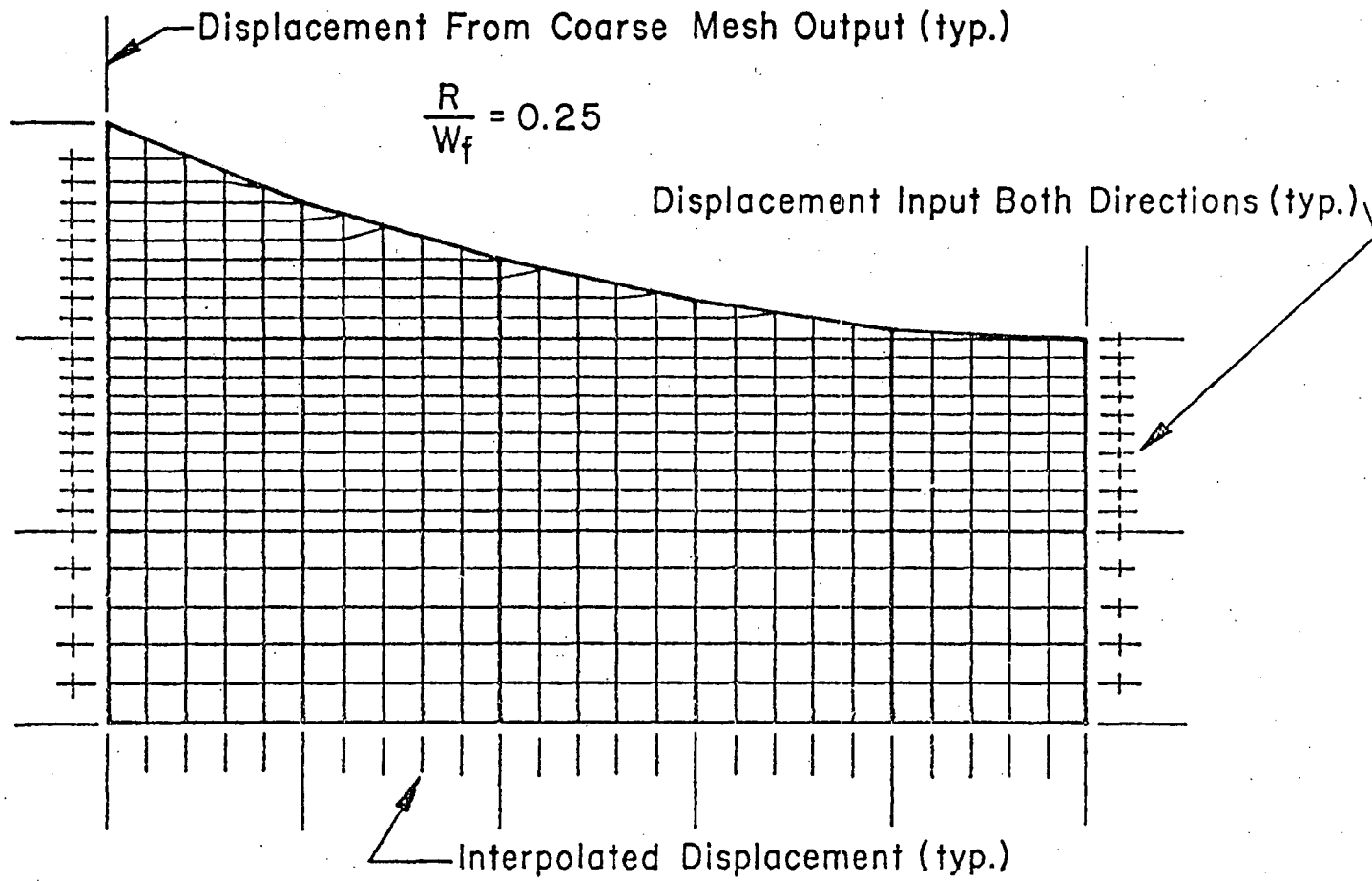
Fig. 2.37 Displacement Input to Sample Fine Mesh from Coarse Mesh Output
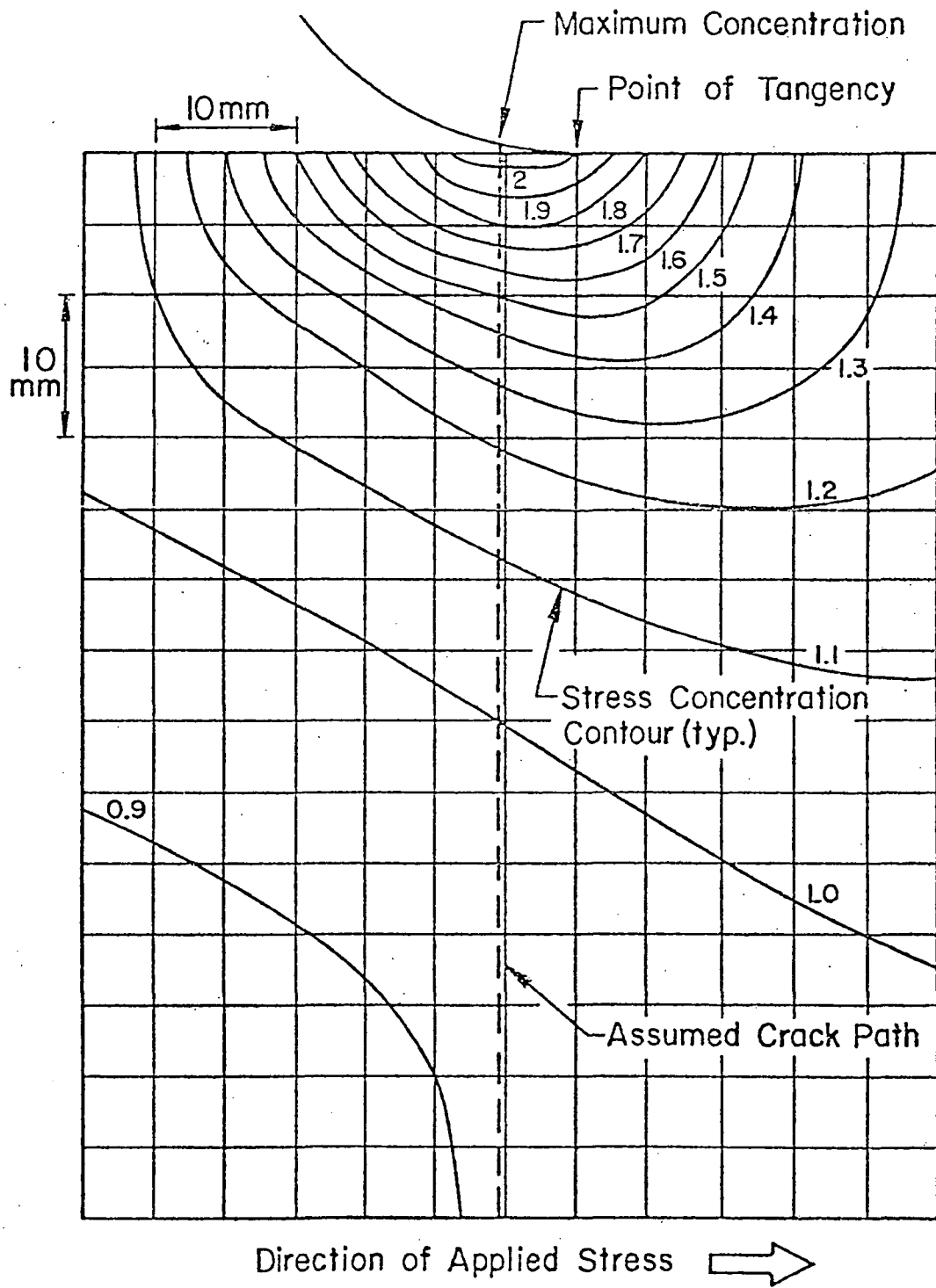
Fig. 2.38   Sample Gusset Plate Detail Stress Concentration Factor
Contours for Local Stress in Direction of Applied Stress

Fig. 2.39 Stress Concentration Factor Variation Along Prospective Crack Path across Flange Width at Sample Gusset Plate Detail

Fig. 2.40   Variation of Maximum Stress Concentration Factor
with Gusset Plate Transition Radius

-249-

Fig. 2.41   Variation of Maximum Stress Concentration Factor with Gusset Plate Length

Fig. 2.42 Variation of Maximum Stress Concentration Factor
with Gusset Plate Width

Fig. 2.43   Variation of Maximum Stress Concentration Factor with Gusset Plate Thickness
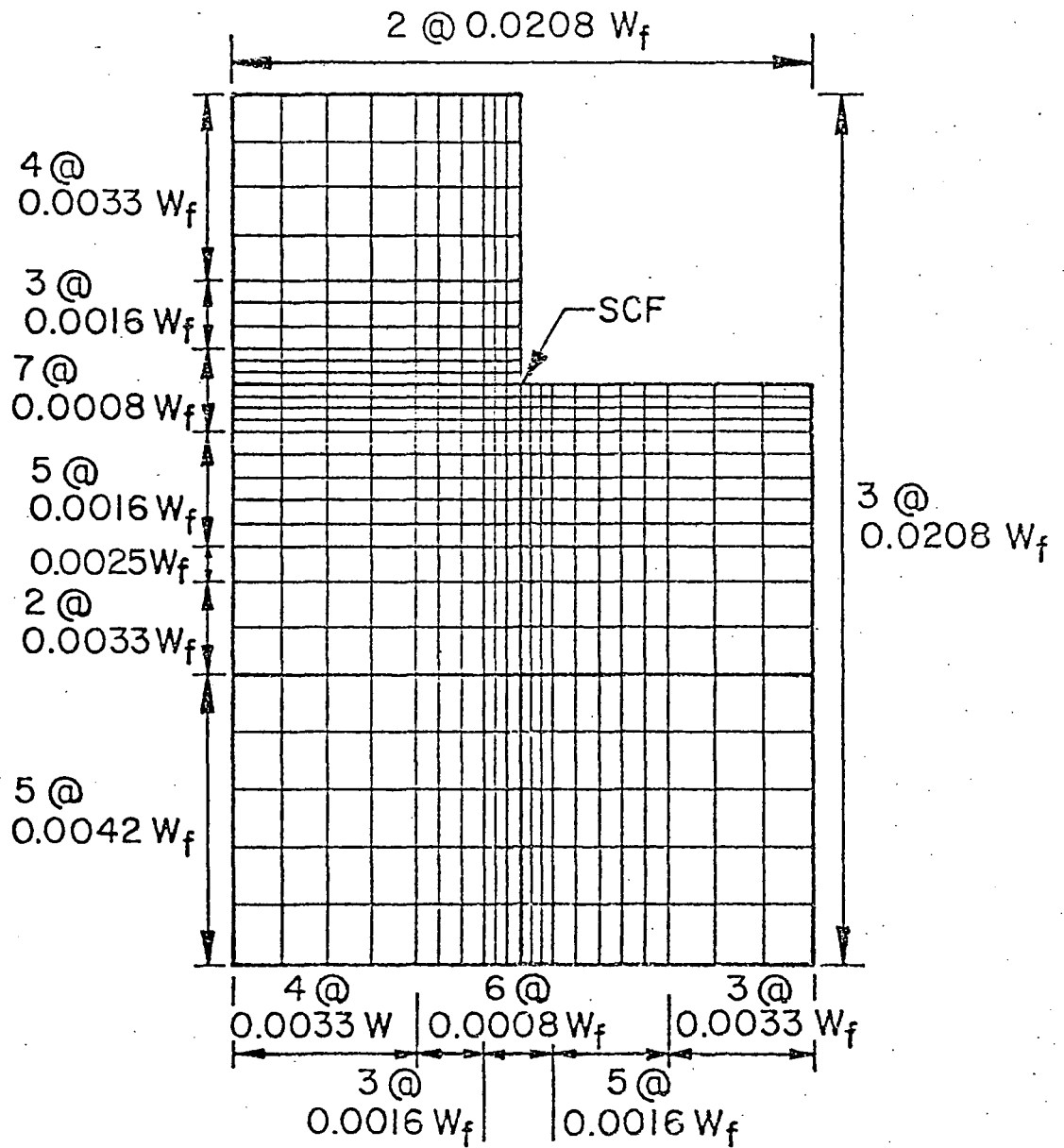
Fig. 2.44   Fine Mesh for Singular Gusset Plate Investigation

$P_{gp}/P_f = 1/12$

σ_{gp}

$P_{gp}/4$

$0.1667\,W_f$

$0.3333\,W_f$

Region of Interest

Symmetry

$W_f/2$

σ_f
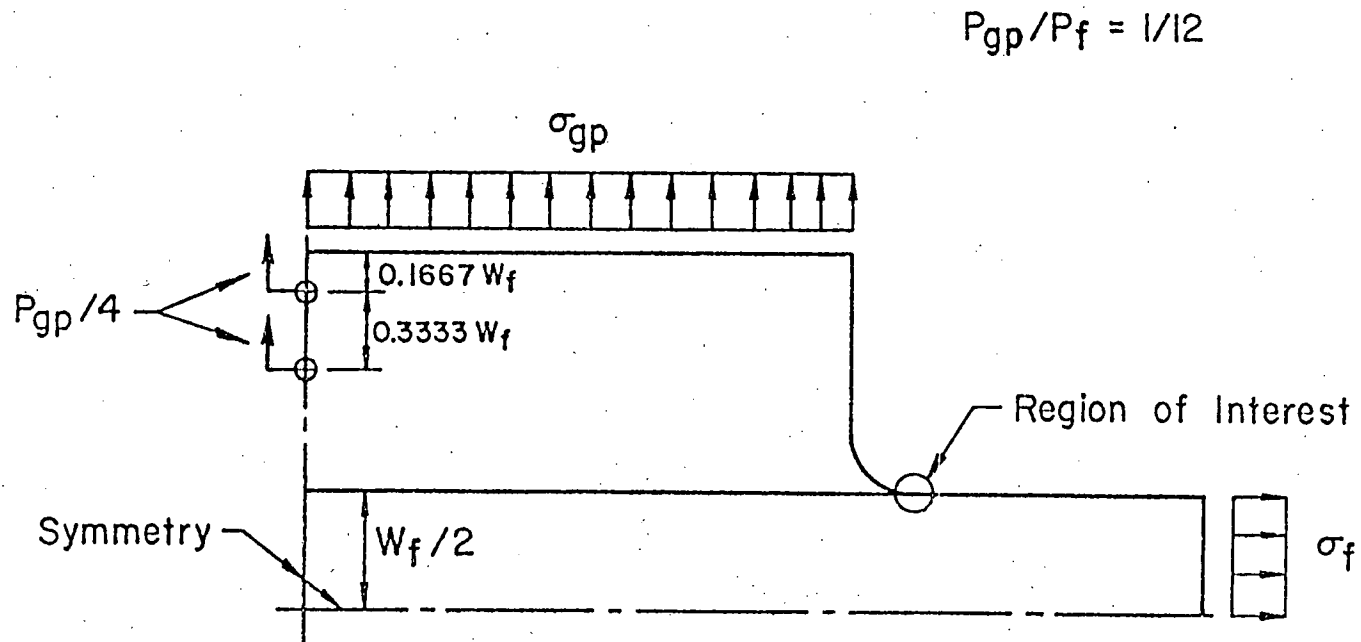
Fig. 2.45 Loading Schemes for Investigation of Gusset Plate Secondary Force Effects
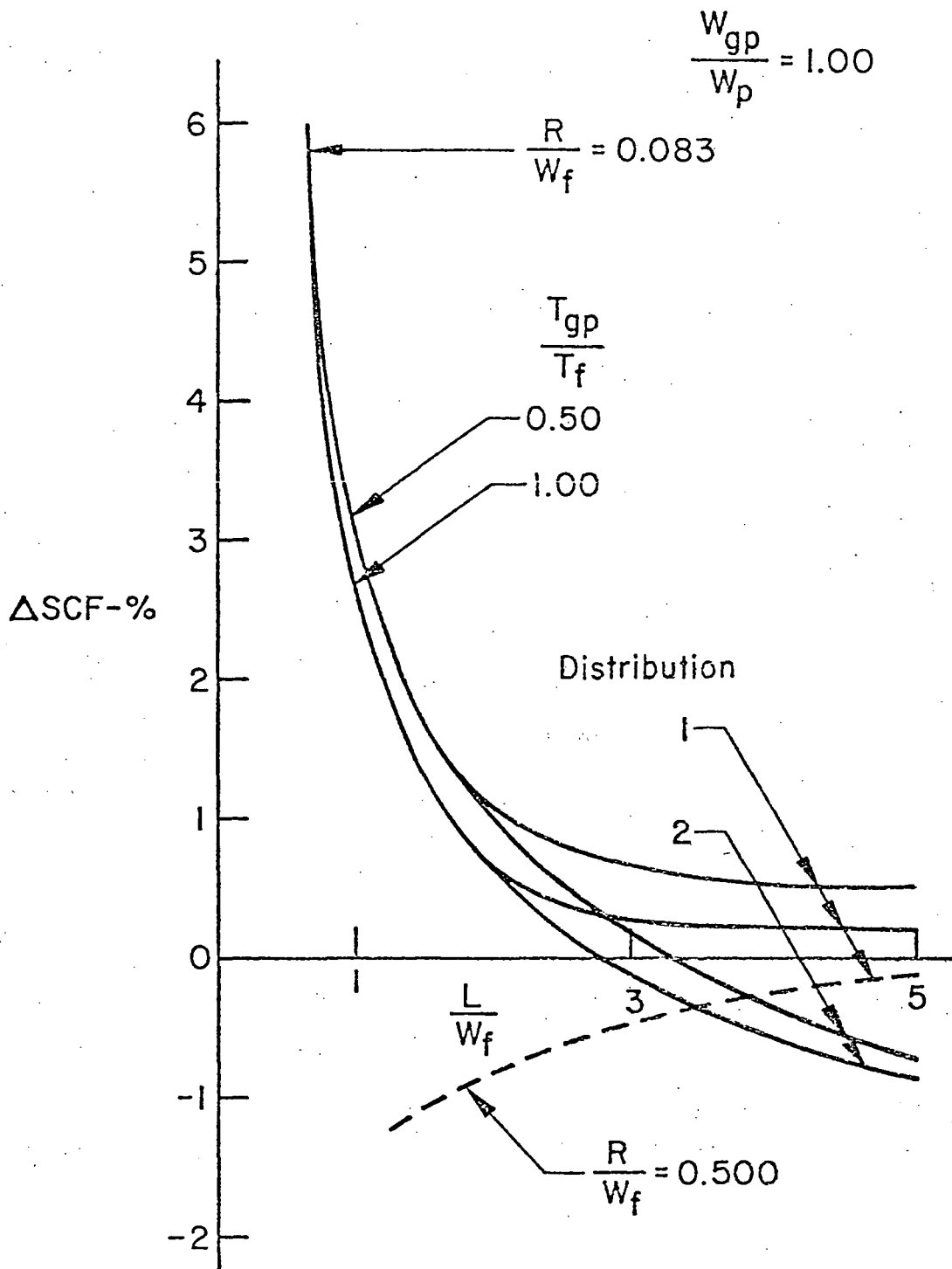
Fig. 2.46   Percent Change in Maximum Stress Concentration
Factor due to Gusset Plate Secondary Forces
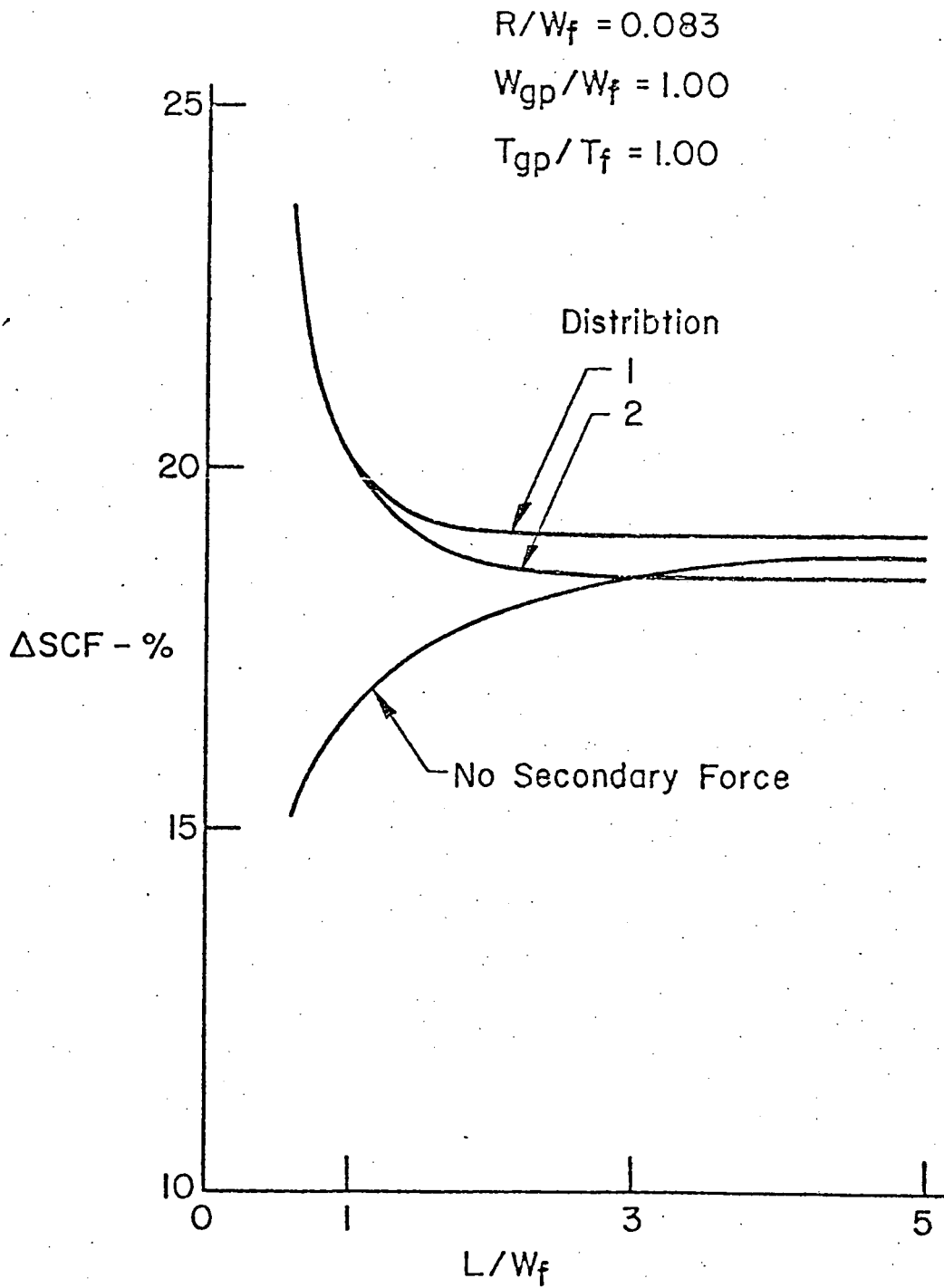
Fig. 2.47   Percent Change in Maximum Stress Concentration
Factor for Maximum Principal Stress Concentrations
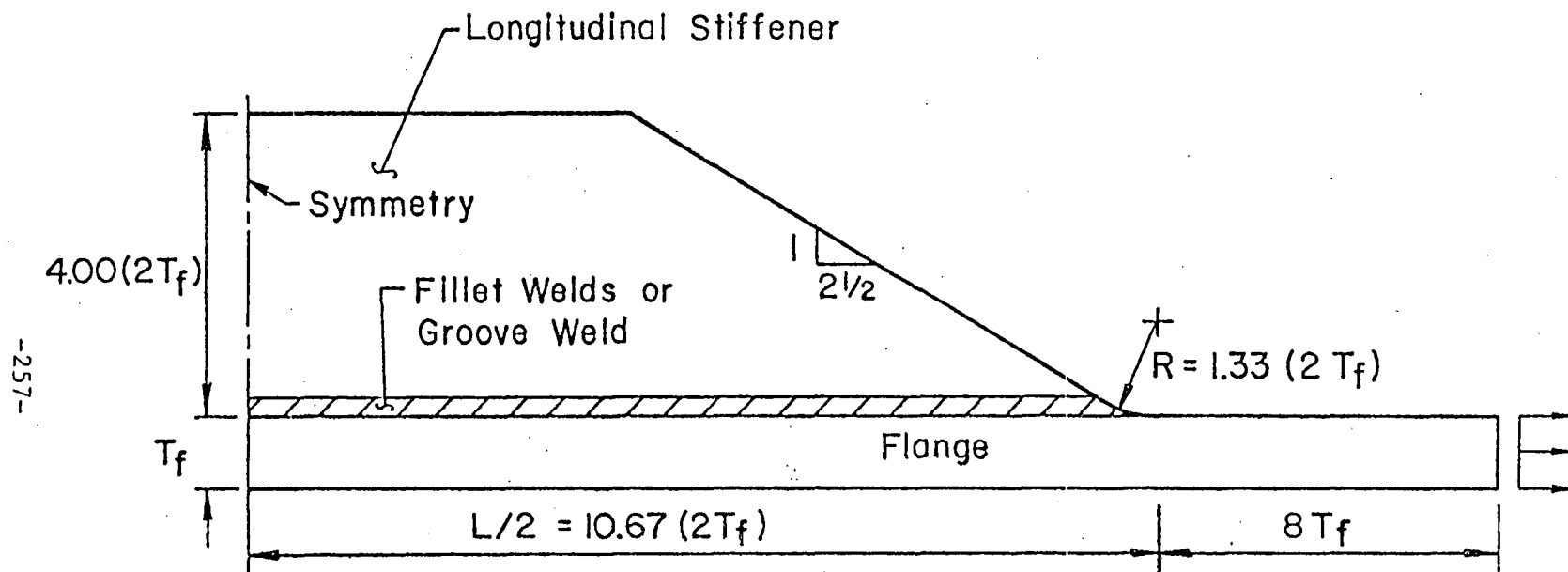
Fig. 2.48   Schematic Geometry for Longitudinal Stiffener Investigation
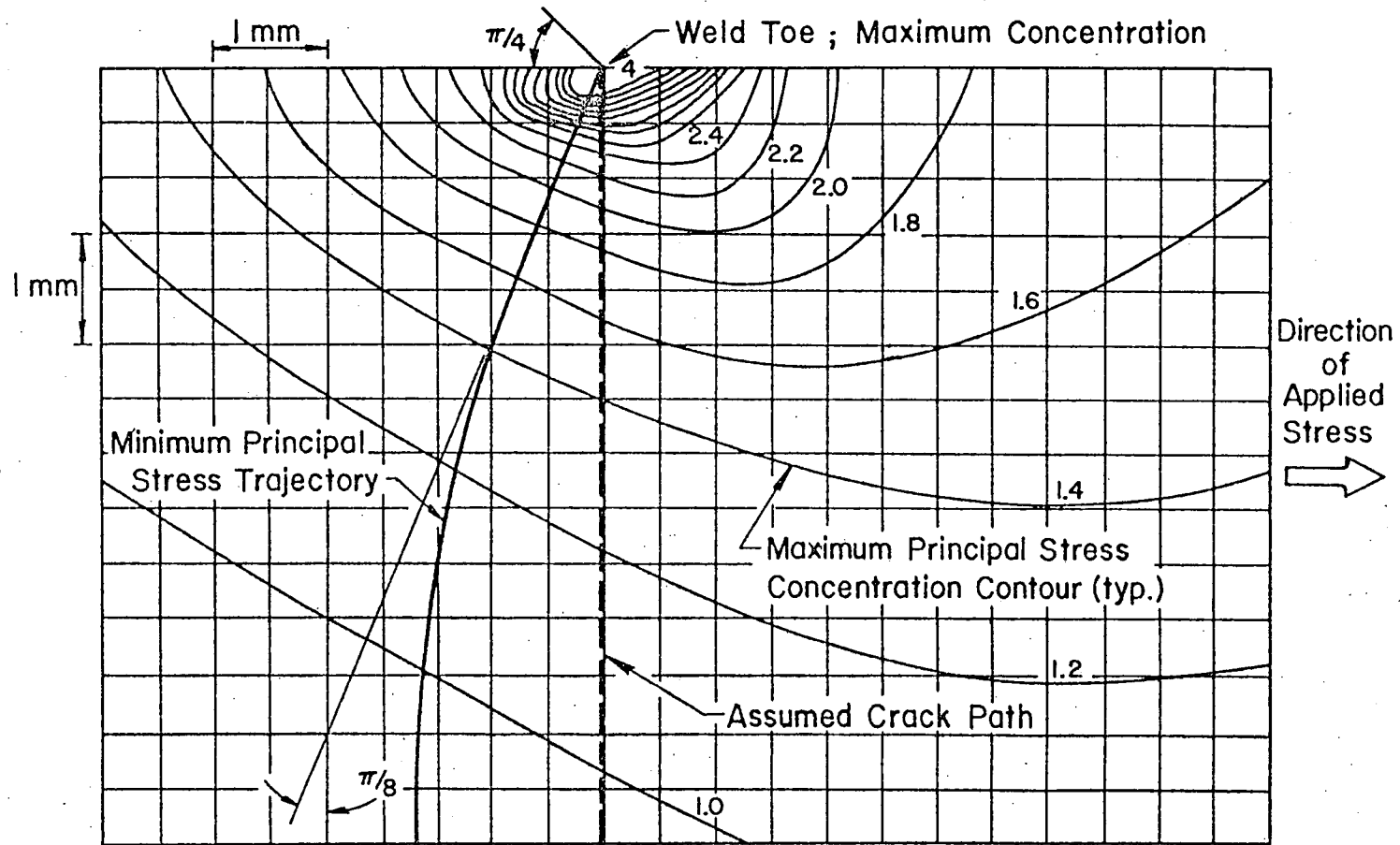
Fig. 3.1 Maximum Principal Stress Concentration Factor Contours for
Sample Cover Plate Detail with Superimposed Limits of Crack Path
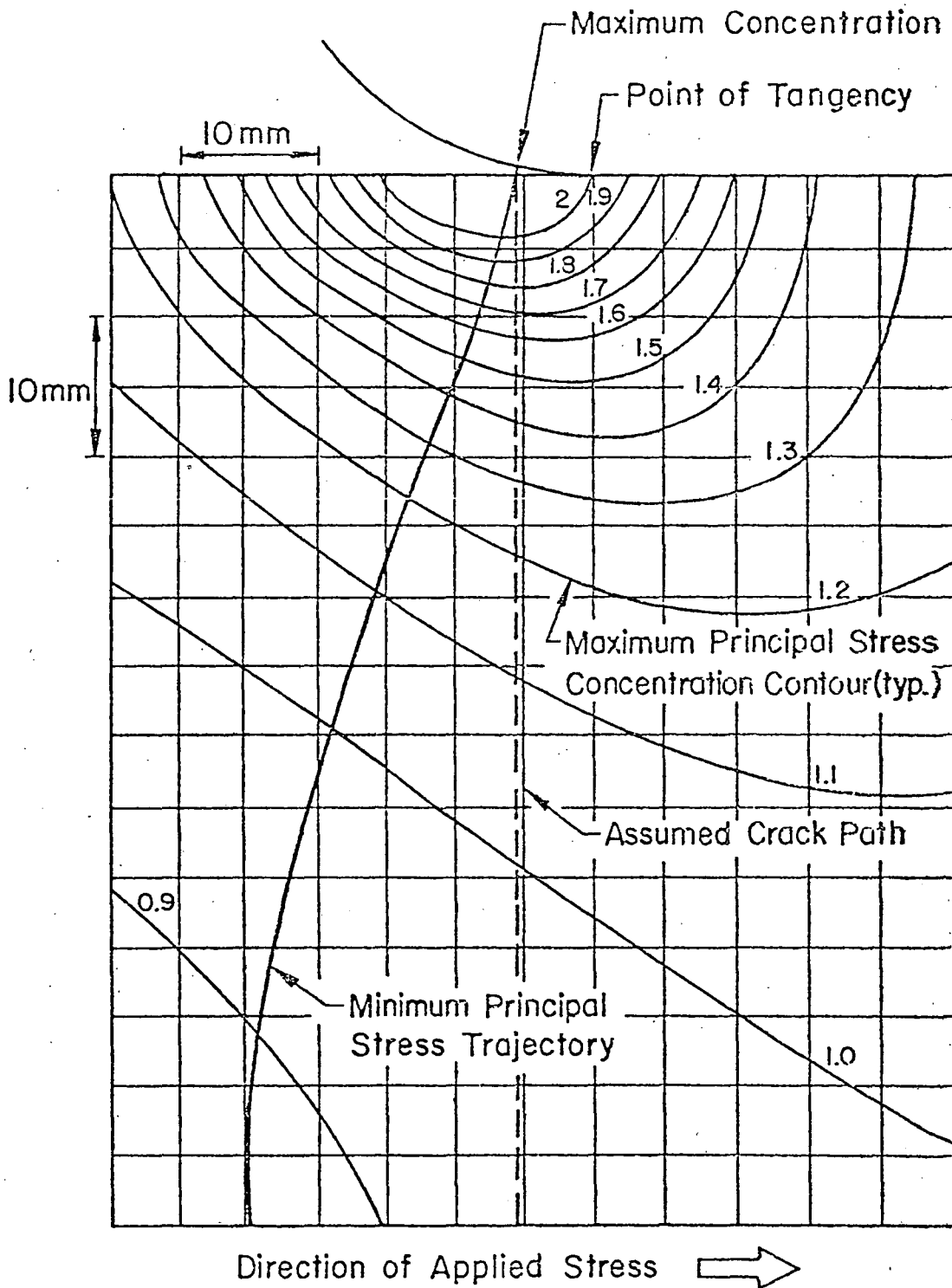
Fig. 3.2   Maximum Principal Stress Concentration Factor Contours
for Sample Gusset Plate Detail
with Superimposed Limits of Crack Path

-259-
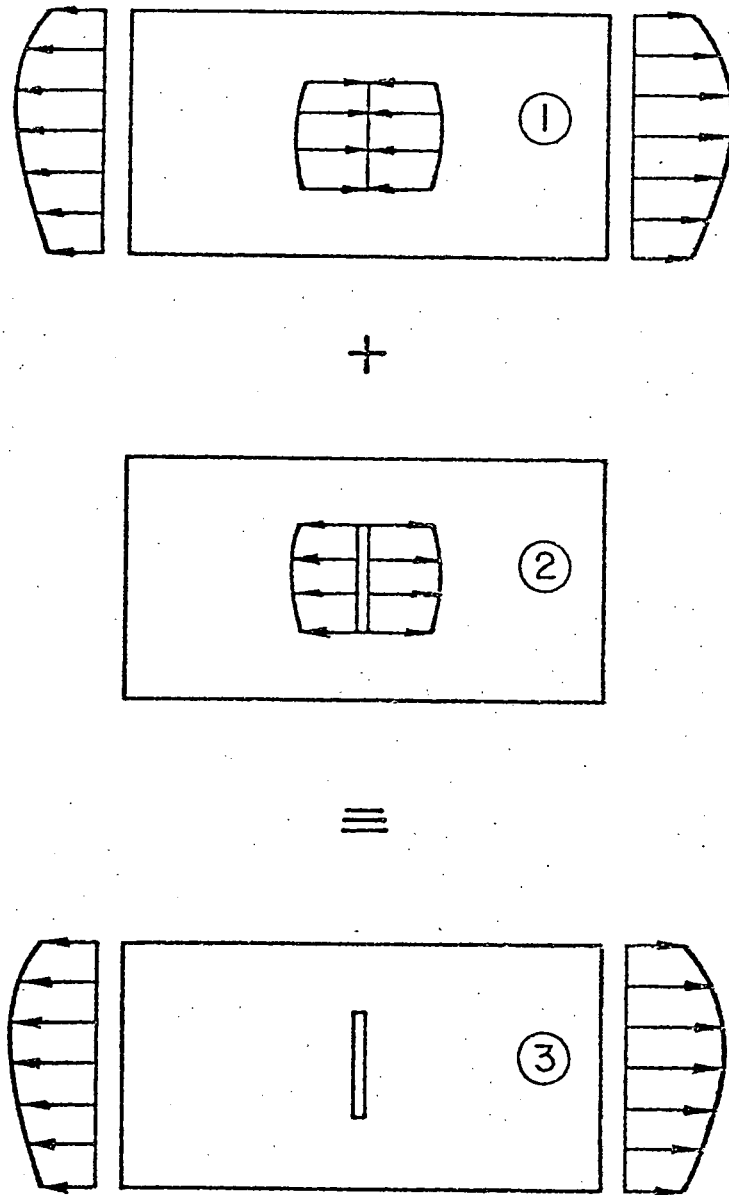
Fig. 3.3 Superposition of Surface Tractions
on Cracked Body[45]
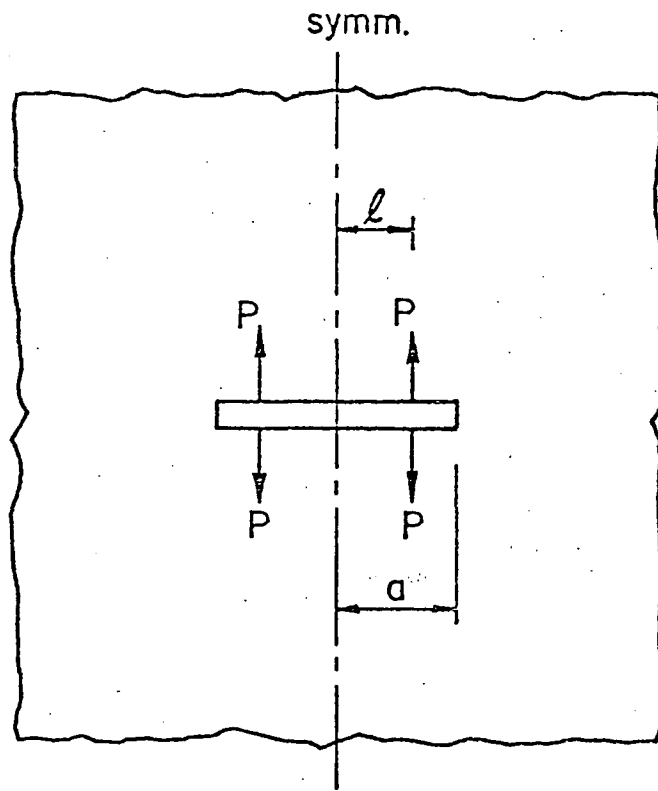
Fig. 3.4   Through Crack in Infinite Plate Subjected
to Two Pairs of Splitting Forces[2]
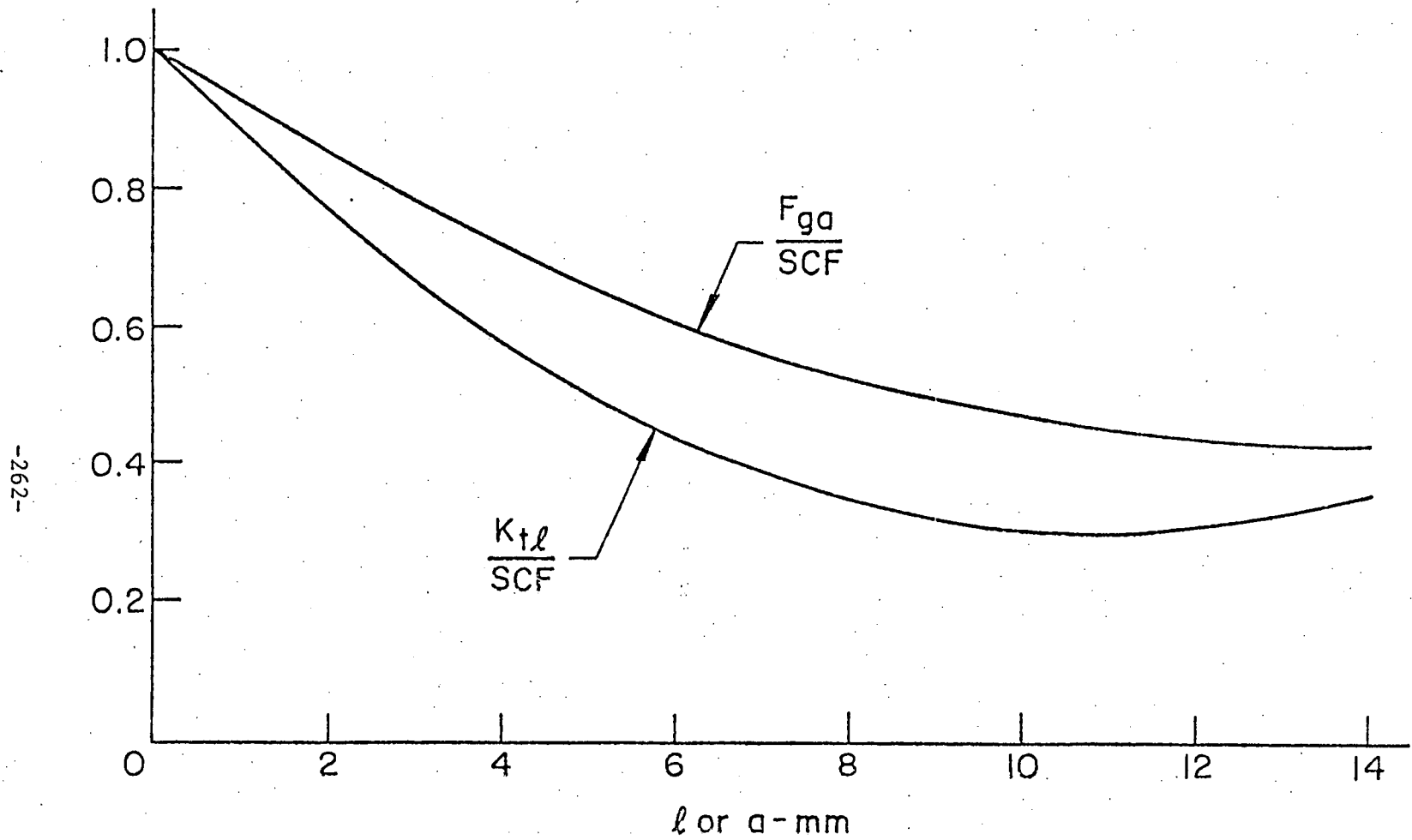
Fig. 3.5 Stress Concentration and Stress Gradient Correction
Factor Decay Curves for Sample Polynomial
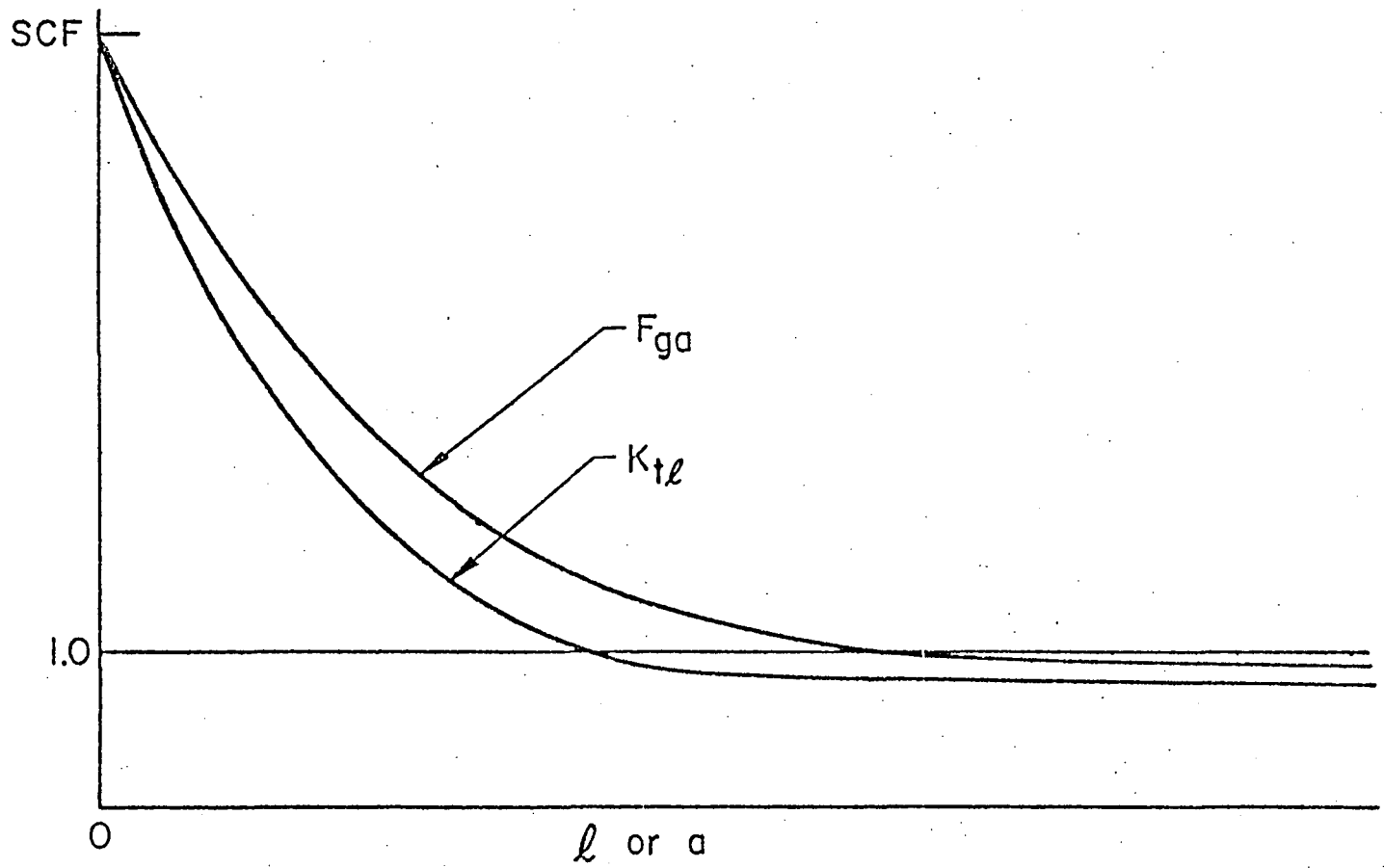
Fig. 3.6 Schematic Stress Concentration and Stress Gradient Correction
Factor Decay Curves for Typical Welded Details

Detail	Z/T_f	T_{cp}/T_f	SCF
CP	0.3205	0.6410	7.198
CP	0.6410	0.2000	7.014
CP	0.6410	0.6410	6.040
ST	0.6410		3.651
ST	0.3205		3.161
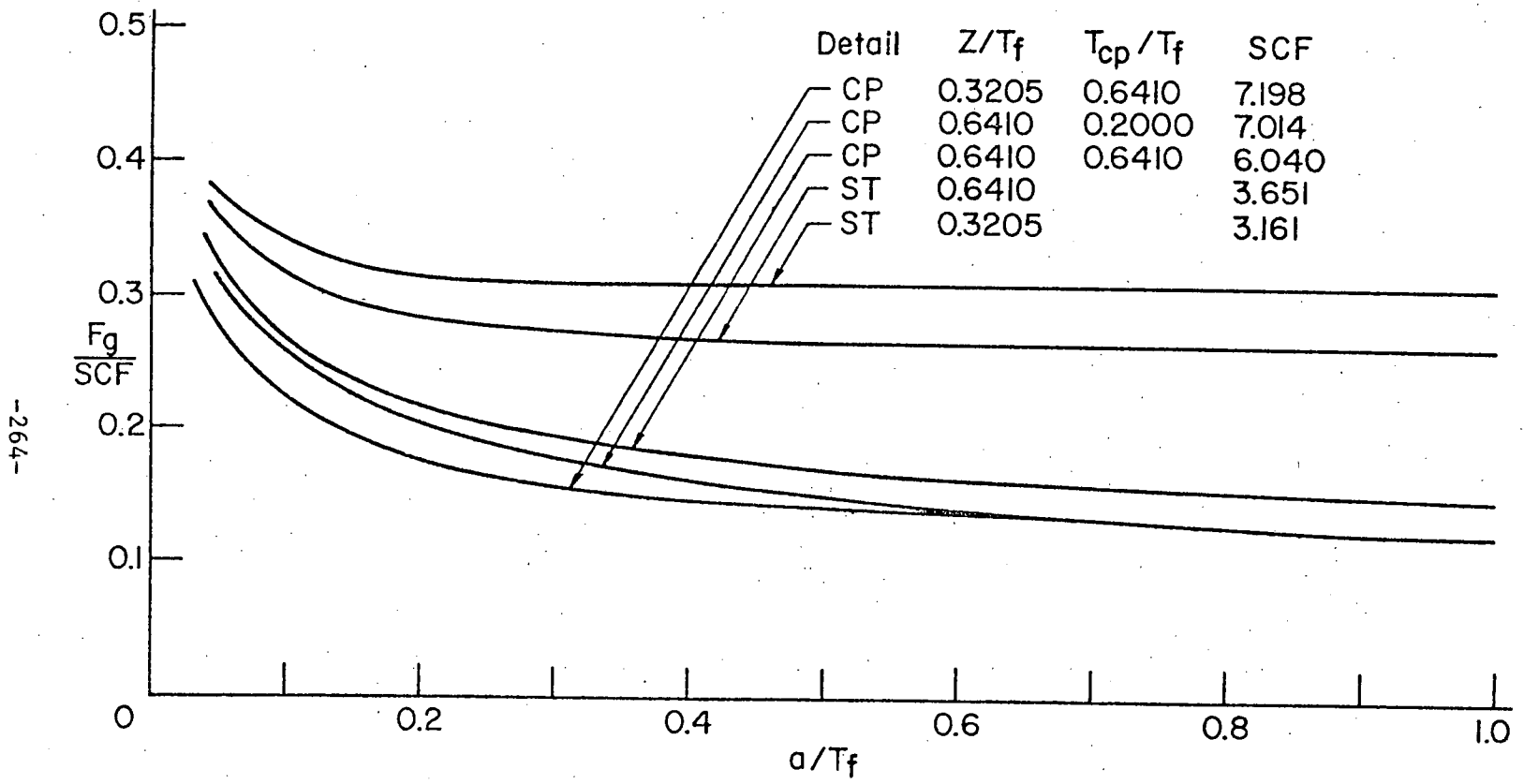
Fig. 3.7 F_g Decay Curves for Sample Stiffener and Cover Plate Details

R/W_f	L/W_f	W_{gp}/W_f	T_{gp}/T_f	SCF
0.500	4.33	1.0	1.0	1.465
0.083	0.67	1.0	0.5	1.770
0.083	0.67	1.0	1.0	2.022
0.167	8.67	2.0	1.0	2.229
0.083	4.33	1.0	1.0	2.788
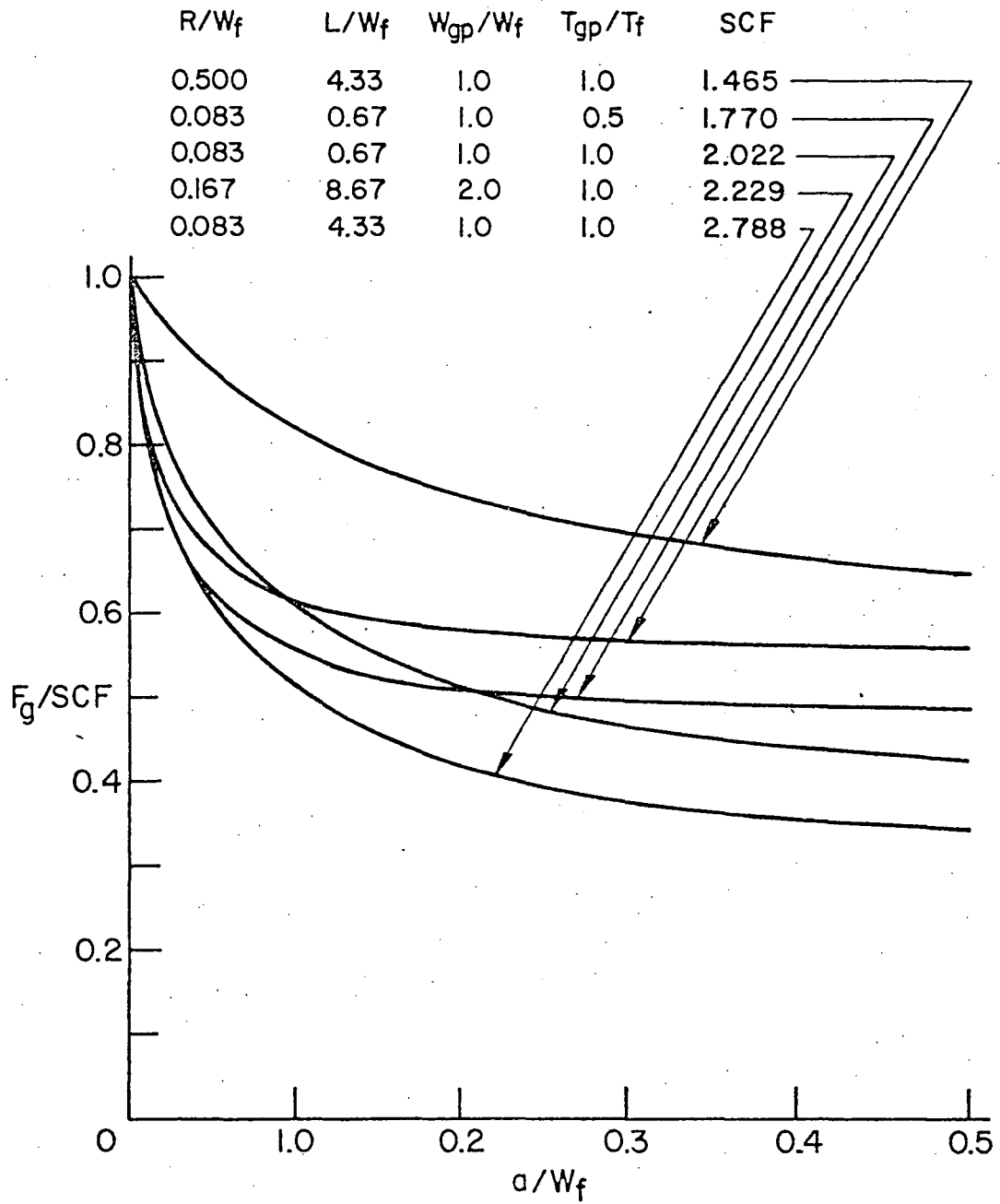
Fig. 3.8 F_g Decay Curves for Sample Gusset Plate Details
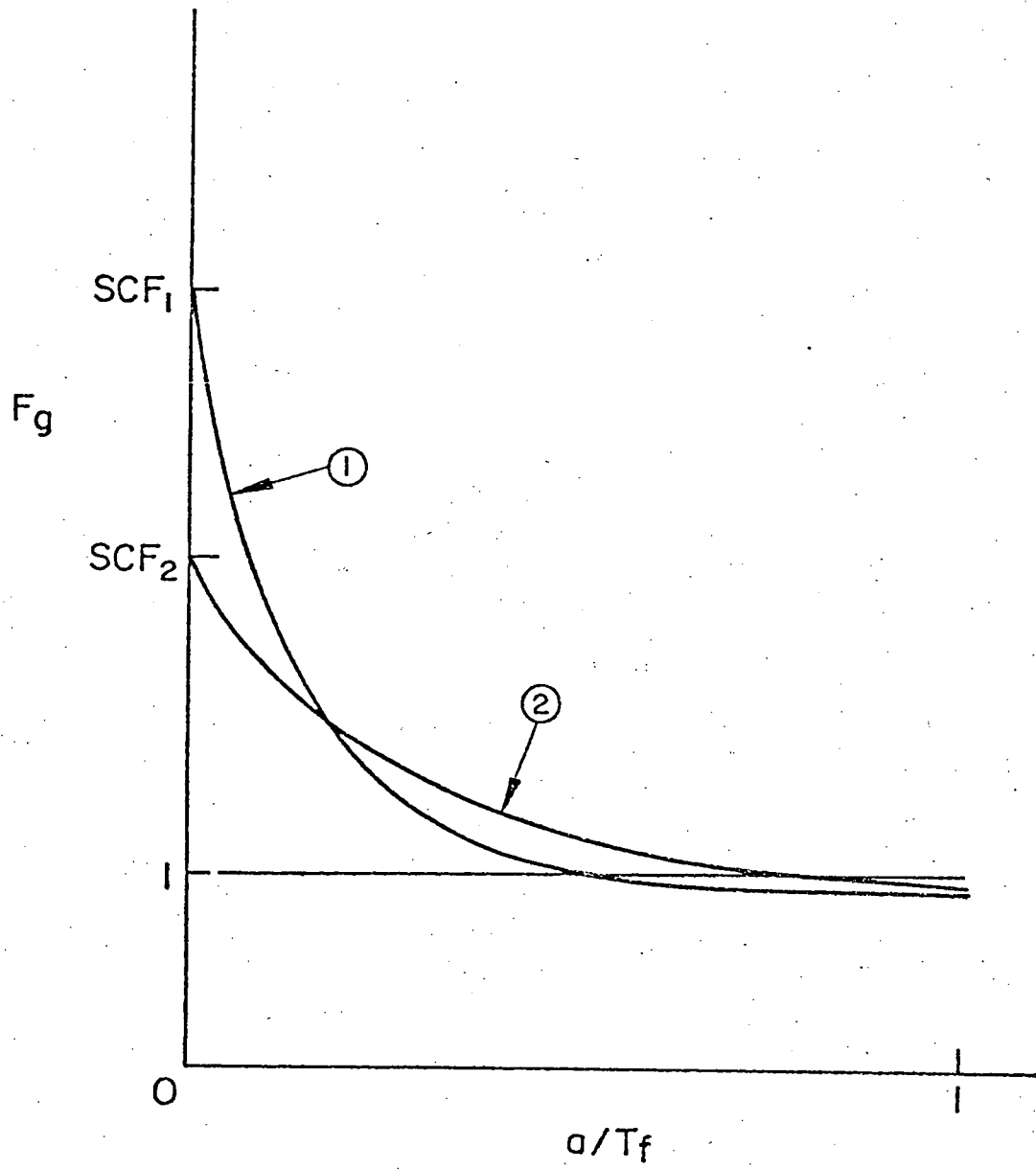
Fig. 3.9 Schematic Compaison of F_g Decay Curves
for Fillet-Welded Details

$$SCF = 1 + 2\frac{g}{h} > 3.0$$

$$SCF = 3.0$$

$$1.0 \leq SCF = 1 + 2\frac{h}{g} < 3.0$$
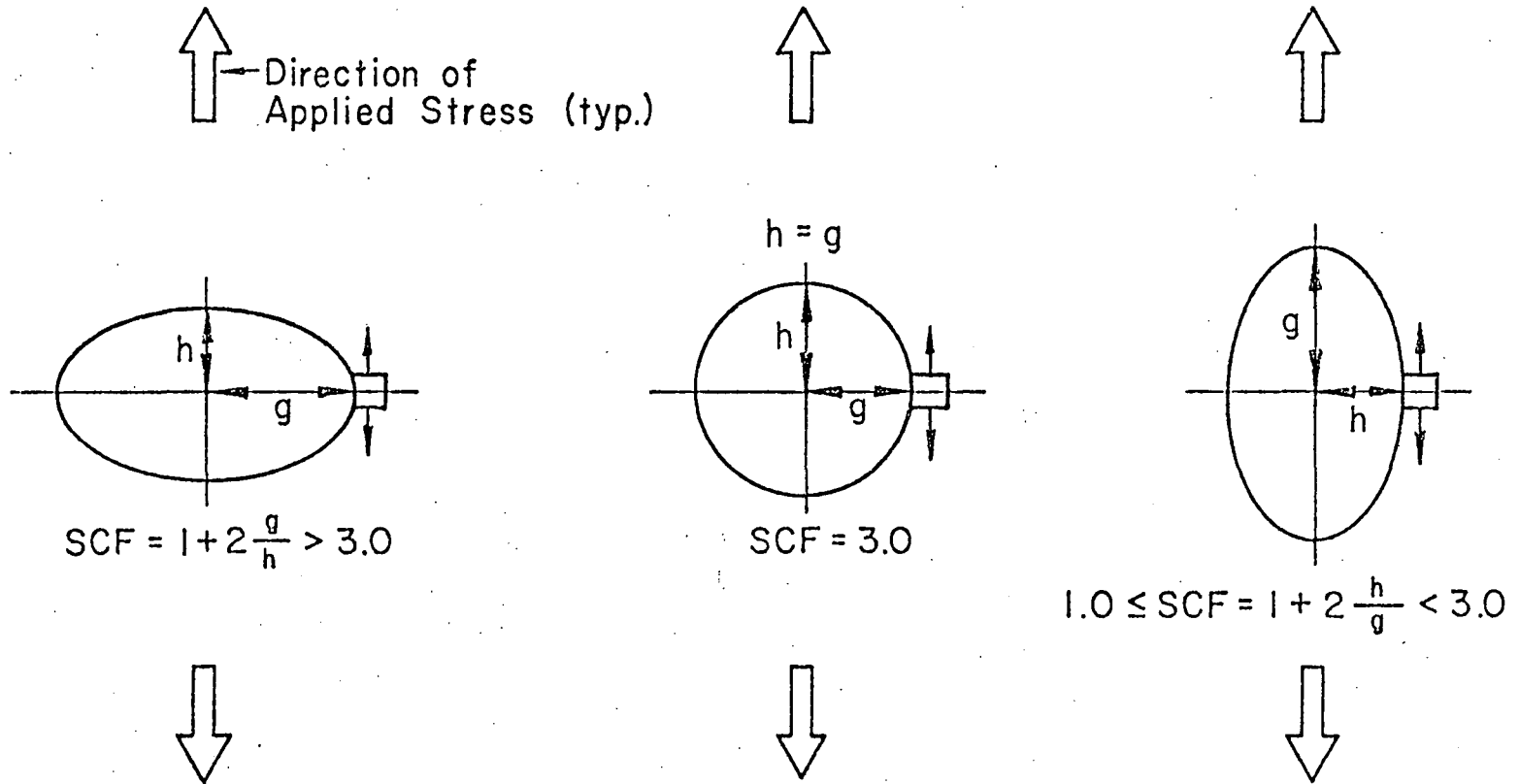
Fig. 3.10 Maximum Stress Concentration Factors for Elliptical and Circular Holes
in Infinite, Uniaxially Stressed Plate
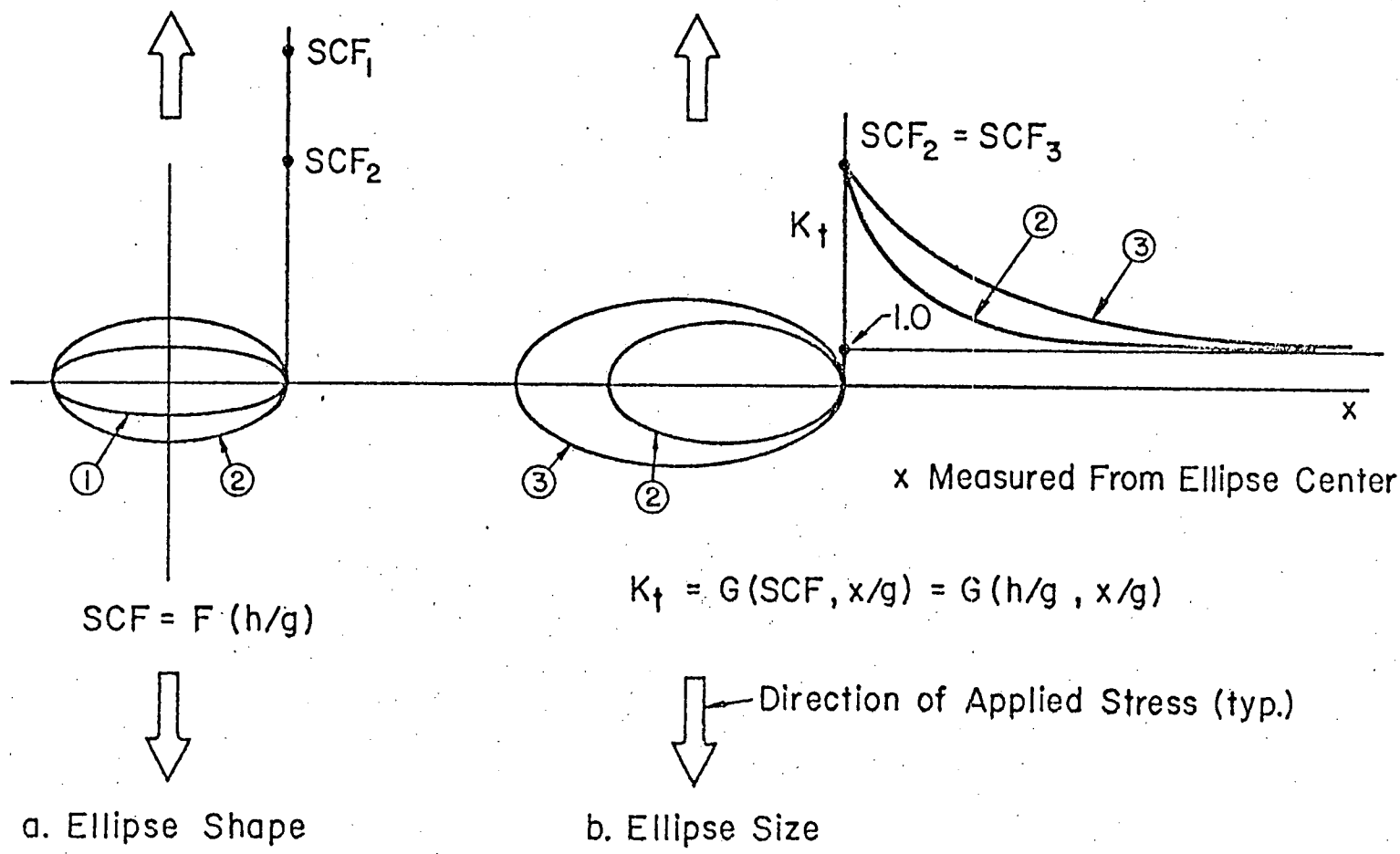
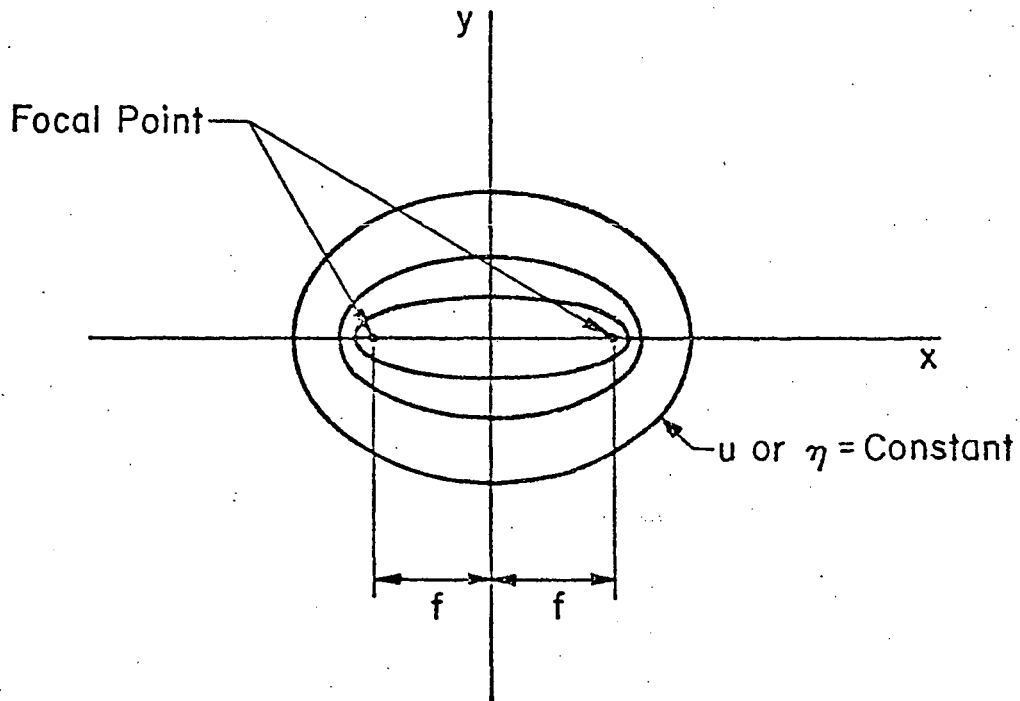Fig. 3.11 Two Steps Required for Ellipse Correlation
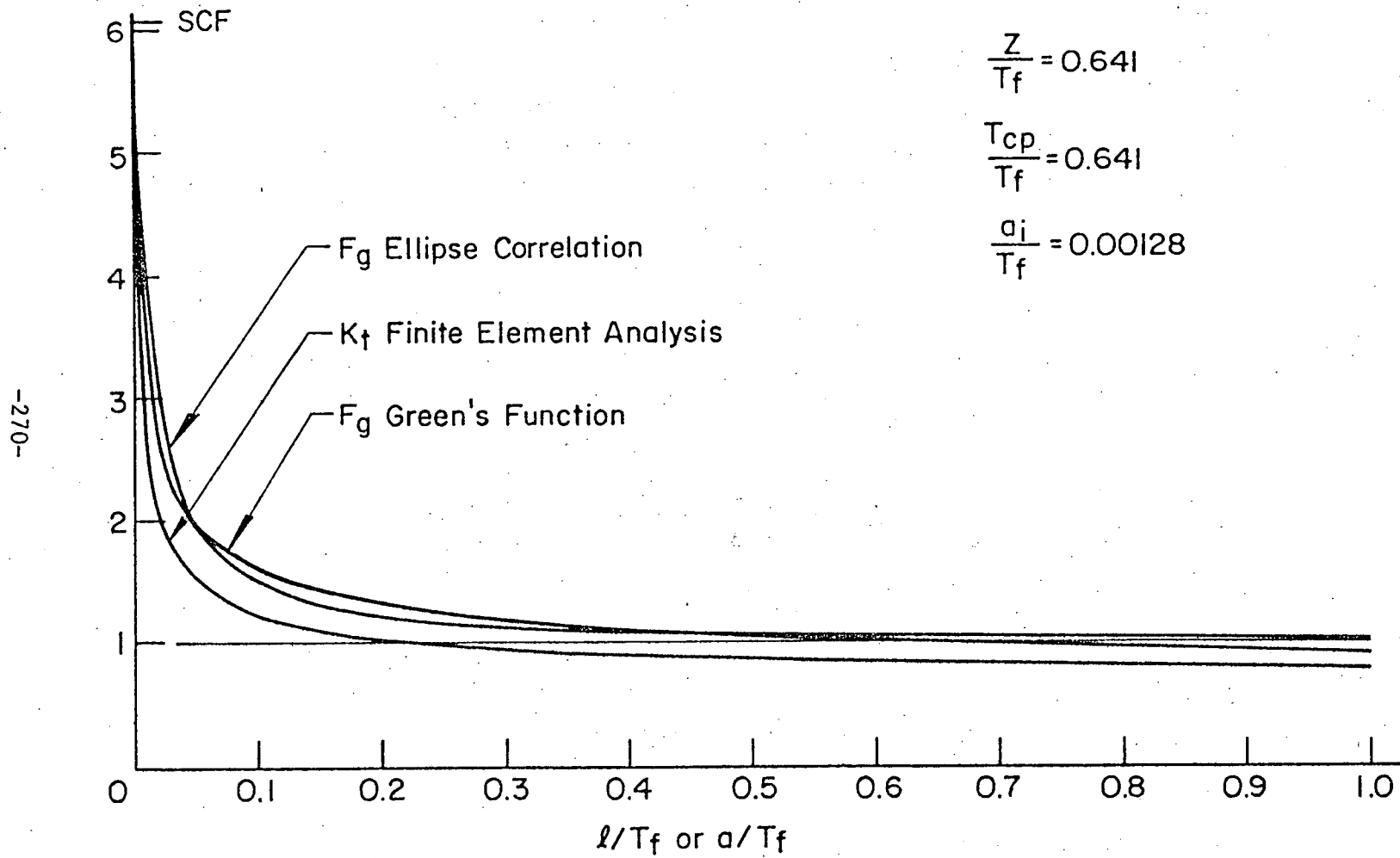
Fig. 3.12 Confocal Ellipses for Elliptic Coordinates[43]

6 — SCF

$\dfrac{Z}{T_f} = 0.641$

$\dfrac{T_{cp}}{T_f} = 0.641$

$\dfrac{a_i}{T_f} = 0.00128$

F_g Ellipse Correlation

K_t Finite Element Analysis

F_g Green's Function

ℓ/T_f or a/T_f

Fig. 3.13 Compairson of K_t and F_g Decay Curves for Sample Cover Plate Detail
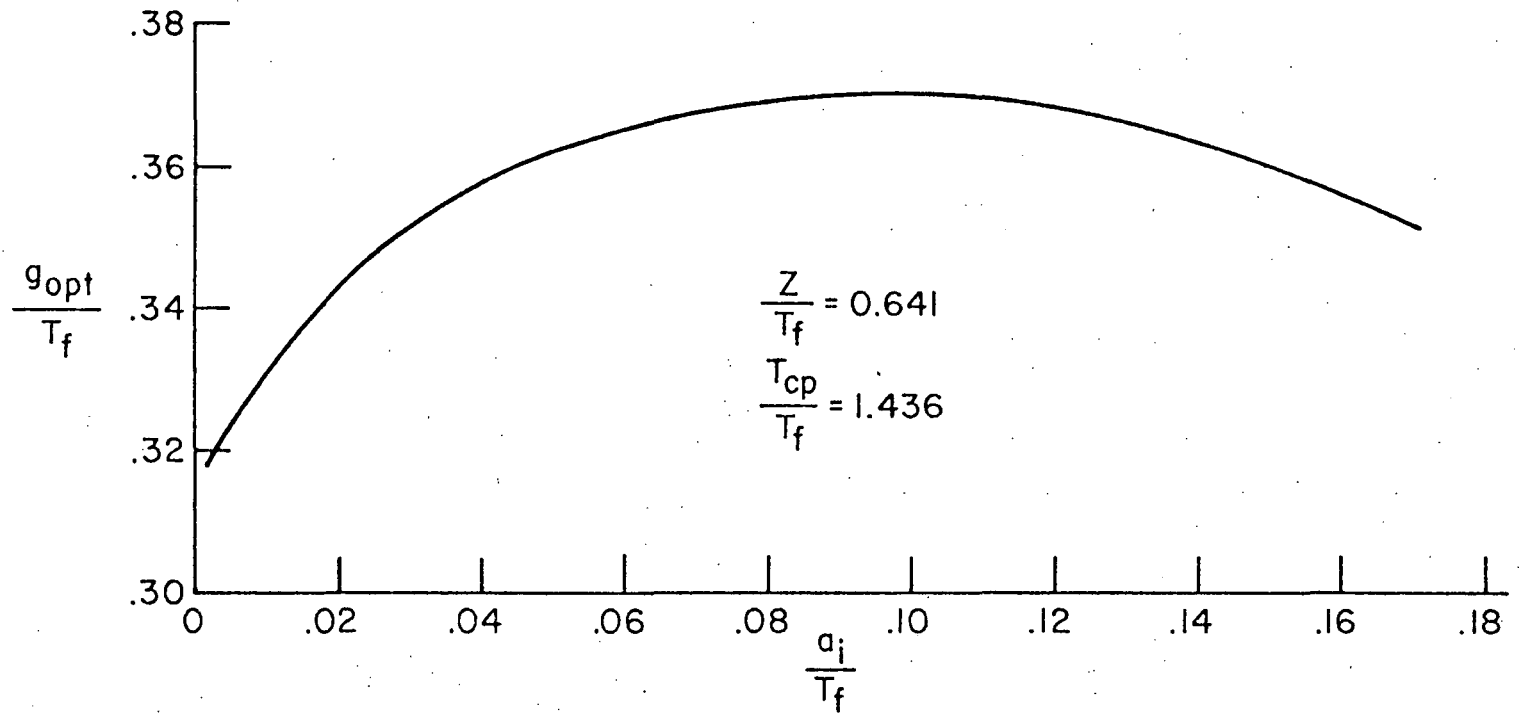
Fig. 3.14 Variation of Optimum Ellipse Size with Initial
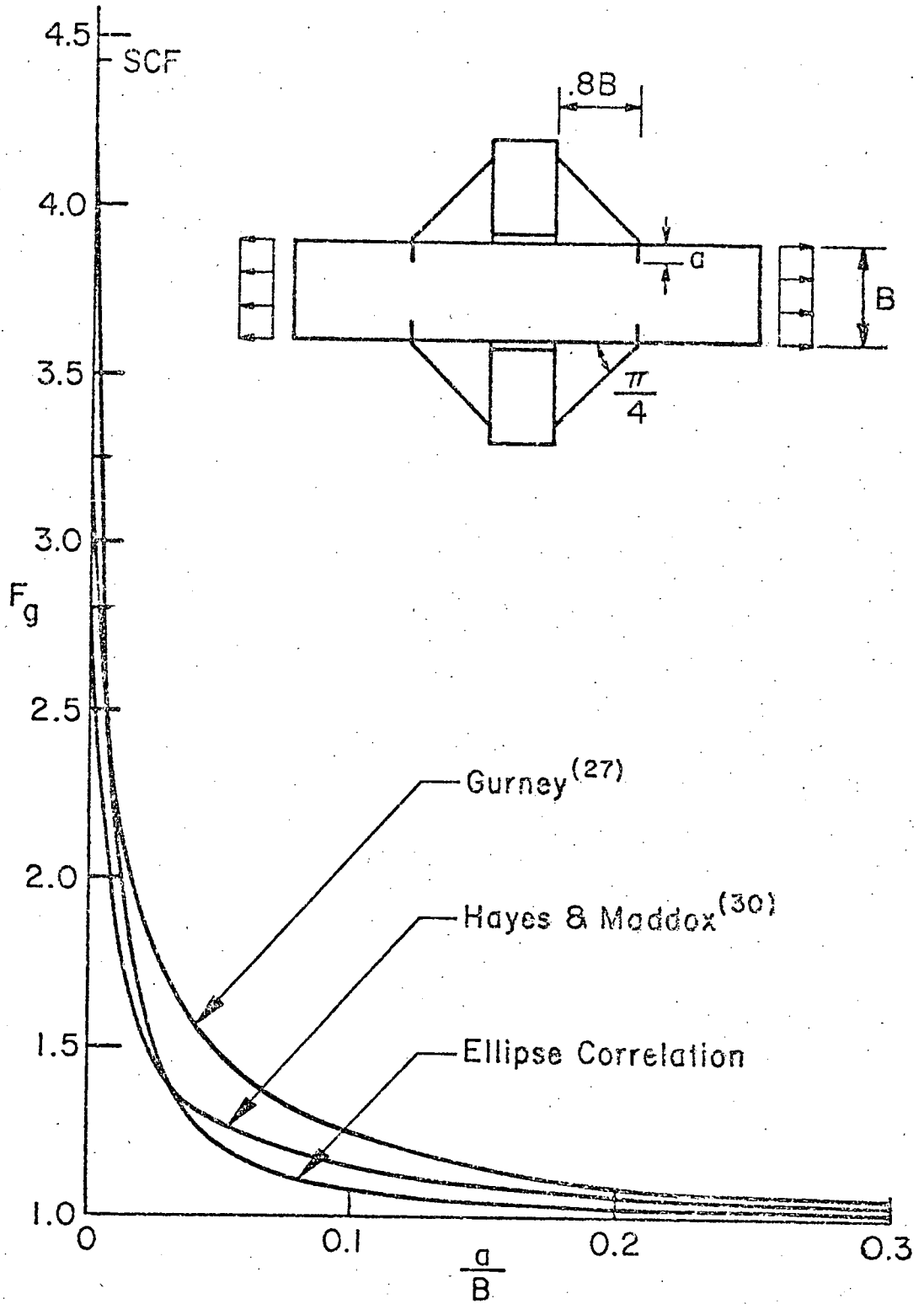Crack Size for Sample Cover Plate Detail

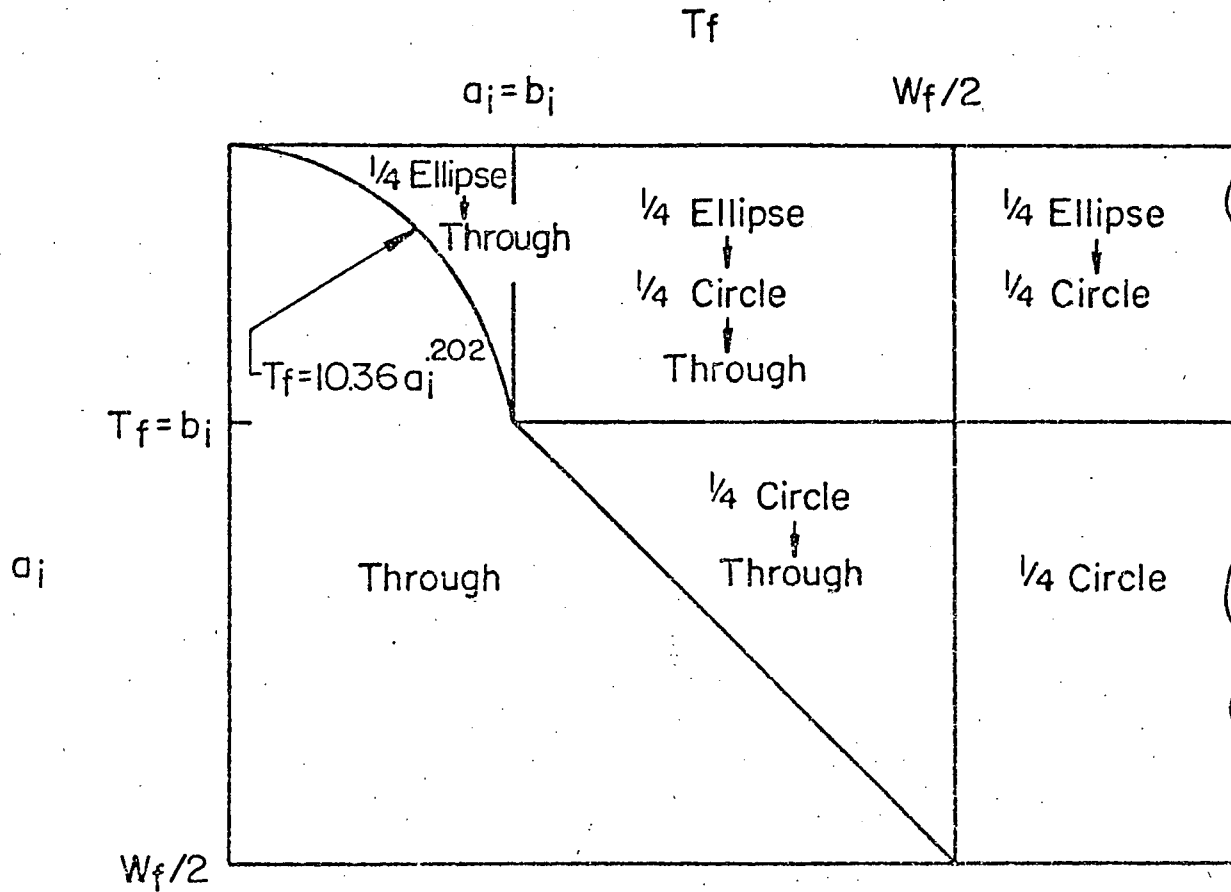Fig. 3.15 Comparison of F_g Decay Curves for Cruciform Joint

-272-

Tf

$a_i = b_i$　　　　　　$W_f/2$

¼ Ellipse
↓
Through

¼ Ellipse
↓
¼ Circle
↓
Through

¼ Ellipse
↓
¼ Circle

$T_f = 10.36\,a_i^{.202}$

$T_f = b_i$

a_i

Through

¼ Circle
↓
Through

¼ Circle

$W_f/2$

Fig. 3.16　Crack Shape Regions for Groove-Welded Gusset Plates
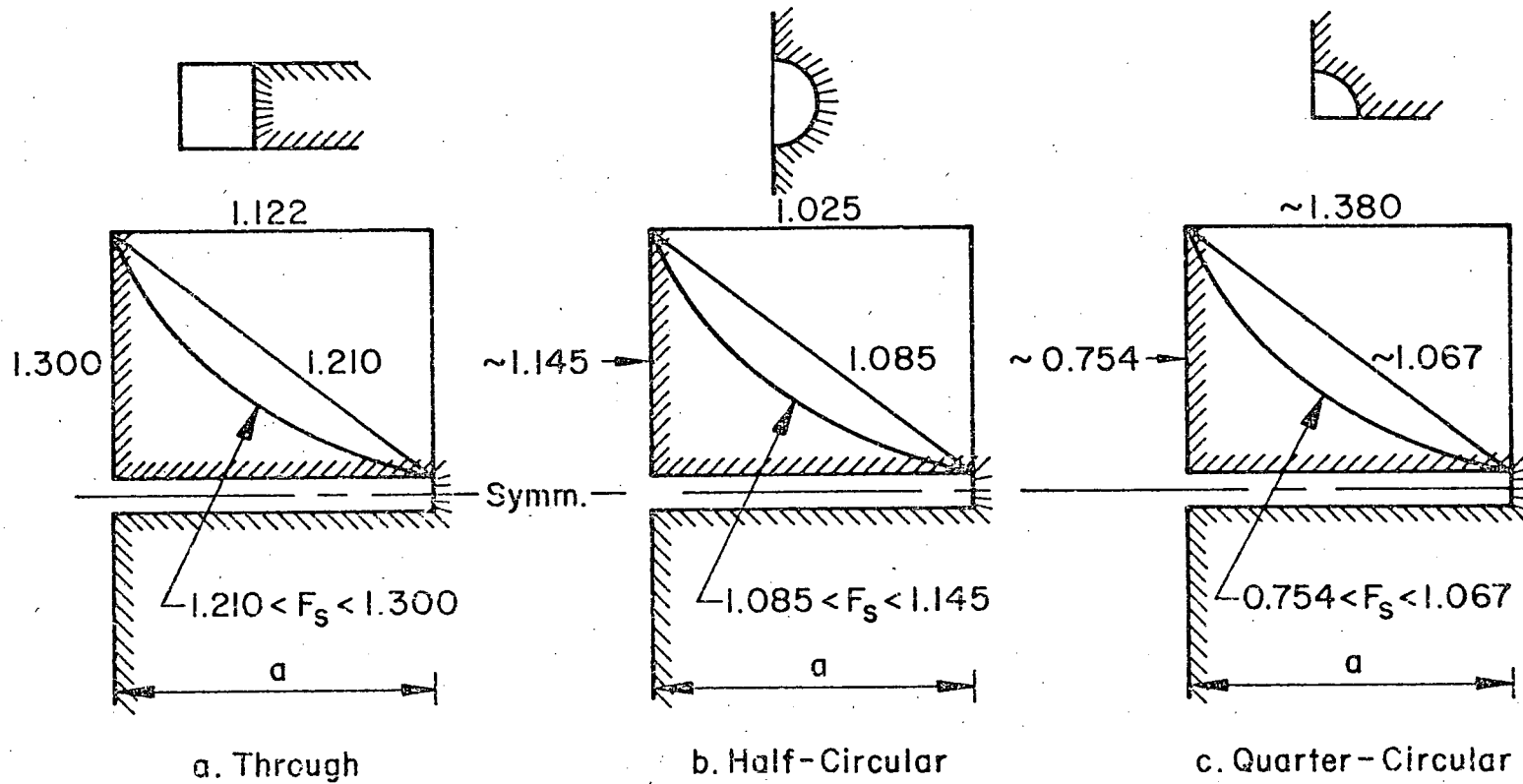
a. Through   b. Half-Circular   c. Quarter-Circular

Fig. 4.1 Front Free Surface Correction Factor for Various Crack Shapes and Stress Distributions[62,76,81,82]

$$\left[\sec\left(\frac{\pi\alpha}{2}\right)\right]^{1/2} \qquad\qquad \left[\frac{2}{\pi\alpha}\tan\left(\frac{\pi\alpha}{2}\right)\right]^{1/2}$$
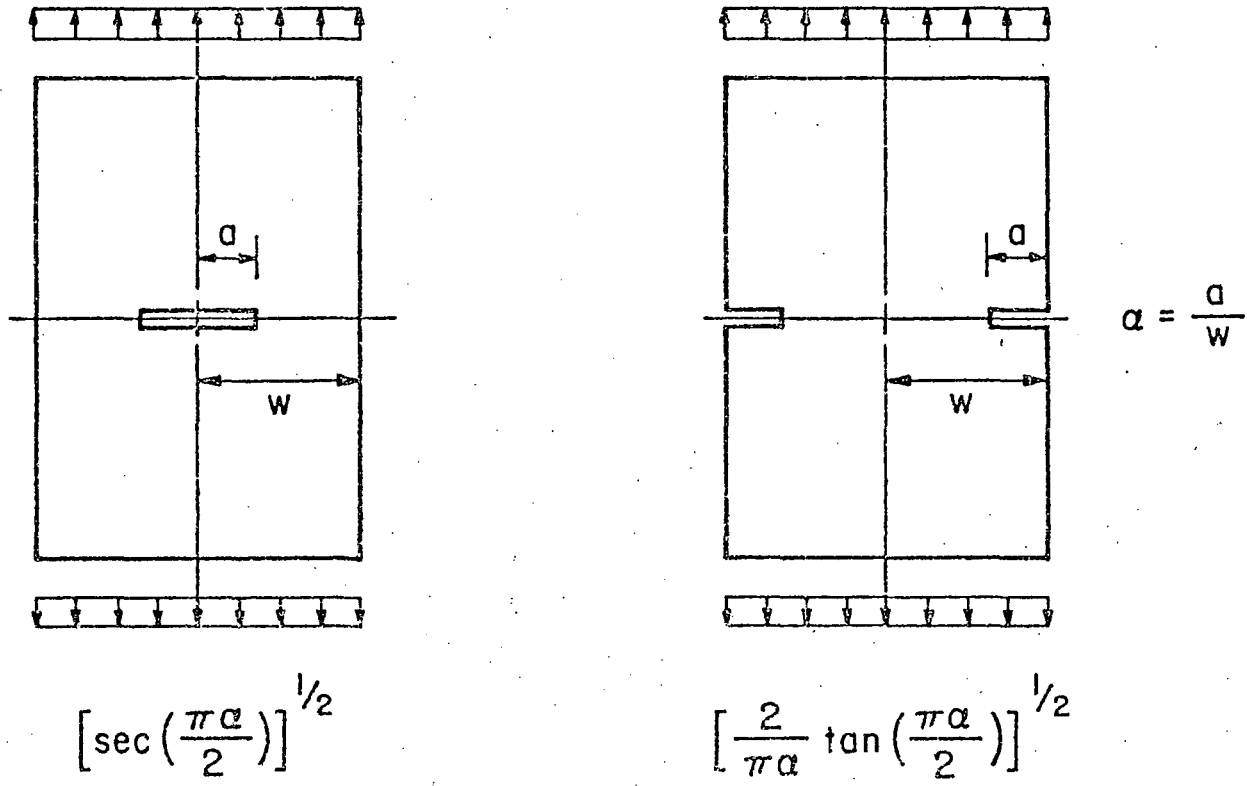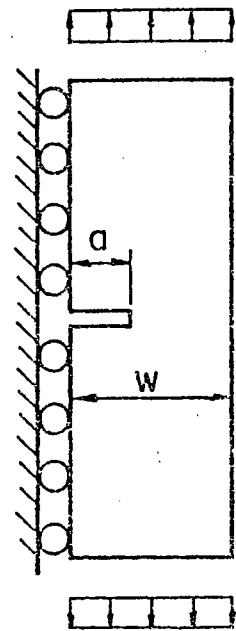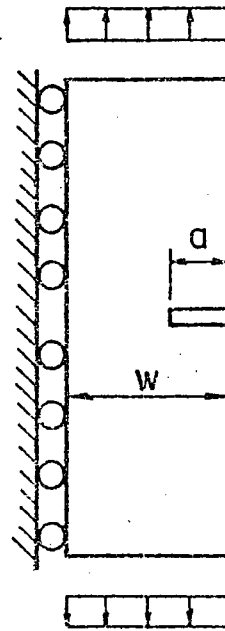
$$\alpha = \frac{a}{w}$$

Fig. 4.2 Back Free Surface Correction Factor for Two, Symmetrical, Through Crack Configurations[62,76,81,82]

$$\left[\sec\left(\frac{\pi\alpha}{2}\right)\right]^{1/2} \qquad\qquad \left[\frac{2}{\pi\alpha}\,\tan\left(\frac{\pi\alpha}{2}\right)\right]^{1/2} \qquad\qquad \alpha = \frac{a}{w}$$

Fig. 4.3 Back Free Surface Correction Factor for Two, Nonsymmetrical, Through Crack Configurations with Bending Prevented
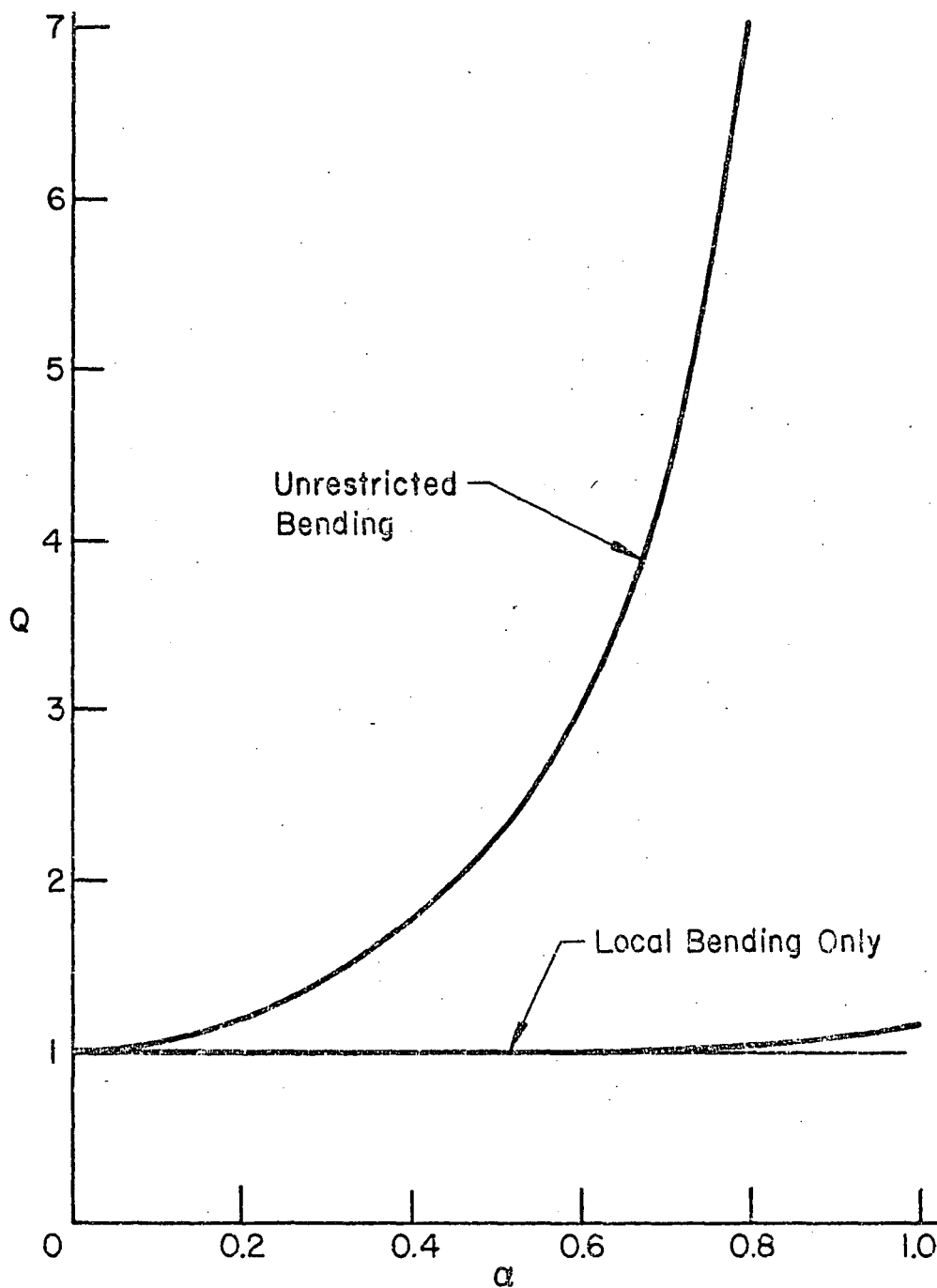
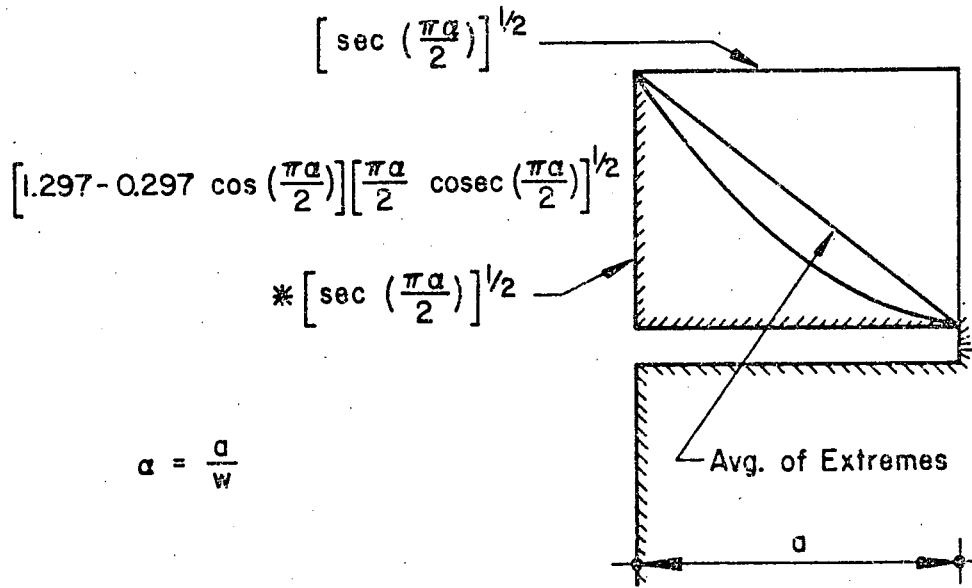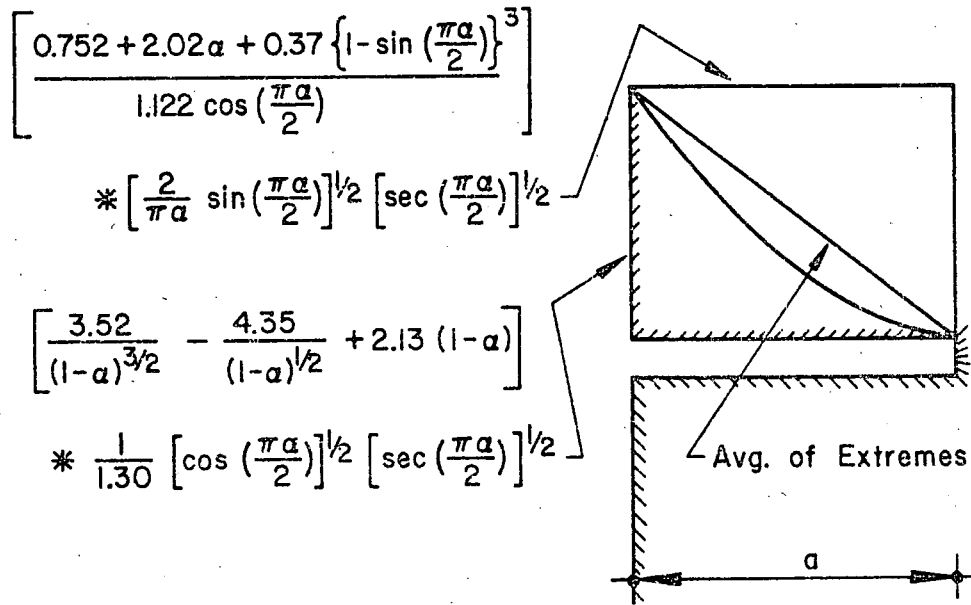Fig. 4.4   Amplification of Back Free Surface Correction Factor
for Unrestricted Bending and Local Bending Only

$$\left[\sec\left(\frac{\pi\alpha}{2}\right) \right]^{1/2}$$

$$\left[1.297 - 0.297 \cos\left(\frac{\pi\alpha}{2}\right) \right]\left[\frac{\pi\alpha}{2} \cosec\left(\frac{\pi\alpha}{2}\right) \right]^{1/2}$$

$$\ast \left[\sec\left(\frac{\pi\alpha}{2}\right) \right]^{1/2}$$

$$\alpha = \frac{a}{W}$$

Avg. of Extremes

a

a) No Bending

$$\left[\frac{0.752 + 2.02\alpha + 0.37\left\{1 - \sin\left(\frac{\pi\alpha}{2}\right)\right\}^3}{1.122 \cos\left(\frac{\pi\alpha}{2}\right)} \right]$$

$$\ast \left[\frac{2}{\pi\alpha} \sin\left(\frac{\pi\alpha}{2}\right) \right]^{1/2} \left[\sec\left(\frac{\pi\alpha}{2}\right) \right]^{1/2}$$

$$\left[\frac{3.52}{(1-\alpha)^{3/2}} - \frac{4.35}{(1-\alpha)^{1/2}} + 2.13(1-\alpha) \right]$$

$$\ast \frac{1}{1.30} \left[\cos\left(\frac{\pi\alpha}{2}\right) \right]^{1/2} \left[\sec\left(\frac{\pi\alpha}{2}\right) \right]^{1/2}$$

Avg. of Extremes

a

b) Bending

Fig. 4.5   Back Free Surface Correction Factor for Through
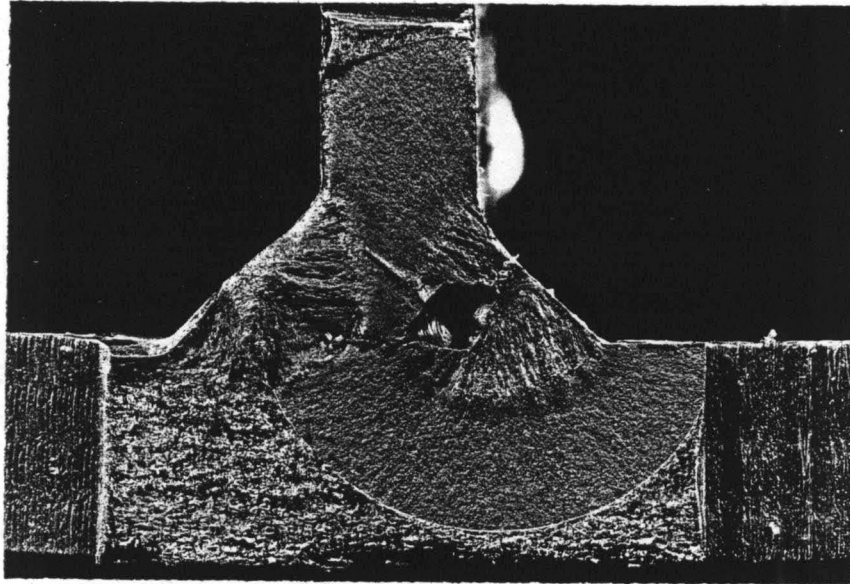Cracks with Various Stress Distributions

-278-

Fig. 4.6 Fatigue Crack Growth from Gas Pore in
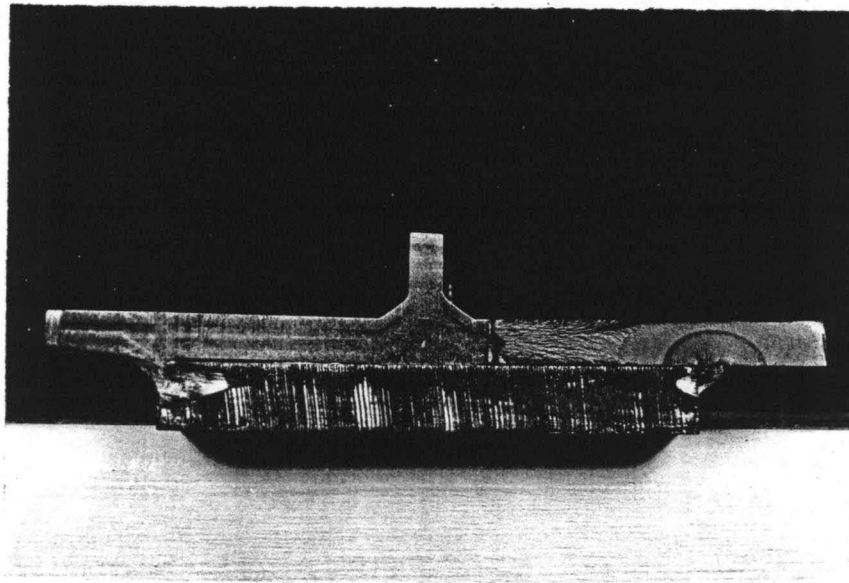Web-to-Tension Flange Fillet Weld[19]

Fig. 4.7 Fatigue Crack Growth from Termination of
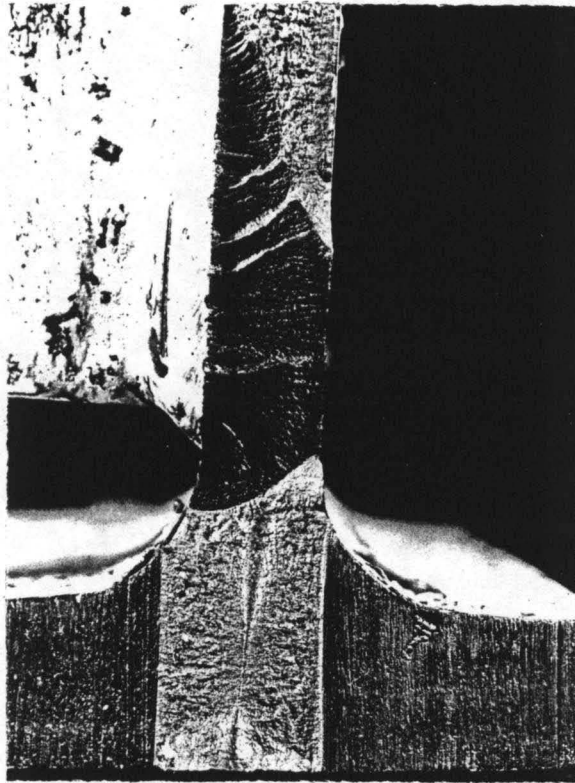Longitudinal Cover Plate-to-Flange Fillet Weld[19]

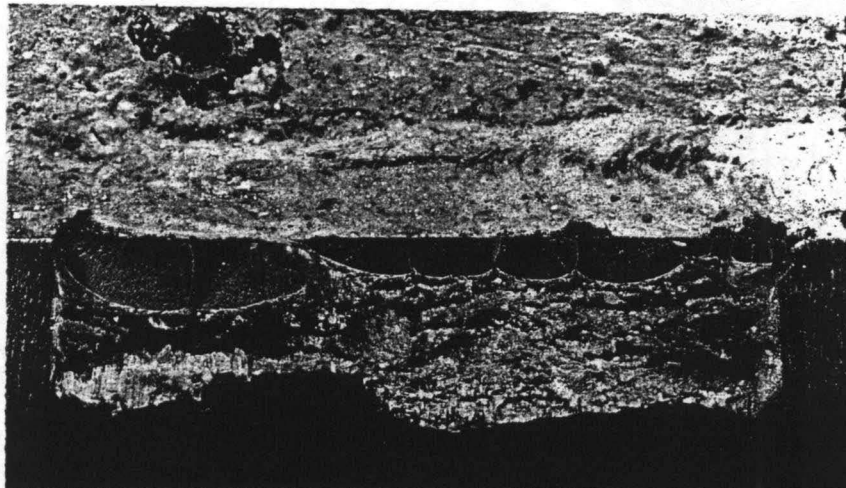Fig. 4.8   Fatigue Crack Growth at Termination of
Stiffener-to-Web Fillet Weld[20]

Fig. 4.9   Multiple Fatigue Crack Growth at Toe of
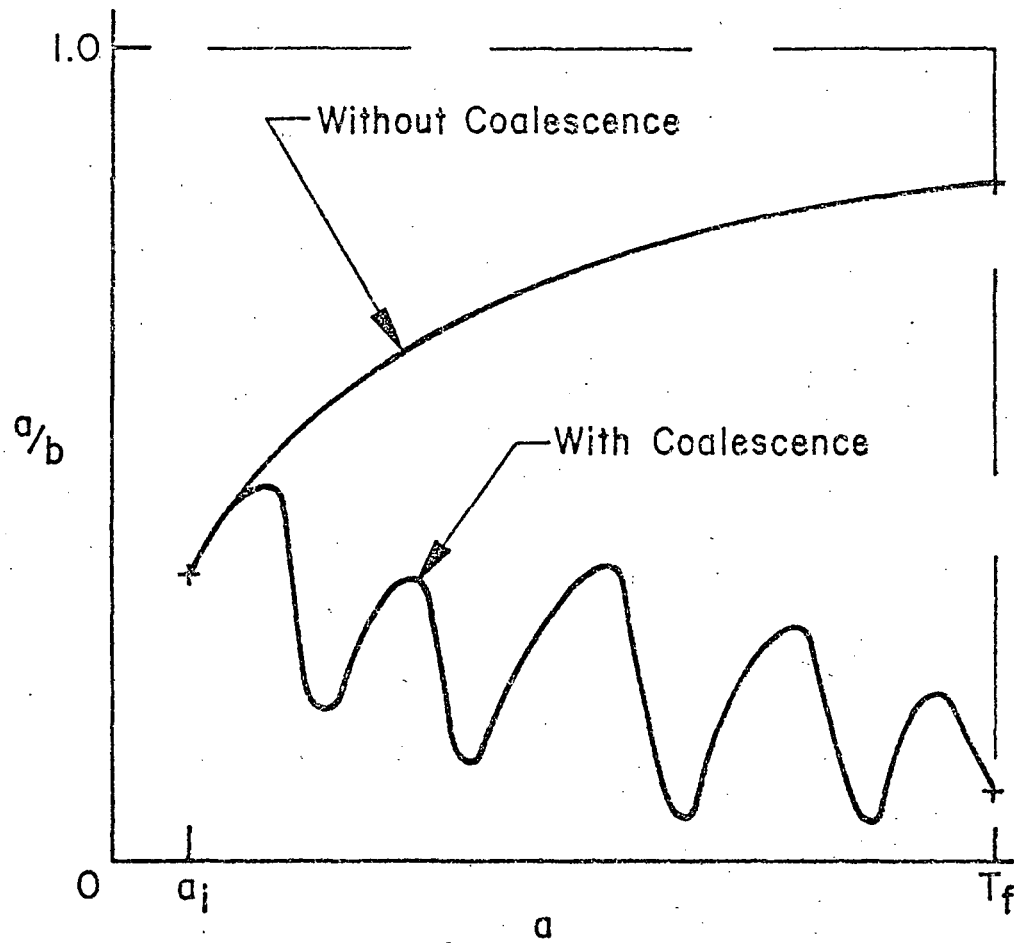Stiffener-to-Tension Flange Fillet Weld[20]

Fig. 4.10   Schematic Crack Shape Variation for Details
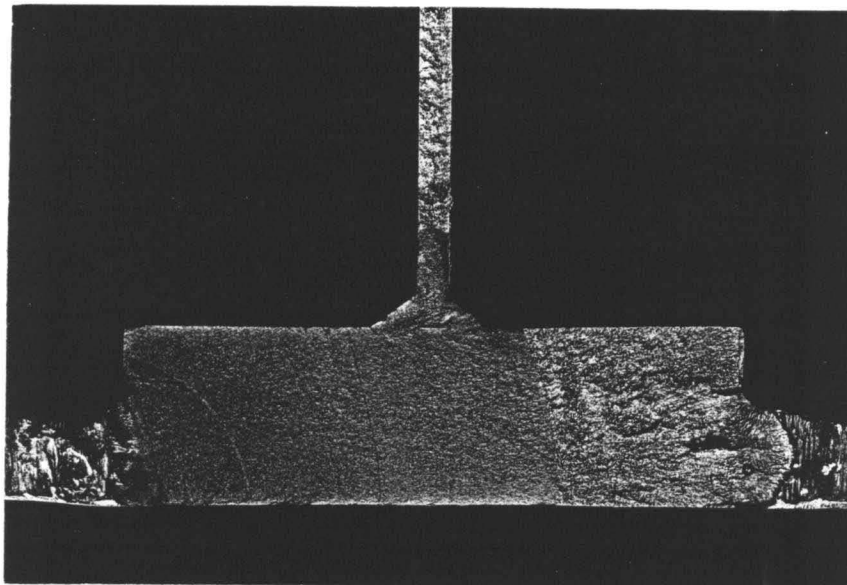With and Without Coalescence of Surface Cracks

Fig. 4.11   Fatigue Crack Growth from Circular Transition
of Groove-Welded Gusset Plate[12]
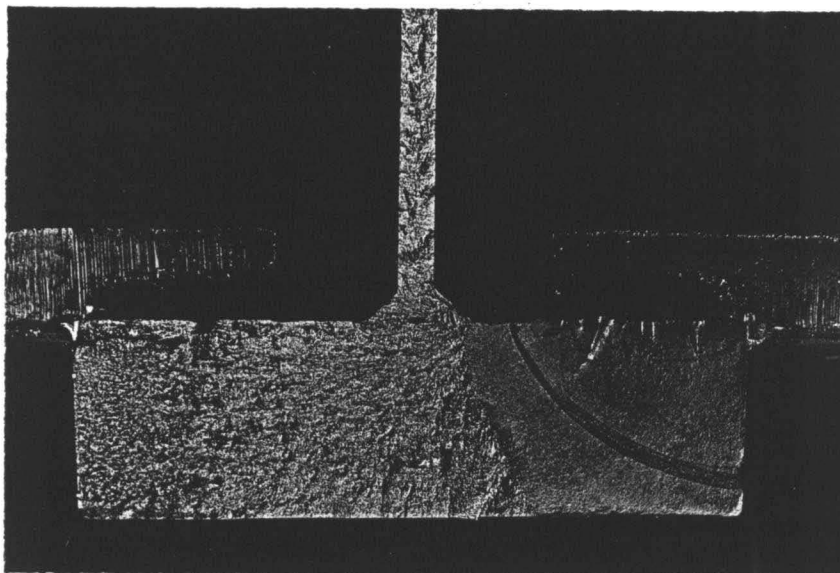
Fig. 4.12   Fatigue Crack Growth from Fillet Weld Toe
of Lap-Welded Gusset Plate[12]

Fillet
8mm

12.7mm

152 mm

a) Sections

100 mm

610 mm

b) Plan View
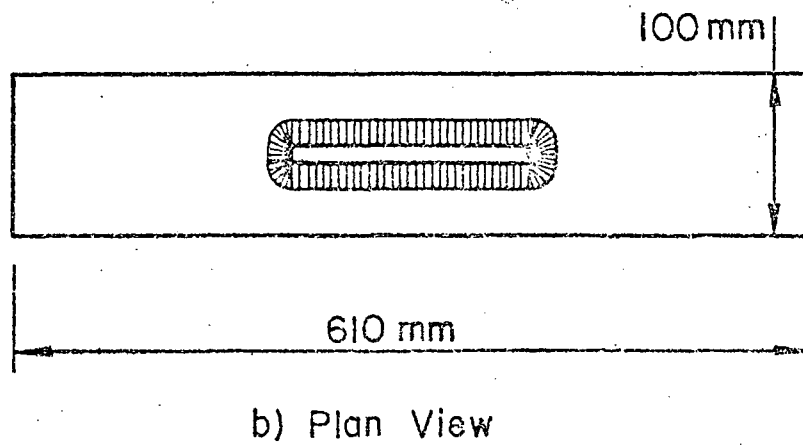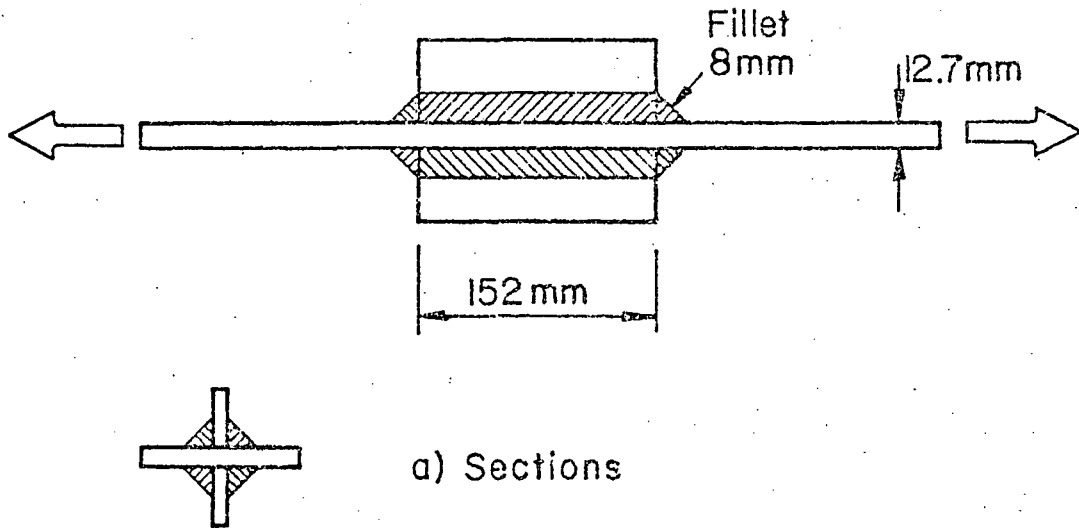
Fig. 4.13   Maddox Gusset Detail for Development
of Crack Shape Variation Equation[51]
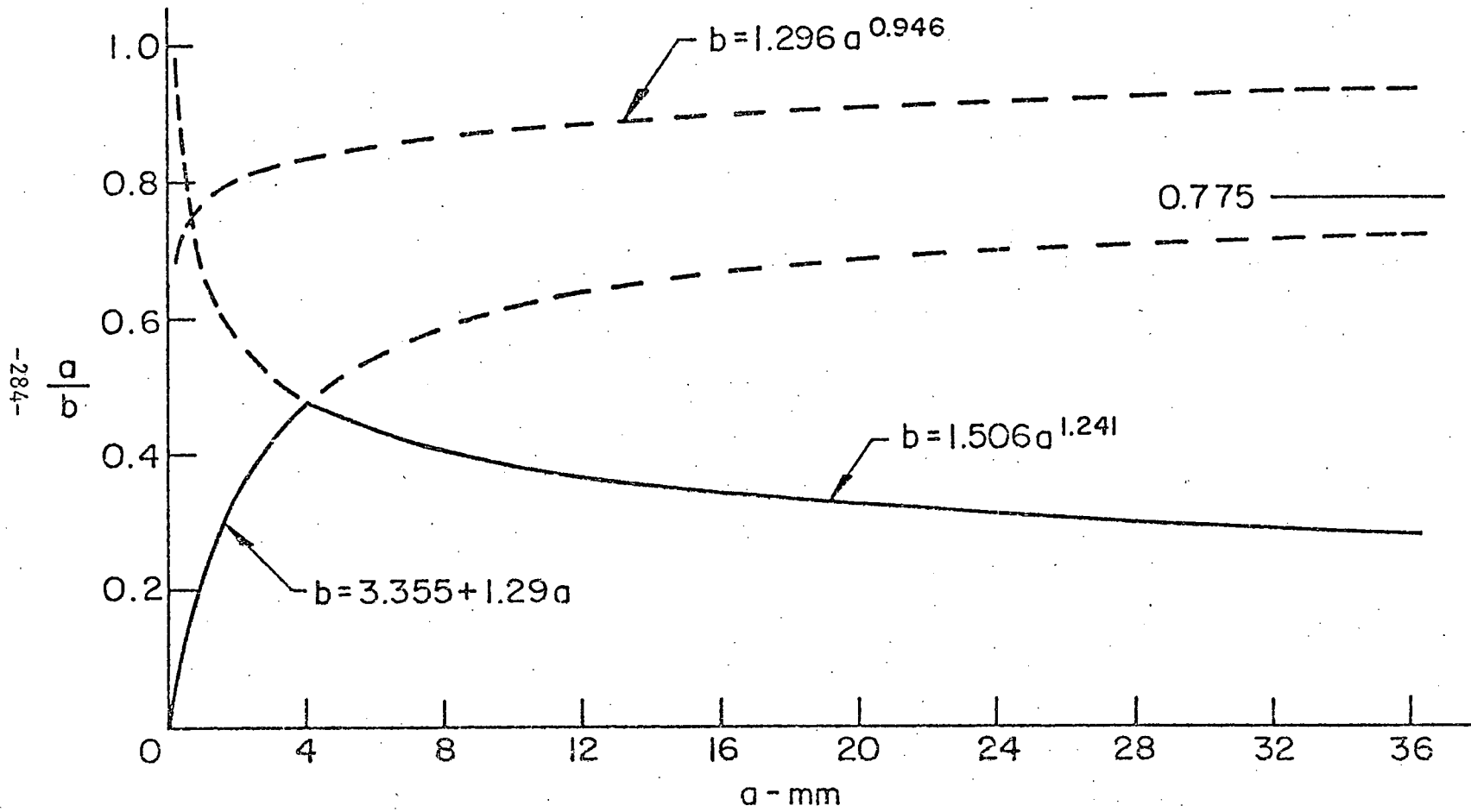
Fig. 4.14 Crack Shape Variation with Crack Depth

$$\alpha = \frac{a}{w} \qquad \lambda = \frac{\ell}{w}$$
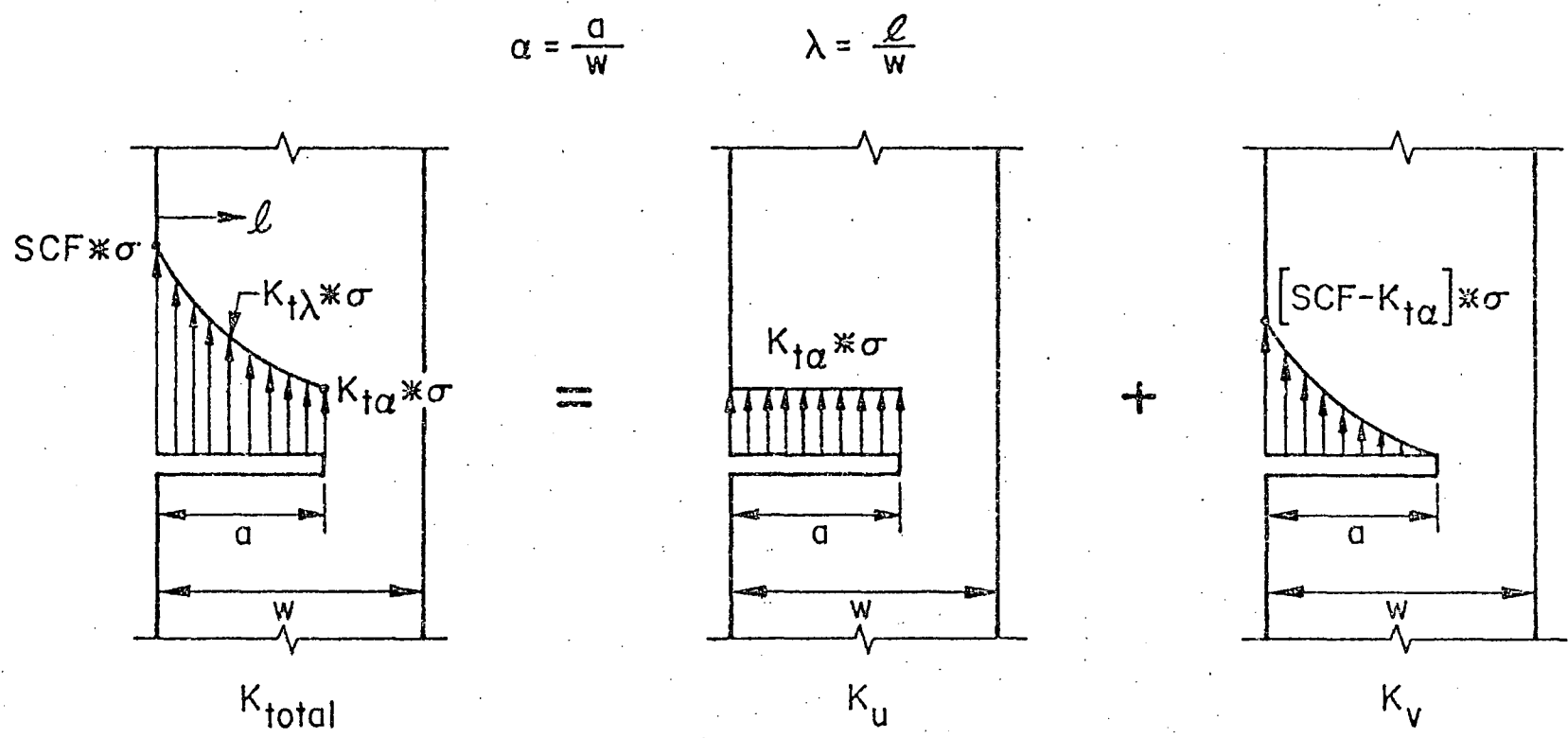
Fig. 5.1   Superposition of Stress Intensity Factors
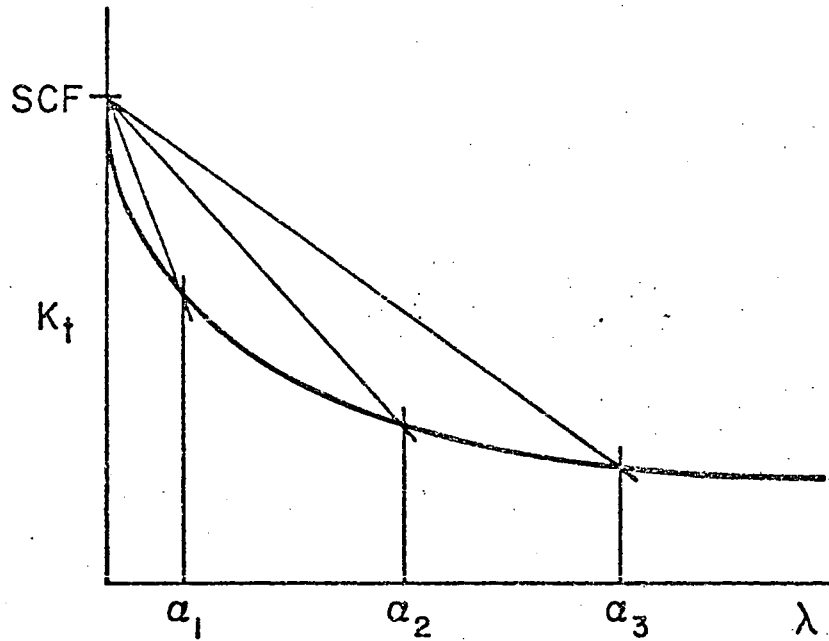
(a) Proximity of variable stress subdistribution to linearity as a function of a
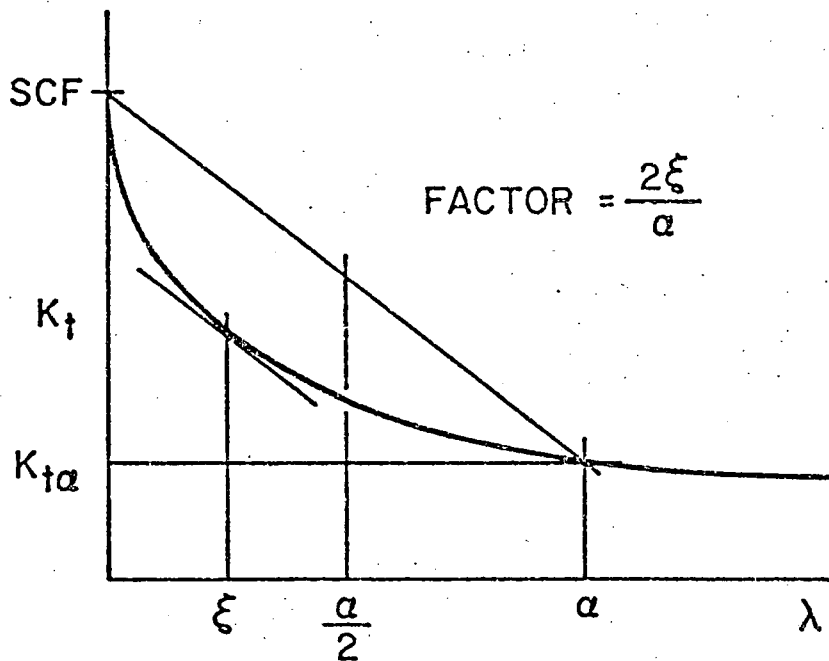
$$\text{FACTOR} = \frac{2\xi}{a}$$

(b) FACTOR evaluation based on chord slope

Fig. 5.2 F_s Estimation for Variable Stress Subdistribution
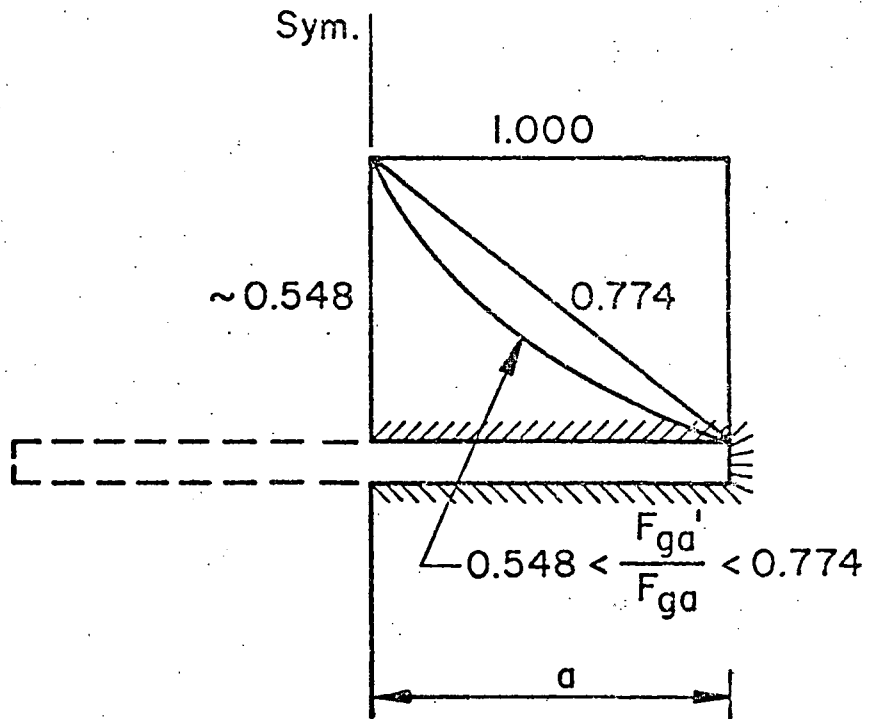
Fig. 5.3 Ratio of Circular to Through Crack Stress Gradient
Correction Factors for Various Stress Distributions
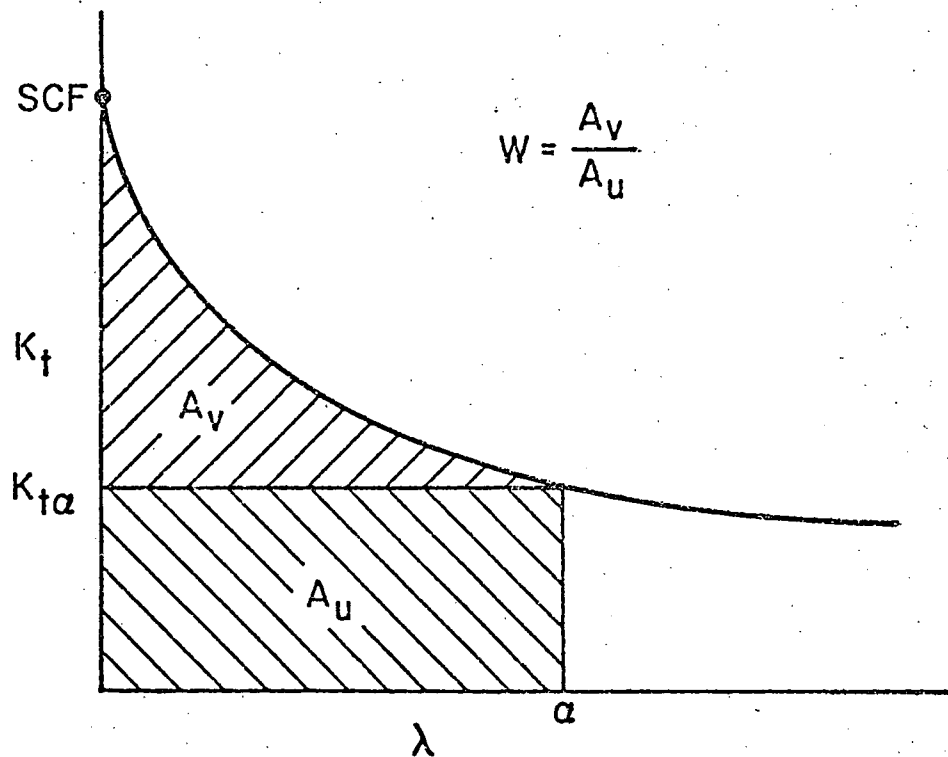
Fig. 5.4 Evaluation of Weighting Factor for Modifying Through
Crack Stress Gradient Correction Factor
Due to Crack Shape
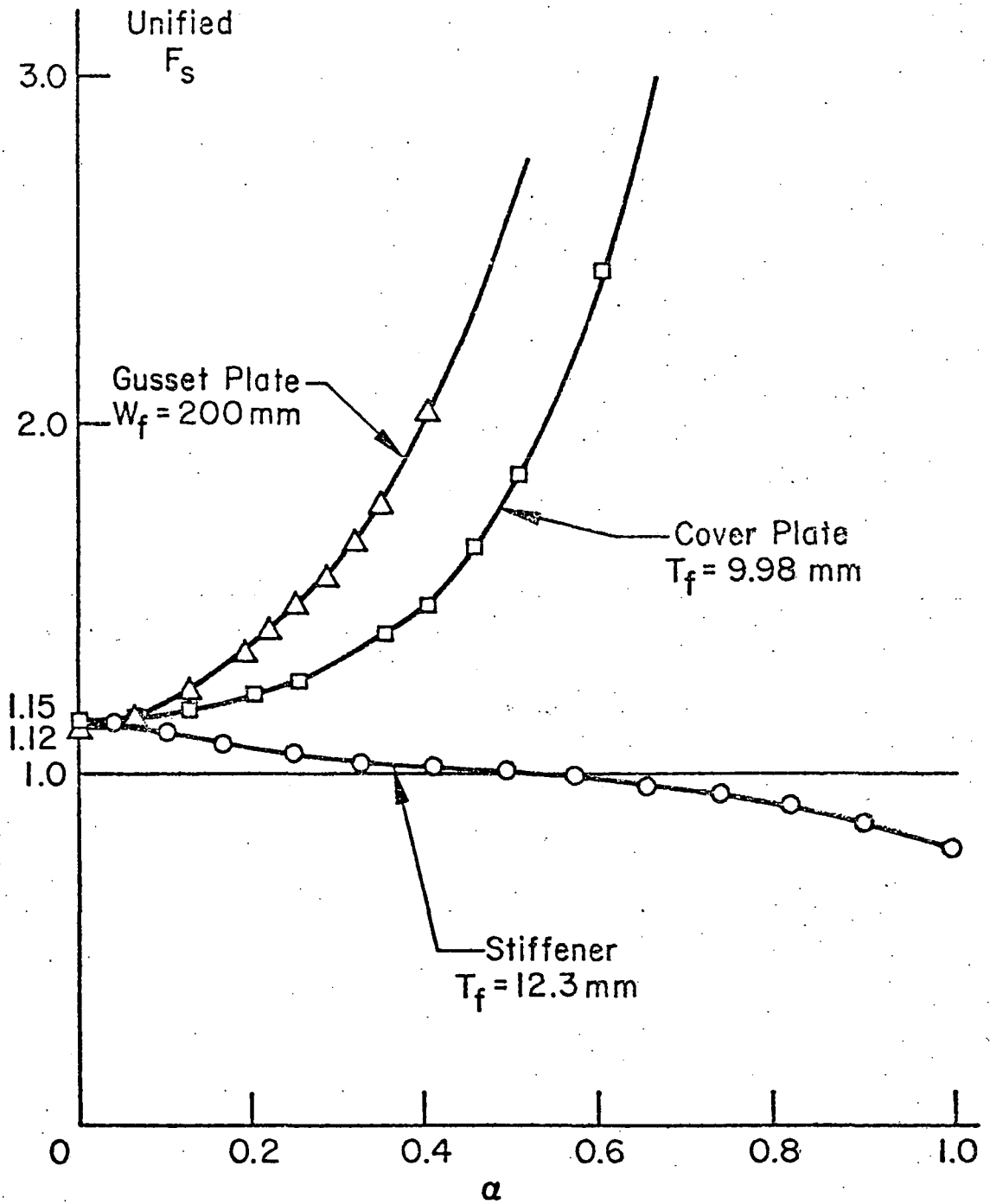
Fig. 5.5 Comparison of Unified Front Free Surface Correction
Factors for Typical Welded Details
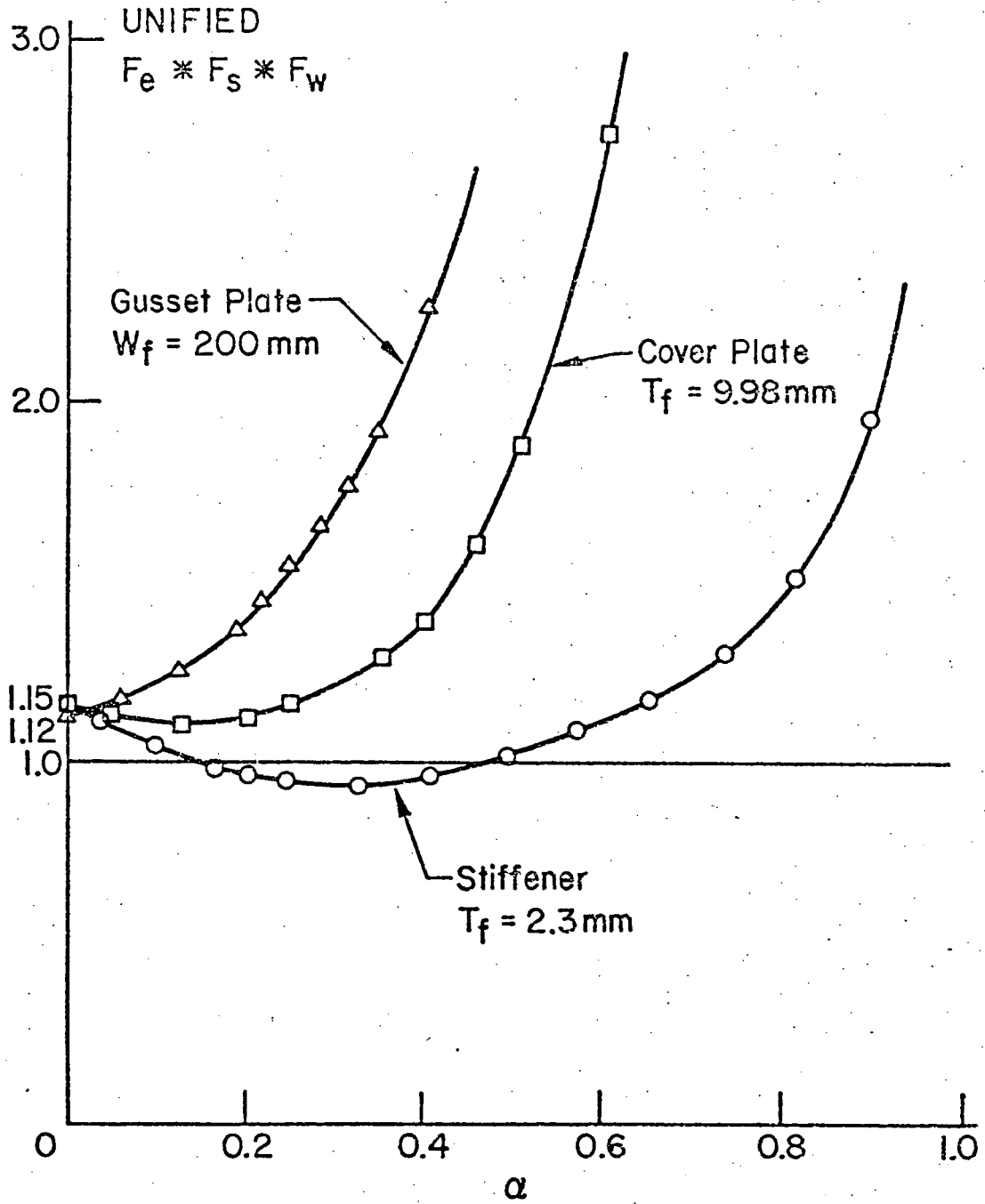
Fig. 5.6   Comparison of Collective Unified Correction Factors
for Typical Welded Details

The figure shows a log-log plot of S_r (MPa) versus Cycle Life with the following annotations:

95% Confidence Limits

a_i - mm

Unified Estimates:
- ■ 0.076
- ▲ 0.508

$\log(.96N) = 13.5165 - 3.505 \log S_r$

$s = 0.1024$

(Ref. 20)

$\log(.96N) = 12.6644 - 3.097 \log S_r$
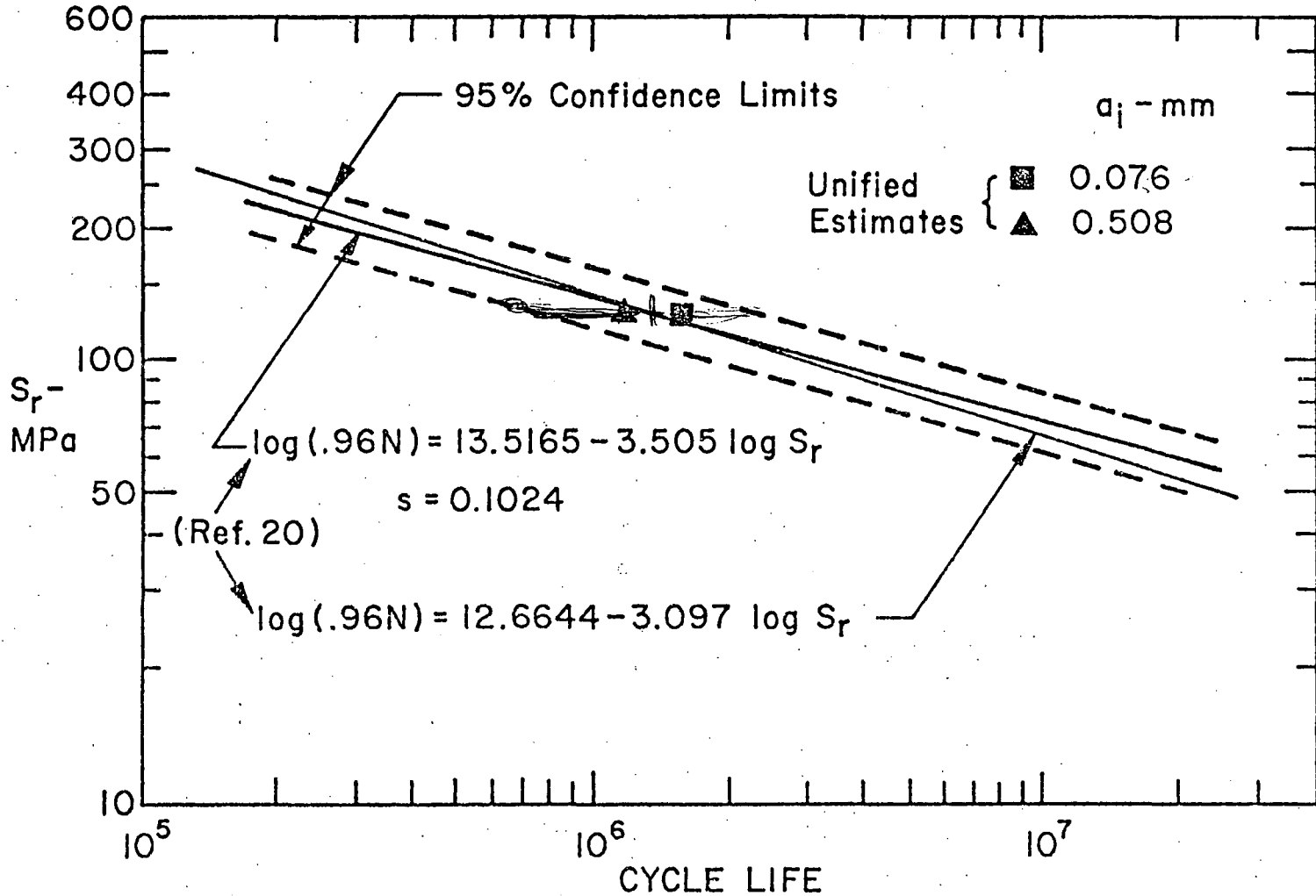
Fig. 6.1 Fatigue Life Estimates for Stiffeners Fillet-Welded to Flanges
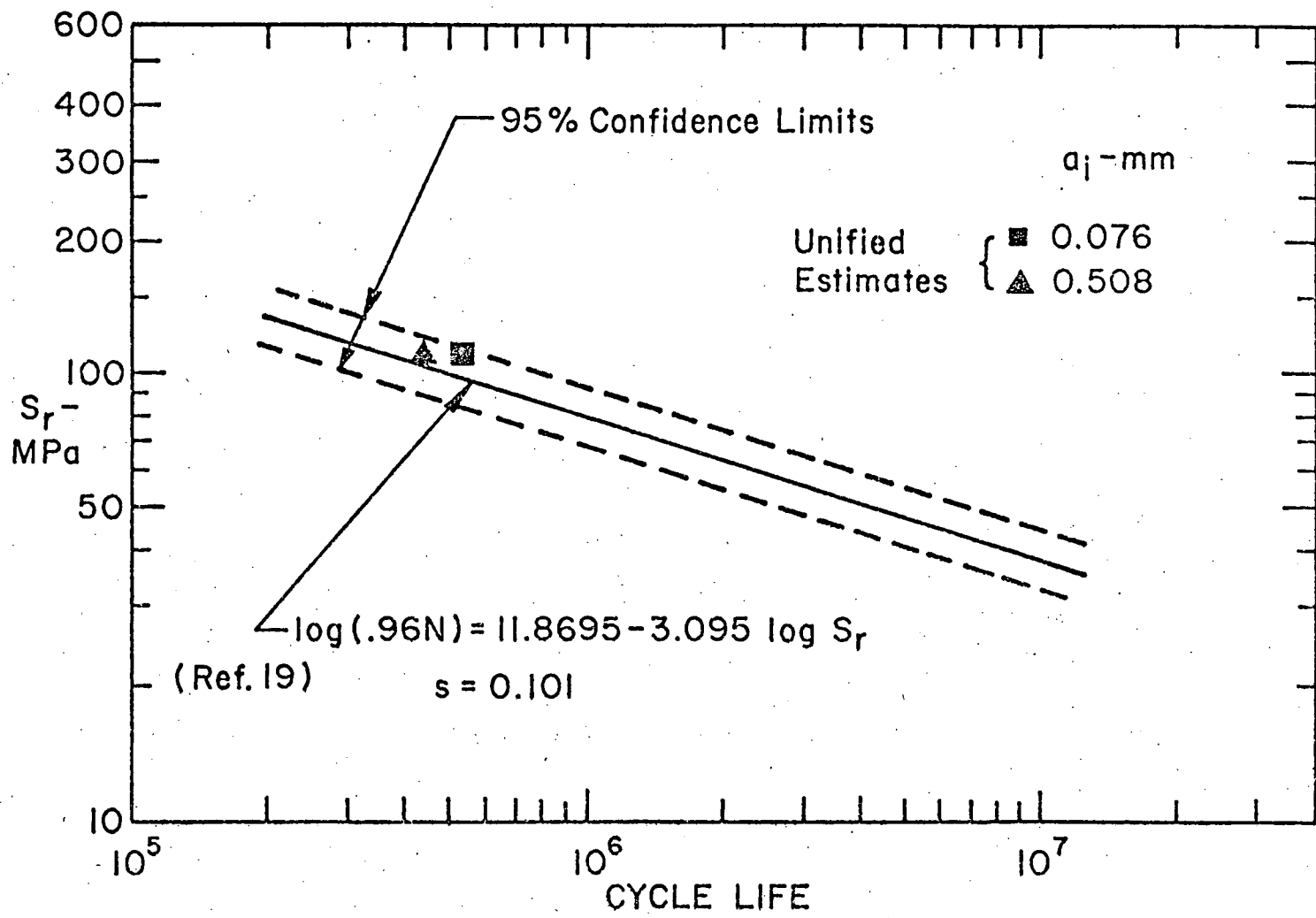
Fig. 6.2 Fatigue Life Estimates for Cover Plates with Transverse End Welds
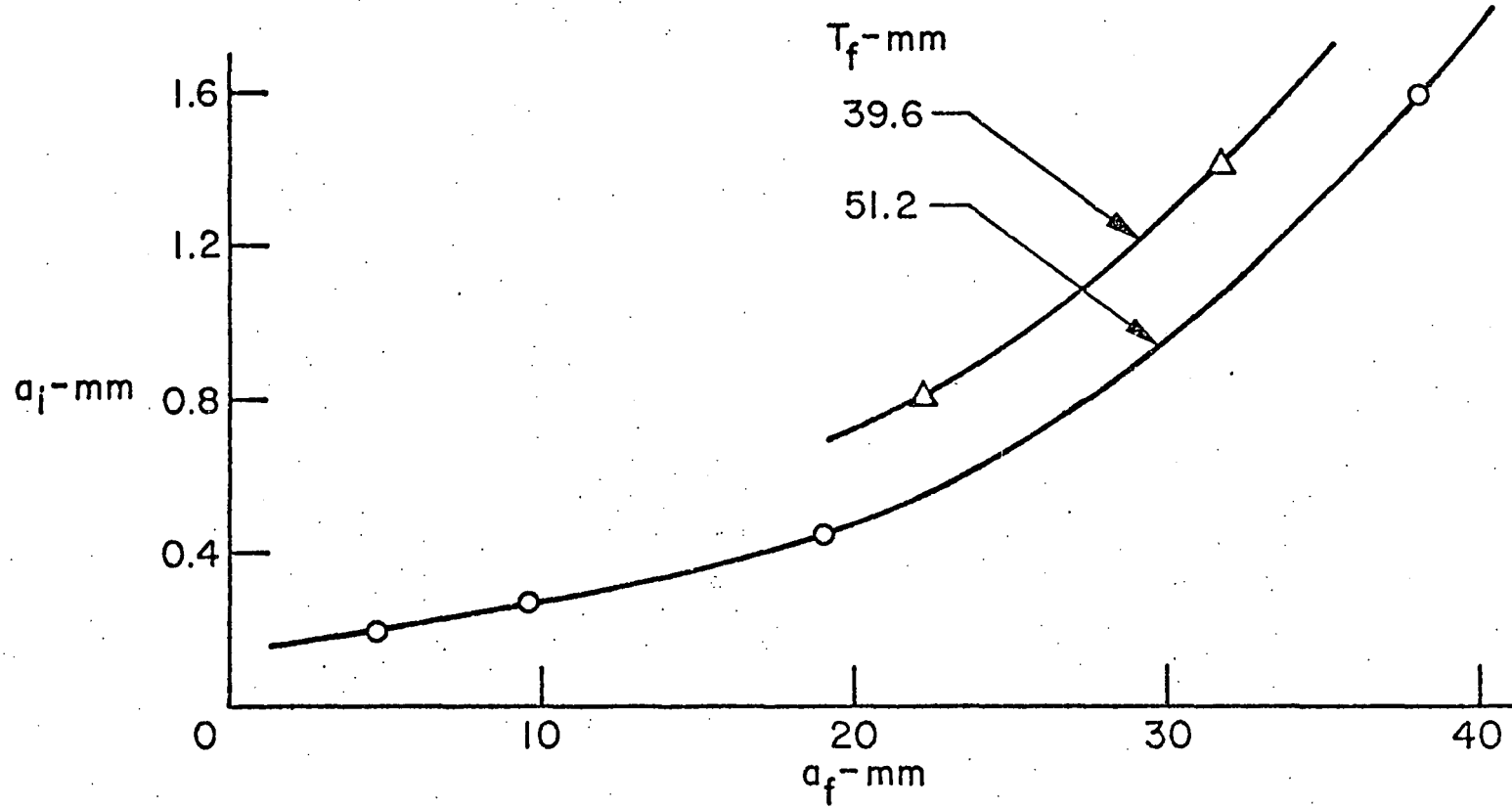
Fig. 6.3 Required Initial Crack Size for Given Final Crack Size and Two Million Cycles[12]
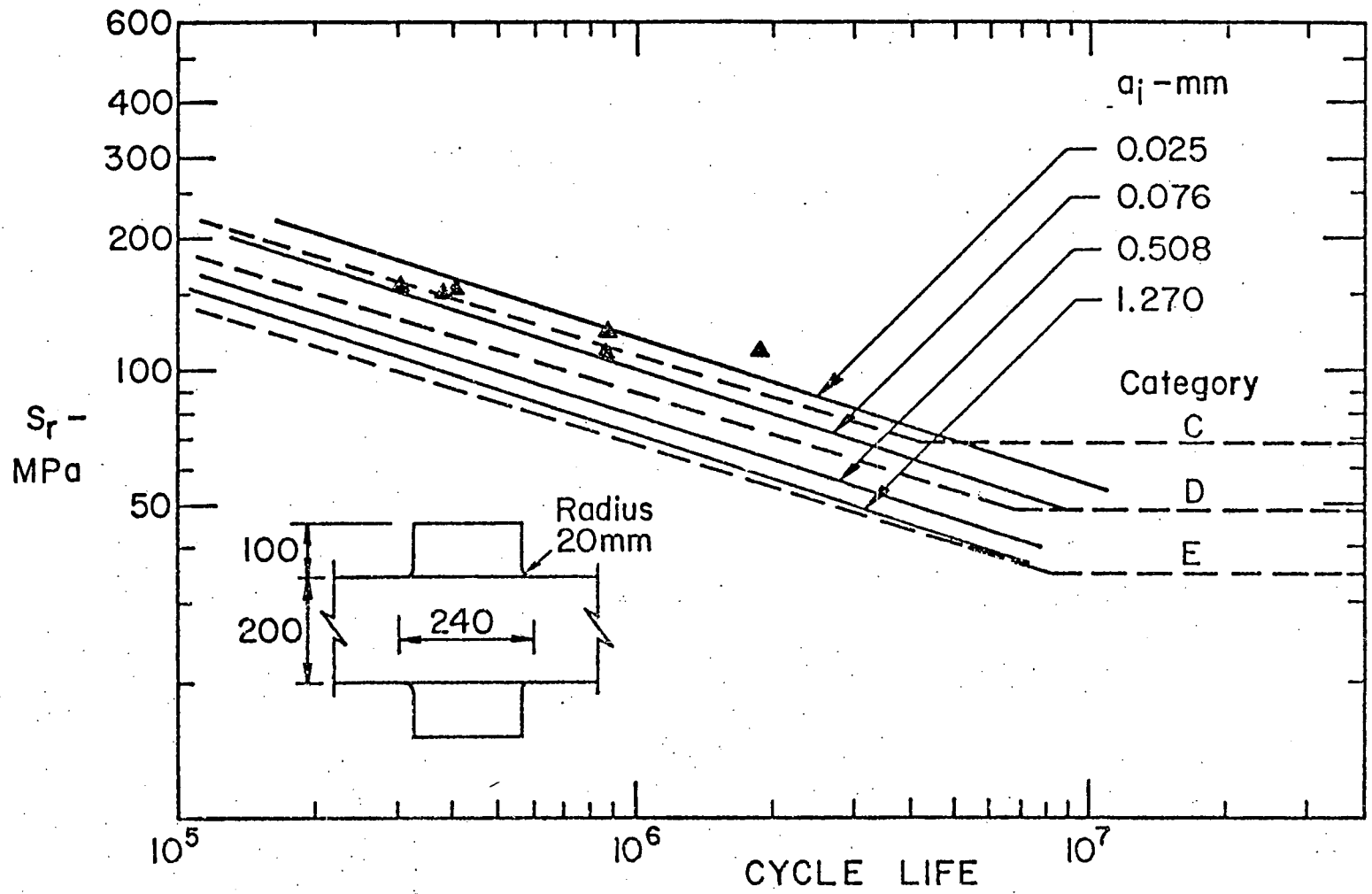
Fig. 6.4   Comparison of Actual and Estimated Fatigue Lives of CECA,
Groove-Welded Gusset Plate, Geometry A[16]
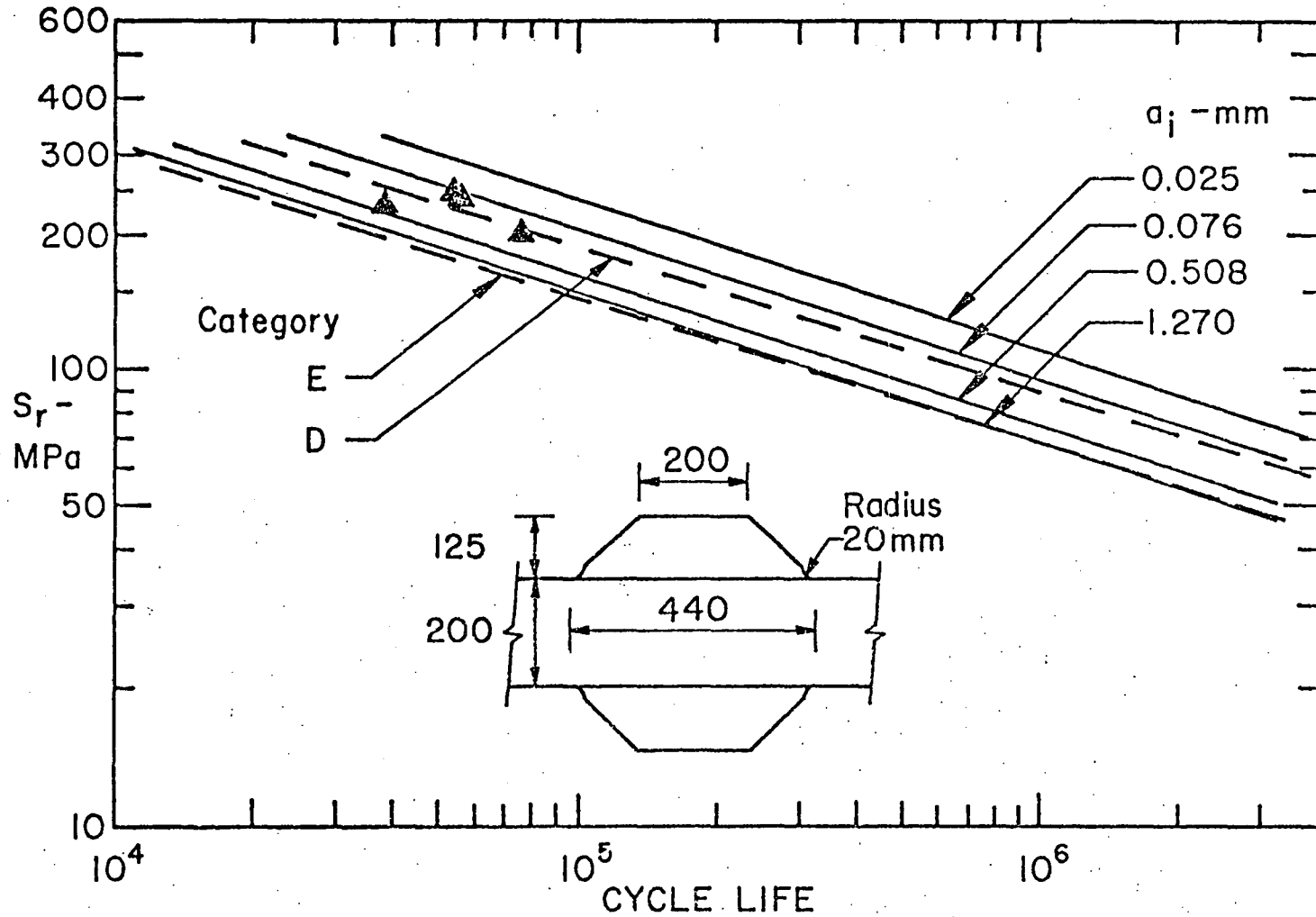
Fig. 6.5 Comparison of Actual and Estimated Fatigue Lives of CECA,
Groove-Welded Gusset Plate, Geometry B[16]
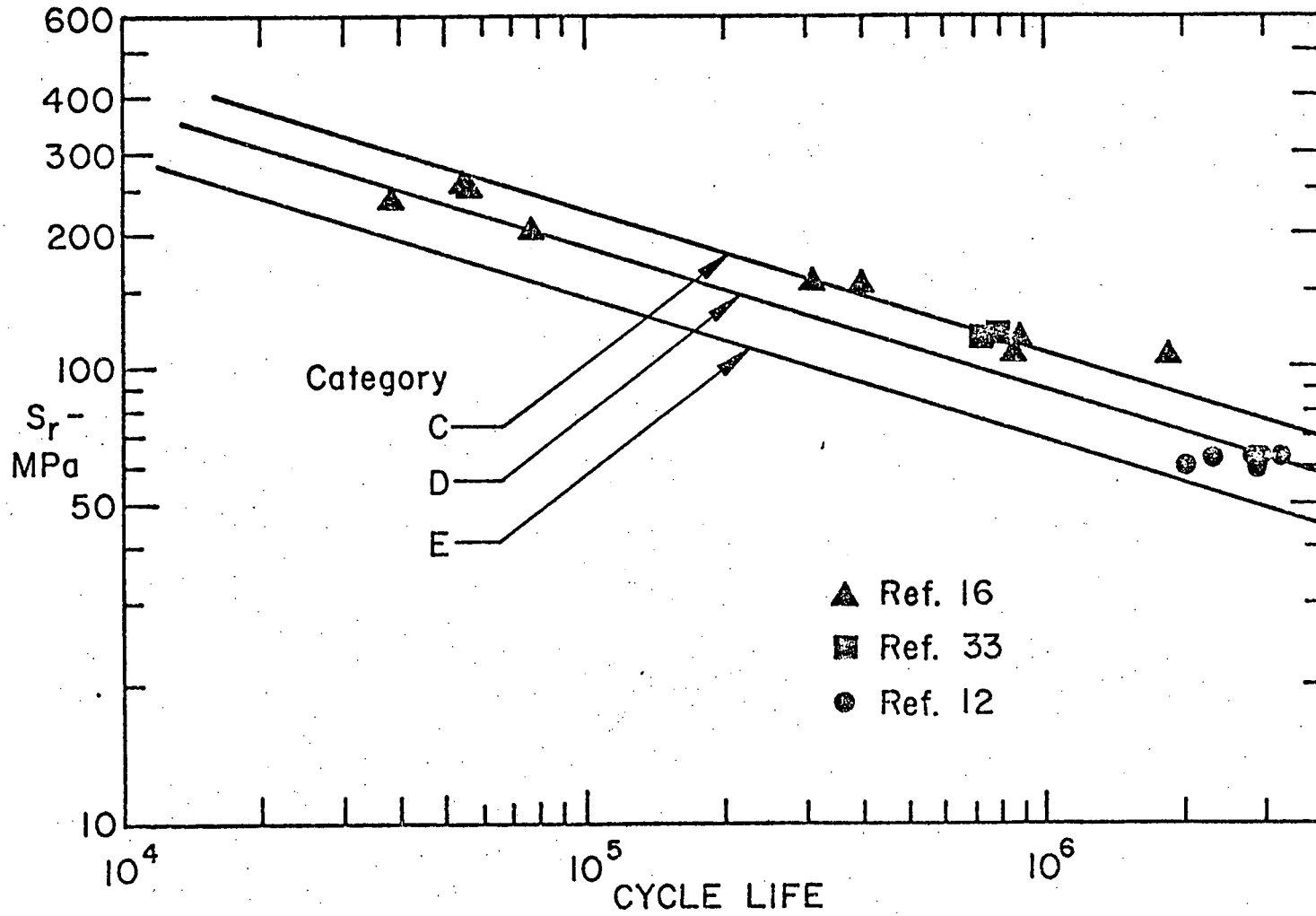
Fig. 6.6 Comparison of Fatigue Lives of Groove-Welded
Gusset Plates with AASHTO Category Curves
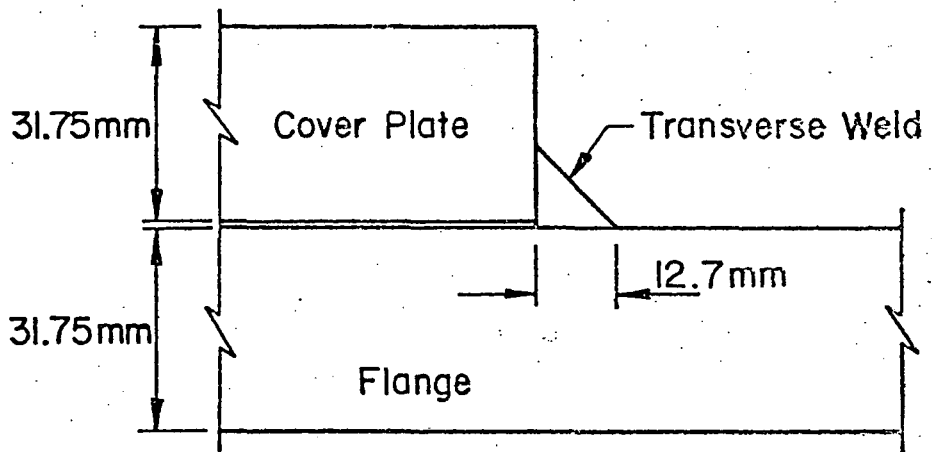
Fig. 6.7 Cover Plate Detail – Yellow Mill Pond Bridge[10,40]
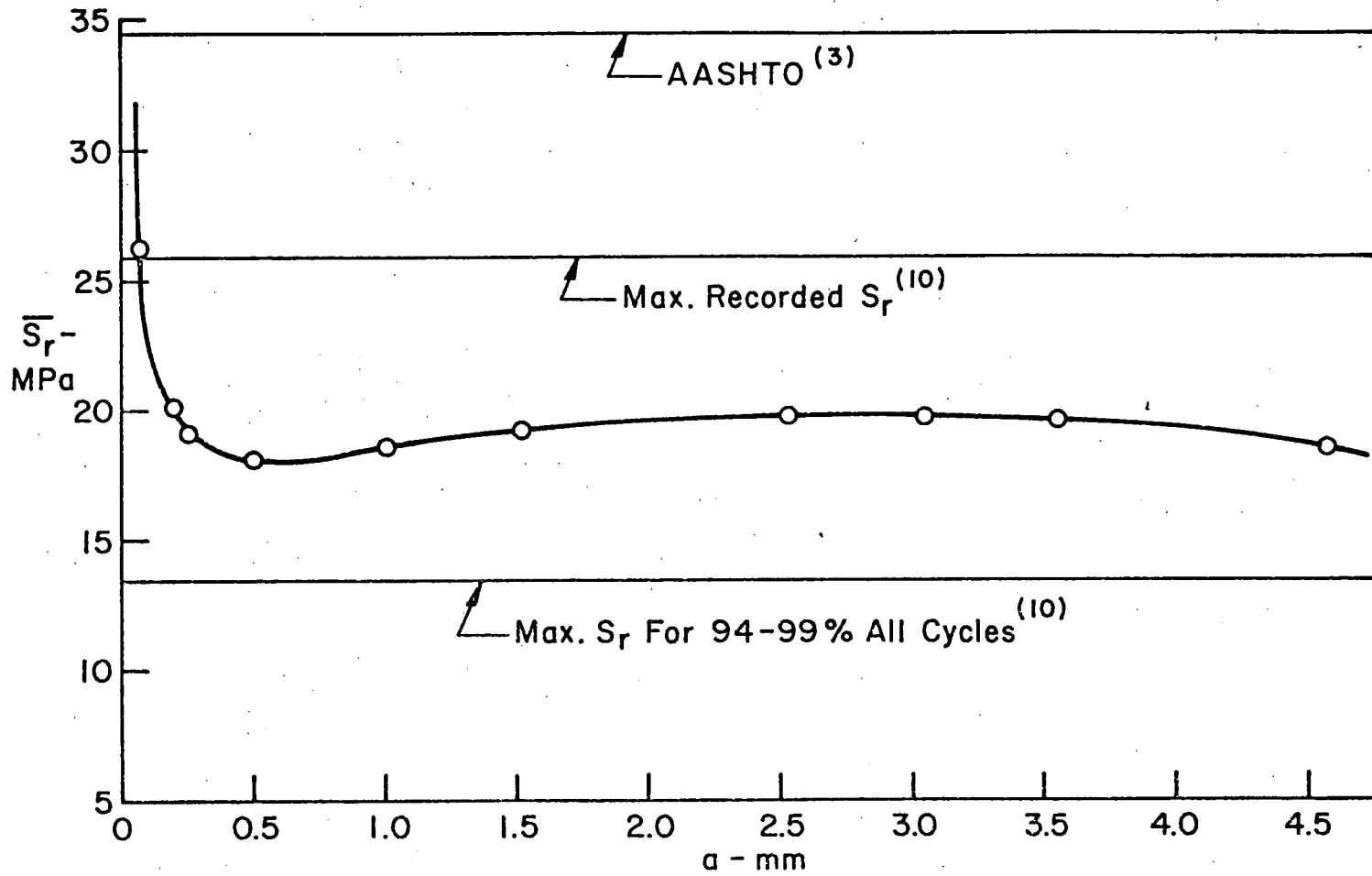
Fig. 6.8 Fatigue Limit Variation with Crack Size – Yellow Mill Pond Bridge[10,40]

REFERENCES

1. Abramowitz, M. and Stegun, L. A., eds.
        HANDBOOK OF MATHEMATICAL FUNCTIONS, Applied Mathematics
        Series, No. 55, National Bureau of Standards, Washington,
        D. C., June, 1964, p. 752

2. Albrecht, P. and Yamada, K.
        RAPID CALCULATION OF STRESS INTENSITY FACTORS,
        (Submitted for publication in ASCE Journal of the
        Structural Division)

3. AASHTO Subcommittee on Bridges and Structures
        INTERIM SPECIFICATIONS BRIDGES 1974, American Association
        of State Highway and Transportation Officials,
        Washington, D. C., 1974

4. AASHO Subcommittee on Bridges and Structures
        STANDARD SPECIFICATIONS FOR HIGHWAY BRIDGES, American
        Association of State Highway Officials, Washington, D. C.,
        1973

5. ASTM Committee on Fracture Testing of High Strength Sheet
    Materials
        REPORT NO. 1, ASTM Bulletin, American Society for Testing
        and Materials, Philadelphia, Pa., January, 1960, p. 29

6. Barsom, J. M.
        FATIGUE BEHAVIOR OF PRESSURE-VESSEL STEELS, Welding Research
        Council Bulletin No. 194, New York, N.Y., May, 1974

7. Batcheler, R. P.
        STRESS CONCENTRATION AT GUSSET PLATES WITH CURVED
        TRANSITIONS, C.E. 103 Report, Lehigh University, Bethlehem,
        Pa., May, 1975

8. Bathe, K. J., Wilson, E. L., and Peterson, F. E.
        SAP IV - A STRUCTURAL ANALYSIS PROGRAM FOR STATIC AND
        DYNAMIC RESPONSE OF LINEAR SYSTEMS, Earthquake Engineering
        Research Center Report No. EERC 73-11, University of
        California, Berkeley, California, June, 1973
        (revised April, 1974)

9.   Biezeno, C. B. and Grammel, R.
          ELASTIC PROBLEMS OF SINGLE MACHINE ELEMENTS,
          Vol. II of Engineering Dynamics, Blackie & Son Ltd.,
          London, England, 1956, pp. 84-90

10.   Bowers, D. G.
          LOADING HISTORY, SPAN NO. 10, YELLOW MILL POND BRIDGE,
          I-95, BRIDGEPORT, CONNECTICUT, Research Project HPR 175-332
          Report, Bureau of Highways, Connecticut Department of
          Transportation, Wethersfield, Conn., May, 1972

11.   Bowie, O. L.
          ANALYSIS OF AN INFINITE PLATE CONTAINING RADIAL CRACKS
          ORIGINATING AT THE BOUNDARY OF AN INTERNAL CIRCULAR HOLE,
          Journal of Mathematics and Physics, Vol. 35, 1956, p. 60

12.   Boyer, K. D., Fisher, J. W., Irwin, G. R., Roberts, R.,
      Krishna, G. V., Morf, U., and Slockbower, R. E.
          FRACTURE ANALYSES OF FULL SIZE BEAMS WITH WELDED LATERAL
          ATTACHMENTS, Fritz Engineering Laboratory Report No.
          399-2(76), Lehigh University, Bethlehem, Pa., April, 1976

13.   Bueckner, H. F.
          THE PROPAGATION OF CRACKS AND THE ENERGY OF ELASTIC DE-
          FORMATION, Transactions, American Society of Mechanical
          Engineers, Vol. 80, 1958, p. 1225

14.   Cherry, W. R.
          STRESS CONCENTRATION FACTORS IN MAIN MEMBERS DUE TO WELDED
          STIFFENERS, Welding Journal, Vol. 20, No. 12, December,
          1941, p. 603-s

15.   Collipriest, J. E., Jr.
          AN EXPERIMENTALIST'S VIEW OF THE SURFACE FLAW PROBLEM,
          The Surface Crack: Physical Problems and Computational
          Solutions, Proceedings of the 1972 Winter Annual Meeting
          of ASME, American Society of Mechanical Engineers, 1972,
          p. 43

16.   CECA Convention No. 6210-45
          FATIGUE INVESTIGATION OF HIGHER STRENGTH STRUCTURAL STEELS
          IN NOTCHED AND IN WELDED CONDITION, Final Report,
          Communauté Européenne du Charbon et de l'Acier, Brussels,
          Belgium, April, 1974

17. Cruse, Thomas A.
    ELASTIC FRACTURE MECHANICS ANALYSIS FOR 3-DIMENSIONAL
    CRACKS, Meeting Preprint 2430, ASCE National Structural
    Engineering Convention, New Orleans, La., April, 1975

18. Ferguson, P. M.
    REINFORCED CONCRETE FUNDAMENTALS, 3rd ed., Wiley, New York/
    London/ Sydney/ Toronto, 1973, p. 86

19. Fisher, J. W., Frank, K. H., Hirt, M. A., and McNamee, B. M.
    EFFECT OF WELDMENTS ON THE FATIGUE STRENGTH OF STEEL BEAMS,
    NCHRP Report No. 102, Highway Research Board, National
    Academy of Sciences – National Research Council,
    Washington, D. C., 1970

20. Fisher, J. W., Albrecht, P. A., Yen, B. T., Klingerman, D. J.,
    and McNamee, B. M.
    FATIGUE STRENGTH OF STEEL BEAMS WITH WELDED STIFFENERS AND
    ATTACHMENTS, NCHRP Report No. 147, Transportation Research
    Board, National Research Council, Washington, D. C., 1974

21. Fisher, J. W.
    GUIDE TO 1974 AASHTO FATIGUE SPECIFICATIONS, American
    Institute of Steel Construction, New York, N.Y., 1974

22. Frank, K. H.
    THE FATIGUE STRENGTH OF FILLET WELDED CONNECTIONS,
    Ph.D. Dissertation, Lehigh University, Bethlehem, Pa.,
    October, 1971

23. Green, A. E. and Sneddon, I. N.
    THE DISTRIBUTION OF STRESS IN THE NEIGHBORHOOD OF A FLAT
    ELLIPTICAL CRACK IN AN ELASTIC SOLID, Proceedings,
    Cambridge Philosophical Society, Vol. 46, 1950, p. 159

24. Gross, B., Srawley, J. E., and Brown, W. F.
    STRESS INTENSITY FACTORS FOR SINGLE-EDGE-NOTCH TENSION
    SPECIMEN BY BOUNDARY COLLOCATION OF A STRESS FUNCTION,
    NASA TN D-2395, NASA Langley Research Center, Hampton, Va.,
    August, 1964

25. Gurney, T. R.
    FATIGUE OF WELDED STRUCTURES,
    Cambridge University Press, London, England, 1968

26. Gurney, T. R. and Maddox, S. J.
      A RE-ANALYSIS OF FATIGUE DATA FOR WELDED JOINTS IN STEEL,
      Welding Research International, Vol. 3, No. 4, 1973

27. Gurney, T. R.
      FINITE ELEMENT ANALYSES OF SOME JOINTS WITH THE WELDS
      TRANSVERSE TO THE DIRECTION OF STRESS, Welding Institute
      Report No. R/RB/E62/74, Cambridge, England, December, 1974

28. Gurney, T. R.
      CUMULATIVE DAMAGE CALCULATIONS TAKING ACCOUNT OF LOW
      STRESSES IN THE SPECTRUM, Welding Institute Report No.
      R/RB/E66/76, Cambridge, England, January, 1976

29. Harrison, J. D.
      AN ANALYSIS OF THE FATIGUE BEHAVIOR OF CRUCIFORM JOINTS,
      Welding Institute Report No. E/21/12/68, Cambridge, England,
      December, 1968

30. Hayes, D. J. and Maddox, S. J.
      THE STRESS INTENSITY FACTOR OF A CRACK AT THE TOE OF A
      FILLET WELD, Welding Institute Research Bulletin, Vol. 13,
      No. 1, January, 1972

31. Hayes, D. J.
      A PRACTICAL APPLICATION OF BUECKNER'S FORMULATION FOR
      DETERMINING STRESS INTENSITY FACTORS FOR CRACKED BODIES,
      International Journal of Fracture Mechanics, Vol. 8, No. 2,
      June, 1972, p. 157

32. Hirt, M. A. and Fisher, J. W.
      FATIGUE CRACK GROWTH IN WELDED BEAMS,
      Engineering Fracture Mechanics, Vol. 5, 1973, p. 415

33. Hirt, M. A. and Crisinel, M.
      LA RESISTANCE A LA FATIGUE DES POUTRES EN AME PLEINE
      COMPOSEES-SOUDEES - EFFET DES PLAQUETTES ET GOUSSETS SOUDES
      A L'AILE, Institute de la Constuction Métallique Report
      No. 17, École Polytechnique Fédérale de Lausanne, Lausanne,
      Switzerland, December, 1975

34. Irwin, G. R. and Kies, J. A.
      CRITICAL ENERGY RATE ANALYSIS OF FRACTURE STRENGTH,
      Welding Journal, Vol. 33, No. 4, April, 1954, p. 193-s

35. Irwin, G. R.
    ANALYSIS OF STRESSES AND STRAINS NEAR THE END OF A CRACK
    TRAVERSING A PLATE, *Transactions*, American Society of
    Mechanical Engineers, Series E, Vol. 79, September, 1957,
    p. 361

36. Irwin, G. R.
    FRACTURE, Handbuch der Physik, Vol. VI, Springer,
    Berlin, Germany, 1958, p. 551

37. Irwin, G. R.
    PLASTIC ZONE NEAR A CRACK AND FRACTURE TOUGHNESS,
    Proceedings, Seventh Sagamore Ordinance Materials Research
    Conference, August, 1960

38. Irwin, G. R.
    THE CRACK EXTENSION FORCE FOR A PART-THROUGH CRACK IN A
    PLATE, *Transactions*, American Society of Mechanical Engi-
    neers, Series E, Vol. 84, December, 1962, p. 651

39. Irwin, G. R.
    LINEAR FRACTURE MECHANICS, FRACTURE TRANSITION AND FRACTURE
    CONTROL, *Engineering Fracture Mechanics*, Vol. 1, 1968,
    p. 241

40. Jackson, C. A. and Feldt, G. V.
    MECHANICAL STRAIN RECORDER ON A CONNECTICUT BRIDGE,
    T.I. Report No. 54520-73-4, Technology Incorporated,
    Instrument and Controls Division, Dayton, Oh., January,
    1974

41. Kobayashi, A. S. and Moss, W. C.
    STRESS INTENSITY MAGNIFICATION FACTORS FOR A SURFACE FLAWED
    TENSION PLATE AND NOTCHED ROUND TENSION BAR, *Proceedings*,
    Second International Conference on Fracture, Welding
    Institute, Brighton, England, 1969, p. 31

42. Kobayashi, A. S.
    A SIMPLE PROCEDURE FOR ESTIMATING STRESS INTENSITY FACTOR
    IN REGION OF HIGH STRESS GRADIENT, *Significance of Defects
    in Welded Structures*, Proceedings of the 1973 Japan-U.S.
    Seminar, University of Tokyo Press, Tokyo, Japan, 1974,
    p. 127

43. Korn, G. A. and Korn, T. M.
    MATHEMATICAL HANDBOOK FOR SCIENTISTS AND ENGINEERS,
    2nd ed., McGraw-Hill, New York/ San Francisco/ Toronto/
    London/ Sydney, 1968, pp. 182-183

44. Krylov, V. I.
APPROXIMATE CALCULATION OF INTEGRALS, MacMillan, New York/
London, 1962, pp. 100-111 and pp. 337-340

45. Lawrence, F. V.
ESTIMATION OF FATIGUE-CRACK PROPAGATION LIFE IN BUTT WELDS,
Welding Journal, Vol. 52, No. 5, May, 1973, p. 212-s

46. Liu, H. W.
DISCUSSION, Proceedings, Crack Propagation Symposium,
Vol. II, Cranfield, England, 1961, p. 514

47. Maddox, S. J.
CALCULATING THE FATIGUE STRENGTH OF A WELDED JOINT USING
FRACTURE MECHANICS, Metal Construction and British Welding
Journal, Vol. 2, No. 8, August, 1970, p. 327

48. Maddox, S. J.
A FRACTURE MECHANICS ANALYSIS OF THE FATIGUE STRENGTH OF
WELDED JOINTS, Ph.D. Thesis, University of London, London,
England, July, 1972

49. Maddox, S. J.
FATIGUE CRACK PROPAGATION DATA OBTAINED FROM PARENT PLATE,
WELD METAL AND HAZ IN STRUCTURAL STEELS, Welding Institute
Report No. E/48/72, Cambridge, England, 1972

50. Maddox, S. J.
ASSESSING THE SIGNIFICANCE OF FLAWS IN WELDS SUBJECT TO
FATIGUE, Welding Journal, Vol. 53, No. 9, September, 1974,
p. 401-s

51. Maddox, S. J.
AN ANALYSIS OF FATIGUE CRACKS IN FILLET WELDED JOINTS,
International Journal of Fracture Mechanics, Vol. 11,
No. 2, April, 1975, p. 221

52. Madison, R. B. and Irwin, G. R.
FRACTURE ANALYSIS OF KING'S BRIDGE, MELBOURNE, Journal of
the Structural Division, American Society of Civil
Engineers, Vol. 97, No. ST9, September, 1971, p. 2229

53. Mattos, R. J.
ESTIMATION OF THE FATIGUE CRACK INITIATION LIFE IN WELDS
USING LOW CYCLE FATIGUE CONCEPTS, Ph.D. Thesis, University
of Illinois, Urbana, Ill., 1975

54. Neal, D. M.
    STRESS INTENSITY FACTORS FOR CRACKS EMANATING FROM
    RECTANGULAR CUTOUTS, International Journal of Fracture
    Mechanics, Vol. 6, No. 4, December, 1970, p. 393

55. Neuber, H.
    KERBSPANNUNGSLEHRE, 2nd ed., Springer-Verlag, Berlin,
    Germany, 1958, pp. 52-56

56. Newman, J. C., Jr.
    AN IMPROVED METHOD OF COLLOCATION FOR THE STRESS ANALYSIS
    OF CRACKED PLATES WITH VARIOUS SHAPED BOUNDARIES, NASA TN
    D-6376, NASA Langley Research Center, Hampton, Va.,
    August, 1971

57. Newman, R. P. and Gurney, T. R.
    FATIGUE TESTS OF PLAIN PLATE SPECIMENS AND TRANSVERSE BUTT
    WELDS IN MILD STEEL, British Welding Journal, Vol. 6, No. 12,
    December, 1959, p. 569

58. Norris, C. H.
    PHOTOELASTIC INVESTIGATION OF STRESS DISTRIBUTION IN TRANS-
    VERSE FILLET WELDS, Welding Journal, Vol. 24, No. 10,
    October, 1945, p. 557-s

59. Ozell, A. M. and Conyers, A. L.
    TRANSFER OF STRESSES IN WELDED COVER PLATES, Welding
    Research Council Bulletin No. 63, New York, N.Y.,
    August, 1960, p. 29

60. Paris, P. C., Gomez, M. P. and Anderson, W. E.
    A RATIONAL ANALYTICAL THEORY OF FATIGUE,
    The Trend in Engineering, University of Washington,
    Seattle, Wa., Vol. 13, No. 1, January, 1961

61. Paris, P. C.
    THE FRACTURE MECHANICS APPROACH TO FATIGUE, Fatigue -- An
    Interdisciplinary Approach, Proceedings of the Tenth
    Sagamore Army Materials Research Conference, Syracuse
    University Press, 1964, p. 107

62. Paris, P. C. and Sih, G. C.
    STRESS ANALYSIS OF CRACKS, Fracture Toughness Testing and
    Its Applications, STP 381, American Society for Testing
    and Materials, Philadelphia, Pa., 1965, p. 30

63. Peterson, R. E.
     STRESS CONCENTRATION FACTORS,
     J. Wiley & Sons, New York, N.Y., 1974

64. Popov, E. P.
     MECHANICS OF MATERIALS, Prentice-Hall, Englewood Cliffs,
     N.J., 1952

65. Randall, P. N.
     SEVERITY OF NATURAL FLAWS AS FRACTURE ORIGINS, AND A STUDY
     OF THE SURFACE-CRACKED SPECIMEN, AFML-TR-66-204, August,
     1966,(Published in ASTM STP 410, p. 88)

66. Rice, J. R.
     MECHANICS OF CRACK TIP DEFORMATION AND EXTENSION BY FATIGUE,
     Fatigue Crack Propagation, STP 415, American Society for
     Testing and Materials, Philadelphia, Pa., 1966, p. 247

67. Rice, J. R.
     PLASTIC YIELDING AT A CRACK TIP, Proceedings, First
     International Conference on Fracture, Sendai, Japan, 1965,
     p. 283

68. Scheffey, C. F.
     PT. PLEASANT BRIDGE COLLAPSE - CONCLUSIONS OF THE FEDERAL
     STUDY, Civil Engineering, American Society of Civil
     Engineers, July, 1971, p. 41

69. Schijve, J.
     ANALYSIS OF THE FATIGUE PHENOMENON IN ALUMINUM ALLOYS,
     NRL - TR M2122, 1964

70. Schilling, C. G., Klippstein, K. H., Barsom, J. M., and
     Blake, G. T.
     FATIGUE OF WELDED STEEL BRIDGE MEMBERS UNDER VARIABLE-
     AMPLITUDE LOADING, Final Report, NCHRP Project 12-12,
     U.S. Steel Research, Monroeville, Pa., August, 1975

71. Seely, F. B. and Smith, J. O.
     ADVANCED MECHANICS OF MATERIALS, 2nd ed., Wiley, New York/
     London/ Sydney/ Toronto, 1952

72. Selby, S. M., ed.
     STANDARD MATHEMATICAL TABLES, 20th ed., Chemical Rubber
     Company, Cleveland, Oh., 1972, p. 355-356

73. Shah, R. C. and Kobayashi, A. S.
    ON THE SURFACE FLAW PROBLEM, The Surface Crack: Physical
    Problems and Computational Solutions, Proceedings of the
    1972 Winter Annual Meeting of ASME, American Society of
    Mechanical Engineers, 1972, p. 79

74. Signes, E. G., Baker, R. G., Harrison, J. D., and Burdekin, F. M.
    FACTORS AFFECTING THE FATIGUE STRENGTH OF WELDED HIGH
    STRENGTH STEELS, British Welding Journal, Vol. 14, No. 3,
    March, 1967, p. 108

75. Sih, G. C.
    A REVIEW OF THE THREE-DIMENSIONAL STRESS PROBLEM FOR A
    CRACKED PLATE, International Journal of Fracture Mechanics,
    Vol. 7, No. 1, March, 1971, p. 39

76. Sih, G. C.
    HANDBOOK OF STRESS INTENSITY FACTORS, Institute of Fracture
    and Solid Mechanics, Lehigh University, Bethlehem, Pa.,
    1973

77. Smith, F. W.
    STRESS INTENSITY FACTORS FOR A SEMI-ELLIPTICAL SURFACE FLAW,
    Structural Development Research Memo No. 17, The Boeing
    Company, 1966

78. Smith, F. W., Emery, A. F., and Kobayashi, A. S.
    STRESS INTENSITY FACTORS FOR SEMICIRCULAR CRACKS, PART 2 -
    SEMI-INFINITE SOLID, Transactions, American Society of
    Mechanical Engineers, Series E, Vol. 89, December, 1967,
    p. 953

79. Solakian, A. G.
    STRESSES IN TRANSVERSE FILLET WELDS BY PHOTOELASTIC METHODS,
    Welding Journal, Vol. 13, No. 2, February, 1934, p. 22

80. Sommer, E., Hodulak, L., and Kordisch, H.
    GROWTH CHARACTERISTICS OF PART-THROUGH CRACKS IN THICK-
    WALLED PLATES AND TUBES, (To be published in ASME
    Transactions)

81. Tada, H., Paris, P. C., and Irwin, G. R.
    THE STRESS ANALYSIS OF CRACKS HANDBOOK, Del Research
    Corporation, Hellertown, Pa., 1973

82. Tada, H. and Irwin, G. R.
   K-VALUE ANALYSIS FOR CRACKS IN BRIDGE STRUCTURES,
   Fritz Engineering Laboratory Report No. 399.1, Lehigh
   University, Bethlehem, Pa., June, 1975

83. Thresher, R. W.
   A SURFACE CRACK IN A FINITE SOLID, Transactions, American
   Society of Mechanical Engineers, Series E, Vol. 94, March,
   1972, p. 195

84. Timoshenko, S. and Goodier, J. N.
   THEORY OF ELASTICITY, 2nd ed., McGraw-Hill, New York/
   Toronto/ London, 1951

85. Timoshenko, S.
   STRENGTH OF MATERIALS, PART II - ADVANCED THEORY AND
   PROBLEMS, 3rd ed., D. Van Nostrand, Princeton/ New York/
   Toronto/ London, 1956

86. Watkinson, F., Bodger, P. H., and Harrison, J. D.
   THE FATIGUE STRENGTH OF WELDED JOINTS IN HIGH STRENGTH
   STEELS AND METHODS FOR ITS IMPROVEMENT, Proceedings,
   Fatigue of Welded Structures Conference, Welding Institute,
   Brighton, England, 1971

87. Westergaard, H. M.
   BEARING PRESSURES ON CRACKS, Transactions, American Society
   of Mechanical Engineers, Series A, Vol. 61, June, 1939,
   p. 49

88. Young, E. C.
   PARTIAL DIFFERENTIAL EQUATIONS, Allyn and Bacon,
   Boston, Mass., 1972, p. 127

89. Zienkiewicz, O. C.
   THE FINITE ELEMENT METHOD IN ENGINEERING SCIENCE,
   McGraw-Hill, New York/ Toronto/ London, 1971

VITA

The author was born in Allentown, Pennsylvania on
September 18, 1944. He is the second of five offspring of Dr. and
Mrs. Albert C. Zettlemoyer.

The author received his primary education at Monocacy,
Edgeboro, and Lafayette Elementary Schools in Bethlehem, Pennsylvania.
He then attended Northeast Junior High School and Liberty High School,
also in Bethlehem. In June of 1966 he received a Bachelor of Science
Degree in Civil Engineering from Cornell University in Ithaca,
New York. In December of 1968 he was awarded the Master of Science
Degree in Architectural Engineering from Penn State University in
University Park, Pennsylvania.

In August of 1968 the author was wed to the former Miss
Janet M. Steckbeck of Bethlehem.

After graduation from Penn State the author entered the
U.S. Navy as a member of its Civil Engineer Corps. He was stationed
at N.O.B. Norfolk, Virginia from November 1969 through July 1972.
The first year of this assignment involved coordinating and adminis-
tering new construction contracts for the adjacent Naval Air Station.
The remaining portion of the tour of duty was spent as the stateside
project coordinator (design, construction, and money management) for

the totally new Naval installation at Diego Garcia in the Indian Ocean.

The author entered Lehigh University in August of 1972. Since that time he has worked as a half-time research assistant on two different projects. The first year he was associated with the Planning and Design of Tall Buildings in an editorial capacity. From October of 1973 on he has been involved with the fatigue of curved girders. The exposure to structural fatigue in general has provided the basis for his doctoral work.